Advanced Dielectrophoresis for High-Performance Single-Walled Carbon Nanotube Electronics

TECHNISCHE UNIVERSITÄT DARMSTADT

Vom Fachbereich Material und Geowissenschaften
der Technischen Universität Darmstadt
zur Erlangung des akademischen Grades
DOKTOR DER NATURWISSENSCHAFTEN
genehmigte DISSERTATION
von

M.-Ing. Wenshan Li

aus Shandong in China (中国山东)

Referent: Prof. Dr. Ralph Krupke

Korreferent: Prof. Dr. Wolfgang Ensinger

Prüfer: Prof. Dr. Jörg Schneider

Prüfer: Prof. Dr. Robert Stark

Tag der Einreichung: 28. 09. 2016
Tag der muendlichen Pruefung: 05. 12. 2016

Darmstadt 2017 – D17

– This page intentionally left blank –

The focus of this thesis is to introduce advanced dielectrophoresis technique for integrating single-walled carbon nanotubes in transistors

本论文旨在介绍先进介电泳技术在单壁纳米碳管晶体管组装中的应用

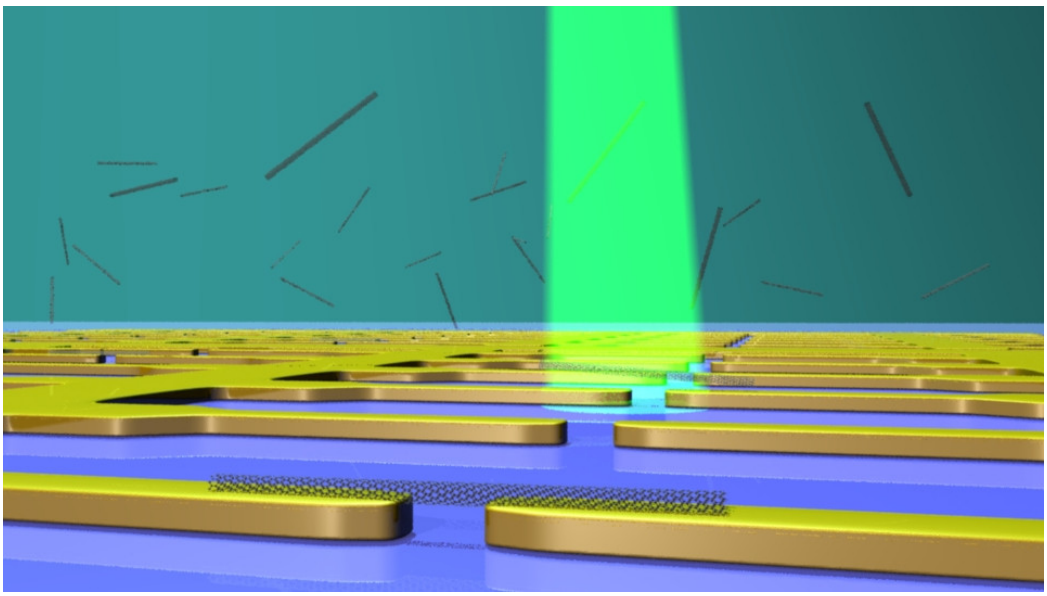

– This page intentionally left blank –

Table of Contents

Abstract

Single walled carbon nanotubes (SWCNTs) are cylindrical tubes with nanometer diameter, which can be thought of a wrapped-up mono-layer graphene sheet equivalently. Benefiting from their unique one dimensional structure, SWCNTs possess many unique electronic properties, such as high electrical conductivity, high charge mobility, low field emission threshold, high current capacity, etc. Additionally, SWCNTs can behave as either metals or semiconductors depending on their electronic band structures. These features make them one of the most promising materials for novel electronics.

The present thesis focuses on the fabrication of high performance electronics based on semiconducting SWCNT (s-SWCNT) using dielectrophoresis (DEP) techniques. There are two key requirements that have to be satisfied for efficient DEPs, i.e. 1) using SWCNT suspensions with the highest possible semiconducting content and 2) depositing s-SWCNT with high packing-density in good alignment.

Recently, toluene-based, polymer-assisted size exclusion chromatography was reported to yield over 99.7% s-SWCNT content in suspensions, which is a promising candidate for high-performance nanotube devices. Therefore, such suspensions were widely used in this thesis.

In order to make dense and well-aligned s-SWCNT deposition by DEPs, the key issue is how to enhance the polarizability of carbon nanotubes more effectively. Basically, three aspects can be taken into considerations, i.e. the s-SWCNT itself, the solvent for suspending s-SWCNTs in and the applied electric field during the DEPs.

By populating excitonic excitations, thereby pumping up free charges of SWCNT themselves using high-power laser, s-SWCNT deposition was improved using laser-coupled DEP technique, as confirmed by scanning electron microscope and electrical properties of the corresponding transistors. The achievement was attributed to the field-dependent exciton relaxations of s-SWCNTs.

In terms of DEP solvents, media with low dielectric properties were verified to be productive for enhancing the polarizability of s-SWCNTs. In addition, through analyzing orientations of nanotubes in such media under an external electric field, an efficient method was also proposed to obtain the chirality-resolved nanotube length distribution. Furthermore, it was evident that

the low-k solvent based DEPs perhaps supports a new approach towards the selective deposition of s-SWCNTs rather than their metallic counterparts when considering the difference of geometry features in SWCNTs.

Effects of electric fields on the SWCNT DEP deposition were studied using proper finite element simulations in combination with experimental characterizations, which further clarified the underlying mechanism of solution-nanotube based DEPs in presence of a direct current (DC) or alternating current (AC) field. As a consequence, low-frequency bias was demonstrated to be beneficial for pronouncing the polarizability of s-SWCNTs compared to high-frequency one. Furthermore, the low-conductive media based DC-DEPs, making use of both low-k solvent and DC bias, was demonstrated to be the most efficient way to perform the s-SWCNT DEPs under the scope of this thesis.

Lastly, s-SWCNT transistors with a hole mobility up to 297 $cm^2V^{-1}s^{-1}$ and On/Off ratio as high as 2×10^8 were achieved using DC based DEPs of toluene dispersed, polymer-wrapped SWCNTs. Moreover, by replacing the Si/SiO_2 based back-gate with weakly oxidized Al top-gate, a sub-threshold swing of 95 mV/decade of SWCNT transistors was realized.

Kurzzusammenfassung

Zukunftsweisende Dielektrophorese für Hochleistungselektronik mit einwandigen Kohlenstoffnanoröhrchen

Einwandige Kohlenstoffnanoröhren (SWCNTs, engl. single-walled carbon nanotubes) sind zylindrische Röhrchen mit einem Durchmesser im Nanometerbereich, und entsprechen einer aufgerollten Monolage von Graphen. Durch ihre einzigartige eindimensionale Struktur besitzen SWCNTs viele außergewöhnliche elektronische Eigenschaften, wie z.B. hohe elektrische Leitfähigkeit, hohe Ladungsmobilität, niedrige Feldemissionsschwelle, hohe Stromkapazität usw. Außerdem weisen SWCNTs je nach Bandstruktur metallische oder halbleitende

Eigenschaften auf. Diese Eigenschaften machen SWCNTs zu einem vielversprechenden Material für die zukünftige Elektronik.

Die vorliegende Arbeit konzentriert sich auf die Herstellung von Strukturen aus halbleitenden Nanoröhren (s-SWCNTs, engl. semiconducting SWCNTs) durch die Methode der Dielektrophorese (DEP). Für eine effiziente DEP sind dabei zwei wesentliche Anforderungen zu erfüllen. Zum Einen die Verwendung von SWCNT-Suspensionen mit einem hohen Anteil an halbleitenden SWCNTs und zum Anderen das Abscheiden von s-SWCNT in einer hoher Packungsdichte und idealer Ausrichtung.

Vor kurzem wurden Toluol Suspensionen mit einem über 99,7% Anteil an polymer umwickelten s-SWCNTs mittels Größenausschlusschromatographie hergestellt. Solche Suspensionen sind besonders geeignet für die Herstellung leistungsfähiger elektronischer CNT-Bauteile dar, und wurden im Rahmen dieser Arbeit verwendet.

Um bei der Abscheidung mittels DEP eine hohe Packungsdichte an ausgerichteten s-SWCNTs zu erreichen, sollte die Polarisierbarkeit von s-SWCNTs vergrößert werden. Dabei können grundsätzlich drei Parameter berücksichtigt werden: die s-SWCNT selbst, das Lösungsmittel zum Suspendieren von s-SWCNTs und das angelegte elektrische Feld während der DEP.

Die s SWCNT Abscheidung wurde mittels lasergekoppelter DEP verbessert, bei der durch exzitonische Anregung freie Ladungen in der SWCNTs erzeugt wurden. Durch Charakterisierung mit dem Rasterelektronenmikroskop und elektrischer Charakterisierung der entsprechenden Transistoren wurde die verbesserte Abscheidung nachgewiesen und konnte auf eine feldabhängige Exzitonenrelaxationen in s-SWCNTs zurückgeführt werden.

Zur Optimierung der DEP wurden Lösungsmittel mit niedriger dielektrischer Konstante als besonders geeignet für eine Verstärkung der Polarisierbarkeit von s-SWCNTs identifiziert. Zusätzlich wurde ein Verfahren zur Ermittlung der chiralitäts-aufgelösten SWCNT-längenverteilung entwickelt, basierend auf der Analyse der Ausrichtung der Nanoröhrchen in solchen Medien unter einem externen angelegten elektrischen Feld. Dabei lassen die Ergebnisse dieser Arbeit den Schluss zu, dass DEP mit Lösungsmitteln niedriger dielektrischer Konstante einen neuen Ansatz zur selektiven Abscheidung von s-SWCNTs bieten. Die Auswirkungen von elektrischen Feldern auf die SWCNT-DEP-Abscheidung wurden durch Finite-Elemente-Simulationen in Kombination mit Experimenten untersucht. Dabei zeigte sich, dass niederfrequente Spannungen vorteilhaft im Vergleich zu hochfrequenten Signalen sind.

Darüber hinaus wurde im Rahmen dieser Arbeit gezeigt, dass die DEP unter Gleichspannung in schwach leitfähiger Lösung die effizienteste Methode zur Abscheidung von s-SWCNTs darstellt.

Schließlich wurden in dieser Arbeit s-SWCNT-Transistoren mit einer Löcherbeweglichkeit von bis zu 297 $cm^2V^{-1}s^{-1}$ und einem On/Off-Verhältnis bis zu 2×10^8 hergestellt, wobei zur Herstellung die DC-basierte DEP von in Toluol dispergierten, polymerumhüllten SWCNTs eingesetzt wurde. Durch Austausch des Si/SiO_2-basierten Backgates mit einem dünn-oxidierten Aluminium Top-Gate wurde zudem ein Schwellenwert von 95 mV/Dekade der gemessenen SWCNT-Transistoren realisiert werden.

Declaration

I declare that this thesis, which I submit to the Technische Universität Darmstadt for examination in consideration of the degree award of Doctor of Natural Sciences is my own personal effort. Any of the content which is the result from a related collaborative research program and presented in this document has been duly acknowledged. I certify that I have not yet submitted this thesis for a degree or diploma in any university. Furthermore, a reasonable care has been taken to ensure that the work is original, and to the best of my knowledge, it does not contain any material previously published or written by another person except where such work has been cited and acknowledged within the text.

Date *Signature*

– This page intentionally left blank –

Acknowledgments

The researches presented in this thesis have been conducted at the Institute of Nanotechnology at Karlsruhe Institute of Technology, Germany and at the Department of Materials and Geosciences at Technische Universität Darmstadt, Germany.

I would like to thank to everybody who once helped and supported me both scientifically and morally during my time at the INT:

I am very grateful to Prof. Dr. Ralph Krupke for encouraging me to study in this exciting field, and supervising me as a mentor. This thesis would not have been completed without his guidance. Best thanks to him for his enduring encouragement during the past 3 years.

I am very much obliged to Prof. Dr. Wolfgang Ensinger for co-refereeing this thesis, and to Prof. Dr. Jörg Schneider and Prof. Dr. Robert Stark to be the dissertation examiners.

Many thanks to Dr. Benjamin Scott Flavel and Dr. Frank Hennrich for supplying me carbon-nanotube materials used in this thesis.

Special thanks to Simone Dehm for fabricating devices employed in this work.

Thanks to all my colleagues for their kind helps and supports. In particular, I did enjoy the moments working with: Asiful Alam, Adnan Riaz, Dr. Romain Danneau, Felix Pyatkov, Dr. Han Li, Ihteaz Hossain, Imtiaz Alamgir, Moritz Pfohl, Pranauv Balaji Selvasundaram, Rainer Kraft and Renjun Du.

Finally, I would like to thank my families. They have been supporting me throughout my studies, helped whenever I needed. I am deeply grateful to them. In particular, thank my wife, Nannan, I am appreciated her never-ending understanding and supporting.

– This page intentionally left blank –

Curriculum Vitae

Personal Information

Name	Wenshan Li
Date of birth	08.12.1987
Citizenship	Chinese

Education

09/2013 – 12/2016	Promotion:	TU Darmstadt, Germany "Advanced Dielectrophoresis for High-Performance Single-Walled Carbon Nanotube Electronics" Supervisor: Prof. Dr. Ralph Krupke
09/2010 – 06/2013	Master:	Material Engineering, Institute of Metal Research, Chinese Academy of Sciences, China
	Master thesis:	„Selective Synthesis of Specific Conductive Single-Walled Carbon Nanotubes by Floating Catalyst Chemical Vapor Deposition"
09/2007 – 07/2010	Bachelor	Computer Science, Guangxi University, China
09/2006 – 07/2010	Bachelor	Physics, Guangxi University, China

Professional Experience

since 09/2013	Research assistant at the Institute of Nanotechnology Karlsruhe Institute of Technology

– This page intentionally left blank –

Publications

The following is a list of the original publications arising from the Author's scientific studies. In particular, this thesis incorporates materials from Articles [1-4], and Conference Contributions [1-4].

Articles:

[1] Wenshan Li, Frank Hennrich, Benjamin S. Flavel, Simone Dehm and Ralph Krupke. Principles of Carbon Nanotube Dielectrophoresis (In preparation).

[2] Wenshan Li, Frank Hennrich, Benjamin S. Flavel, Manfred M. Kappes, and Ralph Krupke. Chiral-Index Resolved Length Mapping of Carbon Nanotubes in Solution Using Electric-Field Induced Differential Absorption Spectroscopy (*Nanotechnology*, 2016, 27, 375706).

[3] Frank Hennrich, Wenshan Li, Regina Fischer, Sergei Lebedkin, Ralph Krupke and Manfred M. Kappes. Length Sorted, Large-Diameter, Polyfluorene-Wrapped Semiconducting Single-Walled Carbon Nanotubes for High Density Short Channel Transistors (*ACS Nano*, 2016, 10, 1888).

[4] Wenshan Li, Feliks Pyatkov, Simone Dehm, Benjamin S. Flavel, and Ralph Krupke. Deposition of Semiconducting Single-Walled Carbon Nanotubes Using Light-Assisted Dielectrophoresis (*Phys. Status Solidi B*, 2014, 251(12), 2475).

[5] Peng-Xiang Hou, Wen-Shan Li, Shi-Yong Zhao, Guo-Xian Li, Chao Shi, Chang Liu, Hui-Ming Cheng. Preparation of Metallic Single-Wall Carbon Nanotubes by Selective Etching (*ACS Nano*, 2014, 8 (7), 7156).

[6] Shisheng Li, Peng-Xiang Hou, Chang Liu, Tianyuan Liu, Wen-Shan Li, Jin-Cheng Li, Hui-Ming Cheng. Honeycomb-like Single-Wall Carbon Nanotube Networks (*J. Mater. Chem. A*, 2014, 2, 3308).

[7] Wen-Shan Li, Peng-Xiang Hou, Chang Liu, Dong-Ming Sun, Jiangtan Yuan, Shi-Yong Zhao, Li-Chang Yin, Hongtao Cong, Hui-Ming Cheng. High-Quality, Highly Concentrated Semiconducting Single-Wall Carbon Nanotubes for Use in Field Effect Transistors and Biosensors. (*ACS Nano*, 2013, 7 (8), 6831).

[8] Guangmin Zhou, Da-Wei Wang, Peng-Xiang Hou, Wenshan Li, Na Li, Chang Liu, Feng Li, and Hui-Ming Cheng. A Nanosized Fe_2O_3 Decorated Single-Walled Carbon Nanotube

Membrane as a High-Performance Flexible Anode for Lithium Ion Batteries. (*J. Mater. Chem.*, 2012, 22, 17942).

Conference Contributions:

[1] Wenshan Li, Frank Hennrich, Benjamin Scott Flavel, Manfred Kappes, Ralph Krupke, Chiral-Index Resolved Length Mapping of Carbon Nanotubes in Solution Using Electric-Field Induced Differential Absorption Spectroscopy, 7th International Conference on the Science and Applications of Nanotubes and Low-Dimensional Materials, August 2016, Vienna, Austria, Oral presentation, CT1.

[2] Wenshan Li, Frank Hennrich, Ralph Krupke, Advanced Dielectrophoresis Based on Toluene Dispersed Single-Walled Carbon Nanotubes, 6th Workshop on Nanotube Optics and Nanospectroscopy, June 2015, Kloster Banz, Germany, Poster ID: SB28.

[3] Wenshan Li, Feliks Pyatkov, Simone Dehm, Benjamin Scott Flavel, Ralph Krupke, Deposition of Small-Diameter Semiconducting Single-Walled Carbon Nanotubes Using Light Assisted Dielectrophoresis, Annual meeting of the GDR-I GNT, September 2014, Strasbourg, France, Poster.

[4] Wenshan Li, Feliks Pyatkov, Simone Dehm, Benjamin Scott Flavel, Ralph Krupke, Deposition of Small-Diameter Semiconducting Single-Walled Carbon Nanotubes Using Light Induced Dielectrophoresis, 28th International Winterschool on Electronic Properties of Novel Materials (IWEPNM 2014), March 2014, Kirchberg, Austria, Poster TUE22.

[5] Peng-Xiang Hou, Wen-Shan Li, Chang Liu, Hui-Ming Cheng, Selective Synthesis of Semiconducting SWCNTs with High Quality and Narrow Diameter Distribution, Thirteenth International Conference on the Science and Application of Nanotubes, Abstract ID:116, June 2012, Brisbane, Australia, Oral presentation.

Patents:

[1] Peng-Xiang Hou, Wen-Shan Li, Chang Liu, Hui-Ming Cheng, "Method for Selective Synthesis of High Quality Semiconducting Single-Walled Carbon Nanotubes by *in-situ* Mild Hydrogen Etching", *Patent number*: CN103011130A, Date of publication: 3rd, April, 2013, China.

Chapter 1: Introduction

1.1. Scope of Thesis

The rapid development of integrated circuits (ICs) for logic computation has to a large extent been enabled due to the fast development of Si transistors[1]. Over decades, IC development has followed the famous trend, known as the Moore's law[2], which stated that the integration number of transistors on a processor chip doubles every 18 months by reducing transistor dimensions and increasing operating frequency. However, the continuation of this trend is now challenged because the performance of Si transistors has been pushed close to its physical limits after undergoing processes such as scaling down dimensions, increasing charge mobility by introducing strain, using high-k gate dielectrics, and designing new gating geometries[1]. With the increasing demand in integration density, transistors suffer from short channel effects such as direct tunneling from source to drain and increased gate-leakage current. Such effects give rise to severe problems for smaller sized transistors. Therefore, both industry and academia are making efforts on researching new materials, capable of replacing Si by offering superior current transport properties and improved electrostatics. One of the most promising materials is the quasi one-dimensional (1D) carbon nanotubes (CNTs), because this material possess many novel electrical properties such as large mean free path, excellent carrier mobility and ballistic conduction[3–5].

CNTs are hollow cylinders only composed of carbon atoms. Their topological structure is equivalent to rolled tubes of graphene. Thus their walls are hexagonal carbon rings[6,7]. Based on the number of walls, CNTs can be classified as single-walled CNTs (SWCNTs), consisting of a single rolled mono-layer graphene sheet, and multi-walled CNTs (MWCNTs) constituted by several concentric graphene cylinders with Van der Waals interaction binding the tubes together[8]. Geometrically, individual CNT wall can be characterized and defined by the orientation of the wrapped-up graphene lattice with respect to the tube axis, known as the chirality. In Typical, the diameters of SWCNTs and MWCNTs range from 0.8 nm to 2 nm and 5 nm to 20 nm, respectively, while their lengths can vary from less than 100 nm to several centimeters, a range bridging molecular and macroscopic scales[9].

Benefiting from their unique 1D geometry, CNTs possess many attracting mechanical, thermal, optical, and electrical properties, as shown in Figure 1.1. In turn, their exceptionally high young's modulus (~ 1TPa), tensile strength (over 50 Gpa) and breaking elongation (up to 16%)

makes them the ideal reinforcement agent for strong composite materials[10], as tips of Atomic Force Microscopy (AFM)[11] and space elevators[12]. Besides, combined with extraordinary thermal stability (2800 °C in vacuum, 750 °C in air, exceeding any other metals) and ultrahigh thermal conductivity (> 6000 $Wm^{-1}K^{-1}$ at 300 K), CNTs offer new possibilities for replacing metals in thermal management applications, such as heat sink in power electronics and heat exchangers[13–15].

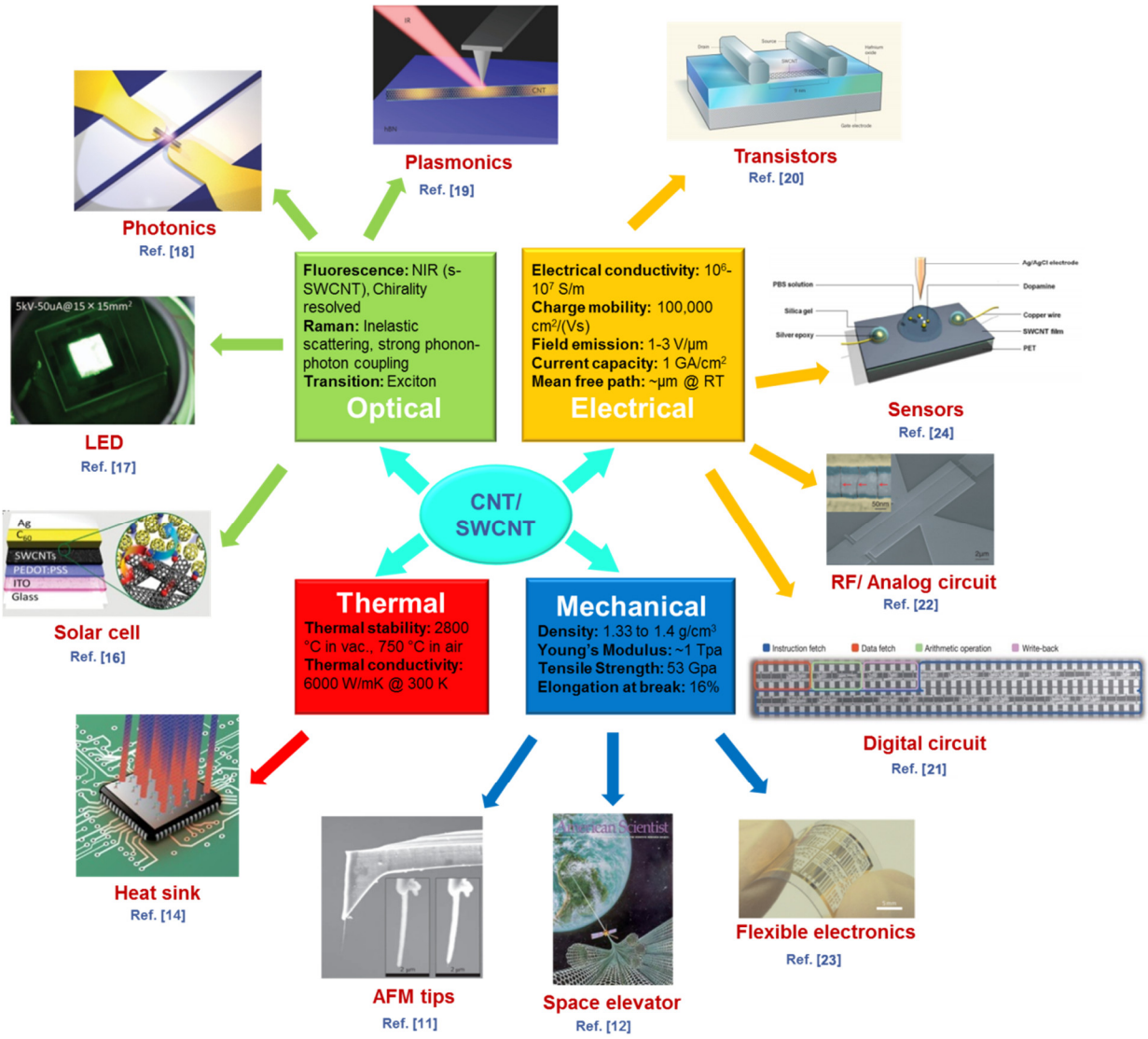

Figure 1.1: Schematic diagram of properties and applications of CNTs. Depicts with respect to applications are reproduced from Ref. [11,12,14,16–24].

The optical properties of SWCNTs arise from their electronic transitions within the one-dimensional density of states (DOS), which consists of chirality-resolved peaks known as Van Hove Singularities (vHs)[25], making them spectroscopically distinguishable. In addition,

the Coulomb interactions between the optically-excited hole and electron pair within CNTs also become stronger due to their nm-scale structural limit[26]. These properties result in not only sharp optical (band-to-band or excitonic) transitions, but also a strong photon-phonon coupling within CNTs, giving rise to many unique optical features, for instance the resonant Raman scattering[27]. Therefore, CNTs have demonstrated great potentials in various optical applications, such as solar cells[16], light-emitting diodes (LEDs)[17], photonics[18] and plasmonics[19].

In terms of the electrical features, SWCNTs exhibit more attractive properties that are not shared by MWCNT variants[28]. In particular, the band-gap of SWCNT which depends on diameter and chirality can vary from 0 to around 2 eV, making conductivity in either metallic or semiconducting way. On the other hand, a MWCNT is usually a zero-gap metal due to statistical probability and inter-wall restrictions on the diameter of each tube[29]. Besides, because of the low electron scattering within the 1D system, SWCNTs possess electrical conductivity of up to 10^6-10^7 Sm^{-1}, charge mobility of 10^5 $cm^2V^{-1}s^{-1}$ and current capacity as high as 1 $GAcm^{-2}$ [28], making them promising for high-performance electronics (such as transistors[20], digital circuits[21], analog circuits[22] and flexible electronics[23]) and sensors[24].

In addition, it has been verified that SWCNT based transistors can be performed with a sub-threshold swing lower than 60 mV/decade[30]. Furthermore, SWCNTs are also compatible with conventional field effect transistor (FET) architectures and high-k dielectrics[31,32]. Table 1-1 displays the brief performance-comparisons between CNT based FETs and Silicon based metal–oxide–semiconductor FETs (MOSFETs). It is evident that CNTs are more likely the idea candidate for miniaturizing nano-electronics beyond the limit of the state-of-the-art Si transistors.

In order to achieve high performance in SWCNT based electronics, material selection and integration are two essential aspects. For the former one, only pure semiconducting SWCNTs (s-SWCNTs), not metallic SWCNTs (m-SWCNTs), are required as channel materials of transistors. However, the efficient separation of m- and s-SWCNTs is still challenging for any synthesis methods, such as arc discharge[33,34], laser ablation[35] and chemical vapor deposition[24,36,37] etc., even combined with post-etching of m-SWCNTs[24,38]. This is because multiple nanotube species preferentially grow and present in the synthesis process. Therefore, further post-synthesis separation of SWCNTs is required according to their diameter, conductivity or even chirality.

Table 1-1: Comparisons of CNT-FETs and Si-MOSFETs, as modified from Ref. [39].

Property	Comparisons
Channel length	Typically in CNT-FET, it is less than 10 nm while in Si-MOSFET, it is 14 nm[40] (by year 2014). Smaller channel length results in better carrier transport.
Carrier mobility	Due to high-k gate dielectrics of CNT-FET, carrier mobility becomes higher than that of Si-MOSFET[41]. Carrier velocity, which is dependent on mobility, almost doubles in CNT-FET.
Ballistic conduction	In CNT-FET, the mean free path of electron is possibly larger than the channel length of device. Only contact scattering of carrier occurs[42], while in traditional MOSFET, boundary scattering occurs. This results in better conduction and lower leakage in CNT-FET.
Threshold voltage	Lower in CNT-FET which contributes to faster switching and lower power dissipation.
Gate capacitance	In p-CNT-FET, an on-current per unit width of ~1500 A/m at a gate overdrive of 0.6 V is realized while traditional p-MOSFET produces only ~500 A/m at the same gate voltage[43].
Contact resistance	Modulation of contact resistance increases the switching capacity of CNT-FET, while in Si-MOSFET, switching occurs by altering channel resistance.
Trans-conductance	Due to a better control over the gate, trans-conductance is four times higher in CNT-FET. As a consequence, small change in voltage gives large current.
Dielectric constant	Due to higher dielectric constant[44], tunneling effect decreases, which causes lower leakage and lower power comsupation in CN-FETs than Si-MOSFET.
Heat dissipation	For a CNT-FET, heat dissipation is non-uniform across the channel with highest value appearing at the source and drain sides of the channel[45]. The temperature rise has a relatively small effect on the I-V characteristics compared to Si-MOSFETs.

Basically, the separation of SWCNTs can be categorized as solid-substrate based and liquid-solution based approaches[46]. Techniques such as microwave purification[47] and electrical breakdown[48], in both of which external high-current fluxes are utilized to remove m-SWCNTs thereby purify s-SWCNTs, are known as substrate based methods. However, the packing density of remaining nanotubes prepared through these methods becomes quite low after treatments. And this density is tough to be recovered or multiplied in the follow wards due to the substrate limit. Thus, these methods are detrimental to the current-carrying performance of transistors. The well-studied solution based techniques include ultracentrifugation[49,50], normal chromatography[51,52], selective chemistry[53–55], and electrophoretic separation[56] etc. The purification and separation of specific-conductive SWCNTs through these methods have been much improved compared to the as-grown ones. However, in terms of applications, drawbacks within these methods, such as strong functionalization, low yield or low purity of s-SWCNTs, are needed to be overcome. Compared to above methods, size-exclusion chromatography (SEC)

which is performed to sort CNTs either using inorganic solvents with surfactant coating or organic ones with polyfluorene-based polymer-wrapping have demonstrated to be one of the highest specific sorting abilities toward generating s-SWCNTs with high purity (even >> 99%) even in a single sonication/centrifugation step[57–59]. Such method potentially offer the access to achieve ultra-high purity s-SWCNTs for commercial applications.

In terms of SWCNT integration, the major challenge is how to assemble individual nanotubes onto chips with precision, reproducibility and optimized packing density (not only high packing density but also low inter-tube dielectric screening). So far, methods like shear force guided SWCNT alignment[60,61] is known to be lack of fine-controlling of orientations and locations of SWCNT arrays. Langmuir-Schaefer method[54,62], a technique has been widely used for fabrication and characterization of single molecule thick films with control over the packing density of molecules, shows poor manipulation capabilities in avoid of forming double-layered SWCNT arrays, which is detrimental to transistor performances due to the increased inter-tube electrostatic screenings. Distinctly, dielectrophoresis (DEP)[63,64] has demonstrated to be more versatile to sort and deposit SWCNTs simultaneously. Unlike electrophoresis, DEP does not require the particles to be charged[65]. It affected by the particle size, geometry and the dielectric properties (a physics determined by material conductivity and permittivity) of both the particle and the solvent. As this technique makes use of induced dipole moments of SWCNT through applying local inhomogeneous electric fields, the depositions of SWCNTs can be precise, and scaled simply by optimizing the electrode structures and tuning the electric fields[63,66].

Depending on the motion of the suspended particles with respect to the field gradient, DEP can be categorized to be positive or negative, defined by the motion of particles moving into or away from the high field gradient region respectively. Because DEP is accessible to selectively manipulate specific-polarizability, charge-less particles with dimension ranging from nm up to 10 μm[67,68], it has been widely used in many applications including medical diagnostics[69], drug discovery and delivery[70], cell therapeutics[71,72] and particle filtration[73] etc.

In terms of SWCNT integration, alternating current (AC) DEP was first introduced by Krupke *et al*. in 2003 to separate out SWCNT bundles from solutions and assemble them into devices[74]. Later on, this technique was employed to produce high packing-density arrays of individual SWCNT devices[75], exhibiting the commercial feasibility of using DEP for SWCNT transistor fabrications. However, achievements of SWCNT-DEP depositions developed so far are mainly concentrated on m-SWCNTs rather than semiconducting counterparts, because the

dielectric properties of the former are much larger, making m-SWCNTs preferentially deposited under similar chip-geometries during DEPs. This phenomenon brings limits on the normal DEP technique for fabricating s-SWCNT based electronics. Thus, methods for improving DEP for this propose are urgently required.

In order to improve the quality of s-SWCNT DEP deposition, a critical question is how to enhance nanotube polarizability under a given electric field. Basically, there are three aspects for improving DEP directly, i.e. the SWCNT itself, the solvent in which the tubes are dispersed in and the applied electric field. The static and frequency dependent polarizabilities of SWCNTs have been theoretically studied[76]. To enhance the dielectric response of SWCNTs, one can either suppress the dielectric environment of nanotubes to pronounce the static component of SWCNT polarizability, or increase the frequency dependent part by tuning the modulation of charge accumulation and conduction of nanotubes using external fields (light, electric fields).

Due to the quasi-1D structure of SWCNTs, the excitonic transitions between the corresponding van-Hove singularities dominate the optical absorption of nanotubes. As studied[77], the relaxation probability of excitons to free charges (with energy states located in the continuum band) depends on the binding energy, and can also be influenced by externally applied electric fields. To enhance the polarizability of the SWCNT, more free charges need to be generated. Reasonably, this can be achieved by generating a high density of excitons with high power-density excitations along with high external electric fields since they contribute to the relaxation of excitons [78].

For high quality positive DEPs for s-SWCNTs, Li *et al*.[79] demonstrated that low dielectric (low-k) media should be employed to significantly reduce the screening effects on SWCNT dielectric properties from solvents, thereby increasing the nanotube polarizabilities. Through this approach, one can expect the increase of CNT polarizability by several orders of magnitude, which efficiently improves the s-SWCNT DEP deposition.

In terms of electric field, the frequency window for performing positive DEP deposition for s-SWCNTs is limited by either the electrolysis of electrodes, formation of electrical double layers (EDLs) at low frequency because of the existing ions in the media, or the existing negative DEPs at high frequency due to the low permittivity of s-SWCNTs compared to the solvents. For example, the frequency ranges between 10 kHz and several MHz are for a standard surfactant-water solution based s-SWCNT DEPs[80]. In order to enhance the polarizability of

s-SWCNTs, a more promising way is to make use of the conductivity role in s-SWCNT dielectric properties in comparison to the permittivity. This is because the s-SWCNT conductivity can be higher than high-diluted electrolytes, while the freedom of utilizing permittivity discrepancy between nanotubes and solvents is normally small. However, the preservation of this conductivity-dominated priority of nanotube polarizabilities is only valid at low field frequencies, which is inaccessible for normal aqueous electrolytes due to the electrolysis effect of metal electrodes and strong potential-loss across the EDLs. Thus, a proper solvent should be selected in order to achieve such low frequency s-SWCNT DEPs.

1.2. Thesis Framework

In this thesis, the principles of nanotube DEPs are investigated regarding both SWCNT separation and corresponding transistor fabrication. In Chapter 2, the theoretical background is presented to comprehend all the measurements and interpretations in the subsequent Chapters. The main content of this Chapter involves an introduction to the electrical and optical properties of SWCNTs, theoretical backgrounds of solution-nanotube motions, electrohydrodynamics of CNT-DEPs and finite element simulations, and a short note on CNT-based electronics. Experimental details of materials and methods regarding to experiments within this thesis are demonstrated in Chapter 3.

Chapter 4 focuses on the exploration of improving s-SWCNT DEP depositions based on conventional aqueous solutions using light-assisted dielectrophoresis (L-DEP), where a high power-density laser is introduced to pump up generation of excitons thereby freeing carriers in nanotubes, contributing to the enhancement of SWCNT polarizability. With observations of scanning electron microscopy (SEM), an increased deposition-density of SWCNTs is observed in L-DEPs compared to conventional DEPs. Besides, through electronic characterization, the performance of transistors fabricated using L-DEP shows higher current on/off ratios but lower on-state currents. This indicates an increase of semiconducting content within the deposited sediments. The improvement of s-SWCNT deposition can be attributed to the combined effect of the high power-density laser and the high DEP electric field: Large amounts of excitons generated by laser relaxes to free charges field-dependently, thereby enhances the S-SWCNT polarizability.

To investigate the influence of dielectric properties of solvents on s-SWCNT polarizability, the dielectric responses of s-SWCNTs dispersed in both aqueous and toluene are discussed through aligning s-SWCNTs in such liquids using an external electric field, as introduced in the Chapter

5. It is concluded that the polarizability of s-SWCNTs can be highly pronounced using toluene as the medium instead of aqueous media due to its extreme low conductance, which is also promisingly beneficial for improving the s-SWCNT deposition as low-frequency DEPs performed. Additionally, an efficient method to derive the chirality-resolved CNT length distributions is achieved, which is named as the electric-field induced differential absorption spectroscopy (EFIDAS). This technique demonstrates great potential for in-time characterization of chirality-resolved CNT lengths in future.

Under the implications from the Chapter 5, a systematic comprehension of CNT-DEPs is displayed in Chapter 6 to provide a clear scope of the physical principles of s-SWCNT DEPs, and to quantize the potential of how well s-SWCNT deposition can be achieved by DEPs. The feasibility of direct-current (DC) based SWCNT DEPs is verified when toluene is used as the solvent. Besides, the efficiency difference between toluene-based DC-DEPs, AC-DEPs and water-based AC-DEPs is also demonstrated with a standard DEP chip using proper finite element simulations. In the end, it is conclusive that the toluene-based DC-DEPs is the most promising way to perform DEPs for s-SWCNT depositions under the scope of this thesis.

In Chapter 7, preparation of toluene dispersed SWCNTs with semiconducting content >99.7% is introduced. This was carried out with SEC using proper polymer-wrapping. The deposition quality of such CNTs based on DC-DEPs is demonstrated, and the performance of nanotube transistors fabricated in this way is discussed. Using toluene-based DC-DEPs, the density of achieved s-SWCNT deposition is larger than 30 tubes/µm, resulting in an on-state conductivity of 10~20 $\mu S \mu m^{-1}$ for s-SWCNT transistors. Besides, due to the high semiconducting content of the channel material, these transistors show a hole mobility of 297 $cm^2V^{-1}s^{-1}$ and On/Off ratio as high as 10^8. Furthermore, by replacing the conventional SiO_2/Si based back-gate modulation with Al formed top-gate, a sub-threshold swing of down to 95 mV/decade for s-SWCNT based transistors is realized. All these achievements demonstrate that s-SWCNT transistors fabricated in this way is promising for future applications.

In Chapter 8, this work is summarized. Outlooks towards further improvement of s-SWCNT DEP technique and transistor performance are given.

Chapter 2: Theoretical Framework

2.1. Single-Walled Carbon Nanotube

Among carbon nanotube (CNT) families, which were reported intensively by Iijima *et al*. in 1991[81], single-walled carbon nanotubes (SWCNTs) possess quasi 1-dimensional physical structures and unique electronic properties varying from conductor to semiconductor. These features make them have been of great interest for both fundamental theoretical study and novel potential applications. In the following sections, a brief introduction on the basic properties of SWCNTs is presented.

2.1.1. Geometry

SWCNTs can be treated as constructed geometrically with rolling up a single monolayer graphene sheet, a honeycomb structure formed with carbon-atom arranged hexagonal lattices as shown in the Figure 2.1(a)[82].

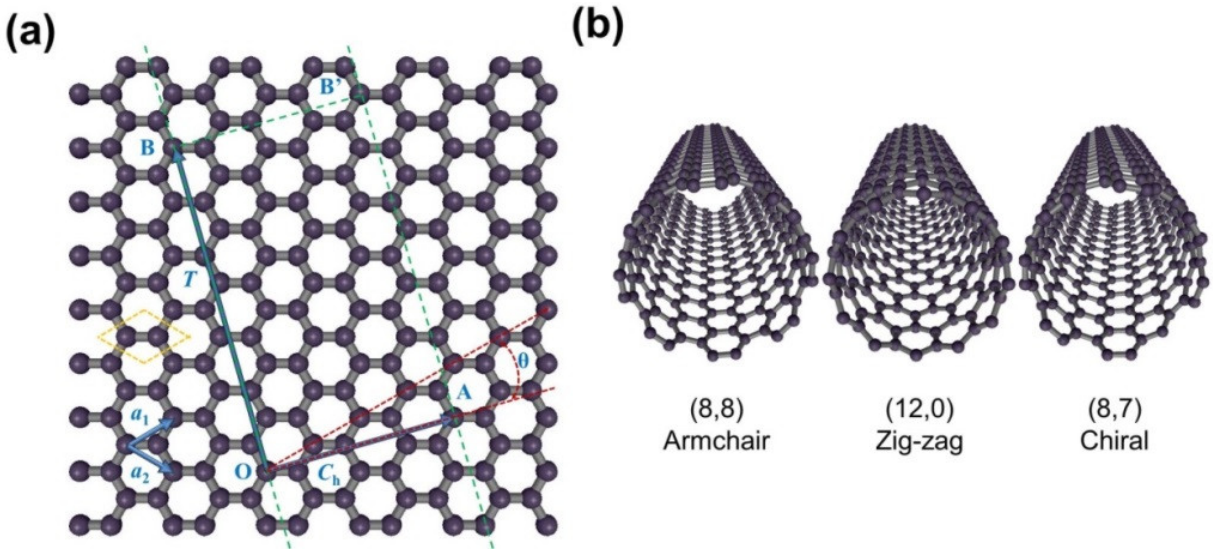

Figure 2.1: (a) The honeycomb lattice of graphene with lattice vectors $\vec{a}_{1,2}$ as well as the unit cell of a (3,1) nanotube defined by the chiral vector $\vec{C}_h$, the chiral angle θ and the translational vector $\vec{T}$. (b) Models of typical armchair (8,8), zig-zag (12,0) and chiral (8,7) nanotubes.

The lattice unit cell, as depicted within the yellow rhomboid as shown in Fig. 2.1(a), of a graphene sheet can be spanned with two vectors $\vec{a}_1$, $\vec{a}_2$. Geometrically, the length of these two vectors is obtainable with the known distance between neighboring carbon atoms $a_{cc} \cong 0.142$

nm through $|\vec{a}_1| = |\vec{a}_2| = \sqrt{3}a_{cc}$. Based on the basis of $\vec{a}_1$, $\vec{a}_2$, a specific chiral vector $\vec{C}_h$ along which the graphene sheet rolled up to form a SWCNT can be defined. This definition means that $\vec{C}_h$ connects two equivalent atomic sites in the circumference direction of the tube, as shown in Figure 2.1(a).

In practice, $\vec{C}_h$ is represented with a set of indices (n,m) known as chirality and derived using the expression: $\vec{C}_h = n\vec{a}_1 + m\vec{a}_2$. Based on this, the nanotube diameter d_{CNT} and chiral angle $\theta_{(n,m)}$ between $\vec{C}_h$ and $\vec{a}_1$ is derivable through

$$d_{CNT} = \left|\vec{C}_h\right| / \pi = \frac{\sqrt{3}a_{cc}}{\pi}\sqrt{n^2 + nm + m^2} \tag{2.1}$$

$$\cos\theta_{(n,m)} = \frac{\vec{C}_h \cdot \vec{a}_1}{\left|\vec{C}_h\right||\vec{a}_1|} \tag{2.2}$$

Taking into the symmetry of rotating graphene lattice for forming SWCNTs, magnitude of a chiral angle $\theta_{(n,m)}$ (Figure 2.1(a)) which is directly correlated with chirality is restricted within $0^\circ \le \theta_{(n,m)} \le 30^\circ$. Similarly, this also restricts the chiral indices to $n \ge m \ge 0$. Normally, when $m = 0$, indicating $\theta_{(n,m)} = 0^\circ$, the circumference of nanotubes is in a zig-zag pattern, as shown in Figure 2.1(b). Therefore, such tubes are known as zig-zag tubes. Similarly, when $n = m$, meaning $\theta_{(n,m)} = 30^\circ$, the nanotubes are called armchair tubes due to an armchair pattern along the circumference direction. Other tubes ($n \ne m \ne 0$) are known as chiral tubes.

Except for $\vec{C}_h$, another vector $\vec{T}$ (known as translational vector, Figure 2.1(a)) which denotes the lattice translational period along the tube-axis direction is needed to span the unit cell of the CNT. The length of $\vec{T}$ is strongly dependent on the CNT chirality, and can be derived by

$$\vec{T} = \frac{(2m+n)}{\gcd(2n+m, 2m+n)}\vec{a}_1 - \frac{(2n+m)}{\gcd(2n+m, 2m+n)}\vec{a}_2 \tag{2.3}$$

with “gcd” denoting the greatest common divisor.

2.1.2. Band Structure

The Brillouin zone of reciprocal space for a SWCNT are defined with two vectors, $\vec{k}_{\|}$ along the nanotube-axis direction and $\vec{k}_{\perp}$ along CNT circumference direction, as shown in Figure 2.2(a). These two vectors can be derived through the following relations

$$\begin{aligned} &\vec{k}_{\perp}\cdot\vec{C}_h = 2\pi, \quad \vec{k}_{\perp}\cdot\vec{T} = 0, \\ &\vec{k}_{\|}\cdot\vec{C}_h = 0, \quad \vec{k}_{\|}\cdot\vec{T} = 2\pi. \end{aligned} \tag{2.4}$$

Due to the high aspect ratio of a SWCNT, the longitudinal axis vector $\vec{k}_{\|}$ can be regarded as continuous within the range of $-\pi/\left|\vec{T}\right| < k_{\|} \le \pi/\left|\vec{T}\right|$ along the tube-axis direction. Unlikely, the vector $\vec{k}_{\perp}$ is quantized, because the wave function along the circumference of the nanotube must match a phase shift of integer multiple of 2π to allow for the formation of a standing wave expressed as

$$\mu\cdot\frac{2\pi}{k_{\perp,\mu}} = \left|\vec{C}_h\right| = \pi d_{CNT} \Leftrightarrow k_{\perp,\mu} = \frac{2}{d_{CNT}}\cdot\mu \tag{2.5}$$

here μ is an integer related to the graphene-hexagon number $N = 2(n^2+nm+m^2)/\gcd(2n+m, 2m+n)$ within the unit cell of nanotubes, and defined by $\mu = -N/2, ..1, 0, 1, .., N/2$. These above features result in N lines of allowed k-states within the first Brillouin zone of the nanotube (Figure 2.2 (a)), with direction of these lines parallel to the tube-axis and being separated by a factor of π/d_{CNT} (For more information, see literatures of e.g., Thomsen *et al.*[7]).

For an infinite graphene lattice in which four valence orbitals of carbon atoms present sp^2 hybridization, $2s$, $2p_x$ and $2p_y$ orbitals form the strong in-plane covalent bonding σ and anti-bonding σ^*, while the $2p_z$ orbital forms the non-localized van der Waals bands of π and π^*, as shown in Figure 2.2(b). Based on the zone-folding approximation, the potential separation between the σ and σ^* bands is high up to several eV, which is too large to bridge the conduction of graphene, while the π and π^* bands showing a linear dispersion near the K

points (Figure 2.2(b)) of the Brillouin zone, dominating the electronic properties of graphene and make it a conductor.

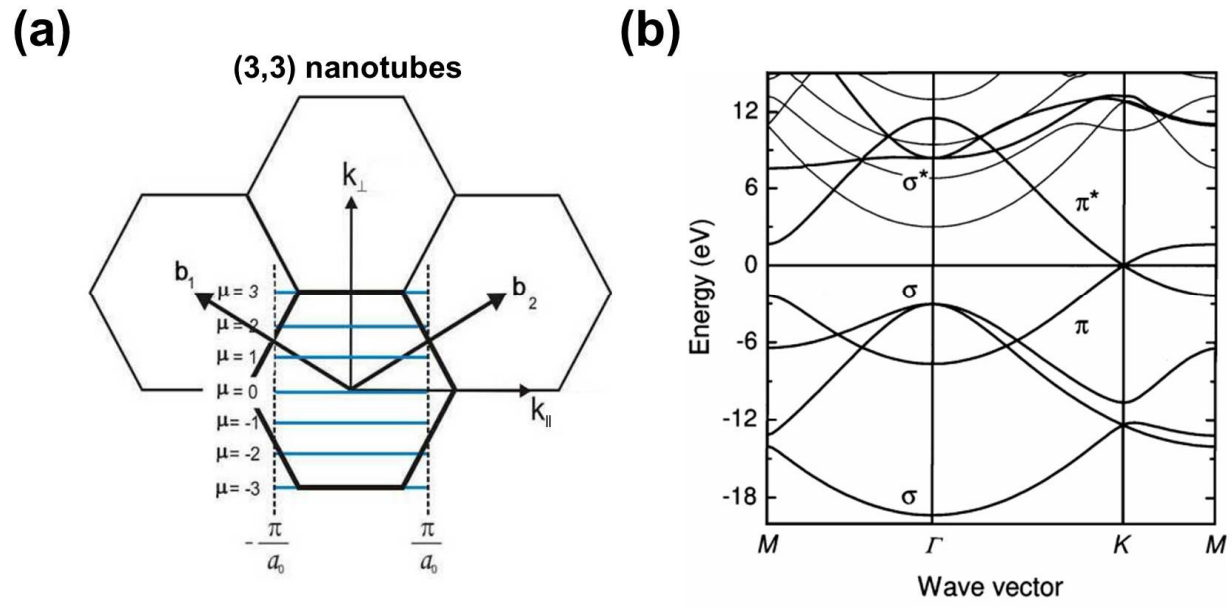

Figure 2.2: (a) Schematic drawing of the first Brillouin zone of a (3,3) nanotube. (b) Electronic band structure of graphene along the *Γ*, *K*, *M* direction. Modified from Ref. [7].

The zone-folding approximation is also accessible for simulating SWCNT band-structure (as shown in Figure 2.3(b)). This can be done with folding the $\vec{k}_z$-direction electronic energies $E_\mu^{\pi,\pi^*}(k_x,k_y)$ of graphene (Figure 2.3(a)) along the parallel lines of allowed k-states.

Within the Brillouin zone of graphene, the only cross between its valence and conduction bands occur at the K points (Figure 2.2(b)) with location of $\vec{K}=1/3(\vec{b}_1-\vec{b}_2)$ in reciprocal space, which implies that the nanotube presents metallic merely when the allowed k-state lines pass through these K points, otherwise it is a semiconductor. Thus, a chirality-resolved electrical properties of SWCNTs can be derived, and expressed as

$$\vec{K}\cdot\vec{C}_h = 2\pi\mu = \frac{1}{3}(\vec{b}_1-\vec{b}_2)(n\vec{a}_1+m\vec{a}_2) \Leftrightarrow n-m=3\mu. \tag{2.6}$$

This equation indicates that the SWCNT is metallic (m-SWCNT) when $n-m$ is integer multiple of three, meaning the density of states at the Fermi level is non-zero as shown in Fig. 2.3(b). Unambiguously, the definition for a semiconducting SWCNT (s-SWCNT) can be

given by $n-m=3\mu\pm1$. In this situation, an energy gap ΔE exists which describes the energy distance between the valence and conduction bands at the Fermi level, and can given in the first approximation as

$$\Delta E=\frac{2\pi a_{cc}\gamma_0}{\left|\vec{C}_h\right|}=\frac{2a_{cc}\gamma_0}{d_{CNT}}. \tag{2.7}$$

Here, $\gamma_0=2.9\text{eV}$ presents the transfer integral between first neighbor π orbital employed in the binding derivation of graphene energy dispersion.

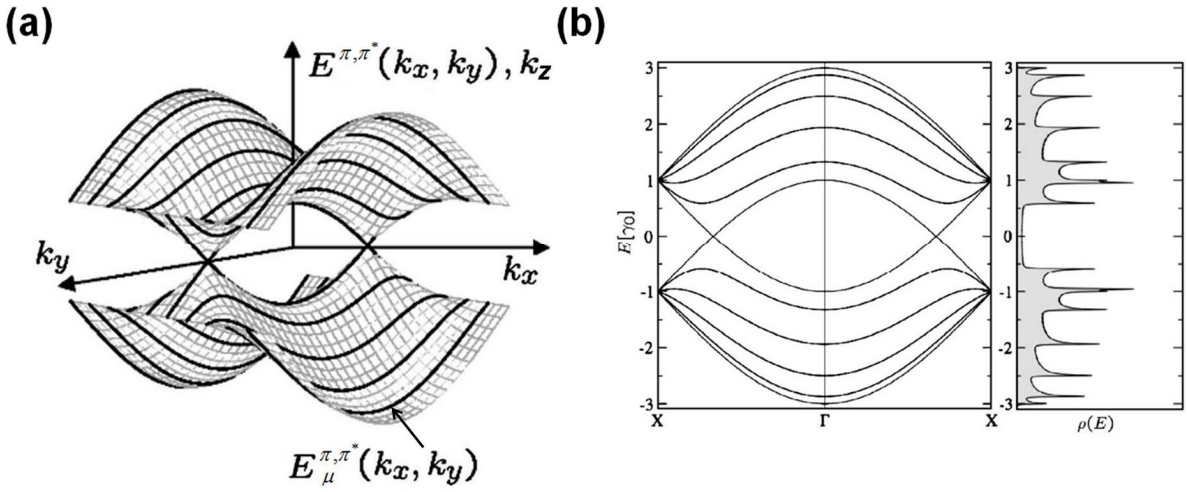

Figure 2.3: (a) Energy dispersion of $\pi,\pi*$ bands within the Brillouin zone of graphene, and the corresponding $\vec{k}_z$-direction projection $E_\mu^{\pi,\pi^*}(k_x,k_y)$ for one armchair nanotube. (b) Band structure (left graph) and density of states (right graph) for one (5,5) armchair nanotube. Reproduced from Ref. [83].

Although the zone-folding approach yields reliable descriptions for electrical properties of SWCNTs, typically for those with $d_{CNT}\geq1.5$ nm, it fails to explain one shift known as the curvature effect of Fermi vector k_F from the graphene Brillouin zone corners K for small diameter SWCNTs[84]. For that case, the *ab initio* method is needed to derive electronic band structures for SWCNTs[83].

The density of states $n(E)$ of one-dimensional materials consists of a set of singularities $\sim1/\sqrt{E}$, known as van Hove singularities (vHs), located near the extrema of energy bands.

The vHs play crucial roles in determining physical properties of materials due to the high density of states at these points. In terms of SWCNTs, this physics can be derived using[7]

$$n(E) \propto \sum_i \int dk \delta(k - k_i) \left| \frac{\partial E_i^{\pm}}{\partial k} \right|^{-1}. \quad (2.8)$$

with $E_i^{\pm}$ standing for the i^{th} eigenvalues of band energy of graphene under the tight binding approximation, and given by $E - E_i^{\pm}(k) = 0$. The right section of Figure 2.3(b) demonstrates the calculated density of states for a (5,5) nanotube. It is evident that the positions of vHs correspond to the points of vanishing slope in the energy dispersion as displayed in the left graph. Because of such high density of states at vHs, many physical properties of SWCNTs, for instance the optical absorption/emission[85], scanning tunneling[86] and resonant Raman scattering[87], are pronounced at these points.

2.1.3. Optical Properties

The unique energetic band features of SWCNTs give rise to many attracting optical properties, which can be demonstrated in optical spectroscopies such as the UV-Vis-IR absorption spectroscopy, photoluminescence, Raman spectroscopy etc.

1. Absorption

As mentioned above, the density of states at the vHs is quite high which makes optical transitions between electronic states of corresponding singularities becoming significant [88].

When a CNT is illuminated with incident light that is linearly polarized and propogating parallel to the tube axis, its optical transitions E_{ii} between two vHs sub-bands with the same angular momentum number μ are allowed[89,90]. Moreover, because the CNT band gap is strongly dependent on the nanotube's chiral properties, this interpretation indicates that the chirality of SWCNT can be characterized via the optical absorption measurement (Figure 2.4(a)). However, for multi-chiral nanotubes, especially for those with large diameters, E_{ii} transitions become too close to each other, making chirality assignment difficult.

For the optical absorption perpendicular to the longitudinal direction of nanotubes, cross-polarized excitation is needed. This transition follows the selection rule of $\Delta\mu = \pm 1$, which provides more details regarding the electron-hole asymmetry of nanotubes between the

valence and the conduction bands, and beneficial for the chirality-assignment in many cases, such as polarized photoluminescence (PLE) excitation spectroscopy[91].

2. Photoluminescence

PLE (Figure 2.4(b)) is widely used for the characterization of isolated semiconducting nanotubes[85,92]. It involves the exciting of CNTs using monochromatic light of a broad energy range, for instance varying from E_{11}^{S} to E_{44}^{S}, and detecting of the emission from the nanotubes[93]. Typically, the relative emission intensity is referred to the relative abundance of the different (n,m) species in the specimen of interest. However, this technique is not suitable for identifying metallic tubes because the non-radiative electron-hole recombination processes such as acoustic phonon assisted recombination inhibit fluorescence[94] in them. Deducibly, light emission from isolated m-SWCNTs or s-/m-SWCNT bundles is strongly suppressed and invisible under PLE characterizations.

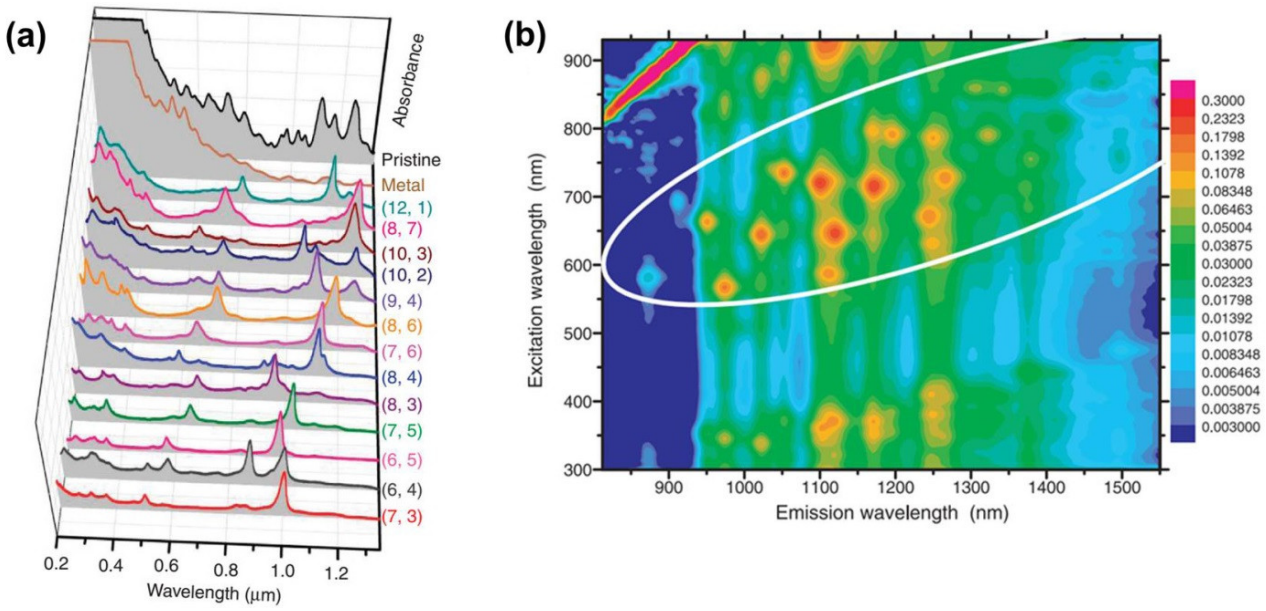

Figure 2.4: (a) Chirality-resolved optical absorption spectra of SWCNTs, reproduced from Ref. [95]. (b) Typical PLE maps of SWCNTs, modified from Ref. [96].

Although both absorption and photoluminescence spectroscopy allow for a comparative population analysis of different nanotube species in a sample, an absolute value cannot be derived without the known corresponding (n,m) optical absorption efficiency and cross section.

As both the efficiency and transition are strongly dependent on the dielectric ambient[97], further studies are required to derive these parameters with respect to specific conditions.

3. Excitons

Arising from the 1D character of SWCNTs, the Coulomb interaction between the optically excited electron-hole pairs is strongly enhanced compared to bulk semiconductors. Under such situation, single-particle interband theory in which electronic excitations are predominantly at the inter-band transitions (As shown in Fig.2.5(a and b), here k_ψ denotes the tube-axis electron wave vector) and contribute to free electron–hole pairs, deviates substantially from experimental observations[98,99]. Thus multi-body effects should be accounted[100] in which electron–hole interactions allow for the formation of bound electron–hole pairs (known as excitons) below the free particle continuum (Fig.2.5(c)) even at the room temperature[101].

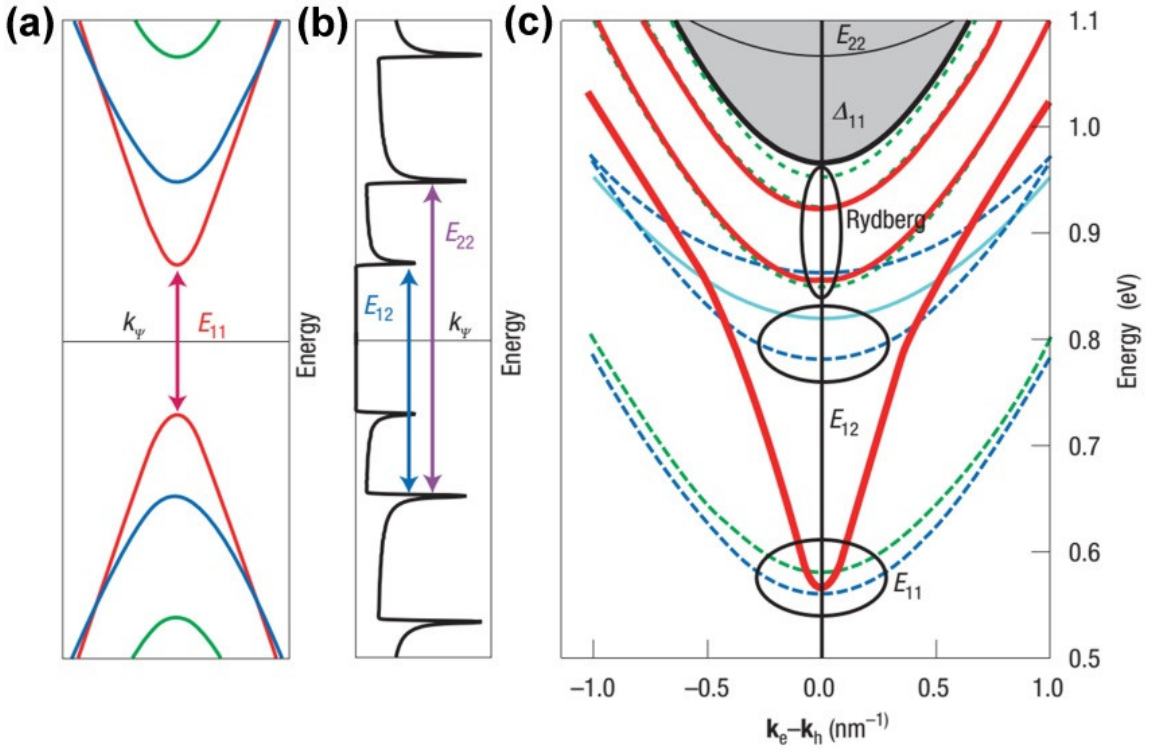

Figure 2.5: (a) Band structure of a (19, 0) SWCNT, and corresponding (b) single-particle interband model based density of states as well as (c) low-lying excitonic states based on the multi-body effect simulation. Modified from Ref. [102].

The binding energies E_b of excitons in nanotubes have been theoretically predicted[103] and experimentally measured to be as large as several hundred meVs for s-SWCNTs[104] and tens

of meVs for m-SWCNTs, the latter being a result of enhanced screening effect within the nanotube[105]. Numerical correlations between E_b and the CNT diameter, chirality as well as the ambient dielectric property, has been studied by Perebeinos *et al.*[106] which is given by $E_b \approx A_b (d_{CNT}/2)^{\alpha-2} m^{*\alpha-1} \varepsilon^{-\alpha}$, with the empirical parameters $\alpha = 1.4$, $A_b = 24.1$ eV, derived by solving the Bethe-Salpeter equation. Thus it is speculated that E_b decreases with respect to the increase of d_{CNT} or surrounding dielectric ε. Moreover, in low dielectric environments, most of the oscillator strength of SWCNT optical transitions is transferred from the inter-band transitions to the excitonic ones as studied in Ref. [101].

Strong electron–electron interactions within SWCNTs squeeze the degeneracy of the fourfold degenerate electron–hole excitations originating from the doubly degenerate valence and conduction bands within the single-particle model. Considering a (19,0) SWCNT[97,102], a new set of excitonic states (wave vector $k_e - k_h$, with k_e, k_h denoting the wave vectors of electrons and holes respectively) including "dark excitons" which is a forbidden state due to selection rules mentioned above, appeared below the free particle continuum band Δ_{11} of the (19,0) SWCNT after the removal of this degeneracy (Fig.2.5(c)). The "dark excitons" include the lowest energy even parity exciton with zero circumferential angular momentum and double degenerate excitons with finite circumferential angular momenta above the optically active excitons, which is in odd-symmetry of zero circumferential angular momentum thereby optically forbidden. Notably, the lowest-energy forbidden transition can acquire oscillator strength and thus be 'brightened' through defects, distortions or the application of external fields[107,108].

4. Raman

Raman scattering demonstrates the inelastic scattering of light-matter interactions during their optical phonon emission or absorption process[109]. The intensity of Raman scattering is normally low as only the direct virtual states are excited. However, it becomes well pronounced when the optical phonon absorption or emission is coupled with a real electronic excitation of interesting materials, known as resonant Raman scattering. For SWCNTs, it is possible to directly measure the Raman signal of an individual nanotube due to the specific resonance condition of each CNT species (Figure 2.6), making resonant Raman spectroscopy one of the most sensitive approaches for SWCNT characterization[110].

For SWCNTs, two dominant Raman scattering modes are significant for characterizations. One is the radial breathing mode (RBM) with its shift ω_{RBM} ranging between 120 and 350 cm^{-1} for tubes with 0.7 nm $< d_{CNT} <$ 2 nm. This mode demonstrates the coherent vibration of carbon atoms in the radial direction and is (n,m) specific, as shown in Figure 2.6. Based on the excitation of this mode, the presence of carbon nanotubes within a given specimen can be verifed efficiently. Besides, the diameter d_{CNT} of SWCNTs can also be derived using RBM mode according to $\omega_{RBM} = A/d_{CNT} + B$ with two constants A, B being determined experimentally[111]. Another well-known mode called the G mode which has a Raman shift ω_G of 1550–1590 cm^{-1}. G mode arises from the tangential vibration (a single peak at 1582 cm^{-1}) between two neighboring carbon atoms within the unit cell of graphite (Figure 2.6)[6]. For CNTs, the G mode is composed of two parts, G^- and G^+, correlated with vibrations along and perpendicular to the longitudinal axis of tubes respectively. As studied[112], the line shape of G^- mode is significantly dependent on the nanotube conductive properties. It indicates the existence of m-SWCNTs when a line shape of Breit-Wigner-Fano accompanying the peak-frequency downshift is observed in this mode. This feature is normally used to make a distinguish between s- and m-SWCNTs[24,37].

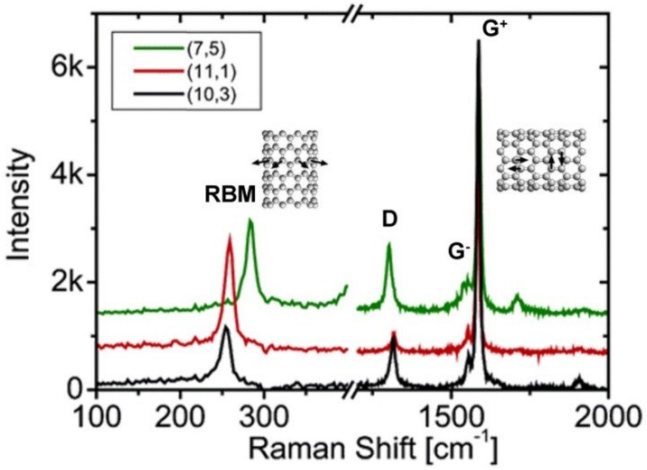

Figure 2.6: Raman spectra of isolated SWCNTs by 633 nm excitations, reproduced from Ref.[113].

2.1.4. Electronic Properties

m-SWCNTs have sub-bands intersecting the symmetric Fermi points $k = \pm K$. Since each Fermi point contributes a forward wave-vector and a backward wave-vector, there are exactly four forward and four backward electron states under the consideration of the spin degeneracy.

Without considering charge transport scattering, each state can contribute to a quantum conductance of $G_0 = e^2/h = (26k\Omega)^{-1}$.

Based on the Landauer theory[114] which includes the elastic scattering of charge transport within SWCNTs by using a non-unity transmission coefficient T, one can convert the total conductance of all four channels to

$$G = G_o \sum \mathrm{T}_i \tag{2.9}$$

For an idealized m-SWCNT with four parallel, unity-transmission channels (T=1), this conductance is a constant of ~ 155 μS and temperature independent.

Unlike traditional metal conductors where inelastic electron-phonon scattering from acoustic phonons limit their electrical conductivity, this scattering within SWCNTs is strongly suppressed. The reason is that the electron states within CNTs can only be scattered into a few number of unoccupied electronic states that require a large momentum transfer[115]. This phenomenon gives rise to the mean free path l_{e-ph} (~0.5 μm at room temperature) for inelastic scattering, indicating that the electron-phonon scattering is suppressed in submicron-scaled CNT devices.

Figure 2.7(a) demonstrates the conduction dependence of SWCNTs with respect to their lengths. It depicts that for short nanotubes (< 0.5 μm in this case), the conductance is almost equivalent to the ideal value of 155 μS derived by equation (2.9). With an increase of bias across the nanotube, the electron-phonon scattering becomes significant, which gives rise to the SWCNT resistance as shown in Figure 2.7(b). The electrons can accumulate energy under an applied electric field due to the suppression of electron scattering and thermalization within nanotubes. Once the energy of an optical phonon is achieved (about 0.18 eV), spontaneous emission will occur[116]. In contrast to metals, where optical phonon emission is rarely observed due to heavy self-heating and electro-migration degradation before the phonon emission regime can be reached, SWCNTs can carry currents of up to 20 μA, corresponding to a current density of over 10^8 A/cm^2 without degradation. Thus, the I-V curve is nearly constant under these conditions. However, when the optical phonon emissions become pronounced, the current saturates with an increase in source-drain bias. Therefore, in order to achieve larger currents, this emission should be suppressed. By efficiently scaling down the dimension of devices, it is evident that

the reduction of electron-optical phonon scattering in nanotubes under high bias can be realized[117,118].

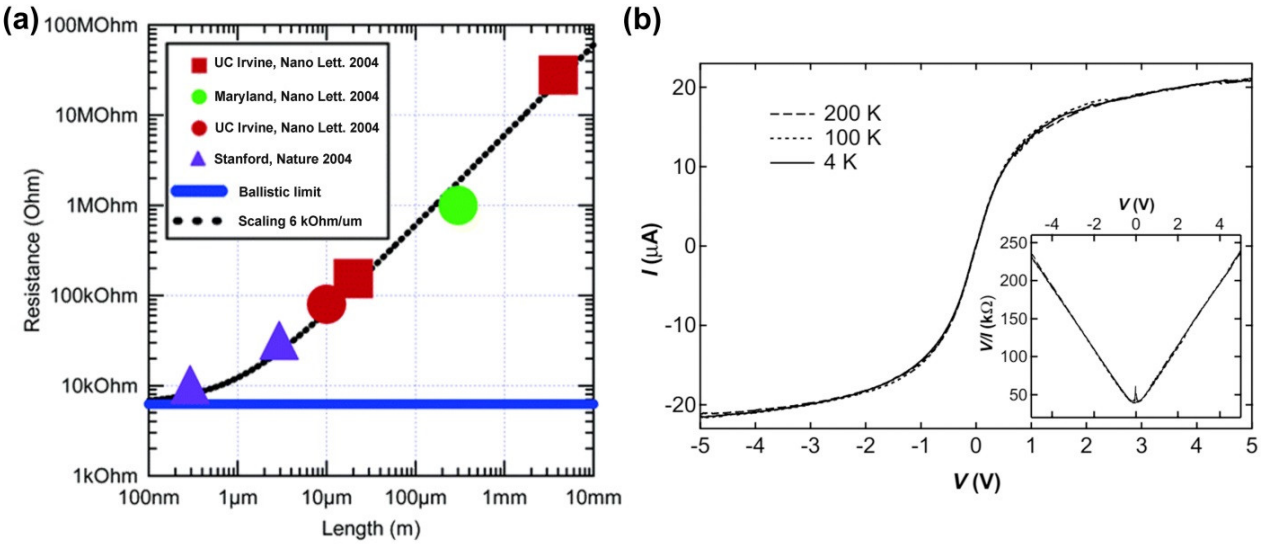

Figure 2.7: (a) The dependence of SWCNT resistance versus device length, reproduced from Ref. [119] (with data taken from Ref. [119] (red square), [120] (green sphere), [121] (red sphere) and [122] (blue triangle). (b) I-V performance of SWCNT devices, as well as the voltage-dependence of resistance (inset), reproduced from Ref. [116].

A field-effect transistor (FET), a device in which an electric field is applied to control the electrical conductivity of the channel material, is used for the study of s-SWCNT electrical properties. Since all carriers reside on the wall surface, the field sensitivity of s-SWCNTs is exquisitely pronounced compared to bulk semiconductors, which is desirable for high-performance FETs. This topic is explained in details in the Chapter 2.6.

2.2. SWCNT Synthesis

The first developed method for carbon nanotube synthesis is the electric arc discharge. This technique was once used in the preparation of carbon fibers by R. Bacon *et al*. in early 1960s, and fullerenes by Krätschmer and Huffman in 1990s. Later on, this technique was improved and applied for the synthesis of multi-walled CNTs and SWCNTs. Other methods such as the laser evaporation/ablation and chemical vapor deposition (CVD) were also developed for growing carbon nanotubes. For more information, a review of A. Szabó *et al*. [123] is recommend. Based on the experimental requirements in the following Chapters, two types of CNT-synthesis techniques will be briefly introduced within this section.

2.2.1. High Pressure Carbon Monoxide

In 1999, Richard E. Smalley *et al*. developed a chemical-vapor-deposition (CVD) technique for synthesis of CNTs, known as HiPco[124]. In this method, a continuous-flow gas phase carbon monoxide under high pressure acts as the feedstock, and ion clusters (derived from thermal decomposition of Fe(CO)5) work as the catalyst for CNT growth. This technique can yield SWCNTs of high quality, and provide continuous growth of nanotubes in the presence of the carbon monoxide[125], making it promising for large scale production of SWCNTs (Figure 2.8).

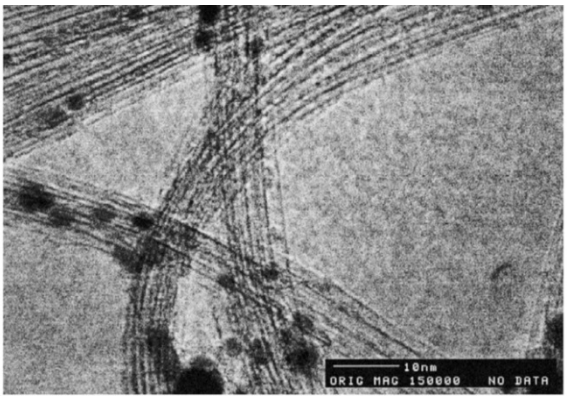

Figure 2.8: Typical high-resolution transmission electron microscopy (TEM) image of CNTs synthesized by HiPco, modified from Ref. [124].

2.2.2. Pulsed Laser Vaporization

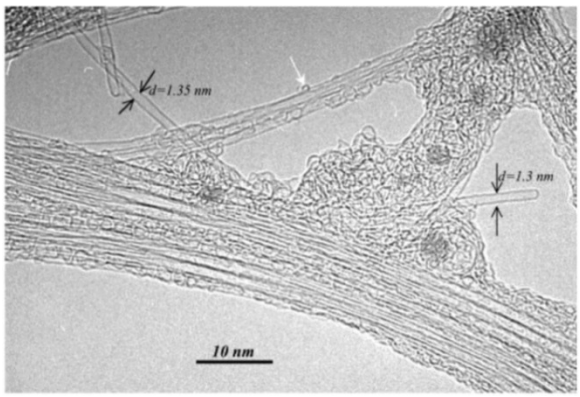

Figure 2.9: Typical high-resolution transmission electron microscopy image of CNTs synthesized using PLV technique, modified from Ref. [126].

The commonly used Nd:YAG lasers for SWCNTs synthesis have been reported to be effective in production of high quality SWCNTs [127,128]. Eklund *et al*[126] first introduced the use of subpicosecond laser pulses for the large-scale production of SWCNTs, known as pulsed laser

vaporization (PLV) technique. Because the temperature distribution of reaction region can be well controlled under this way, PLV yields nanotubes with quite uniform diameters, as shown in the Figure 2.9.

2.3. Dispersion of SWCNTs

Solution-based SWCNTs compared to their solid-based counterparts in which the transferring and sorting of tube samples are much difficult can provide more freedom in well placing nanotubes and SWCNT separations with respect to material conductivities, even chiralities. These priorities make them promising for studies of CNT electronics and optoelectronics. In order to disperse SWCNTs individually into either water[129–131] or organic solvents[132,133], proper functionalization should be applied covalently[134,135] or non-covalently to nanotube walls[131,136,137]. Covalent chemistry routes introduce functional groups to the ends and sidewalls of nanotubes, rendering them soluble with respect to solvents[135,138]. Using these methods, individual nanotubes can be well-dispersed in suspensions, making it possible to sort nanotube with respect to tube diameters[135,139] or electronic types[140]. However, the electrical performance of the SWCNTs functionalized in this way will be lowered due to the disruption of the conjugated π band of the nanotubes induced through sp^3 hybridization[141]. On the other hand, for non-covalent approaches, surfactants such as sodium cholate (SC)/sodium dodecyl sulphate (SDS)[49,95], or organic polymers[132,133], are used to stabilize CNT agents with proper ultra-sonication processing[142].

2.3.1. Surfactant Coating

Among the non-covalent approaches, surfactant coating is widely used in the preparation of SWCNT aqueous suspensions[95,143]. In brief, the added surfactants in water initially form a random layer on the nanotube wall and then more surfactant molecules bind onto it, forming a hemi-micelle. As studied, the correlation between nanotube structure and surfactant coating configuration is dependent on differences in the surface π electron states of the various SWCNT curvatures, which determine the interaction between surfactants and nanotubes[95]. In general, when an SDS molecule surrounds around a small-diameter nanotube of a large bond curvature, a larger energy is required to bend the molecule on to the CNT wall[144]. Thus, the SDS molecules prefer coating larger-diameter nanotubes with smaller curvatures compared to the small-diameter ones[49,145]. Besides, the extent of SDS coating is also dependent on the electronic character of SWCNTs. As a consequence, m-SWCNTs present a higher degree of SDS wrapping than s-SWCNTs because of its higher polarizability[49,130].

2.3.2. Polymer Wrapping

Dispersing SWCNTs with wrapping of aromatic polymers into organic solvents can produce stable nanotube suspensions, which is receiving an increasing attention because it demonstrates attractive sorting-selectivity (>99%) for s-SWCNTs[59,146]. During this approach[147], raw carbon nanotube materials are firstly dispersed in organic solvents using ultra-sonication with the existence of a suitable polymer, then followed by ultracentrifugation. Consequently, only SWCNTs which possess preferential interaction with the polymer can suspend in the solvent.

Polymers for instance poly(9,9-dioctylfluorene-2,7-diyl) (PFO)[132], poly[9, 9-dihexylfluorenyl-2,7-diyl)-co-(9,10-anthracene)] (PFH-A)[148], poly[(9,9-dioctylfluorenyl-2,7-diyl)-co-1,4-benzo-[2,1'-3]-thiadiazole)] (PFO-BT)[133], and poly(9,9-di-n-dodecylfluorenyl-2,7-diyl) (PODOF)[128] have been widely employed in s-SWCNT sorting. Regarding to the sorting mechanism, it is commonly attributed that the polymer interacts with a s-SWCNT by aligning the aromatic backbone along its wall so that maximize π-π stacking[149–151], thereby suspend the nanotube in the liquid. However, disregarding the influence of temperature, in order to achieve individual s-SWCNT wrapping, an upper limit for the polymer concentration exists, beyond which bundling of metallic tubes begins in the sorted-suspension[152].

Wang *et al*.,[153] outlined three rules for the choice of CNT-dispersing solvents. Firstly, the solvent must solubilize the polymer, while the SWCNTs must have a low intrinsic solubility, so that only the polymer-wrapped nanotubes are dispersed. Secondly, the density of the solvent must be lower than SWCNTs in order to assure the unwrapped SWCNTs can sediment out the solution after centrifugation. Additionally, the solvent should be nonpolar (such as toluene, o-xylene, and m-xylene) in order to prevent the solvent interacting with the polarized polymer-wrapped m-SWCNTs, thus allowing for better selective sorting of s-SWCNTs.

2.4. Dielectrophoresis of SWCNTs

The motion of dielectric particles under the influence of an inhomogeneous external electric field is called dielectrophoresis (DEP). Motions of carbon nanotubes during the DEP process are mainly determined by local electric fields which exert imbalanced forces on the induced dipoles of nanotubes, moving them inwards (positive dielectrophoresis) or outwards (negative dielectrophoresis) from deposition regions with respect to gradient directions of the electric fields. Aside from dielectrophoretic forces, other effects, for instance gravitational forces and

Brownian motion, are also responsible for the motion of SWCNTs during DEP. In order to quantitatively describe the motions of SWCNTs thereby precisely integrating them into devices, all mechanical factors contributing to either the translational or rotational motions of nanotubes during DEPs should be analyzed systematically.

2.4.1. SWCNT Polarizability

When a SWCNT is placed in an uniform electric field $\vec{E}$, a dipole moment $\vec{p} = \alpha\vec{E}$ with α denoting the polarizability tensor is induced. Based on the tight-binding model and neglecting local electric field[89], the correlation between the real part of the dielectric function $\varepsilon(\vec{q},\omega)$ and the unscreened polarizability α_0 per unit cell of SWCNTs is given by

$$\lim_{\vec{q}\to 0}\varepsilon(\vec{q},\omega) = 1 + \frac{4\pi}{\Omega}\alpha_0(\omega) \tag{2.10}$$

here Ω stands for the area of the CNT unit cell, and $\vec{q}$ is the wave vector.

Figure 2.10 displays the schematic diagram of SWCNT DEP. Because of the cylindrical structure of nanotubes, only two principal axes 1, 2 representing the parallel and perpendicular directions to nanotube axis respectively out of three Cartesian coordinates 1, 2, 3 should be considered. Through this way, only the elements of polarizability tensors α^{11} and α^{22} are non-zero. When the wave vector $\vec{q}$ along these axes tends to be zero, the unscreened polarizability element of CNTs can be derived by

$$\alpha_0^{11} \sim \frac{d_{CNT}}{2\Delta\overline{E}^2}, \quad \alpha_0^{22} \sim \frac{d_{CNT}^2}{4}. \tag{2.11}$$

with $\Delta\overline{E}$ standing for the average energy of the CNT transition[89].

The relationship between the unscreened polarizability α_0 and screened polarizability α which is the experimentally accessible quantity can be determined by $\vec{p} = \alpha\vec{E} = \alpha_0\vec{E}_{tot}$, with the local electric field $\vec{E}_{loc} = \vec{E}_{tot} - \vec{E}$. If $\vec{E}$ goes along the 2-axis, the SWCNT bound-surface charges leads to a local depolarization field. With assuming this local field is constant inside the nanotube, the corresponding screened polarizability element α^{22} is given by

$$\alpha^{22} = \frac{\alpha_0^{22}}{1 + 8\alpha_0^{22} / d_{CNT}^2}. \tag{2.12}$$

For a given $\vec{E}$ along the 1-axis, the corresponding local electric field $\vec{E}_{loc} > 0$ due to the finite length of SWCNTs in which charges accumulate at the tube ends. However, for nanotubes with significantly larger length/diameter ratio, the 1-axis screened polarizability element can be treated as $\alpha^{11} = \alpha_0^{11}$ due to the negligible charge accumulation at the further ends.

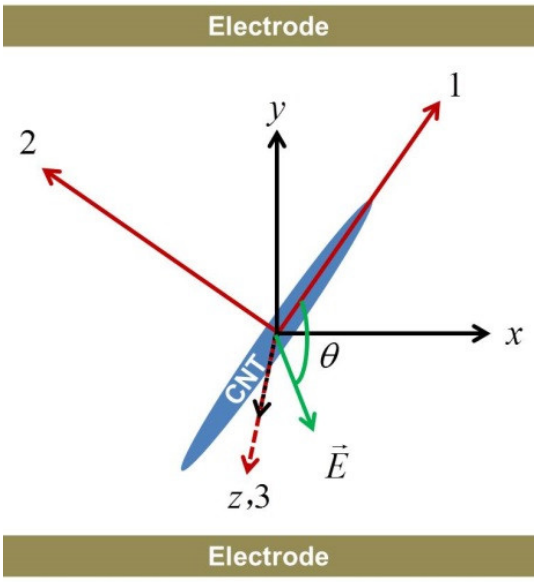

Figure 2.10: Diagram of the SWCNT dielectrophoresis system.

As reported from Ref. [76,154], α^{11} is much larger than α^{22} for SWCNTs because of the heavier dimensional limit of electronic wave-function along 2-axis. This indicates that the electric field induced dipole moment of nanotubes primarily points along the tube axis. Besides, unlike electronic bang-gap independent α^{22}, the longitudinal axis polarizability α^{11} of nanotubes depends critically on their electronic band structures as described by equation (2.11). Therefore, for zero-band-gap metallic nanotubes, their polarizability is significantly larger than that of s-SWCNTs[155].

2.4.2. Translational Motion Analysis

1. Stokes Motion

For a microsystem of fluids, the Reynolds number which is defined as a ratio of inertial forces to viscous forces for given flow conditions is very small[67,156]. Therefore, experienced inertial

forces of particles moving in fluids are negligible compared to the viscous forces exerted from the media, implying that particles moves in the form of Stoke's motion.

The translational movement of a CNT experiencing a force $\vec{F}$ in the fluid, as stated by the Stoke's motion, can be expressed as

$$m_{CNT}\frac{d\vec{u}_{CNT}}{dt} = -\gamma(\vec{u}_{CNT} - \vec{v}) + \vec{F} \tag{2.13}$$

where m_{CNT} is the CNT mass, $\vec{u}_{CNT}$, $\vec{v}$ denotes the velocities of the CNT and fluid respectively.

The term $-\gamma(\vec{u}_{CNT} - \vec{v})$ of the eq. 2.13 represents the drag force of this nanotube as moving in the fluid, with γ standing for the friction factor, governed by $\gamma = 3\pi\eta l_{CNT}/\ln(2l_{CNT}/d_{CNT})$, here l_{CNT}, d_{CNT} are the length and diameter of the CNT, η is the viscosity of the medium[157]. Therefore, under a constant force $\vec{F}$ and fluid velocity $\vec{v}$, the CNT velocity can be given by

$$\vec{u}_{CNT} = \left(\vec{u}_{0,CNT} - \vec{v} - \frac{\vec{F}}{\gamma}\right)\exp^{-(\gamma/m)t} + \vec{v} + \frac{\vec{F}}{\gamma} \tag{2.14}$$

with $\vec{u}_{0,CNT}$ indicating the initial velocity of the CNT. A characteristic time for this motion acceleration, $\tau = m_{CNT}/\gamma$, notably is shorter than 10^{-11} seconds (Figure 2.11, a referrable computation can be found in the Matlab program P2-1 as stored in the attached CD) for a single CNT with length < 1 μm and diameter < 2.5 nm dispersed in either water ($\eta = 0.894$ mPa·s, see Appendix A) or toluene ($\eta = 0.583$ mPa·s) at the room temperature of 300 K. Thus for a given observation time larger than τ, the CNT can be treated as moving at a terminal velocity given by

$$\vec{u}_{CNT} = \vec{v} + \frac{\vec{F}}{\gamma} \tag{2.15}$$

In general, the acceleration process of CNT motions is much more complicated than the above simple analytical solution because the acceleration of fluids and diffusion of vorticity are not considered here.

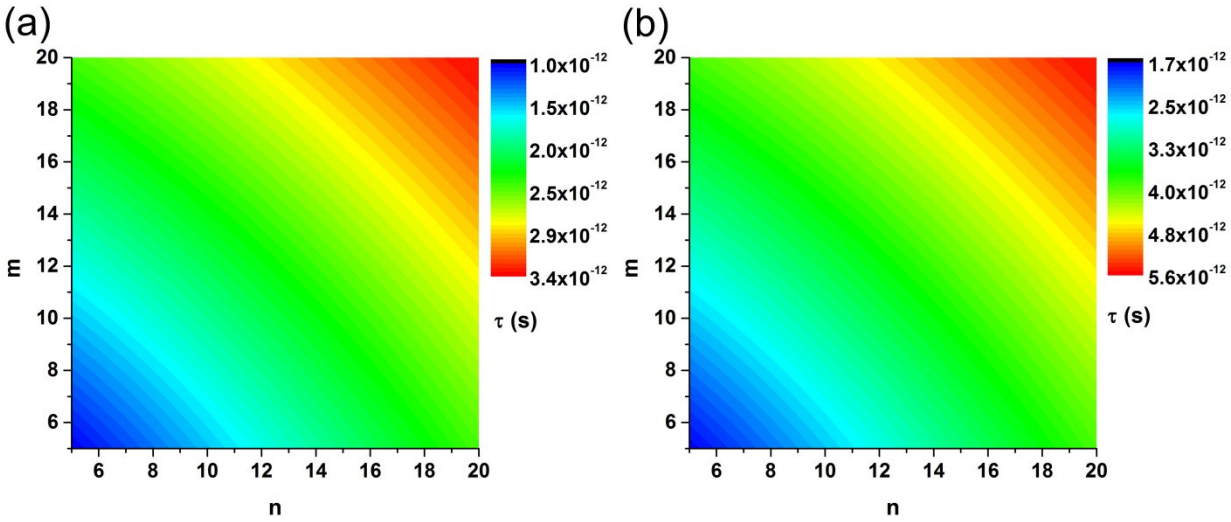

Figure 2.11: The chirality-resolved characteristic time of Stokes motion for carbon nanotubes dispersed in (a) water and (b) toluene with l_{CNT} = 1 μm. Calculation details can be referred to the Matlab program P2-1 as stored in the attached CD.

2. Gravitational Force

Mass densities of pure (n, m) SWCNTs can be simply approximated as $\rho_{CNT} = 3.89\times10^4 / \sqrt{n^2+m^2+mn}$ kg/m^3 through considering nanotubes can be treated as rolled up geometries of monolayer graphenes[158,159]. Thus, the experienced gravitational force for a CNT in a fluid of density ρ_m can be given by

$$\vec{F}_g = \upsilon(\rho_{CNT} - \rho_m)\vec{g} \tag{2.16}$$

where $\vec{g}$ is the gravitational acceleration, $\upsilon = \pi l_{CNT} d_{CNT}^2 / 6$ is the volume of ellipsoid-shaped SWCNTs. Therefore, the magnitude of a CNT velocity induced by the gravity is

$$\vec{u}_g = \frac{\upsilon|\rho_{CNT} - \rho_m|\vec{g}}{\gamma} = \frac{d_{CNT}^2 \ln(2l_{CNT}/d_{CNT})|\rho_{CNT} - \rho_m|\vec{g}}{18\eta} \tag{2.17}$$

Figure 2.12 (calculated through the P2-2) shows the calculated gravitational-force induced, chirality-resolved terminal velocities of 1 μm long SWCNTs dispersed in (a) water ($\rho_m = 1\times10^3$ kg/m^3, see Appendix A) and (b) toluene ($\rho_m = 867$ kg/m^3) respectively based on the equation (2.17). As shown in both cases, the gravitational terminal velocities of the

SWCNTs are below 10^{-10} m/s, which indicates that the influence of gravitational forces on CNT deposition is negligible compared to those of the Brownian motions and dielectrophoretic forces as given below.

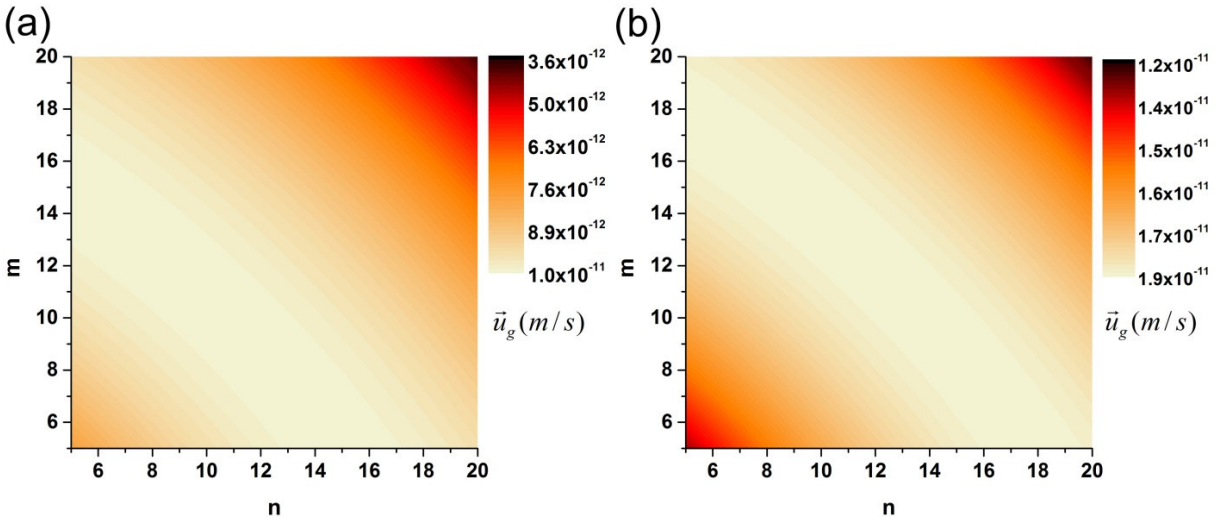

Figure 2.12: Gravitational force induced chirality-resolved terminal velocities of carbon nanotubes dispersed in (a) water and (b) toluene with l_{CNT} = 1 µm. Calculation detials can be referred to the Matlab program P2-2 as stored in the attached CD.

3. Brownian Motion

Brownian motion is the random motion of particles originating from their collisions with atoms or molecules of fluids or gases in which they are suspended[160].

In general, random displacements of solution-dispersed CNTs arising from the Brownian motion follows a Gaussian profile with a root-mean square (rms), and can be presented as[161,162]

$$\Delta L = \sqrt{2Dt} \tag{2.18}$$

where, L is the displacement of CNTs in liquids driven by the Brownian motion, and D denotes the diffusion tensor of the nanotubes moving in solutions, t is the characteristic time for observations. For ellipsoidal particles like CNTs, two translational hydrodynamic friction factors γ_{par} and γ_{per} are needed to describe both the long-axis parallel and perpendicular motions of such uniaxial anisotropic particles in liquids[163–165].

As studied[161], two-dimensional translational diffusion projection D_{trans} of 3D Brownian motions of CNTs, can be written as

$$D_{trans} = \frac{k_B T}{6\pi\eta} \frac{2\ln(l_{CNT} / d_{CNT}) - \gamma_{par} - \gamma_{per}}{l_{CNT}} \tag{2.19}$$

In order to derive the magnitude of the Brownian motion, a nanotube with 1 nm d_{CNT}, 1 μm l_{CNT} is considered here (as shown in the Figure 2.13 and calculated using the program P2-3). The derived D_{trans} is estimated to be 3.06 μm^2/s for tubes in water, and 4.95 μm^2/s for toluene case at a room temperature of 300 K. Therefore, Brownian motion can yield several orders of magnitude larger displacement than the gravitational force regarding to CNT translocations in fluids within the same time interval. Thereby one can address that the effective DEP process occurs only when the translational displacements of CNT-DEPs are larger than that induced by the Brownian motion.

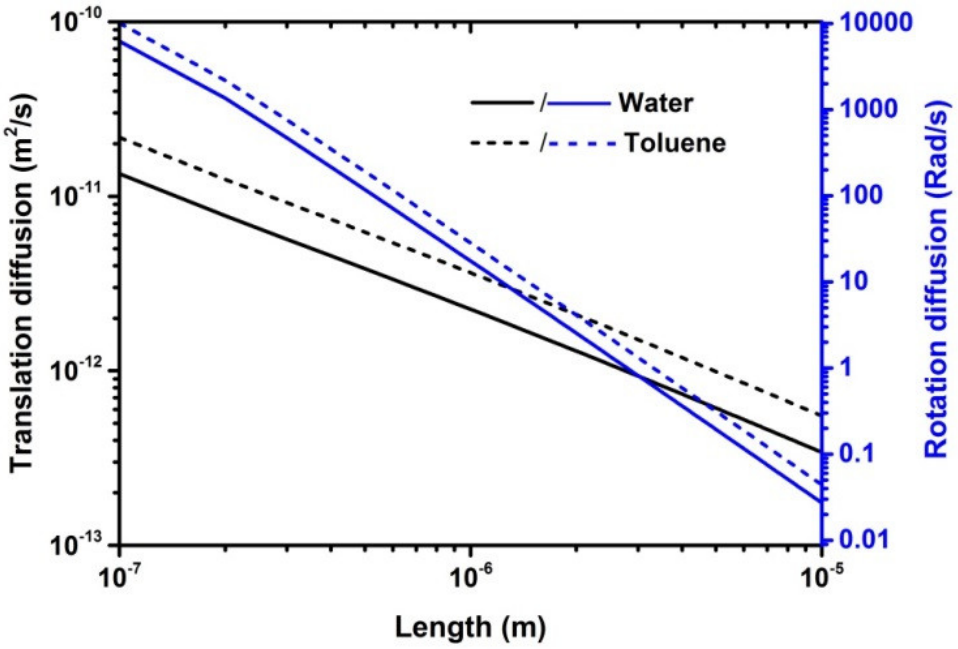

Figure 2.13: Length dependence of translational and rotational Brownian diffusions for CNTs dispersed in water and toluene with d_{CNT} = 1.5 nm. Calculation detials can be referred to the Matlab program P2-3 as stored in the attached CD.

4. Dielectrophoretic Force

Based on Pohl's theory[166], DEP force $\vec{F}_{DEP}$ of particles in the non-uniform electric fields can be expressed as:

$$\vec{F}_{DEP} = (\vec{p} \cdot \nabla)\vec{E} \tag{2.20}$$

where $\vec{p}$ is the induced dipole moment of the particle through the electric field $\vec{E}$. The effective dipole moment of this particle within this field can be formulated as

$$\vec{p} = \upsilon \tilde{\alpha} \vec{E} \tag{2.21}$$

here $\tilde{\alpha}$ presents the unit volume complex effective polarizability of this particle.

The typical DEP system for prolate-ellipsoid particles, such as CNTs, is shown in the Figure 2.10. In order to describe both directions of electric fields and orientations of CNTs, two sets of three orthogonal axes are needed: x, y, z are picked to define the direction of the electric field, and 1, 2, 3 axes depict the radii axis a_1, a_2, a_3 of the CNT respectively. The angle θ represents the relative orientation between the electric field and the long axes 1 of the nanotube. Based on these definitions, the effective polarizability of a single nanotube with respect to each principal axis n (n=1, 2, 3) can be expressed as[157]

$$\tilde{\alpha}_n = \varepsilon_m \tilde{f}_{CM,n} \tag{2.22}$$

with

$$\tilde{f}_{CM,n} = \frac{\tilde{\varepsilon}_{CNT} - \tilde{\varepsilon}_m}{(\tilde{\varepsilon}_m + (\tilde{\varepsilon}_{CNT} - \tilde{\varepsilon}_m) L_n)}, \quad \tilde{\varepsilon} = \varepsilon - i\frac{\sigma}{\omega} \tag{2.23}$$

here, parameters $\tilde{\varepsilon}_{CNT}$, $\tilde{\varepsilon}_m$ stand for complex dielectric permittivities of the nanotube and medium respectively. ε and σ indicate their real parts of permittivity and conductivity, and ω represents the angular frequency of the electric field. Parameter $\tilde{f}_{CM,n}$ is obviously frequency dependent and is known as the Clausius-Mossotti factor (CMF)[79,80,167]. The depolarization index L_n is determined by the CNT geometry, and can be derived through an elliptical integral[168]. In practice, CNT length l_{CNT} is much larger than the width d_{CNT}, which gives rise to the L_2 and L_3, making $L_2 = L_3 \approx 1/2$ but significantly suppressing the component $L_1 = d_{CNT}^2 / l_{CNT}^2 \left[\ln(2l_{CNT}/d_{CNT}) - 1\right] \ll 1$ (as shown in Fig. 2.14 and computated with P2-4).

Typically, the electric field gradient perpendicularly across a nanotube is negligible compared to that along its longitudinal axis, thus the experienced DEP force of the SWCNT can be well

approximated by only considering its longitudinal-axis component. Thereby the time-averaged DEP force of nanotubes is simplified as

$$\left\langle \vec{F}_{DEP} \right\rangle = \frac{1}{2}\Re\left[(\vec{p}\cdot\nabla)\vec{E}^{*}\right] = \frac{1}{4}\upsilon\Re\left[\tilde{\alpha}_1\right]\nabla\left|\vec{E}\right|^2 - \frac{1}{2}\upsilon\,\mathrm{Im}\left[\tilde{\alpha}_1\right](\nabla\times(\Re\left[\vec{E}\right]\times\mathrm{Im}\left[\vec{E}\right])) \quad (2.24)$$

where $*$ indicates complex conjugation, $\Re$ and Im are the real and imaginary parts of variables in concern. The first term $1/4\,\upsilon\Re\left[\tilde{\alpha}_1\right]\nabla\left|\vec{E}\right|^2$ is non-zero for a spatially varying electric field, while the second term $-1/2\,\upsilon\,\mathrm{Im}\left[\tilde{\alpha}_1\right](\nabla\times(\Re\left[\vec{E}\right]\times\mathrm{Im}\left[\vec{E}\right]))$ is non-zero only if there is a spatially varying phase within DEP circuits, implying it is negligible under low field frequencies. This is because the corresponding wavelengths of the applied electric fields are much larger than the characterization lengths of typical DEP devices. Therefore, the spatial phase can be thought of a constant under this situation. Based on this assumption, the time average DEP forces of CNTs can be simplified to

$$\left\langle \vec{F}_{DEP} \right\rangle = \frac{\pi d_{CNT}^2 l_{CNT}}{12}\varepsilon_m\Re\left[\frac{\tilde{\varepsilon}_{CNT}-\tilde{\varepsilon}_m}{(\tilde{\varepsilon}_m+(\tilde{\varepsilon}_{CNT}-\tilde{\varepsilon}_m)L_1)}\right]\nabla\left|\vec{E}_{rms}\right|^2 \quad (2.25)$$

$\vec{E}_{rms}$ is the root mean square of the electric field $\vec{E}$. Regarding to more discussions of DEPs, Ref. [67] is recommended.

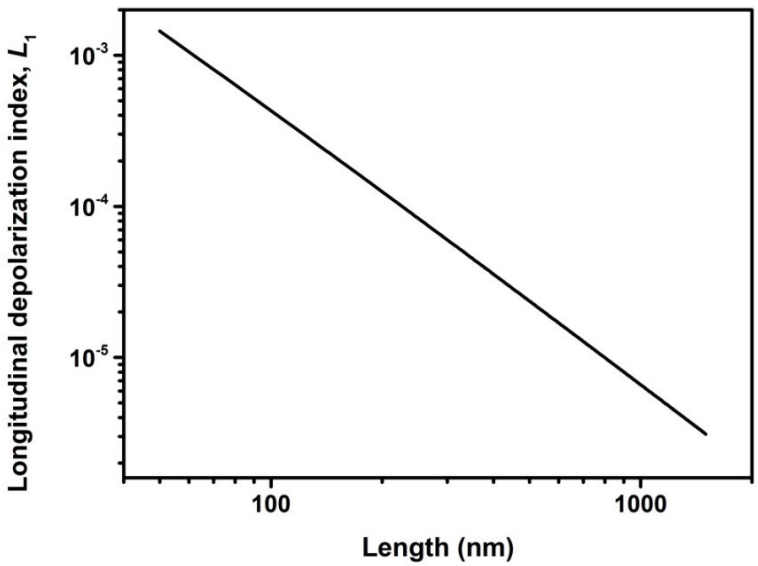

Figure 2.14: Length dependence of the longitudinal depolarization index of CNTs with diameter of 1 nm. Calculation detials can be referred to the Matlab program P2-4 in the attached CD.

Notably, in practice the dipole approximation for DEPs is invalid when the CNT is close to a null field or in a region where the field strength varies significantly, such as the edges of the electrode terminals. Under those circumstances, higher order electrical moments (quadrupole, octopole, etc.) and the corresponding force terms become significant and should be concerned.

Considering dimensionless L_1 is of the order of 10^{-5} for a 1-μm long nanotube (as shown in Fig. 2.14). Subjectively, the high- and low-frequency limits of the CMFs (as described in eq. 2.23) of SWCNTs can be simplified as

$$\lim_{\omega\to\infty} \tilde{f}_{CM} = \frac{\varepsilon_{CNT} - \varepsilon_m}{\varepsilon_m} \tag{2.26}$$

$$\lim_{\omega\to 0} \tilde{f}_{CM} = \frac{\sigma_{CNT} - \sigma_m}{\sigma_m} \tag{2.27}$$

Recently, Li *et al*.[79] reported that the low frequency approximation of the CMFs as displayed in the eq. 2.27 is inaccurate when surfactant-aqueous medium (for instance 0.01w-% sodium dodecyl sulfate (SDS)-water (denoted as 0.01-w%-SDS water), with $\sigma_m \approx 0.004$ S/m, see Appendix A) was replaced by low conductivity solvent, such as toluene ($\sigma_m \le 10^{-11}$ S/m). Under that situation, the role of depolarization index L_1 in determining magnitude of $\tilde{f}_{CM}$ increases when the conductivity of the medium drops dramatically. Thus for the case of toluene, the low frequency approximation of the CMFs becomes only CNT geometry dependent, and the equation (2.27) is transformed into

$$\lim_{\omega\to 0} \tilde{f}_{CM} = \frac{\sigma_{CNT}}{\sigma_{CNT} L_1} = \frac{1}{L_1} = \frac{l_{CNT}^2}{d_{CNT}^2 \left[\ln(\frac{2l_{CNT}}{d_{CNT}}) - 1 \right]} \tag{2.28}$$

Therefore, one can speculate that the deposition rates of longer s-SWCNTs may exceed those of shorter m-SWCNTs with toluene working as the dispersing medium during DEPs with DC electric fields. However, this phenomenon normally is not accessible due to the occurrence of electrolysis when a large DC bias is applied in DEP.

2.4.3. Rotational Motion Analysis

1. Brownian-Motion Induced Torque

Aside from the translational displacements of the Brownian motion, SWCNT can also rotate freely in liquids. Hence the dissipative coupling of translational to rotational motions needs to be considered, which can be described with a diffusion coefficient γ_r.

According to the Broersma theory[162], the rotational diffusion tensor D_{rot} of a prolate ellipsoid is given by

$$D_{rot} = \frac{3k_B T}{\pi\eta} \frac{\ln(l_{CNT} / d_{CNT}) - \gamma_r}{l_{CNT}^3} \tag{2.29}$$

under same assumptions as mentioned in Chapter 2.4.2, here the calculated D_{rot} are 24.29 and 39.31 rad/s for CNTs dispersed in water and toluene respectively (as shown in Fig. 2.14). Therefore, the effective integrations in which CNTs can be well aligned are accessible only when the DEP induced rotational displacements of CNTs are larger than those induced by the Brownian motion.

2. DEP Torque

DEP torque $\vec{T}_{DEP}$ of particles can be expressed as[166]:

$$\vec{T}_{DEP} = \vec{p} \times \vec{E} \tag{2.30}$$

In terms of the rotation of SWCNTs during DEPs, one common approach to derive the dielectrophoretic torques is to define the electric field vectors within the 1-2 plane (as shown in the Fig. 2.10), meaning $\vec{E}_{rms,3} = 0$. Therefore $\langle T_{DEP} \rangle_1 = \langle T_{DEP} \rangle_2 \equiv 0$ and the time averaged dielectrophoretic torques are derived using the expression[7]

$$\langle T_{DEP} \rangle_3 = \frac{\pi d_{CNT}^2 l_{CNT}}{6} (L_2 - L_1) \vec{E}_{rms,1} \vec{E}_{rms,2} \varepsilon_m \Re\left[\tilde{f}_{CM,1} \cdot \tilde{f}_{CM,2} \right] \tag{2.31}$$

with $\vec{E}_{rms,1} = \vec{E}_{rms} \cos\theta$ and $\vec{E}_{rms,2} = \vec{E}_{rms} \sin\theta$. Integrating eq. 2.23 into above equation, one can derive

$$\langle T_{DEP} \rangle_3 = \frac{\pi d_{CNT}^2 l_{CNT}}{6} \left| \vec{E}_{rms} \right|^2 \varepsilon_m \Re\left[\frac{\tilde{\varepsilon}_{CNT} - \tilde{\varepsilon}_m}{(\tilde{\varepsilon}_m + (\tilde{\varepsilon}_{CNT} - \tilde{\varepsilon}_m) L_1)} - \frac{\tilde{\varepsilon}_{CNT} - \tilde{\varepsilon}_m}{(\tilde{\varepsilon}_m + (\tilde{\varepsilon}_{CNT} - \tilde{\varepsilon}_m) L_2)} \right] \sin\theta \cos\theta \tag{2.32}$$

3. SWCNT Alignment

SWCNT alignment can be characterized using the Nematic order parameter S, which is zero in the disordered phase and non-zero in the ordered phase of CNT orientation based on the external electric-field induced torques T_{DEP} [79,169]. In order to derive S, the rotational energy U_{ROT} of the CNT is needed

$$U_{ROT} = \int \langle T_{DEP} \rangle_{CNT} \, d\theta \tag{2.33}$$

Compared to the thermal energy $k_B T$ (with k_B being the Boltzmann constant and T the temperature) which contributes to the Brownian motion, U_{ROT} follows a Boltzmann distribution of

$$f(\theta) d\Omega = \frac{\exp(-U_{ROT} / k_B T) d\Omega}{\int_0^{\pi} \exp(-U_{ROT} / k_B T) d\Omega} \tag{2.34}$$

with $d\Omega = 2\pi \sin\theta d\theta$.

For a two-dimensional circumstance, the Nematic order parameter is presented as

$$S_{2d} = \int_{-\pi/2}^{\pi/2} \cos 2\theta \cdot f(\theta, U_{ROT}) d\Omega \tag{2.35}$$

under assuming that the director direction for CNT alignments is placed in the same direction of the external field. For further discussions, Ref. [169] is recommended.

2.4.4. Electrohydrodynamics

As discussed above, large electric fields should be applied for depositing SWCNTs through DEPs in order to achieve high-quality (high-density and good alignment) depositions. However, with the increase of dielectrophoretic electric fields, Joule heating is inevitably pronounced, which gives rise to an electrothermal force (ETF) on liquids, leading to variations in the conductivity and permittivity of the fluids[170]. Furthermore, when the Joule heating becomes strong enough, buoyancy forces are also needed in concern. In addition, based on electrode geometry, the applied AC DEP bias can yield a tangential component of electric field pointing along electrical double layers (EDLs, as shown in Figure 2.15) formed between the electrodes and the electrolytes. This tangential electric field contributes to a fluidic motion which is known

as the AC electro-osmosis (ACEO) slip[157]. This slip is field frequency-dependent and detrimental for CNT deposition, thus it must be suppressed for nanotube DEP depositions. Moreover, when a low-frequency electric field is tangentially applied to the solid substrate bathed in electrolytes, ion-charges in the local double layer also experience a Coulomb force, causing ions to move within the solution with respect to the direction of the electric field. This motion leads to a drag flow, known as the DC electro-osmosis (DCEO) on the liquid, and also needs to be reduced. Therefore, in order to achieve a well-aligned and highly-dense CNT deposition, a systematical comprehension of the fluid electrohydrodynamics involved in electrical, thermal and fluidic aspects of CNT-DEPs is required. For a further discussion involved in this chapter, reviews of Ref. [67,170] are recommended.

1. Potential Field

Electromagnetic fields in liquids are governed by the Maxwell's equations. For microsystems, magnetic effects can be neglected since the energy stored in the magnetic field W_M is smaller than the electrical energy W_E,

$$\frac{W_M}{W_E} = \frac{(1/2)\mu\left|\vec{H}\right|^2}{(1/2)\varepsilon\left|\vec{E}\right|^2} << 1 \tag{2.36}$$

The magnetic field is generated by both conduction and displacement currents. If conduction currents dominate, the magnetic field intensity can be estimated as $\left|\vec{H}\right| \sim \sigma\left|\vec{E}\right| L$, with L being the characteristic length of the system. For conductivity $\sigma < 0.1$ S/m and $L < 1$ mm,

$$\frac{W_M}{W_E} \sim \frac{\mu\sigma^2 L^2}{\varepsilon} < 10^{-5} \tag{2.37}$$

If the displacement currents dominate, an estimation of the magnetic field intensity can be derived from $\left|\vec{H}\right| \sim \omega\varepsilon\left|\vec{E}\right| L$. Thus for frequency $f = \omega/2\pi < 10$ MHz and $L < 1$ mm,

$$\frac{W_M}{W_E} \sim \mu\varepsilon\omega^2 L^2 < 10^{-5} \tag{2.38}$$

Therefore, for linear and isotropic materials with a displacement field of $\varepsilon\vec{E}$, Maxwell's equations reduce to the quasi-electrostatic limit[67,171]:

$$\nabla \times \vec{E} = 0 \tag{2.39}$$

$$\nabla \cdot (\varepsilon \vec{E}) = \rho_q \tag{2.40}$$

where ρ_q is the volume charge density of media. The charge continuity equation derived from Maxwell's equations is given by:

$$\nabla \cdot \vec{j} + \frac{\partial \rho_q}{\partial t} = 0 \tag{2.41}$$

In a bulk electrolyte, the electrical current is given by the Ohm's law: $\vec{j} = \sigma \vec{E}$. And for a binary symmetrical electrolyte the current density is given by

$$\vec{j} = e(n_+ + n_-)\mu_e \vec{E} - eD\nabla(n_+ - n_-) + e(n_+ - n_-)\vec{v} \tag{2.42}$$

with e denoting the absolute value of the electronic charge, and μ_e, D, n_+, n_- being the mobility, diffusion coefficient and number densities of positive and negative ions respectively. Thus the relative difference in the number densities of ions is given by the ratio

$$\mathbb{R} = \frac{n_+ - n_-}{n_0} = \frac{\nabla \cdot (\varepsilon \vec{E})}{en_0} \sim \frac{\varepsilon \left| \vec{E} \right|}{en_0 L} \tag{2.43}$$

with n_0 being the unperturbed ion density. For $\left| \vec{E} \right| \sim 10^5$ V/m, $n_0 \sim 10^{23}$ m^{-3}, and $L \sim 10$ μm, $\mathbb{R} \sim 10^{-4}$ which means that the liquid can be considered as quasi-electroneutral[172].

Comparing the electrical diffusion to electrical drift:

$$\frac{\left| eD\nabla(n_+ - n_-) \right|}{e(n_+ + n_-)\mu_e \left| \vec{E} \right|} \sim \frac{D\varepsilon \left| \vec{E} \right| / L^2}{2en_0 \mu_e \left| \vec{E} \right|} = \left(\frac{\lambda_{De}}{L} \right)^2 \tag{2.44}$$

where $\lambda_{De} = \sqrt{\varepsilon D / 2en_0\mu_e}$ is the Debye length, a length scale over which mobile charge carriers screen out electric fields in solutions (Figure 2.15) or other conductors[173]. Normally λ_{De} is in the order of nanometers for a normal SDS-water medium, but much smaller than the

characteristic length of typical DEP systems. Hence, the ratio between the electrical diffusion to electrical drift is usually small thereby the former is negligible.

Furthermore, when comparing the conduction current $\sigma\ \vec{E}$ with convection current $\rho_q\vec{v}$:

$$\frac{\left|\nabla\cdot(\varepsilon\vec{E})\vec{v}\right|}{\left|\sigma\vec{E}\right|}\sim\frac{\varepsilon/\sigma}{L/v}\sim 7\times10^{-6} \tag{2.45}$$

with given $\sigma\sim10^{-3}$ S/m, $L\sim10$ μm and $v\sim100$ μm/s. The term $\varepsilon v/L\sigma$, known as the electrical Reynolds number[174], represents the ratio of the time-scale of charge convection by fulid flow and charge relaxation by Ohmic conduction. Since this physics is quite small, the electrical equations are decoupled from the mechanical equations as mentioned below.

Based on above discussions, it is convenient to neglect diffusion and convection currents, and assume that σ and ε are time-independent within DEPs. Thereby equations (2.39) and (2.40) can be combined as

$$\nabla\left[(\sigma+i\omega\varepsilon)\vec{E}\right]=0 \tag{2.46}$$

with the electric field is now a complex vector $\vec{E}(\omega,t)=\vec{E}_0e^{i\omega t}$.

In practice, the gradients in permittivity and conductivity are often small within liquids. Thus the solution of electric potential distribution can be described by the Laplace equation

$$\Delta\varphi=0 \tag{2.47}$$

2. Thermal Field

Electric fields of DEPs generate electric currents, which inevitably heat up the systems. In order to derive the temperature distribution of the system, the equation solving for the internal energy of the media is needed, which is coupled to the temperature distribution using the equation[170]

$$\rho_m c_p\left(\frac{\partial T}{\partial t}+(\vec{v}\cdot\nabla)T\right)=\mathrm{K}\nabla^2T+\sigma\left|\vec{E}\right|^2 \tag{2.48}$$

where c_p is the specific heat capacity of the media under the standard pressure, and K is the thermal conductivity of the fluid. In the presence of the electric field, the temperature field

rapidly reaches a stationary state. Similar to the discussions in Chapter 2.4.2, this time interval is given by $t = \rho_m c_p l^2 / \mathrm{K}$. As calculated it is shorter than 0.1 s both for Toluene ($\mathrm{K} = 0.141 \mathrm{W}/mK$) and SDS-water ($\mathrm{K} = 0.6 \mathrm{W}/mK$) based DEPs (see Appendix A). The stationary temperature field possesses a time-independent and an oscillating component. Generally, the effect of the oscillating temperature component on the fluid dynamics is negligible for electrical field frequency higher than 1 kHz[170] due to the existence of milli-second relaxation interval of thermal equilibrium, therefore only the former component matters.

For microsystems, the convection of heat is smaller than the heat diffusion, which is characterized with the Péclet number denoting the ratio of thermal energy convected to the fluid over thermal energy conducted within the fluid[175], and is given by

$$\frac{\left|\rho_m c_p (\vec{v} \cdot \nabla) T\right|}{\left|\mathrm{K} \nabla^2 T\right|} \sim Pe = \frac{\rho_m c_p |\vec{v}| L}{\mathrm{K}} << 1 \tag{2.49}$$

Neglecting the heat convection term, the temperature equation (2.48) can reduce to Poisson's equation, with Joule heating as the energy source

$$\mathrm{K} \nabla^2 T = -\sigma \left\langle \left| \vec{E} \right|^2 \right\rangle \tag{2.50}$$

3. Fluidic Field

Under the mass conservation assumption, the velocity of an incompressible fluid $\vec{v}$ can be described by Navier-Stokes equations[67]

$$\nabla \cdot \vec{v} = 0 \tag{2.51}$$

$$\rho_m \left(\frac{\partial \vec{v}}{\partial t} + (\vec{v} \cdot \nabla) \vec{v} \right) = -\nabla p + \eta \nabla^2 \vec{v} + \vec{f}_{\vec{E}} + \rho_m \vec{g} \tag{2.52}$$

where $\rho_m \left(\partial \vec{v} / \partial t + (\vec{v} \cdot \nabla) \vec{v} \right)$, $-\nabla p$, $\eta \nabla^2 \vec{v}$, $\vec{f}_{\vec{E}}$, $\rho_m \vec{g}$ represents the fluid experienced inertial forces, pressure forces, viscous forces, external electrical forces and gravitational force respectively.

For microsystems with dimension $L < 100$ μm and typical $\vec{v} < 100$ μm/s, the Reynolds number is very small, which yields

$$\frac{\left|\rho_m(\vec{v}\cdot\nabla)\vec{v}\right|}{\left|\eta\nabla^2\vec{v}\right|}\sim \mathrm{Re}=\frac{\rho_m\left|\vec{v}\right|L}{\eta}\leq 0.011(water),0.015(toluene) \tag{2.53}$$

indicating that the convective-inertial forces is much smaller than forces caused by viscosity. However, for high bias CNT DEPs, $\vec{v}$ can be up to cm/s. Under that situation, both two items from equation (2.52) should be considered as discussed in Chapter 6.

A stationary state of fluids can be reached within a time interval of $t=\rho_m L^2/\eta$, which is usually smaller than 0.01 second after electric field is switched on. Thus for CNT-DEPs, the time-averaged component of fluidic motions can be derived through

$$0=-\nabla p+\eta\nabla^2\vec{\upsilon}+\left\langle\vec{f}_{\vec{E}}\right\rangle+\rho_m\vec{g} \tag{2.54}$$

Thereby for incompressible fluids, the time average term of $\vec{f}_{\vec{E}}$ is given by

$$\left\langle\vec{f}_{\vec{E}}\right\rangle=\frac{1}{2}\Re(\rho_q{}^*\vec{E}^*-\frac{1}{2}\vec{E}\cdot\vec{E}^*\nabla\varepsilon) \tag{2.55}$$

here, the charge and electric field on the right-hand side are the complex amplitudes. The first term represents the Coulomb force, and the second term indicates the dielectric force which depends on gradients of conductivities and permittivities of fluids.

In practive, the local heating of electric fields induces gradients of fluid permittivity and conductivity. This in turn exerts a body force known as the electrothermal force (ETF) on the fluid as described in equation (2.55). The ETF can be calculated based on the temperature gradient using[170,176,177]

$$\left\langle\vec{f}_{\vec{E}}\right\rangle=\frac{1}{2}\Re\left(\left(\frac{\sigma_m\varepsilon_m(\wp-\vartheta)}{\sigma_m+i\omega\varepsilon_m}\right)(\nabla T\cdot\vec{E})\right)\vec{E}^*-\frac{1}{2}\wp\varepsilon_m\left|\vec{E}\right|^2\nabla T) \tag{2.56}$$

with $\wp=(1/\varepsilon)(\partial\varepsilon/\partial T)\approx -0.004K^{-1}$ and $\vartheta=(1/\sigma)(\partial\sigma/\partial T)\approx 0.02K^{-1}$ standing for the relative variations of fluid permittivity and conductivity induced through temperature gradients. Based on equation (2.56), it is clear that the ETF is field frequency dependent: As ω is much greater than σ/ε, the second term (the dielectric force) dominates the ETF. Otherwise, as $\omega<<\sigma/\varepsilon$, the Coulomb force dominates.

Gradients of temperature can also generate a gravitational body force $\vec{f}_g$ on fluids, known as Buoyancy. When $\omega\varepsilon/\sigma << 1$, the Buoyancy force is very small compared to the electrical force as denoted in the equation (2.55) since

$$\left|\frac{\vec{f}_g}{\vec{f}_{\vec{E}}}\right| \sim \frac{(\partial\rho_m/\partial T)(L)^3|\vec{g}|}{(1/\sigma)(\partial\sigma/\partial T)\varepsilon V^2} \tag{2.57}$$

yielding a result of $\left|\vec{f}_g / \vec{f}_{\vec{E}}\right|$ smaller than 10^{-3} for all the media used in this work under a given characteristic length $L < 50$ μm and applied voltage $V = 10$ V. Besides, when L is further decreased, for instance down to micro-scales, the influence of the Buoyancy becomes negligible.

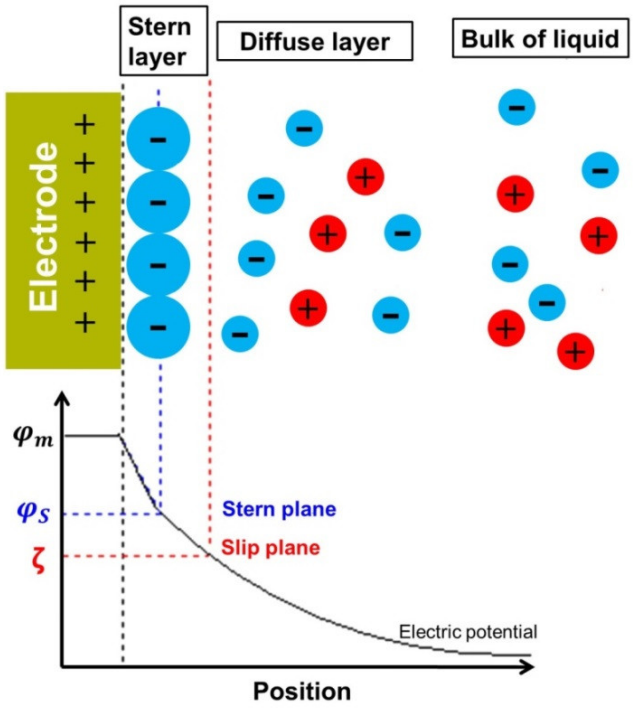

Figure 2.15: Schematic diagram of the Stern modified Gouy-Chapman electrical double layer and corresponding electrical potential distribution.

AC currents can generate divergent electric fields in the planar electrode arrays of DEP chips, which give rise to an electric field component tangential to EDLs at the surface of electrodes (as shown in Figure 2.15). Such a tangential field performs a non-zero time average force on the ions within the diffuse double layers, causing them to move along EDLs, which in turn

results in a drag flow on the fluids. The induced flow, known as AC electroosmotic (ACEO) slip, varies from zero at the slip-plane up to a maximum of v_{ACEO} at the outer surface of electrodes.

Practically, the time-average ACEO slip velocity can be derived through a generalization of Smoluchowski formula[157]

$$v_{ACEO} = \Lambda \frac{\varepsilon_m V^2}{8\eta x} \frac{\mho^2}{(1+\mho^2)^2} \tag{2.58}$$

with a dimensionless frequency $\mho$ expressed as

$$\mho = \frac{\omega C_{DL} \pi x}{2\sigma_m} \tag{2.59}$$

The capacitance C_{DL} represents the capacitance of the electrical double layer, serially composed of an immobile charged stern layer and a Poisson-Boltzmann-distribution charged diffuse layer, formed at the interface between the electrolytes and electrodes (as shown in Figure 2.15). The factor Λ indicates the ratio of the stern layer capacitance C_S over the sum of the capacitance C_S and the diffuse layer capacitance C_D. It dominates the field potential distribution within the EDLs and will be discussed in detail in Chapter 6.

The v_{ACEO} profile is highly electrical-field-frequency dependent and tends to be zero at both low and high frequency limits, but reaching a maximum velocity given at $\mho = 1$. For high field frequencies, both drift and diffusion velocities of the surface charges is rather low compared to the change frequency of electric fields because the EDLs could not relax and rebuild sufficiently. Whereas at low frequencies, the applied potential, especially for high ion-concentration media, drops mainly across the double layer and results in a very small electric field remaining in the solution.

For a low ion-concentration media such as toluene, the ACEO can be annihilated even under rather high field frequency becasue the thickness of EDLs is much larger than the channel length (as discussed in Chapter 6), making C_D much smaller than high ion-concentration media. Thus in this thesis, one can only consider the ACEO for surfactant-water (for instance

0.01-w%-SDS water) based DEPs, not for toluene (e.g. 100-ppm-H_2O toluene, with water content ≈100 ppm, $\lambda_{De} = 9.519 \cdot 10^{-6}$ m, see Appendix A).

The maximum DC electroosmotic (DCEO) velocity above the double layer can be determined using the Helmholtz-Smoluchowski equation [178]

$$v_{DCEO} = -\frac{\varepsilon_m \zeta}{\eta} E_x \tag{2.60}$$

where ζ is the zeta-potential at the slip-plane, denoting the potential difference between the micelle forming surfactant solution and the dielectric layer of the substrate[179], and E_x denotes the tangential electric field to the solid surface of the substrate. Unlike the ACEO, the driven potential of the DCEO across the dielectric-layer/electrolyte interface becomes negligible under high-frequency AC conditions, making this slip velocity neglected.

2.5. Finite Element Simulation

The equations discussed in Chapter 2.4.4 for solving electrical potential, thermal temperature, and fluidic velocity distributions of DEP systems are coupled with each other and must be simulated sequentially depending on specific DEP conditions. In order to numerically study an interested geometry-based DEP, an effective technique known as the finite element method (FEM) simulations should be employed.

FEM is a numerical technique used to approximate, but numerically stable solutions for partial differential equations (PDEs) or integral equations[180]. As for a given PDE problem,

$$\begin{aligned} &-\Delta u = f, \\ &u\big|\Gamma_1 = \gamma, \\ &\left.\frac{\partial u}{\partial n}\right|\Gamma_2 = 0. \end{aligned} \tag{2.61}$$

where u , f are multivariate functions defined within a domain U with boundaries $\partial U = \Gamma_1 \cup \Gamma_2$, and Δu exists on U . The boundary condition of boundary Γ_1 is named as Dirichlet boundary, while Γ_2 the Neumann boundary[180].

In order to solve this PDE problem, firstly, its weak formulation in which the highest order of derivatives can be minimized during integral process, can be derived using one test function v through

$$\begin{aligned} &\int_U \nabla u \cdot \nabla v dA = \int_U f v dA, \\ &v\big|\Gamma_1 = 0. \end{aligned} \tag{2.62}$$

making u mathematically smooth.

Then by dividing the whole domain U into proper subdomains U_i with $i \in \{1,2,\ldots,n\}$, the equation 2.62 can be integrated over each U_i, which contributes to a basis function φ_i (with $\varphi_i\big|\Gamma_1 = 0$) for the discretization of u. Thus an approximate solution $\tilde{u}$ of u is derived as

$$\tilde{u} = \sum_{i=1}^{n} c_i \varphi_i \to u \ \ as \ \ n \to \infty \tag{2.63}$$

Assuming the test function equation $v = \{\varphi_1, \varphi_2, \ldots, \varphi_n\}$, equation (2.62) is then reformed as

$$\sum_{j=1}^{n} \int_\Gamma c_j \nabla \varphi_j \cdot \nabla \varphi_i dA = \int_\Gamma f \varphi_i dA \tag{2.64}$$

which holds true for all $i \in \{1,2,\ldots,n\}$. Thus one derives the discretization matrix of A with

$$A_{ij} = \int_\Gamma \nabla \varphi_i \cdot \nabla \varphi_j dA \,. \tag{2.65}$$

In practice, the choice of the set φ_i cannot be satisfied with all orthogonal functions, thus a proper approximation is chosen as

$$A_{ij} \begin{cases} \neq 0 & for \quad j = i-1, i, i+1 \\ = 0 & else. \end{cases} \tag{2.66}$$

With definitions of vectors $x = (c_1, c_2, \ldots, c_n)^T$ and $b = (b_1, b_2, \ldots, b_n)^T$ for which $b_i = \int_\Gamma f \varphi_i dA$, equation (2.64) is expressed as a linear equation of $Ax = b$ which is solvable in an iterative method with a proper initial conditions, thereby deriving the approximate solution $\tilde{u}$ for u.

2.6. Field Effect Transistor of SWCNTs

The DEP-deposition configuration of SWCNTs has a crucial impact on the performance of the corresponding transistors. In order to achieve high-performance transistors, the m-SWCNT content within the sediment of CNTs should be removed to the greatest extent. Besides, the packing density of the s-SWCNTs should be extremely enhanced as neglecting inter-tube screening. Thus a high-quality CNT deposition gives rise to the device performance. Conversely, the performance of transistors also reflect the quality of SWCNT-DEP depositions.

2.6.1. Schottky Barrier

Schottky barrier is a potential barrier for charge transport at a metal–semiconductor interface[181], which performs current rectifying characteristics as a diode. The first CNT FET was demonstrated by Tans *et al*.[182] and Martel *et al*.[183] in 1998. It was initially thought that CNT transistors were operated in a similar way as conventional metal–oxide–semiconductor field-effect transistors (MOSFETs) where the channel material potential is predominant for controlling current going through. However, it was soon realized that Schottky barriers at the CNT-metal contacts dominates the device transport properties[184].

When a metal is in contact with a semiconductor of different work function, a Schottky barrier appears at the junction via charge exchange induced because of mismatch between their Fermi levels. In the absence of interface states which is believed to be a good approximation for the metal/tube interface[185], the Schottky-barrier heights for hole and electron injections are given by

$$\Phi_{SB}^{p} = \phi_{CNT} + E_g/2 - \phi_M, \;\; \Phi_{SB}^{n} = \phi_M - \phi_{CNT} + E_g/2. \tag{2.67}$$

Here ϕ_M represents the work function of the metal, ϕ_{CNT} the work function of the nanotube and its energy gap ϕ_g (see Fig. 2.16(a)). When the Fermi level of metals lies at the mid-gap of the nanotube band structure (Fig. 2.16(b)), there is an equivalent Schottky barrier for both n and p carrier injection, whereas when it aligns close to the hole band (Fig. 2.16(c)), the barrier for hole injection is reduced but that for electron injection is enhanced.

As shown in the literature of Ref. [122,186–188], high work function metals, for instance Pd, Rh, make good p-type contacts for SWCNTs, whereas low work function ones such as Al, Ca yield better n-type contacts. However, the work function itself is not sufficient to assure ohmic

contacts with nanotubes. For instance, for a p-type contact, Pt has a larger work function than Pd, but forms more resistive contacts. This can be attributed to additional tunneling barriers due to poor wetting of the nanotube as using Pt[122].

Based on eq. 2.7, there is a critical SWCNT diameter, below which a Schottky barrier with finite height increasing with the decreasing CNT diameter, for each metal existing. Figure 2.16(d) shows the on-current as well as Schottky barrier height within the p-regime of SWCNT transistors of different diameters and contact metals[188]. Consistently, a notable barrier grows with the decrease in CNT diameter. The first Ohmic p-type contacts were achieved by Javey *et al.*[122] with nanotubes of diameter >1.5 nm deposited across Pd electrodes. This provides not only a consistent picture regarding to the contact properties of s-SWCNTs, but also stimulates the motivation for selecting Pd metal as CNT contacts within this thesis.

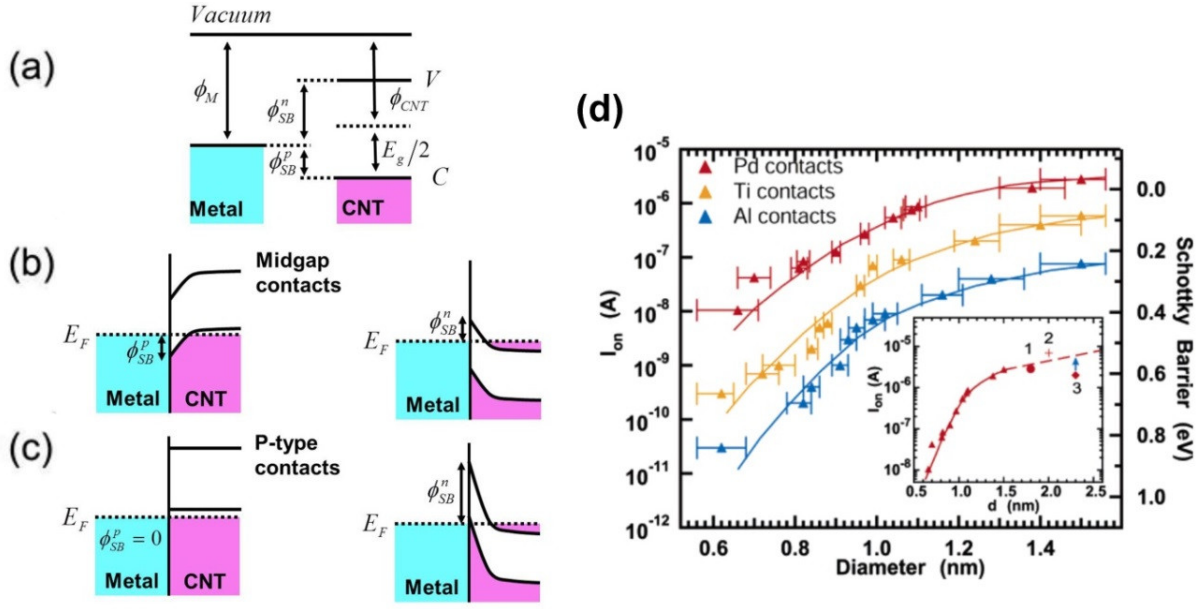

Figure 2.16: Schematics of the Schottky-barrier for hole and electron injections of (a) the nonaligned metal-CNT contacts, (b) contacts with metal work function at the nanotube mid-gap and (c) p-type contacts. Modified from Ref. [189]. (d) The diameter dependence of on-current and Schottky-barrier height of SWCNT contacts with respect to different metals. Inset includes data for Pd-contacted CNT FETs from other publications. Modified from Ref. [188].

2.6.2. Classification and Properties

Based on the working principle of transistors, two types of s-SWCNT FETs have been commonly studied, as shown in Figure 2.17 (a) Schottky barrier dominated FETs,

SB-CNTFET[190] and (b) MOSFET like transistors[191], MOS-CNTFET. The former works on the principle of charge tunneling through a Schottky barrier at the source-channel junction as shown in Figure 2.17(c). Thereby the barrier width is modulated with the gate voltage, resulting in gate-voltage dependent trans-conductance. Distinctly, MOS-CNTFETs in which the source and drain regions of CNTs are heavily doped, are operated under the principle of gate-voltage-dominated barrier-height modulation (Figure 2.17(d)).

Compared to conventional FETs, Trans-conductance g and carrier mobility μ are two common metrics which can be extracted from SWCNT device characteristics[28]. The trans-conductance $g = dI_{SD}/dV_g$ of FETs is a measure for the sensitivity of the source-drain current I_{SD} to changes in the gate voltage V_g, determing the width of the switching transition of devices. In contrast to conventional devices where g directly describes the capacitive coupling between the gate electrode and charge carriers of the transistor channel materials, it is wholly determined by the gate modification of the barrier width for a SB-CNTFET. However, the derived SWCNT trans-conductance of 10-20 μS[192,193] cannot display the device physics conventionally. Similarly, the mobility μ denotes the conductivity per individual charge carrier, which represents the carrier velocity per unit of applied field for conventional FETs. However, for SB-CNTFETs, μ stands for the effective charge transport mobility, i.e. not merely reflect carrier velocity but also the tunneling characteristics of the Schottky barriers.

One type of SB-CNTFETs is called back-gated transistors[128] (as introduced in Chapter 3.6.3) in which degenerately doped Si wafer serves as a supporting substrate and global gate electrode. The working principle of these devices can be simply described as: With the increase of negative gate voltage V_g, the role of hole carrier transport become pronounced, indicating the Fermi level E_F shifts close to the valence band of the SWCNTs. While for an increase of positive gate voltages V_g, E_F moves closer to the conduction band, thus electron transport dominates. From the technological standpoint, the low conductance at the “On” state limits the achievable drive currents and hence requires high voltages for operating the device, thereby more power cost needed. On the other hand, high conductance at the “Off” state will result in unacceptable static power dissipation. Therefore, one prefers achieving a CNT device with a high on-conductance and a low off-conductance. This requires not only a good device architecture but also a high-quality s-SWCNT conducting channel.

Compared to SB-CNTFETs, MOS-CNTFETs yield higher on-currents and higher trans-conductances as they are limited only by the amount of gate-induced charge in the channel[43,44], making them promising for applications in complementary metal–oxide–semiconductor (CMOS) logics[194,195]. In these devices, both p- and n-type CNTs are required to conduct charge transport. However, pristine nanotubes normally exhibit p-type majority charge carriers due to oxygen impurity in the ambient[196,197]. Thus, one challenge in the study of MOS-CNTFETs is how to render n-type CNT stable in air for a long term. Aiming at this problem, methods such as utilizing potassium doping[191] and applying electrostatic effect[198] have been employed to convert p-type nanotube transistors to n-type ones.

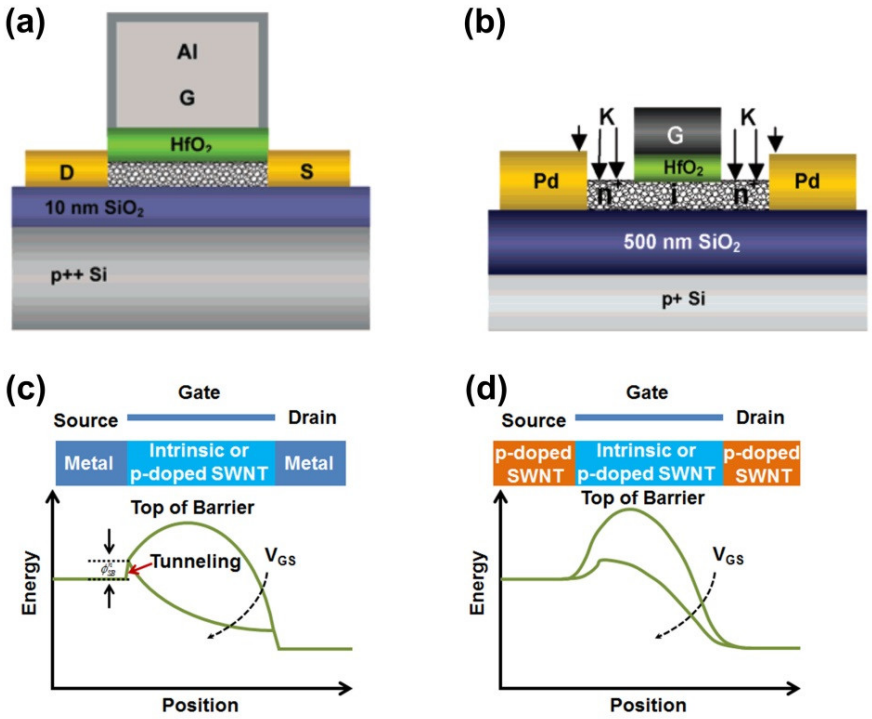

Figure 2.17: Side-view schematics of (a) a SB-CNTFET with top-gated architecture (reproduced from Ref. [190]) and (b) a MOS-CNTFET (from Ref. [191]). (c) and (d) demonstrate the energy band diagrams of the typical SB-CNTFETs and MOS-CNTFET respectively.

– This page intentionally left blank –

Chapter 3: Materials and Methods

3.1. Synthesis of SWCNT Specimen

Within this thesis, Commercial HiPco CNTs were directly ordered from NanoIntegris for correlated studies as displayed in Chapter 4, 5 and 6.

The preparation of PLV CNTs used in this work (Chapter 5, 6 and 7) was performed by Dr. Frank Hennrich of the Karlsruhe Institute of Technology, using carbon targets doped with 1 atom % Ni and Co catalyst in 0.5 bar argon atmosphere flowing at ca. 80 sccm through an oven operated at 1050 °C. Further details can be found in Ref. [127].

3.2. Preparation of SWCNT Suspension

Size Exclusion Chromatography (SEC), a method demonstrates effective control over the length distribution of SWCNTs in solutions based on their length-dependent chromatographic velocity in the filtering process, has been wildly used in the length-sorting of nanotubes[199–201].

In this thesis, solution-SWCNTs were prepared via SEC fractionation of nanotube suspensions using two kinds of solvents, i.e. water and toluene. The water based solutions were kindly prepared by Dr. Benjamin Scott Flavel of the Karlsruhe Institute of Technology, while the toluene based materials were provided by Dr. Frank Hennrich of the Karlsruhe Institute of Technology.

3.2.1. Water Based Suspension

For aqueous CNT solutions, HiPco SWCNT raw materials NanoIntegris were used. At first, 20 mg of raw SWCNT materials were suspended in 30~80 mL of water (VWR CA1.16754.5000) with 1~2 wt % SDS (Sigma Aldrich) using a tip sonicator (Weber Ultrasonics, 20~35 kHz, 500 W, in continuous mode) applied for 15 h at 10~20% power. In order to cool down the suspension during this sonication, the system was normally placed in a water-circulation bath. After sonication, a centrifugation at 20,000g was carried out to remove larger agglomerates. The resulting suspension was then fractionated with SEC using a Sephacryl S-200 gel filtration medium (Amersham Biosciences) filled in a glass column of 20 cm length and 1.6 cm inner diameter. In practice, after filling the filtration medium, the gel was

slightly compressed to yield a final height of 2 cm. Separation was performed with a SECcurity gel permeation chromatography (GPC) 1260 Infinity system (Agilent Technologies).

3.2.2. Toluene Based Suspension

In terms of toluene based SWCNT suspensions[127], 100-mg raw PLV SWCNT soots and 100-mg polymer poly(9,9-di-n-dodecylfluorenyl-2,7-diyl) (PODOF) (Sigma-Aldrich) were mixed in toluene (Alfa Aesar, CAS-number 108-88-3) and subjected to sonication treatment for 2 hours by using a titanium sonotrode (Bandelin, ~20% power). During sonication, the suspension was also placed in a water-circulation bath to aid cooling. Then the suspension was centrifuged for 2 hours at 20000g. In order to generate the starting suspensions for SEC separation, the obtained supernatant was then concentrated to ~20 mL by evaporating the excess toluene. The SEC process was performed using Toyopearl HW-75 resin (Tosoh) which was filled into a High-performance liquid chromatography steel column with 16 mm inner diameter and 20 cm length. Similarly, the separation was also performed with a SECcurity GPC 1260 Infinity system, as mentioned above.

3.3. Characterization of Suspension

After preparation, CNT suspensions were used to be preferentially characterized with proper optical characterizations, such as UV-Vis-IR absorption spectroscopy, Raman spectroscopy and photoluminescence as described in Chapter 2.1.3, to derive inforamtions about the nanotube concentration, chirality etc.

3.3.1. Absorption Spectroscopy

UV-Vis-NIR absorption spectra (Chapter 4-7) of the nanotube suspensions were recorded with a Varian Cary 500 spectrophotometer. Notably, the absorption spectra of toluene-based CNT suspensions in Chapter 7 were kindly collected by Dr. Frank Hennrich from the Karlsruhe Institute of Technology.

3.3.2. Raman Spectroscopy

Raman spectra (Chapter 7, also conducted by Dr. Frank Hennrich) were taken with a WITec CRM200 (excitation at 633 nm) and Renishaw inVia (532 and 785 nm) Raman microscope from flakes of SWCNTs which were derived through sedimenting CNTs out of suspensions using 1 hour centrifugation of 100000~200000g.

3.3.3. Photoluminescence

Photoluminescence (PLE) maps (as shown in Chapter 5 and 7, conducted by Dr. Frank Hennrich from the KIT) were measured using a modified FTIR spectrometer (Bruker IFS66) equipped with a liquid-nitrogen-cooled Ge-photodiode and a monochromatized excitation light source[202]. The typical measurements were performed with an emission range of ~900-1700 nm and excitation range of 500-950 nm (scanned in 3 nm steps).

3.4. Characterization of SWCNT Deposition

3.4.1. Scanning Electron Microscopy

Scanning electron microscope (SEM) in which a focused beam of electrons is used for scanning surface-configuration of materials, is a typical fast imaging technique for solid-substrate (e.g. Si) based CNT specimens. The resolution of SEM is normally better than 1 nanometer, which provides the opportunity for scientists to directly image the geometry profile of CNTs.

In this thesis, the secondary-electron SEM images of CNT depositions (Chapter 4, 6 and 7) were taken using a Zeiss Ultra Plus field emission SEM with extra high tension (ETH) voltage of 1.00 kV, working distance (WD) of 2.1 mm, aperture size 20 µm and a magnification of 20~50 K×.

3.4.2. Atomic Force Microscopy

Atomic force microscopy (AFM) is a type of scanning probe microscopy with resolution in the order of fractions of one nm, making it widely used to characterize the geometry (diameter and length) of CNTs today.

The AFM measurements (Chapter 5 and 7, Collected by Dr. Frank Hennrich of the Karlsruhe Institute of Technology) included in this thesis were directly performed in an air environment with a multimode head and Nanoscope III controller (Digital Instruments), operating in tapping mode[143]. Commercially available silicon cantilevers with fundamental resonance frequency of 320 kHz were employed. 10×10 µm or 5×5 µm topographic (height) and amplitude images were collected simultaneously at a scan rate of 1 Hz with the parameters set point, amplitude, and feedback control optimized for each sample. Typical samples for AFM were prepared by dropping 0.5 µL of SWCNT solution onto a ~1cm^2 silicon wafer then spin coating at 4000 rpm for 60 s.

3.5. Calculation and Simulation Tool

Analytical calculations were coded and performed using commercial Matlab R2014a software (All programs used in this thesis can be found in the enclosed CD). Then the obtained results were replotted using commercial OriginLab Origin 9.0.

Analog simulations of DEP circuits as presented in Chapter 6 were performed using the Multisim Analog Devices Edition (MADE) 10.0.410 of National Instruments. For details, one can refer to the corresponding programs included in the attached CD.

For the FEM simulations (also see programs enclosed in the CD) contained in this thesis, the software packages FlexPDE 6 and COMSOL MULTIPHYSICS 5.0 were used. In particular, COMSOL is a commercially-available finite element solver for partial differential equations of various physics, especially for coupled phenomena. Since both temperature and fluidic velocity distributions of SWCNT-DEP system arising from the applied electric field, this software turns to be a good option to analyze the electrohydrodynamics of the fluid involved in DEPs. A further discussion is presented in the Chapter 6.

3.6. Preparation of CNT-FETs

3.6.1. Electron Beam Lithography

In terms of transistor fabrication, electron-beam lithography (EBL) was chosen to pattern and make metallic contacts of the devices in this work. The schematic diagram of the transistor fabrication is shown in the Figure 3.1. In simple, a piece of clean Si wafer with a 800-nm-thick SiO_2 layer was cut into 1×1 cm^2 pieces, then a positive resist, poly(methyl methacrylate) (PMMA) with designation of 950K A4.5, was spincoated at 5000 rpm for 1 minute to yield a film thickness of about 200 nm. After spin-coating, the sample was baked in a hot-air oven at 165 °C for 30 min in order to evaporate the residual solvent. Then an electron beam with exposure dose of about 360 μC/cm^2 at 30 kV was used to pattern the samples with the desired layout: 1×1 μm^2 (As shown in Chapter 4, 6 and 7) and 1×90 μm^2 (Chapter 6 and 7) channel gaps. After the exposure, a 1:3 mixture of methyl isobutyl ketone (MIBK) in isopropanol was used for developing those samples, i.e. to dissolve away the exposed PMMA regions, for 30 s. In order to fabricate metallic electrode, the samples were then sputtered with a 50-nm thick Pd over the resist. Followed by removing the unexposed resist with Acetone, thereby the remaining Pd structures take the shape of the designed electrodes.

3.6.2. Dielectrophoresis

Using the obtained Pd electrodes, dielectrophoresis can then be performed with proper AC/DC electric fields for CNT depositions (mentioned in Chapter 3.2) in order to make nanotube transistors. During DEP process (as demonstrated in Chapter 4-7), a drop of 50 µL diluted dispersion was placed onto the fabricated electrode array under a nominal DC or AC (300 kHz ~ 1MHz) electric field of 1- 10 V_{rms}/µm. After 5 min, the deposition was terminated by rinsing the surface repeatedly with proper solvents (10 × water-rinsing followed by 5 × methanol-rising for aqueous-based DEPs, or 10 × toluene-rinsing for toluene-based ones) before switching the field off.

3.6.3. Back-Gated Transistor

After the above DEP process, the fabrication of the back-gated FETs had been completed. However, in order to make a good metal/CNT contact, the obtained devices were preferentially annealed in air at 165 °C for 90 mins to remove the remaining solvent before electrical characterizations.

3.6.4. Top-Gated Transistor

Within this thesis, one kind of transistors working under the principle of MOS-CNTFETs is also studied. These devices are known as top-gated transistors because an extra dielectric layer and electrode are fabricated on top of the CNT-deposited wafer, as shown in Figure 2.18. Distinct from n-type rendering mentioned in Chapter 2.6.2, one strategy to induce different doping of CNTs within these transistors is realized through sputtering proper Al electrodes onto the gating nanotube-segments, protecting them from being p-doped as annealed in air. This method not only preserves the intrinsic or slightly p-doping of nanotube-segments underneath the top-gate electrodes because of using an active alkali metal—Al, but also generates a thin dielectric layer of Al_2O_3 via the weak air-oxidization, which gives rise to the gate modulation of devices compared to the back-gated case. In terms of fabricating the top-gated transistors (Chapter 3.1), a second lithography process (conducted by Simone Dehm of the Karlsruhe Institute of Technology) is needed to make top-gate electrodes on CNT-deposited devices achieved through DEPs. In brief, a 90-µm-long, 1-µm-wide electrode layout was patterned in the middle of the device channel through an additional lithography under the same conditions as mentioned in Chapter 3.6.1. Then it was sputtered with a 35-nm-thick Al followed by a same

lift-off as for back-gated devices. Now a top-gated transistor is achieved. And it can be performed with electrical characterizations after a 250-°C, 90-minute annealing in air.

3.7. Characterization of CNT-FET

Electrical characterization of CNT-FETs was conducted using an Agilent 4155C semiconductor parameter analyzer system and a probe station with TRIAX probes with a low current detection limit of 30 fA.

Transfer characteristics (Chapter 4 and 7) were measured either with a back-gate (using Silicon layer as the gate electrode) voltage sweeping from V_G= -80 to +80 V (step size 400 mV, scan rate 4 V/s), or with a top-gate voltage of -0.5 V ~ +1.5 V (step size 5 mV, scan rate 50 mV/s) using source-drain voltages of 0.5, 1.0 and 1.5 V. The charge mobility μ was calculated based on the standard linear model using formula $\mu=(L_{Ch}/W_{Ch})(1/(C_G \cdot V_{SD}))(dI_{SD}/dV_G)$, with C_G determined with the parallel plate capacitor model $C_G = \varepsilon\varepsilon_0/t_{ox}$ and ε = 3.9 for the relative permittivity of the silicon oxide layer[24], t_{ox} = 800 nm for its thickness.

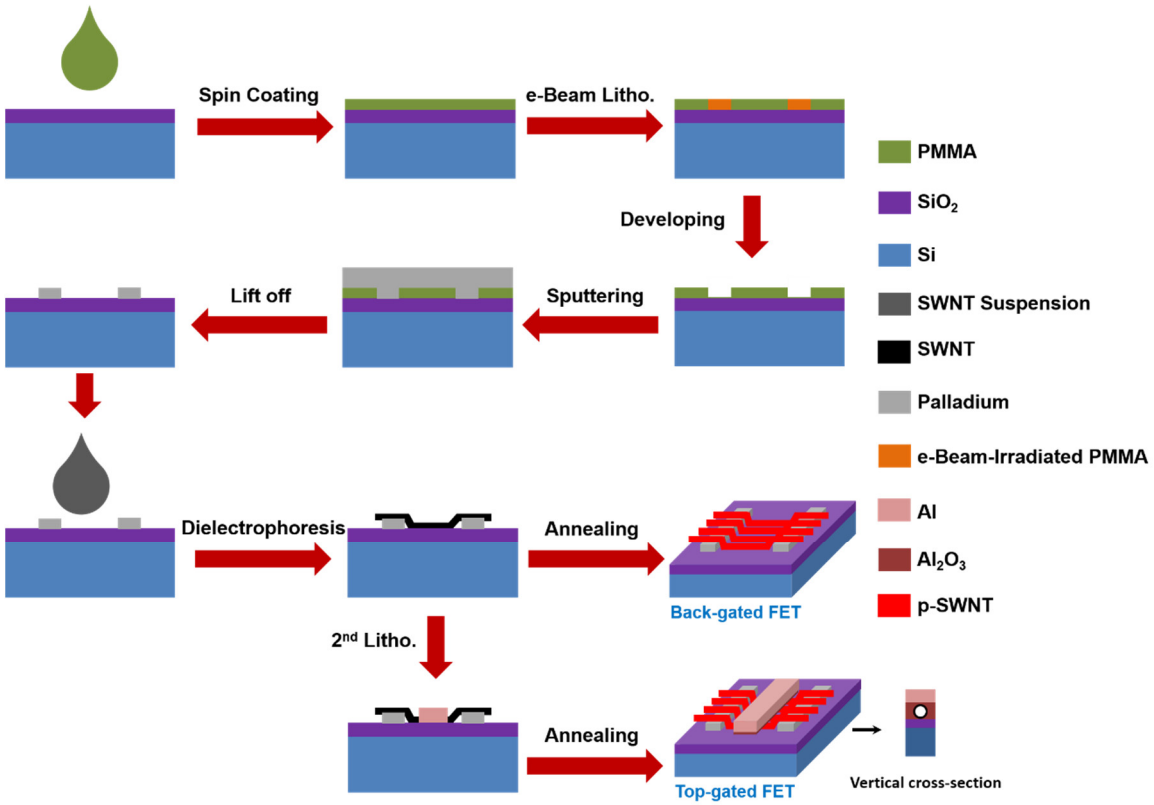

Figure 3.1: Schematic diagram of the fabrication process of CNT transistors used in this work.

Chapter 4: Light Assisted Dielectrophoresis

The work contained in this Chapter can be found in Ref.[78].

4.1. Introduction

Dielectrophoresis (DEP) has been shown to preferentially deposit m-SWCNTs from dispersions containing mixtures of m-SWCNTs and s-SWCNTs[63,80]. This phenomenon directly reflects on the relative difference in the electric-field induced dipole moment of the SWCNTs. Numerically, it has been shown that the dielectric permittivity of m-SWCNTs is several orders of magnitude larger than that of s-SWCNTs in which the permittivity scales inversely with the square of the band gap[89,155]. Therefore, m-SWCNTs are enriched during conventional dielectrophoretic deposition, impeding s-SWCNT based transistor fabrication using dispersions with residual m-SWCNTs[22]. Besides, the alignment of s-SWCNTs, especially for small diameter ones, along the electric field lines is also weak as compared to m-SWCNTs because of their weak torque. These effects hinder the reproducibility of integrating s-SWCNTs into single-tube or thin film devices.

This Chapter introduces a method to enhance the excess polarizability by irradiating the dispersed s-SWCNTs in the presence of an AC electric field and thereby improving the DEP deposition of s-SWCNTs. A laser source was added to the DEP system, and the feasibility of preferential deposition of s-SWCNT using such light assisted DEP (L-DEP) was systematically studied. Transistors fabricated from s-SWCNT dispersions were characterized with electrical measurements and scanning electron microscopy to observe the differences between device fabrications involving in either conventional DEP or L-DEP. The results indicated that the L-DEP improves the deposition of s-SWCNTs, which is helpful for the fabrication of high-purity s-SWCNT single-tube or thin film devices. This effect was attributed to a pronounced polarizability of the irradiated semiconducting nanotubes, and provided the opportunity to comment on the underlying mechanism behind spontaneous and field-driven exciton dissociation.

4.2. Experimental

A schematic of the L-DEP system is shown in Figure 4.1. The setup comprises of a probe station, a microscope with video camera, an AC signal generator, and a laser source to irradiate the central electrode structure as indicated. An array consisting of 12 pairs of 50 nm thick electrodes

(5 nm Cr / 45 nm Pd) was patterned on a p-doped silicon wafer with an 800-nm-thick thermal oxide layer using standard electron beam lithography and sputtering (as introduced in Chapter 3.6.1). All the electrodes share a common drain electrode 1 µm away, which was biased during DEP with respect to the global back gate in order to promote simultaneous SWCNT deposition.

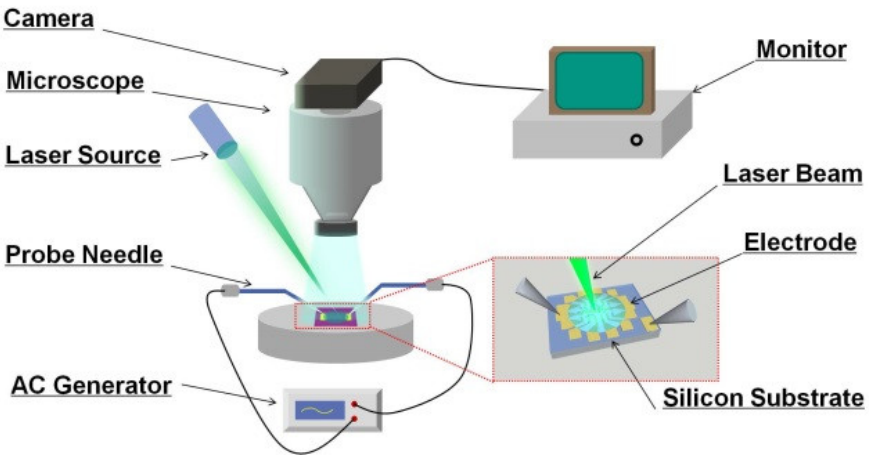

Figure 4.1: Schematic of the L-DEP experimental setup[78].

Additionally, a fiber-coupled frequency-doubled Nd:YAG diode laser (532 nm, 30 mW) was added to irradiate the sample surface during DEP. A collimator in combination with a lens was used to focus the fiber-coupled laser into a spot with a diameter of ~200 µm, which is comparable to the area of electrode array. This yields an irradiation density on the order of 10^6 W/m^2.

(6,5) SWCNTs were chosen for the L-DEP experiment, since their E_{22} optical transition is close to the irradiation wavelength of the laser (as shown in Figure 4.2). The corresponding aqueous dispersion was prepared with 3×10^{-5} wt.% (6,5) nanotubes in 1 wt.% sodium dodecyl sulfate (SDS) by size-exclusion chromatography[143], as introduced in Chapter 3.2.1. The nanotube concentration was estimated from the absorption spectrum taking into account the E_{11} peak absorption cross-section (σ_{11}) of 2.54×10^{-17} cm^{2}C^{-1}[203]. The absorption spectrum of the (6,5) dispersion is shown in Fig. 4.2. The spectrum displays two dominant optical absorption peaks at 986 nm (with intensity of A_{11}) and 571 (A_{22}) nm corresponding to the first and second optical transition of (6,5) SWCNTs. The purity w of the (6,5) dispersion has been estimated to be 92 % by a standard de-convolution process of the absorption spectrum, assigning spectral weight to specific SWCNTs with absorption peak shaped Voigt lines as described in Ref. [204]. Prior to

deposition, the dispersion was diluted with double-distilled water by a factor $f_{dilution}$ of 1:300 in order to adjust the nanotube concentration c_{tube} to ~0.001 (6,5)-SWCNTs/μm^3, based on the average length l_{CNT} of the (6,5) SWCNTs of ~0.6 μm, which can be presented by

$$c_{tube} = \frac{2.30 w A_{ii}}{L \sigma_{ii} N_{n,m} l_{CNT}} \cdot f_{dilution} \tag{4.1}$$

here the index i denotes the levels of the optical transitions of SWCNTs, $N_{n,m}$ is known as the linear density of carbon atom along the (n,m) tube axis, given by $N_{n,m} = 4\sqrt{n^2 + nm + m^2}/3a_{cc}$ [205], the propagation path length $L = 1$ cm is derived from the thickness of solutions under the absorption measurements.

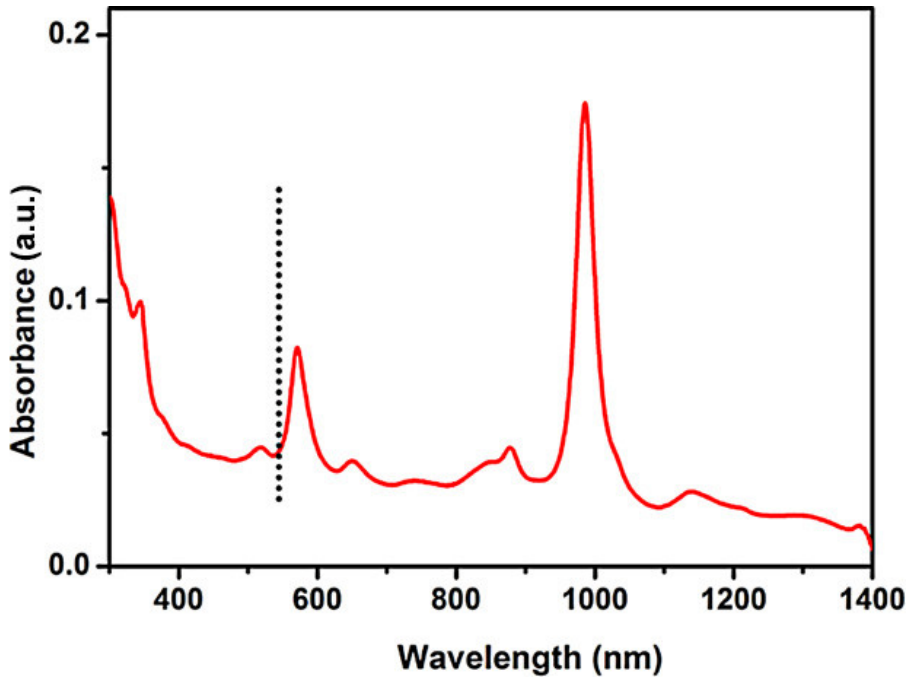

Figure 4.2: Optical absorption spectrum of the (6,5) SWCNT dispersion used in this work. The dotted line marks the 532 nm wavelength of the laser used in the L-DEP experiment[78].

AC electric fields were generated between multiple electrode pairs using a function generator with a peak to peak voltage of 5 V and frequency of 1 MHz. This yielded a nominal electric field strength in the electrode gap in the order of 10^6 V/m. Further details of DEP depositions, SEM observations and electrical characterizations of nanotube transistors have been mentioned in Chapter 3.

4.3. Results and Discussion

Figures 4.3 (a) and (b) represented the scanning electron micrographs of the devices prepared from (6,5) dispersions by normal DEP and L-DEP, respectively. The images indicate that for both cases, the deposition of individual SWCNTs form low-density thin films. Although the morphology does not seem to vary much, a slightly enhanced density and alignment for the samples prepared by L-DEP was observed.

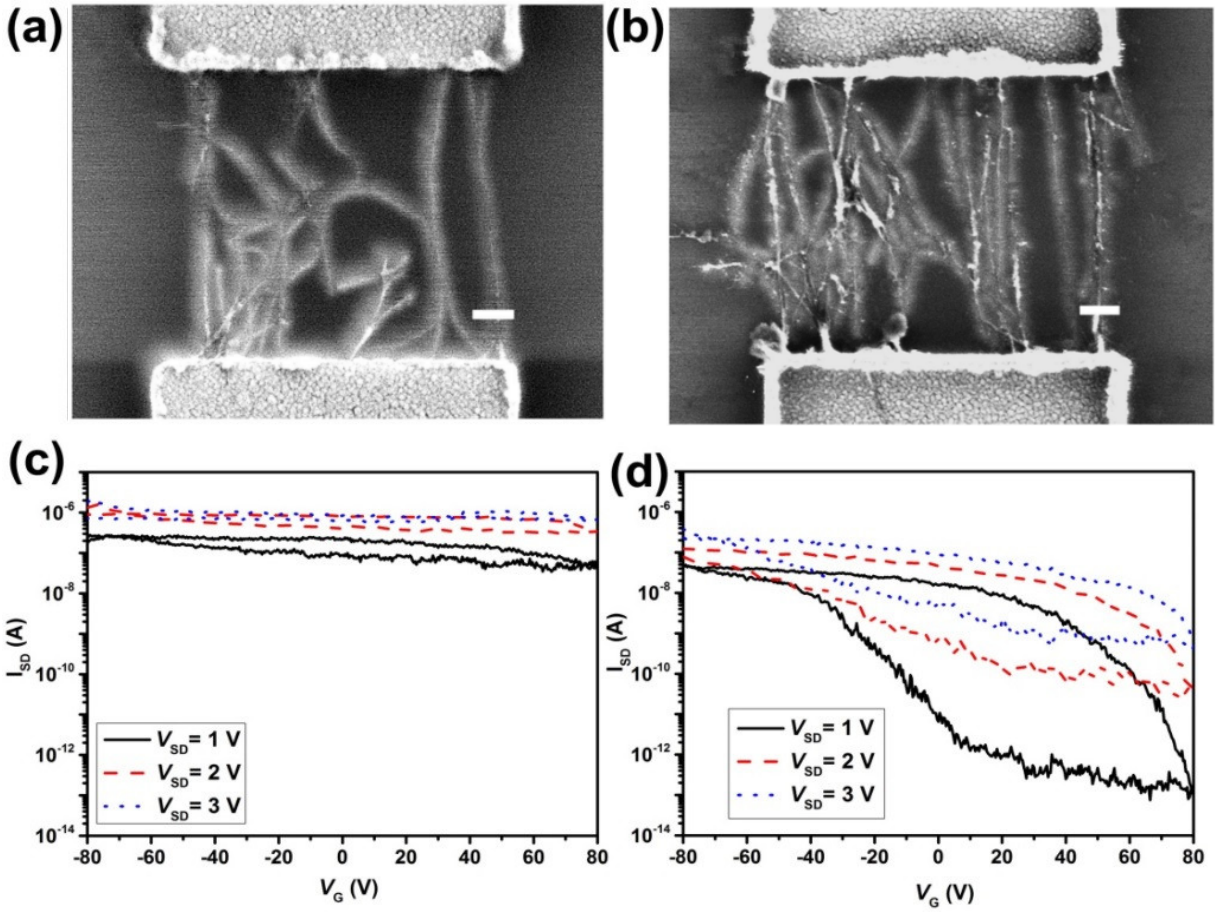

Figure 4.3: Scanning electron micrographs of the devices prepared by normal DEP (a) and L-DEP (b). Scale bar equals 100 nm. Corresponding transfer characteristics, source-drain current I_{SD} vs gate voltage V_G, prepared by normal DEP (c) and L-DEP (d)[78].

This observation coincides with significant differences in the electrical transport as shown in Fig. 4.3 (c) and (d). The devices prepared by L-DEP show a systematically higher on/off-ratio but a lower on-state current as compared to devices prepared by normal DEP. This can be attributed to the increased semiconducting content while decreased metallic content within the channel material of devices fabricated by L-DEP. For a statistical evaluation, the transfer

characteristics of 32 devices fabricated by normal DEP and 24 devices prepared by L-DEP were measured. Figure 4.4 shows the statistical evaluation of the device characteristics by plotting the on-state current versus the on/off-ratio.

It is evident that L-DEP promotes the fabrication of devices with high on/off-ratio but slightly low on-state current. The improved transistor characteristics indicates that DEP under illumination improves the deposition of (6,5) SWCNTs. This implies that the polarizability of (6,5) SWCNT becomes larger due to the absorption of photons. A possible mechanism accounting for this effect could be attributed to a spontaneous or field-driven dissociation of excitons.

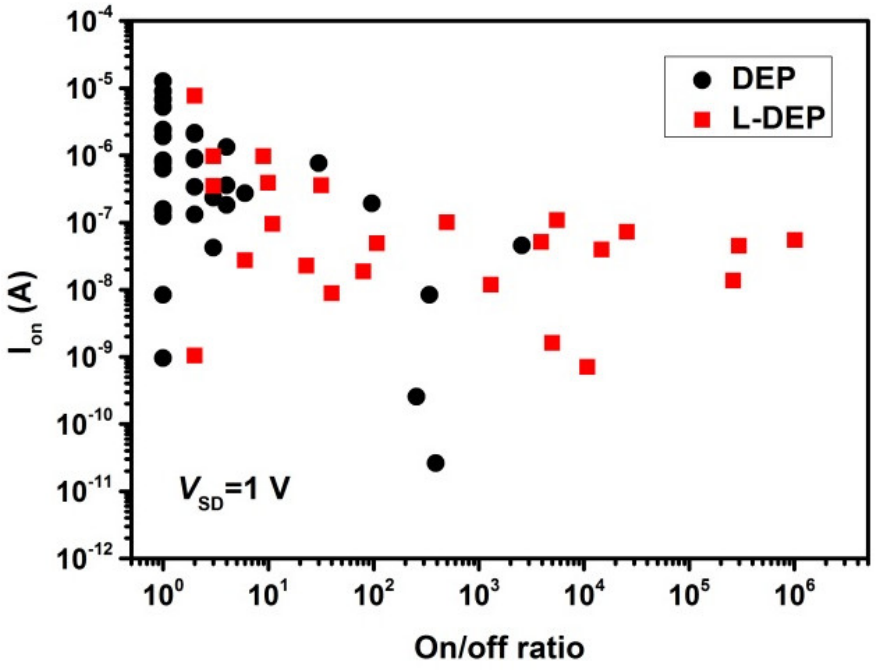

Figure 4.4: Statistical evaluation of devices prepared with illumination (L-DEP) and without illumination (DEP). Plotted is the on-state current I_{on} versus the on/off ratio at source-drain voltage of 1V[78].

Notably, L-DEP is different from optical trapping and tweezing[206–209] techniques that have been used for capturing and manipulating nano/micro-particles in suspensions. Optical trapping is DEP at optical frequencies where the light-induced dipole moment interacts in phase with the light-induced electric field gradient. Tan *et al.*[210] reported optical trapping of DNA-wrapped s-SWCNTs in the focal point of a laser spot and achieved extraction of s-SWCNTs out of a SWCNT mixture, as shown in Figure 4.5(a). The result indicates a stronger

response of s-SWCNTs to the light field than m-SWCNTs. However, optical trapping technique, as reported, makes use of the imaginary part of particle polarizability, and should be performed with lasers of red-detuned waveline approaching the optical resonance of the particle, which is inconsistent with the L-DEP where a blue-detuned excitation of 532 nm with respect to the second resonance S_{22} of (6,5) SWCNTs was used.

The dielectric response of s-SWCNTs has been studied in detail by Fagan *et al.*[211], as shown in the Figure 4.5(b). Indeed the real part of the intrinsic permittivity of a s-SWCNT diverges at each optical transition energy, as expected due to the Kramers-Kronig relation to the optical absorption peaks. On the other hand, the real part of the permittivity must change sign when tuning the laser energy from below to above the transition energy and hence the DEP force has to change from attractive to repulsive. Moreover, the change of the real part of the permittivity close to the transition energy is well below a factor of ten and therefore rather weak compared to the permittivity of m-SWCNTs. This phenomenon is known from molecular systems where the so-called excess polarizability is limited by the weak polarizability of excitons. Therefore, the permittivity change of SWCNTs during L-DEP fails to explain the increased nanotube polarizability, thereby deposition.

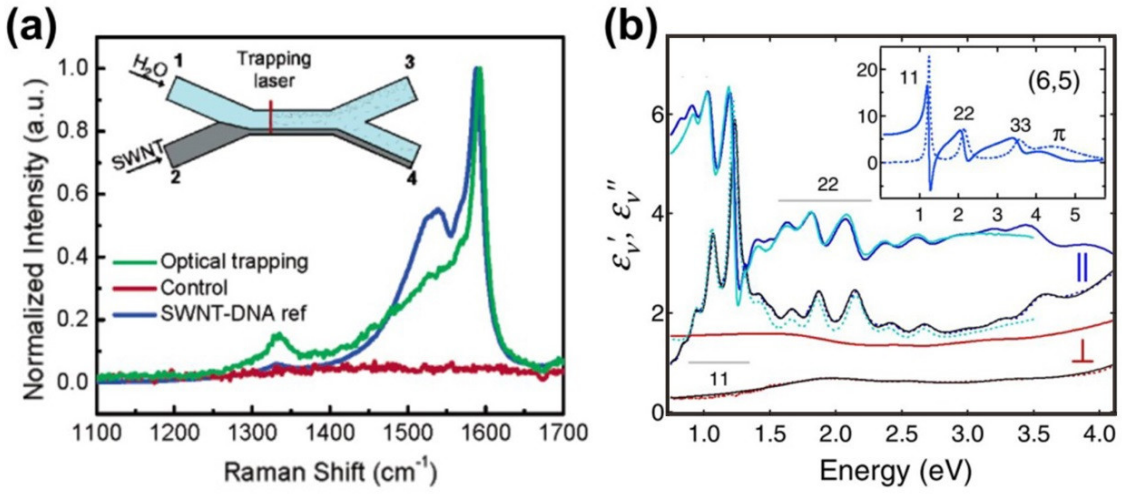

Figure 4.5: (a) 514-nm Raman spectra of CNTs employed in optical trapping experiments. The inset shows a schematic of the microfluidic chip with two inputs and two outputs (modified from Ref. [212]). (b) Intrinsic permittivity of CoMoCat SWCNTs with a number of different chiralities evident in the S_{11} and S_{22} transitions. Upper (lower) traces denote parallel (normal) to the SWCNT symmetry axis. The real (imaginary) part is shown as solid (dotted) traces. The inset shows the (6,5) SWCNT response (modified from Ref. [211]).

Excitons in s-SWCNTs are only weakly polarizable because photoexcited electrons and holes are spatially bound to each other on a length scale of a few nanometers. Unlike in bulk semiconductors, excitons in s-SWCNTs should not spontaneously dissociate since the exciton binding energy is an order of magnitude higher than the thermal energy[213]. Recently, Kumamoto *et al*. have discussed a spontaneous dissociation mechanism based on exciton-exciton annihilation (EEA) or Auger ionization (AI), in order to explain a high conversion efficiency of photoexcited excitons into free electrons and holes in their photocurrent experiment, as shown in Figure 4.6[214]. Bindl *et al*., have also discussed spontaneous exciton dissociation in the context of free carrier generation in s-SWCNT solar cells[215].

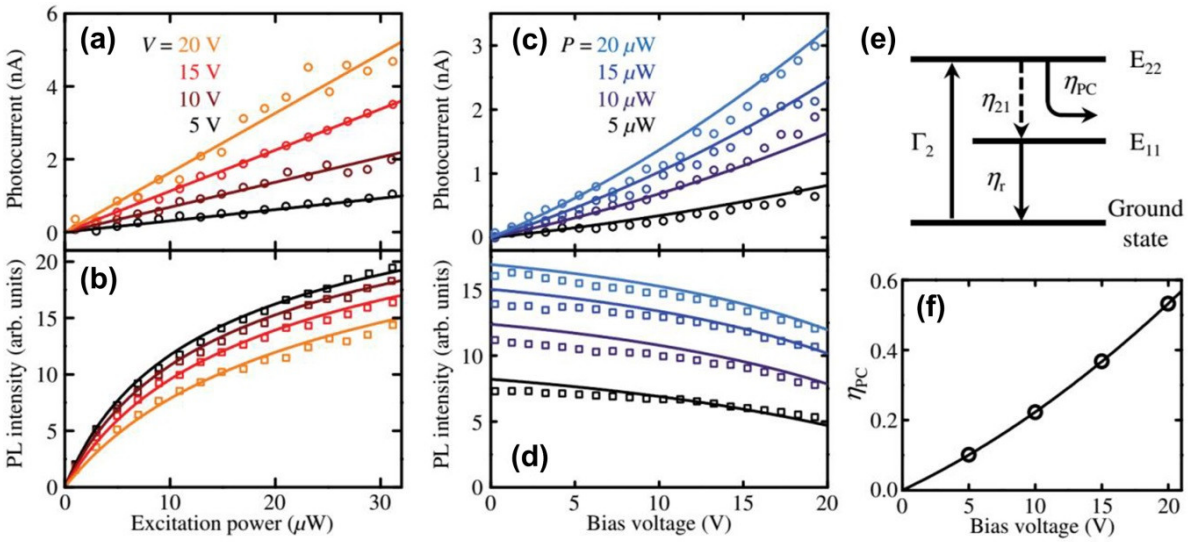

Figure 4.6: Excitation power P dependences of nanotube (a) photocurrent (PC) (b) photoluminescence (PLE) under different bias voltage V. and the correlations between the bias voltage and (c) PC, (d) PLE using different excitation power. Notably, the laser polarization is parallel to the nanotube axis. (e) A schematic of the model used to produce the curves as shown in (a)–(d). Here Γ_2 denotes the E_{22} exciton generation rate, η_{21} represents the exciton fraction that relax down to the E_{11} sublevel, η_r stands for the PLE-contributed radiative-exciton fraction of E_{11} transitions, and the PC extracted excitation fraction of excitons η_{PC} is bias voltage dependent(f) (modified from Ref. [214]).

EEA/AI requires the co-existence of two excitons and the probability for bi-exciton generation is expected to increase with the photon flux. Bindl *et al*. however observed a decrease of free carrier generation with a low-density photon flux and hence concluded that the spontaneous

exciton dissociation might rather occur at defects and/or traps, as displayed in Figure 4.7(a)[215]. In Kumamoto *et al.*'s experiment, the importance of EEA/AI-induced spontaneous exciton dissociation is difficult to infer since the free carriers were extracted with an external electric field[214]. Such a field can induce exciton dissociation by itself and generates free carriers as predicted theoretically (Figure 4.7(b))[77] and confirmed experimentally[216,217]. Thereby the field-induced exciton dissociation rate depends on the exciton binding energy and on the field strength, and is predicted to be significant above 100 V/µm for a 1 nm diameter s-SWCNT[77]. Furthermore exciton dissociation can be induced by optical-phonon scattering at room temperature if the exciton binding energy is smaller than the relevant optical phonon energy (200 meV) [77].

In the L-DEP experiment, the polarizability of s-SWCNTs is enhanced by the absorption of photons, which requires the dissociation of excitons. Although the different mechanisms responsible for exciton dissociation in this experiment cannot be distinguished, it is very likely that the AC electric field is of central importance. The free carrier generation rate was estimated under illumination and in the presence of an electric field by comparing these experimental conditions to the quantitative photocurrent experiment of Kumamoto *et al.*[214]

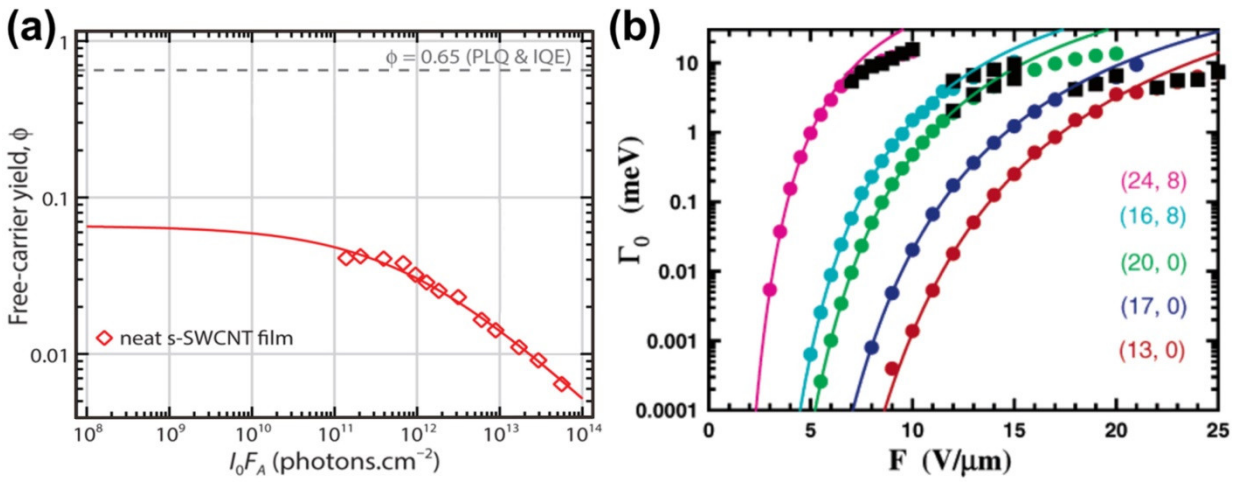

Figure 4.7: (a) Photon fluency dependence of the derived free carrier generation yield ϕ for neat s-SWCNT films (red diamonds) (modified from Ref. [215]). (b) Exciton dissociation rate Γ_0 as a function of field in (13,0) tube with $d_{CNT} = 1.0$ nm (red), (17,0) $d_{CNT} = 1.4$ nm (blue), (20,0) $d_{CNT} = 1.6$ nm (green), (16,8) $d_{CNT} = 1.7$ nm (cyan), and (24,8) $d_{CNT} = 2.3$ nm (magenta), the solid curves are derived using external electric field included Bethe-Salpeter equation (modified from Ref. [77]).

For comparable laser power density (P= 10^6 W/m^2) and electric field strength (10^6 V/m), and taking into account that the absorption cross-section σ for (6,5) SWCNTs at 532 nm is 1/10 of its value at 986 nm, a nominal current generation I on the order 100 fA was estimated for s-SWCNTs using

$$I = \frac{e\eta_{PC}N_{n,m}}{E_{ph}}\sigma P \tag{4.2}$$

with e denoting the electron charge, η_{PC} = 0.01 the PC extracted excitation fraction of excitons, E_{ph} the laser photon energy. This current leads to an accumulation of electrons and holes at the ends of the s-SWCNT and hence generates a dipole moment.

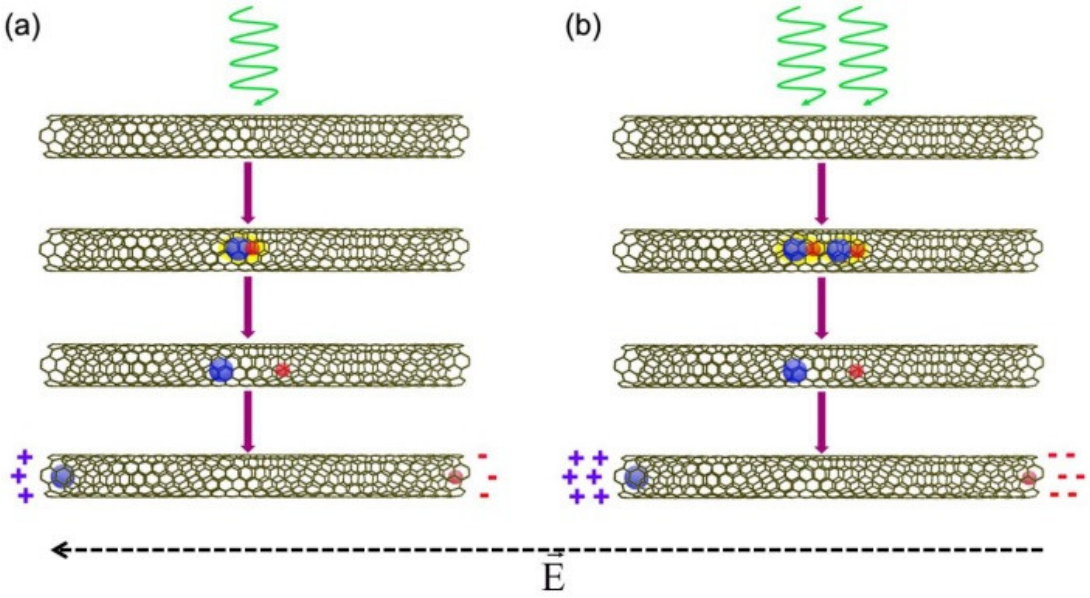

Figure 4.8: Schematics of the mechanism that enhances the polarizability of s-SWCNTs during L-DEP: Electric-field induced exciton dissociation (a), and spontaneous dissociation by exciton-exciton annihilation (b). The external electric field E (---) and the built-up positive (+) and negative charges (-) are indicated[78].

A schematic of the mechanism is shown in Fig. 4.8. The characteristic timescale τ for dipole formation is expected to be on the order of $\tau = \nu \cdot l_{CNT}$, where ν is the carrier saturation velocity, and l_{CNT} is the nanotube length. For $\nu \sim 10^5$ m/s from transport measurements[218] and l_{CNT} =1 µm, τ is ~10 ps and therefore much smaller than the corresponding time scale of AC field frequency (1 µs). Of course the built-up of the dipole is a dynamical and

self-limiting process since the accumulated charges are weakening the internal electric field that is required to separate the electrons and holes. At this point a quantitative modeling is required, which will be addressed in the future. Nevertheless, it can be concluded that under illumination and in the presence of an external field an induced dipole moment develops which oscillates in phase with the external AC field, resulting in an enhanced polarizability of (6,5) SWCNTs.

Fig. 4.8(b) indicates that L-DEP would be more effective if spontaneous EEA/AI is involved. Possibly this mechanism is already in operation. If not, it could be induced by higher photon fluxes. Also adjusting the excitation wavelength to the wavelength of maximum light absorption should enhance the L-DEP. Both aspects have to be addressed to further optimize the L-DEP process.

4.4. Summary

The density and alignment of dielectrophoretic deposition of water-dispersed (6,5) s-SWCNTs were improved using light-assisted dielectrophoresis technique (L-DEP). These improvements were confirmed with SEM observations of CNT depositions based on both normal DEP and L-DEP. Transistors fabricated with L-DEP showed systematically higher on/off ratios but smaller on-state currents as compared to transistors that were fabricated by normal DEP, verifying an increased semiconducting content within the channel materials under L-DEP case. The enhanced nanotube deposition was attributed to the polarizability improvement of s-SWCNTs during L-DEP, which arose from field-induced exciton dissociation. This work demonstrated that the DEP deposition of s-SWCNTs can be improved by directly enhancing their polarizability using external illumination.

Chapter 5: Solvent Effects and Length Mapping

The work contained in this Chapter can be found in Ref.[79].

5.1. Introduction

As mentioned in Chapter 2, the influence of the solvent's dielectric properties on the dielectrophoretic deposition of carbon nanotubes (CNTs) is significant[79]. Compared to aqueous CNT solutions, toluene was verified to be more insulative due to its extremely poor ion-concentration[219] and less dielectric polarizable arising from its small molecular dipole moment[220]. Thus, one can expect toluene to show a better behavior during the dielectrophoresis (DEP) of semiconducting carbon nanotube (s-SWCNT) than water (see eq. 2.26 and 2.27). In practice, such a reasonable comparative analysis should be based on a nanotube specimen with both diameter and length being well characterized. However, for the case of SWCNTs, due to their unique structure-property correlation, the chiral index and hence the diameter can directly be derived through spectroscopic methods such as absorption, fluorescence or Raman spectroscopy[6]. However, the length of a carbon nanotube has little influence on its optical properties and therefore a direct length-dependent spectroscopic method for CNTs with length, as reported[221,222], beyond 100 nm is not available.

Methods that were proven to be accurate in gauging nano-scale and micro-scale dimensions such as Transmission Electron Microscopy (TEM), Scanning Electron Microscopy (SEM) and Atomic Force Microscopy (AFM) were employed to measure the length of a nanotube or the length distribution of a nanotube ensemble. Among them, AFM method has particularly evolved to a standard approach for measuring nanotube length distributions[223,224]. However, it requires specific substrates, additional preparation steps and also reports uncertainties due to nanotube bundling on surfaces or selective adsorption. Therefore, the search for new SWCNT length measurement methods is ongoing, especially in the field of SWCNT liquid phase sorting, where a fast and practical *in-situ* length characterization would be extremely beneficial.

In recent years, a range of *in-situ* methods to measure the CNT length have been explored such as dynamic light scattering[225–228], electrospray differential mobility analysis[229], diffusional trajectory[230], shear-aligned photoluminescence anisotropy[231], and Analytical Ultracentrifugation[232]. The most advanced *in-situ* measurement of the length distribution of dispersed SWNCTs has been reported by Weisman *et al*. who introduced length analysis

through nanotube diffusion method (LAND)[230]. This technique yields length distributions very similar to the comparative ex-situ AFM method, but unfortunately it requires a dedicated fluorescence microscopy setup that is not available to all researchers in the field. Therefore, an *in-situ* method based on standard easily implementable equipment has yet to be reported.

In this Chapter, a rather simple method based on electric-field induced differential absorption spectroscopy (EFIDAS), which allows determining directly the length of SWCNTs in dispersions and provides chiral-index-resolution as an added value, is presented. Using low-k toluene instead of water, it is possible to resolve the field alignment of individually dispersed nanotubes, which comes from the pronounced CNT polarizability. Furthermore, since the used dispersions with only a small number of different SWCNT chiral indices, it becomes possible to resolve the chiral index dependent average length of CNTs. Moreover, a strategy to derive the chirality-resolved length distribution using the EFIDAS is also given.

5.2. Experimental

1. SWCNT dispersion

Dispersions of s-SWCNTs in toluene were prepared from pulsed laser vaporization (PLV) SWCNTs[127] using the polymer Poly(9,9-di-n-dodecylfluorenyl-2,7-diyl) (PODOF). The PODOF wrapped s-SWCNTs in toluene were then further length fractionated with a gel permeation chromatography (GPC) system[128] (as described in Chapter 3.2.2). The resulting dispersions contained (10, 8), (10, 9), (11, 7), (11, 9), (11, 10) and (12, 8) SWCNTs as shown in the Figure 5.1(a, c, d). For comparison, a dispersion enriched in (8, 6) SWCNTs (Figure 5.1(b)) in water was also prepared from high pressure carbon monoxide (HiPco) SWCNTs (NanoIntegris) using the surfactant sodium dodecyl sulfate (SDS) and size exclusion chromatography (SEC) [143] as described in Chapter 3.2.1.

2. Spectroscopy

EFIDAS measurements were performed in a setup (Figure 5.2) comprising of a fiber-coupled Ocean Optics HR4000 High-Resolution Spectrometer, a fiber-coupled Mikropack DH-2000-BAL UV-VIS-NIR light source, Ocean Optics collimating lenses, Thorlabs LPVIS050 linear polarizers and a Hellma 114-QS Quartz cuvette with 12.5mm × 12.5mm outer dimensions and 4mm × 10mm inner dimensions. The cuvette was loaded with its long axis parallel to the light beam, yielding an optical path length of 10mm. Copper electrodes were then

attached from the outside to the cuvette, parallel to the beam axis and biased with a Tesla generator dismantled from a commercial, low-value plasma ball. The generator has been characterized with a Testec TT HVP 15HF high-voltage probe. It produces a 20 kHz signal with $V_{rms} = 2380$ V when connected to the electrodes of a toluene filled cuvette. This voltage translates into an electric field of $E_{rms} = 2.5$ kV/cm in toluene using the expression for a capacitive voltage divider

$$E_{rms}^{toluene} = \frac{1}{t_{toluene}} \cdot \frac{\varepsilon_{glass}/t_{glass}}{\varepsilon_{glass}/t_{glass} + 2\varepsilon_{toluene}/t_{toluene}} \cdot V_{rms} \tag{5.1}$$

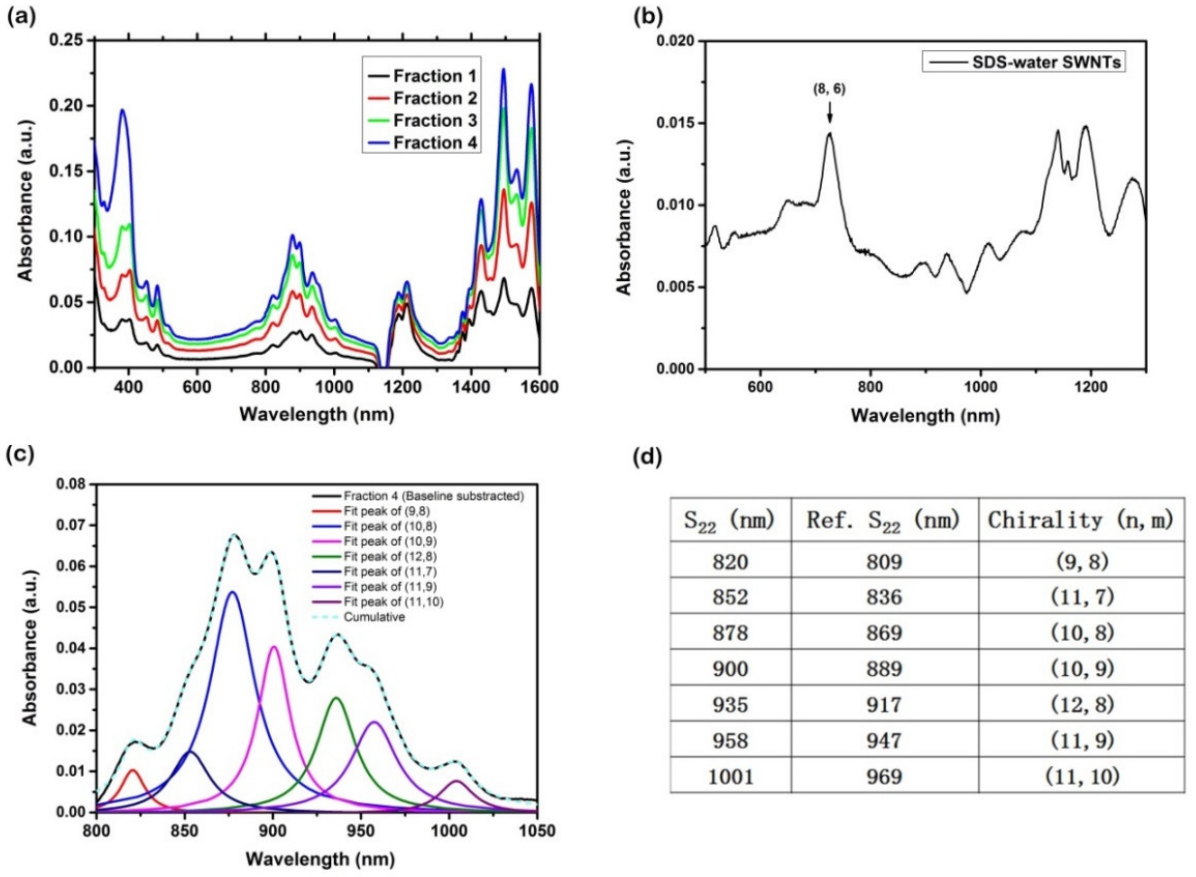

S_{22} (nm)	Ref. S_{22} (nm)	Chirality (n, m)
820	809	(9, 8)
852	836	(11, 7)
878	869	(10, 8)
900	889	(10, 9)
935	917	(12, 8)
958	947	(11, 9)
1001	969	(11, 10)

Figure 5.1: Absorption spectra of PODOF-wrapped semiconducting SWCNTs in toluene (a) and (8,6) dispersed in SDS/water (b). The data has been measured with a complementary setup that extends the range of the EFIDAS setup towards the near infrared. (c) Zoom-in to the S_{22} region that is relevant for the EFIDAS measurements. The absorption data has been de-convoluted into individual (n,m) contribution using Lorentzian fit functions after subtracting a linear background. The dashed line is the cumulative of the individual contributions and fits very well to the data. (d) (n m) assignment of the individual peaks

based on reference data from SWCNTs in aqueous surfactant medium[233]. Differences in the peak positions are due to the different solvents (toluene versus water)[79].

with the thickness of the two quartz glass walls $t_{glass} = 4.25$ mm, the thickness of the toluene layer $t_{toluene} = 4$ mm, the dielectric constant of quartz glass $\varepsilon_{glass} = 3.75$ and the dielectric constant of toluene $\varepsilon_{toluene} = 2.38$[219] (see Appendix A).

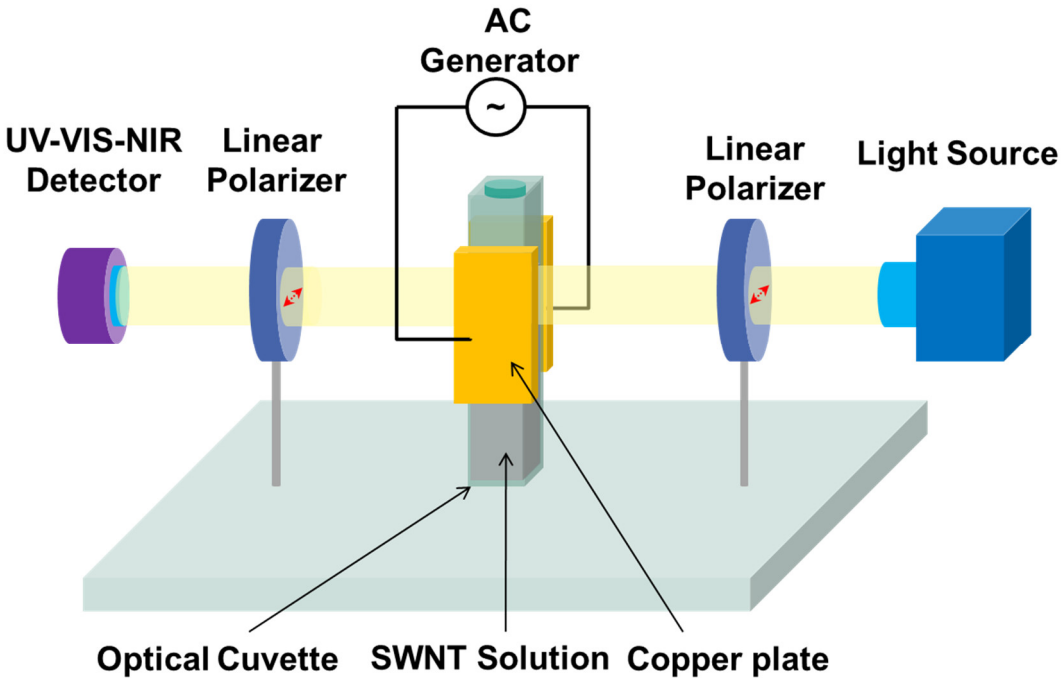

Figure 5.2: Schematic of the electric-field induced differential absorption spectroscopy setup. The linear polarizers are horizontally aligned indicated by red arrows and parallel to the direction of the electric field generated across the cuvette[79].

For calculations (as referred to the P5-1) of the electric field in water ($\varepsilon_{water} = 81$), the ionic conductance has been taken into account ($\sigma = 0.1$ S/m for 1 wt-% SDS) yielding a frequency dependence of the field amplitude as shown in Figure 5.3. In the EFIDAS setup both polarizers were aligned parallel to the electric field axis. The spectral range of the setup was 300 - 1000 nm.

In addition, range-extended absorption spectra of CNT suspensions (Figure 5.1(a)) were measured with a Varian Cary 500 spectrometer (as described in Chapter 3.3.1) without electric fields. Photoluminescence excitation maps (Figure 5.4) were employed for the analysis of CNT chiralities in fractions using the way described in Chapter 3.3.3[202].

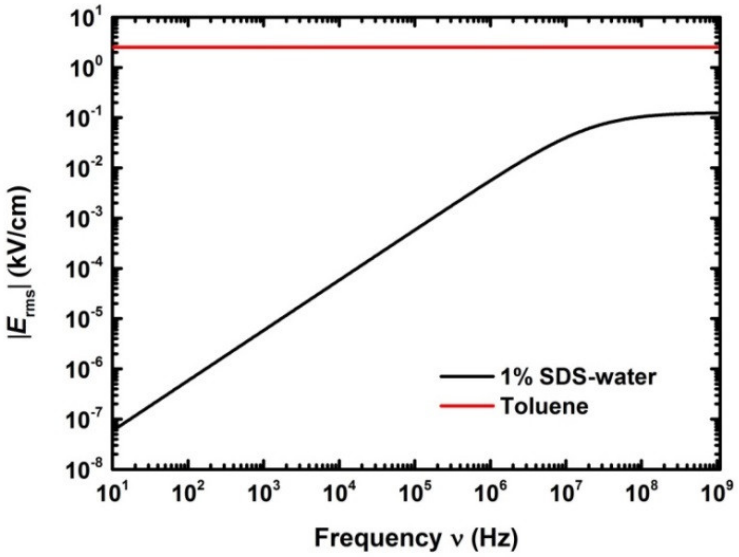

Figure 5.3: Electric field E_{rms} versus field frequency ν in toluene and in water with 1 wt-% SDS. The voltage amplitude applied to the cuvette is $V_{rms} = 2380$ V in both cases[79]. Calculation detials can be referred to the Matlab program P5-1 in the attached CD.

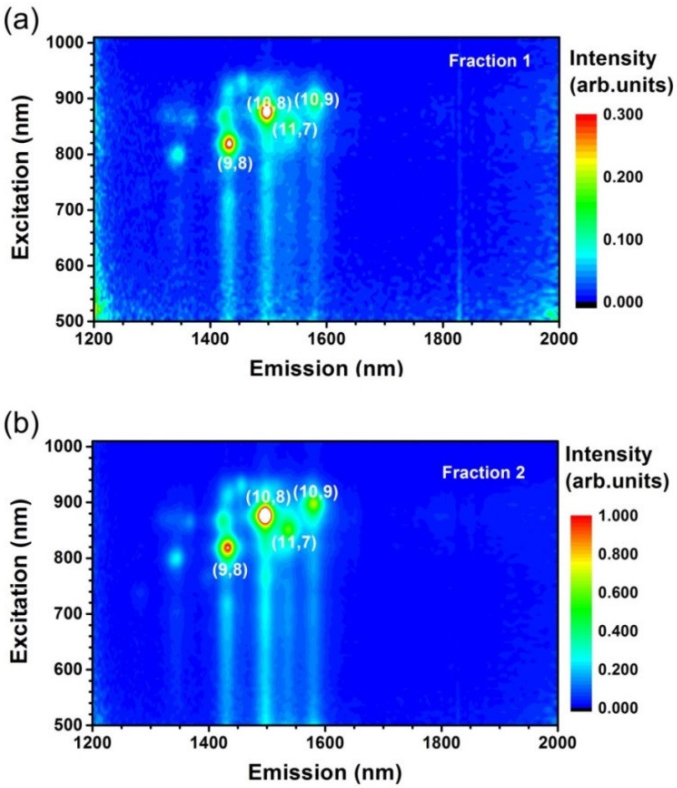

Figure 5.4: Photoluminescence excitation maps of PODOF-wrapped semiconducting SWCNTs in toluene. (a) fraction 1, (b) fraction 2. CNT species with emission line above 1650 nm are not detectable due to the strong absorption of toluene between 1650-1700 nm[79].

5.3. Results and Discussion

Excluding the inconvenience in obtaining same CNT materials but suspended in different solvents, in order to discuss solvent effects on nanotube polarizability, it is a good option to spectroscopically analyze the alignment of CNTs dispersed in different solvents when external electric fields are applied on. This strategy makes use of the nanotube torque arising from the rotating dipole moment of the SWCNT as placed in electric fields. The electric-field induced alignment of SWCNTs in dispersion has been reported in the literatures of Ref. [234–236]. However, previous reports in aqueous media could only resolve alignment of SWCNT bundles and not well dispersed individual SWCNTs.

The derivation of the electric-field induced differential absorption (EFIDAS) by considering the optical absorption of carbon nanotubes in between two parallel linear polarizers $A_{\parallel}$ is modelled as[237,238]

$$A_{\parallel} = \sum_i \zeta_i \times N_i \times \frac{2S_{3D,i} + 1}{3} \tag{5.2}$$

where i denotes the different (n, m) SWCNT species in solution with absorption coefficient ζ_i and counting number N_i. S_{3D} stands for the three-dimensional nematic order parameter[238], which has a lower-limit of $S_{3D} = 0$ for a completely disordered phase, $S_{3D} \neq 0$ for a weakly ordered phase and an upper-limit of $S_{3D} = 1$ corresponding to a perfectly ordered phase, as described in Chapter 2.4.3. For SWCNTs with diameter d_{CNT} and length l_{CNT} exposed to a homogeneous electric field $\vec{E}$ with angular frequency ω, the nematic order parameter can be expressed as $S_{3D} = S_{3D}(\left|\vec{E}\right|, \omega, l_{CNT}, d_{CNT}, \varepsilon^*_{CNT}, \varepsilon^*_{\ell})$, with the complex dielectric functions ε^*_{CNT} and ε^*_{ℓ} of the nanotubes and the solvent medium, respectively.

S_{3D} is a direct measure of the orientation of SWCNTs under an external electric field, provided that the absorption coefficient ζ_i in equation (5.2) is constant under the applied electric field. In this Chapter, this assumption is valid when considering the electro-absorption experiments of surface-pinned SWCNTs carried out by Izard *et al.*[239,240]. It has been reported by them that upon applying an electric field of 12.5 kV/cm, the changes of ζ_i are on the order of 10^{-4}, whereas in this study with dispersed SWCNTs changes in $A_{\parallel}$ are observed in the order of 10^{-1}

at an electric field of 2.5 kV/cm. Thus $A_{\parallel}$ is predominantly determined by the orientation of SWCNTs as reflected by S_{3D}. The electric-field induced differential absorption ΔA is then simply the relative difference of the optical absorption with and without an electric field. Since ζ_i is not electric field dependent, ΔA is only proportional to S_{3D},

$$\Delta A = \frac{A_{\parallel}(E) - A_{\parallel}(E=0)}{A_{\parallel}(E=0)} = \frac{\left(\frac{2S_{3D}(E)+1}{3}\right) - \frac{1}{3}}{1/3} = 2S_{3D}(E) \tag{5.3}$$

S_{3D} can be expressed in terms of the alignment angle θ as,

$$S_{3D} = \frac{1}{2}(3\overline{\cos^2\theta_i} - 1) = \int \frac{1}{2}(3\cos^2\theta - 1)\cdot f(\theta, U_{ROT})d\Omega \tag{5.4}$$

The bar indicates that the mean value, θ is measured between the long-axis of the nanotube and the electric field direction, which is also the polarization direction of the incident light in this experiment, and here Ω is the solid angle. U_{ROT} is the rotational energy of the SWCNT in the electric field and $f(\theta, U_{ROT}, T)$ is the Boltzmann distribution function. U_{ROT} is calculated on the basis of the polarizability of SWCNTs in solution as described in detail by Blatt *et al.*[169]. T is the temperature and is set to 300K. On this basis S_{3D} and ΔA can be calculated as a function of $\left|\vec{E}\right|$, ω, l_{CNT}, d_{CNT}, ε^*_{CNT}, ε^*_l. Here ε^* can be written as $\varepsilon^* = \varepsilon + i\sigma/\omega$, with $\varepsilon_\ell = 2.38\varepsilon_0$ and $\sigma_\ell = 1.0\times10^{-11} S/m$ for toluene[219] (see Appendix A). For SWCNTs, $\varepsilon_{CNT}(d_{CNT})/\varepsilon_0 = 33.8 + 3.28nm^2/d^2$ deduced from first-principles calculations reported by Marzari *et al.*[155], yielding values between $35.4\varepsilon_0$ and $36.3\varepsilon_0$ for the SWCNTs under consideration. From previous dielectrophoresis experiments σ_{CNT} is on the order of $0.1 S/m$ [80,169]. It should be emphasized that the simulation contains no additional free parameters.

In order to derive the differential absorption ΔA [237], the CNT rotational energy U_{ROT} dependent Boltzmann function $f(\theta, U_{ROT}, T)$ (as shown in eq. (5.3) and (5.4)) should be derived. This function can be expressed as the eq. 2.34[169], with $f(\theta)d\Omega$ standing for the probability of

having CNT orientation (with respect to the predicted electric field) within the unit radian angle of $d\theta$ in the spherical coordinate (as shown in Figure 5.5).

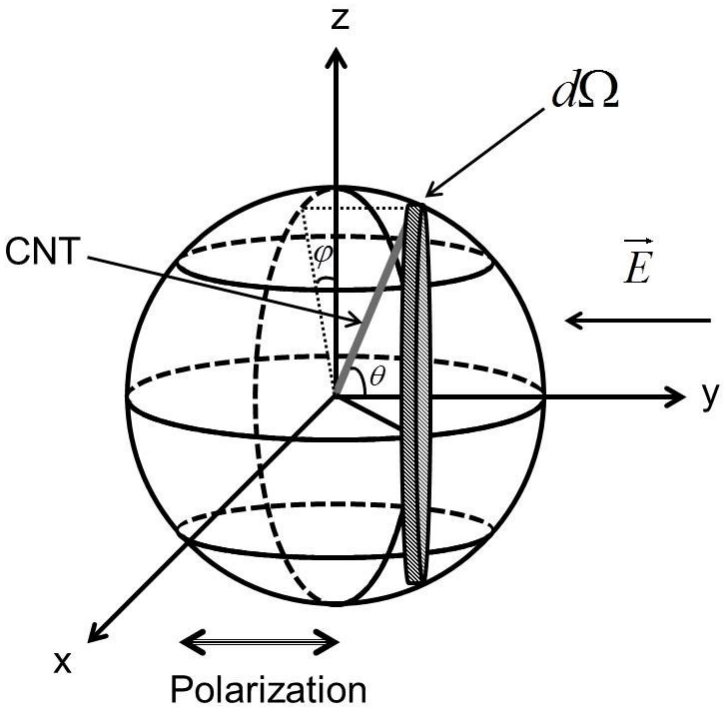

Figure 5.5: Cartesian and spherical coordinates for the EFIDA spectroscopy-based model of SWCNTs, the direction of polarized light is parallel to the electric field[79].

Figure 5.6 shows the dependence of differential absorption of semiconducting SWCNTs in toluene on the nanotube length and diameter when exposed to an electric field E = 2.5 kV/cm at a frequency $v = \omega/2\pi = 20$ kHz. For SWCNTs with length up to 1.5 µm and diameter between 1-1.5 nm, ΔA can reach values of unity and therefore is experimentally verifiable. A perfect alignment would correspond to $\Delta A = 2$. However, this value cannot be reached due to depolarization effects, which is more pronounced for smaller diameter SWCNTs and will be discussed below. The sensitivity of ΔA to a certain nanotube length range can be tuned by varying E, as shown in Figure 5.7.

For measuring ΔA , the set-up shown in Figure 5.2 was used. The core is a cuvette with external electrodes driven by a signal generator to generate an electric field that is perpendicular to the light path and parallel to the horizontal alignment of the two linear polarizers. Light from a halogen lamp is guided through the polarizers and cuvette, and detected by a silicon charge-coupled device (CCD) based spectrometer. Each measurement of ΔA comprises a

zero-field measurement and a field measurement. The signal generator supplies a 20 kHz signal with a voltage amplitude of 2380 V, resulting in an electric field strength of 2.5 kV/cm in toluene. Such field strength has also been used for the simulation in Figure 5.6 as mentioned above.

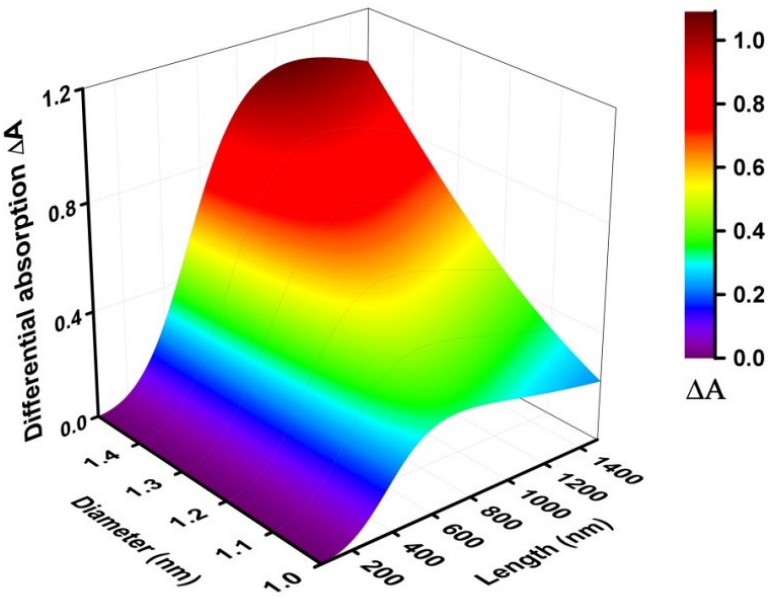

Figure 5.6: Simulation of differential absorption ΔA as a function of SWCNT diameter d_{CNT} and length l_{CNT} for s-SWCNTs dispersed in toluene. The electric field and frequency was set to E_{rms} = 2.5 kV/cm and v = 20 kHz[79]. Calculation detials can be referred to the Matlab program P5-2.

The used dispersions consists of polymer-wrapped SWCNTs in toluene containing primarily (9, 8), (10, 8), (10, 9), (11, 7), (11, 9), (11, 10) and (12, 8) SWCNTs detectable by the EFIDAS setup via their S_{22} transitions. This is confirmed with absorption (Figure 5.1) and photoluminescence spectroscopy (as shown in Figure 5.4. (11, 9), (11, 10) and (12, 8) SWCNTs are absent because their S_{11} transitions are within the optical range of strong absorption of toluene as introduced in Appendix B).

EFIDAS with 4 fractions that were length sorted as described in Ref. [128] were measured in this study. For reference their length distribution was characterized using atomic force microscopy (AFM). Fitting the measured length distribution to a Gaussian and lognormal distribution function (as shown in Figure 5.8), the Gaussian mean value and lognormal peak values of the fractions were determined for fraction 1 to 790±18 nm and 720±27 nm, for

fraction 2 to 543±19 nm and 465±24 nm, for fraction 3 to 564±19 nm and 480±39 nm, and for fraction 4 to 390±18 nm and 345±20 nm, respectively. Hence it was noted that the average length of SWCNTs decreases from fraction 1 to fraction 4, which is a consequence of the longer retention time of shorter nanotubes in the column[241].

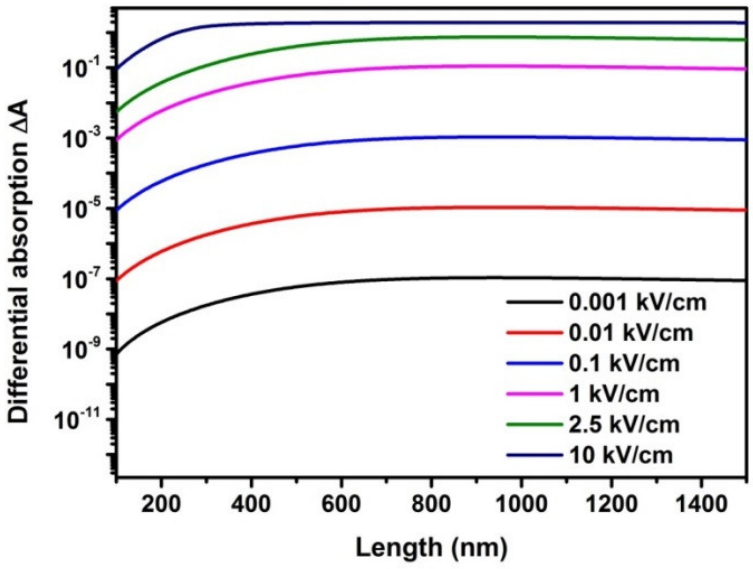

Figure 5.7: Differential absorption ΔA as a function of electric field strength field E and nanotube length l_{CNT}. Simulations were done for semiconducting SWCNTs with diameter d_{CNT} = 1.30 nm, dispersed in toluene. The field frequency was set to $\nu = 20$ kHz[79]. Calculation detials can be referred to the program P5-2.

The EFIDAS setup allows measuring ΔA associated with the second optical transitions S_{22} of the dispersions. Figure 5.8 shows the differential absorption spectra ΔA derived from the absorption spectra with and without applied electric field for the fractions 1-4 in (a, c, e, g), next to the corresponding length distributions determined by AFM in (b, d, f, h). Firstly, as shown, the overall minimum and maximum of ΔA is 0.1 and 0.75, respectively, and hence within the range of the simulation. Secondly, the observed ΔA scales systematically with the SWCNTs average length, with the highest value measured for fraction 1 and the lowest for fraction 4. This observation shows that EFIDAS is sensitive to the length of SWCNTs in dispersion and shows qualitatively a dependence that is consistent with the simulations shown previously. Lastly, the derived ΔA is wavelength dependent, with the maxima and minima correlating to structures in the absorption spectra.

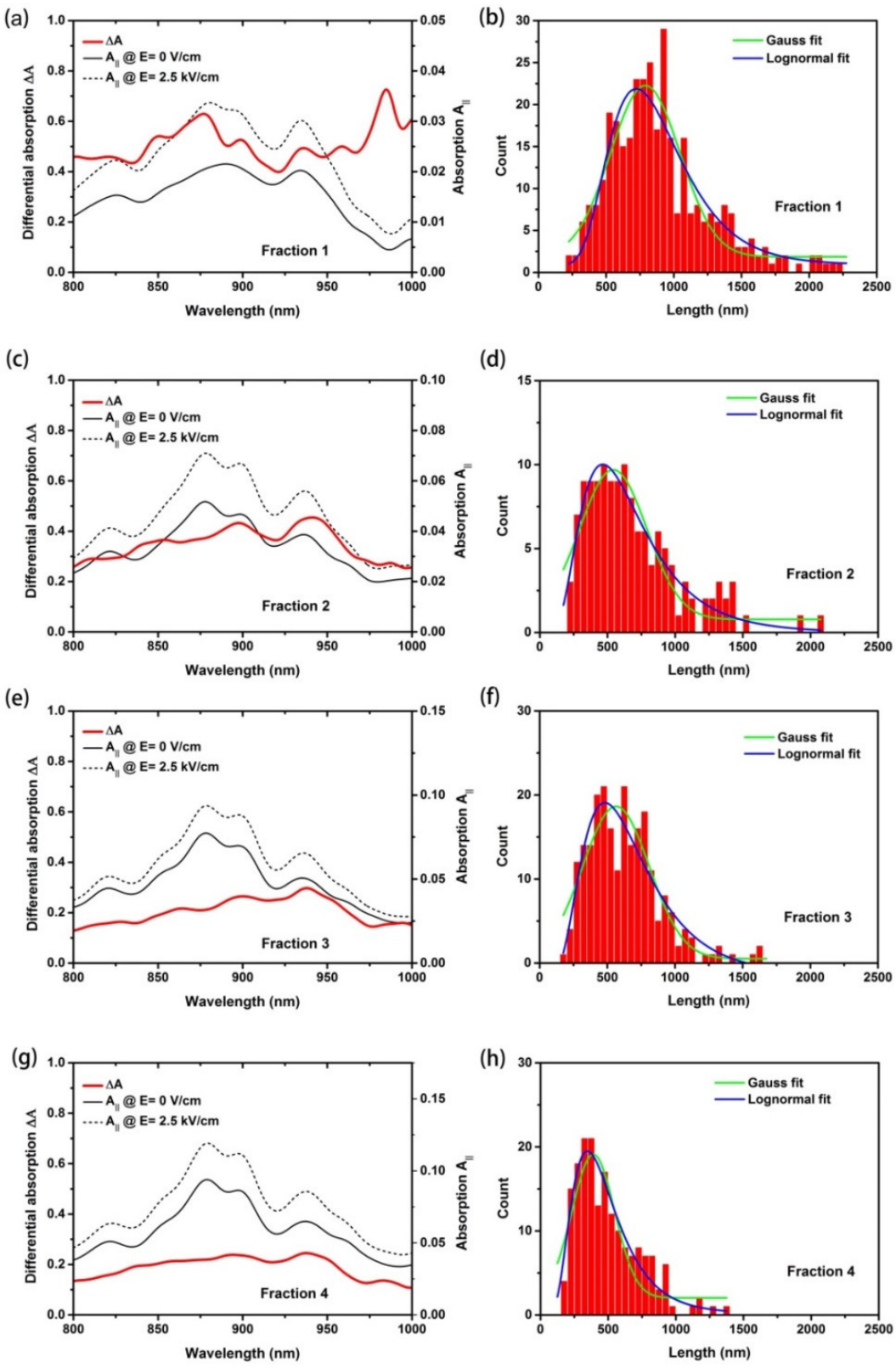

Figure 5.8: Differential absorption spectra ΔA and absorption spectra $A_{\parallel}$ of semiconducting SWCNTs in toluene, measured at zero field and at E_{rms} = 2.5 kV/cm and ν = 20 kHz. The data is shown for fractions 1-4 (a, c, e, g) together with AFM length measurements (b, d, f, h)[79].

Figure 5.9(a) shows for fraction 1 an assignment of the peaks in ΔA to the SWCNT chiral index based on reference absorption and photoluminescence spectra shown in the Figures 5.1 and 5.4. Since the concentration effects drop out in EFIDAS, the modulations in ΔA can be traced back to a chiral-index dependent degree of alignment. Interestingly the modulations in ΔA are also present in the shorter SWCNT fractions 2-4, where, according to Figure 5.6, ΔA is no longer sensitively dependent on the SWCNT chiral index or diameter. Hence a still observable modulation of ΔA must reflect a heterogeneous length distribution across the chiral index specific SWCNT subpopulations in the different fractions.

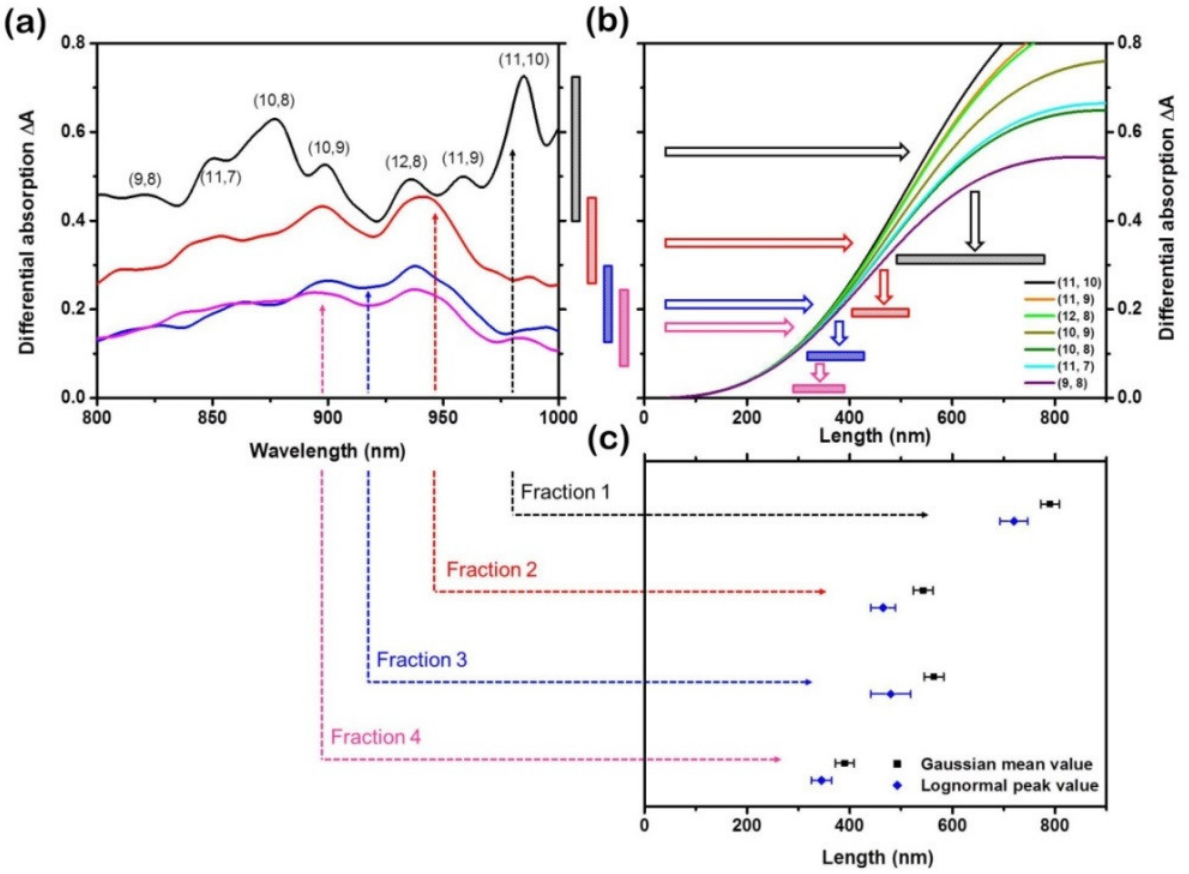

Figure 5.9: Length determination with EFIDAS. (a) Differential absorption spectra ΔA measured for fractions 1-4 with indicated (n, m)-specific contributions. (b) (n, m)-specific calculations of ΔA versus nanotube length l_{CNT}. Ranges of ΔA are converted into ranges of l_{CNT} as indicated by bars and arrows. The results are compared to fitted AFM mean and peak length values for the fractions shown in (c)[79].

Now, the length of SWCNTs l_{CNT} in the dispersion can be extracted from the differential absorption spectra ΔA. Figure 5.9(a) shows ΔA for fractions 1-4. Ranges of ΔA are indicated

for each fraction by vertical bars. The experimental ΔA values can be converted into l_{CNT} by using the simulation-derived correlation between ΔA and l_{CNT} as shown in Figure 5.9(b). The values of l_{CNT} measured by EFIDAS are on the same order of magnitude as the AFM mean length and also follows a similar trend, where higher fraction numbers have on average shorter SWCNTs (Figure 5.9(c)). As shown, for all fractions the EFIDAS derived values fit very well to the AFM mean length.

The agreement between the two methods is noteworthy, in particular since EFIDAS is based only on the dielectric functions of the SWCNTs and the solvent, and hence without free parameters. Critical to the methods quantitative applicability is certainly the correlation between ΔA and l_{CNT}. It is interesting to see that the calculated curves in Figure 5.9(b) do not fall on top of each other. This is due to small variations in ε_{CNT} and d_{CNT} for the chiralities of interest.

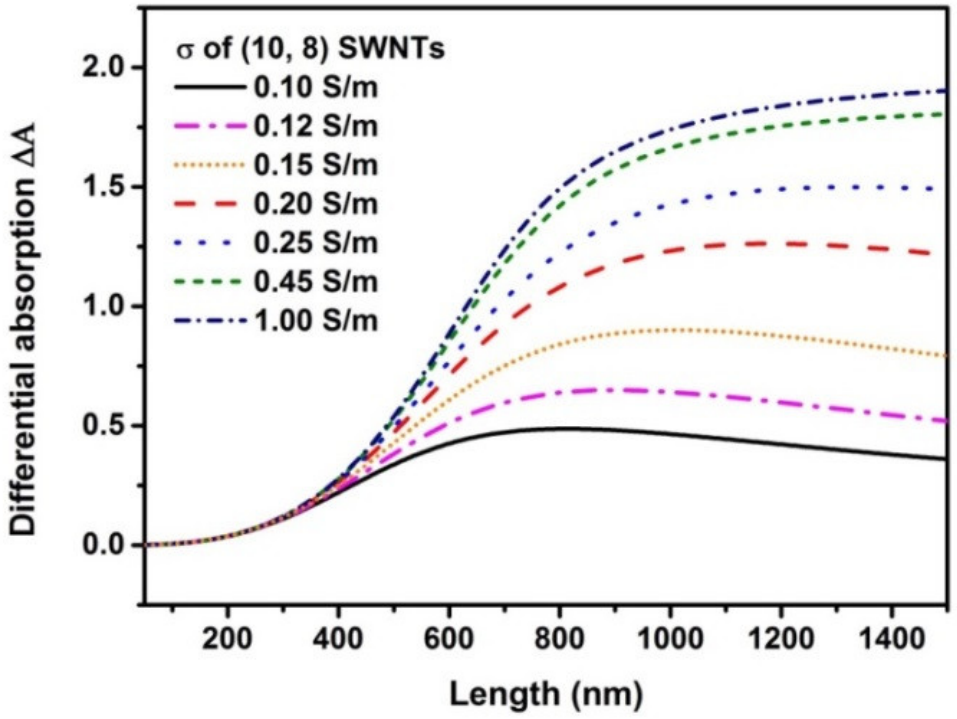

Figure 5.10: Differential absorption ΔA as a function of nanotube conductivity σ_{CNT} and nanotube length l_{CNT} for (10, 8) SWCNTs dispersed in toluene. The electric field and frequency was set to E_{rms} = 2.5 kV/cm and ν = 20 kHz[79]. Calculation detials can be referred to the Matlab program P5-2 in the attached CD.

The influence of σ_{CNT} is shown in Figure 5.10. For the simulation of Figure 5.9(b) and Figure 5.6, $\sigma_{CNT} = 0.12 S/m$ was used, which is a value that provides the best fit to the AFM data and also happens to be comparable to that obtained from the earlier dielectrophoresis experiments with SWCNTs in aqueous medium[169]. Previously, the non-zero value of σ_{CNT} has been attributed to surface-induced conductivity mediated by ions in the aqueous double layer. For polymer-wrapped un-doped SWCNTs in toluene, σ_{CNT} would be expected to be negligibly small. However simulations in Figure 5.10 show that for $\sigma_{CNT} = 0.1 S/m$ for which the maximum value for ΔA does not exceed 0.6. This is in contradiction with the experimental observations of (10,8) SWCNTs, yielding a peak value of 0.63 from fraction 1. On the other hand a significantly larger value would shift the curve towards shorter l_{CNT} and lead to an underestimation of the true length when benchmarked with the AFM measurements. Since surface-induced conductivity mediated by ions can be excluded in this work, σ_{CNT} must be related to intrinsic free charge carriers present in the SWCNTs.

The estimation of σ_{CNT} in toluene case can be given by considering 4 conduction channels that are thermally activated by $\exp(-\Delta/2kT)$. With a transport gap of $\Delta = 1$ eV[242] and $kT = 0.025$eV, this would correspond to a thermally activated resistance of $R \approx 3 \cdot 10^{12}\ \Omega$. Assuming $l_{CNT} \approx 1 \mu m$ and $d_{CNT} \approx 1 nm$, R can then formally be converted into $\sigma = 4 l_{CNT} / \pi R d_{CNT}^2 \approx 0.4$ S/m, yielding the right order of magnitude. This oversimplified approach should be further developed including the influence of doping. However this would be beyond the scope of this study.

Based on the differential absorption for different (n,m) species extracted from Figure 5.9(a), the length of chiral index subpopulations encoded in the EFIDAS data can be derived. The $\Delta A(n,m)$ values are converted into $l_{CNT}(n,m)$ and plotted against the fraction number as shown in Figure 5.11. The graph shows that overall the SWCNT length decreases with fraction number. Interestingly, the (n,m) length order, according to EFIDAS, is changing from fraction 1 to fraction 2, which would mean that the elution time in GPC-based sorting not only depends on the SWCNT length but also on the chiral index. Whether the EFIDAS results are significant or whether the measurement error is underestimated remains currently unresolved. Unfortunately, this result cannot be confirmed by AFM measurements since AFM is not

sensitive to the chiral index, but the data indicates the potential of EFIDAS for chirality-resolved length measurements in solution.

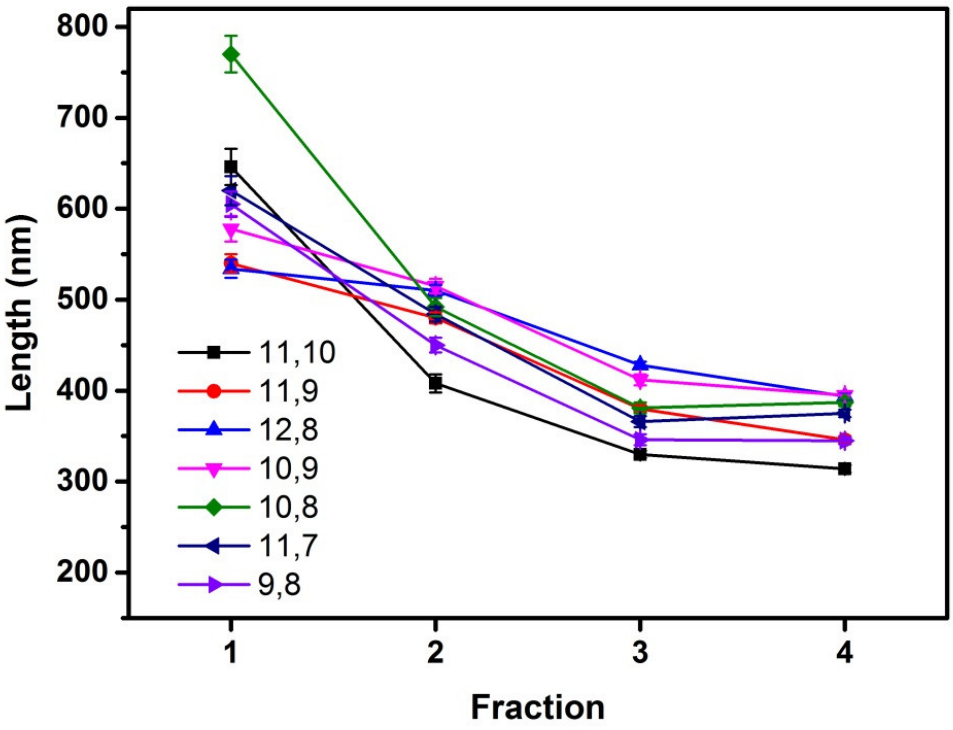

Figure 5.11: Chirality-resolved mean length determined by EFIDAS for SEC-sorting fractions 1-4[79].

The dependence of EFIDAS on the electric field frequency is essential to understand the non-monotonic length dependence of ΔA for small diameter nanotubes in Figure 5.6. As explained before, ΔA is calculated from the rotational energy U_{ROT} using equations 5.3 and 5.4. U_{ROT} is defined as the integral over the time-averaged torque $\langle T \rangle$ imposed on the SWCNTs in the oscillating field (eq. 5.5), whereas $\langle T \rangle$ is proportional to the difference of the real parts of the longitudinal and transverse Clausius-Mossotti factors $CM_{\parallel}$ and $CM_{\perp}$, respectively (eq. 5.6). The Clausius-Mossotti factors contain the frequency-dependent dielectric functions of the CNT and the solvent (eq. 5.7):

$$U_{ROT} = \int \langle T \rangle_{CNT} \, d\theta \tag{5.5}$$

$$\langle T \rangle_{CNT} = \vec{E}_{RMS}^{2} \frac{\pi}{6} l_{CNT} d_{CNT}^{2} \varepsilon_l \left[\mathrm{Re}\{CM_{\parallel}\} - \mathrm{Re}\{CM_{\perp}\} \right] \sin\theta \cos\theta \tag{5.6}$$

$$CM(\omega)_{\parallel,\perp} = \frac{\varepsilon_{\parallel,\perp}^{CNT\,*}(\omega) - \varepsilon_{\ell}^{*}(\omega)}{\varepsilon_{\ell}^{*}(\omega) + (\varepsilon_{\parallel,\perp}^{CNT\,*}(\omega) - \varepsilon_{\ell}^{*}(\omega)) L_{\parallel,\perp}} \tag{5.7}$$

$L_{\parallel}$ and $L_{\perp}$ are the longitudinal and transverse depolarization factors, respectively, with $L_{\perp} = 1/2$ and $L_{\parallel} = d_{CNT}^{2} / l_{CNT}^{2} \left[\ln(2l_{CNT}/d_{CNT}) - 1 \right]$ [80,168]. The expressions can be simplified for semiconducting SWCNTs since $\varepsilon_{\parallel}^{CNT} = \varepsilon_{\perp}^{CNT} = \varepsilon_{CNT}$ and $\sigma_{\parallel}^{CNT} = \sigma_{\perp}^{CNT} = \sigma_{CNT}$, as outlined by Blatt *et al.*[169]

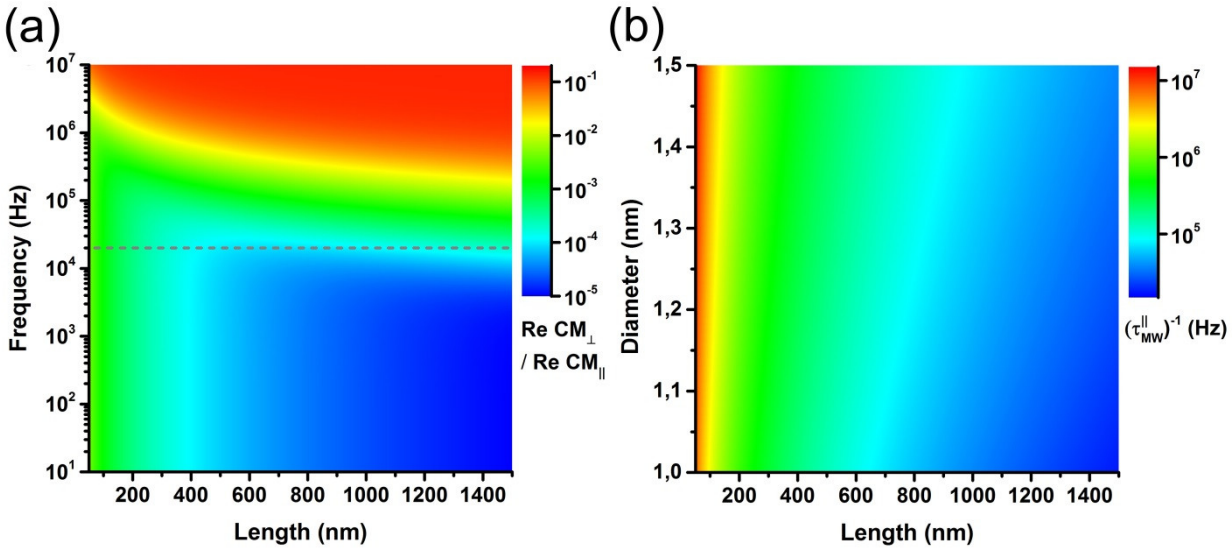

Figure 5.12: Simulation of (a) the ratio of the real part of the transverse and longitudinal Clausius-Mossotti factors Re{CM∥} / Re{CM⊥} as a function of field frequency ν and nanotube length l_{CNT}, and (b) the longitudinal Maxwell-Wagner relaxation frequency $\left(\tau_{MW}^{\parallel}\right)^{-1}$ versus nanotube length l_{CNT} and nanotube diameter d_{CNT}. Simulations were done for semiconducting SWCNTs dispersed in toluene. In (a) d_{CNT} = 1.30 nm and E_{rms} = 2.5 kV/cm, and the horizontal dashed line indicates the field frequency used for the EFIDAS measurements[79]. Calculation detials can be referred to the Matlab program P5-3 in the attached CD.

Figure 5.12(a) shows that $\mathrm{Re}\{CM_{\parallel}\} >> \mathrm{Re}\{CM_{\perp}\}$ throughout the simulation space. Hence the frequency dependence of U_{ROT} and thus of ΔA is entirely determined by $\mathrm{Re}\{CM_{\parallel}\}$. Figure 5.13(a) shows the plots of $\mathrm{Re}\{CM_{\parallel}\}$ as a function of field frequency and SWCNT length

for d_{CNT} = 1.30 nm. The data shows that $\mathrm{Re}\{CM_{\|}\} > 10^3$ for $\nu < 10^5$Hz. Therefore, ΔA reaches sizable values only for $\nu < 10^5$ Hz as shown in Figure 5.13(b). The experimental frequency ν = 20 kHz is hence a good choice for EFIDAS based length measurements of semiconducting SWCNTs in toluene, although larger ΔA values are expected for lower frequencies as shown in Figure 5.13(b). A practical measure for selecting an appropriate field frequency is the so-called Maxwell-Wagner relaxation time τ_{MW}, which accounts for the characteristic time scale of charge accumulation at the interface of two materials. For SWCNTs modelled as prolate ellipsoids[157,168,169], the relevant longitudinal Maxwell-Wagner relaxation $\tau_{MW}^{\|}$ is given by $\tau_{MW}^{\|} = L_{\|}\varepsilon_{CNT} + (1-L_{\|})\varepsilon_l / L_{\|}\sigma_{CNT} + (1-L_{\|})\sigma_l$. The corresponding Maxwell-Wagner relaxation frequency $\left(\tau_{MW}^{\|}\right)^{-1}$ decreases with the SWCNT length and increases with the SWCNT diameter, as shown in Figure 5.12(b), and can be traced back to the diameter and length dependence of $L_{\|}$. A necessary condition for effective EFIDAS measurements is fulfilled if $\nu < \left(\tau_{MW}^{\|}\right)^{-1}$. Also the non-monotonic length dependence of ΔA for small diameter semiconducting SWCNTs in Figure 5.6 is due to the length and diameter dependence of $\left(\tau_{MW}^{\|}\right)^{-1}$ and $\mathrm{Re}\{CM_{\|}\}$.

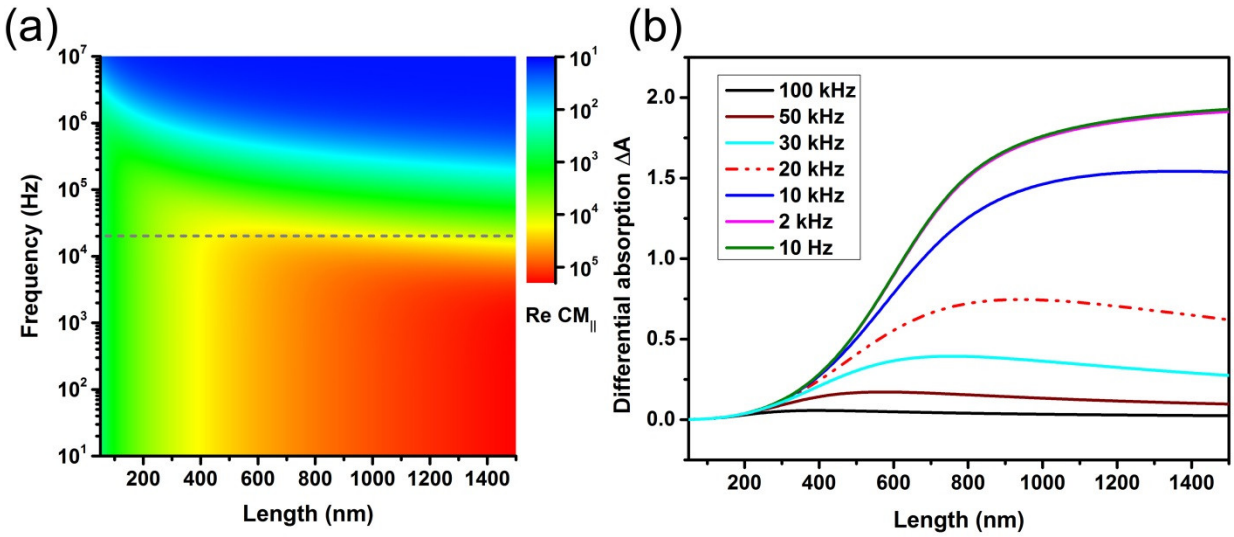

Figure 5.13: Simulations of (a) the real part of the longitudinal Clausius-Mossotti factor $\mathrm{Re}\{CM_{\|}\}$ and (b) the differential absorption ΔA , as a function of field frequency ν and nanotube length l_{CNT} . Simulations were done for semiconducting SWCNTs with diameter d_{CNT} = 1.30 nm, dispersed in toluene and exposed to an electric field E_{rms} = 2.5 kV/cm. The horizontal dashed line in (a) indicates the field frequency used for the EFIDAS measurements[79].

Calculation detials can be referred to the Matlab programs of P5-2 and P5-3 as presented in the attached CD.

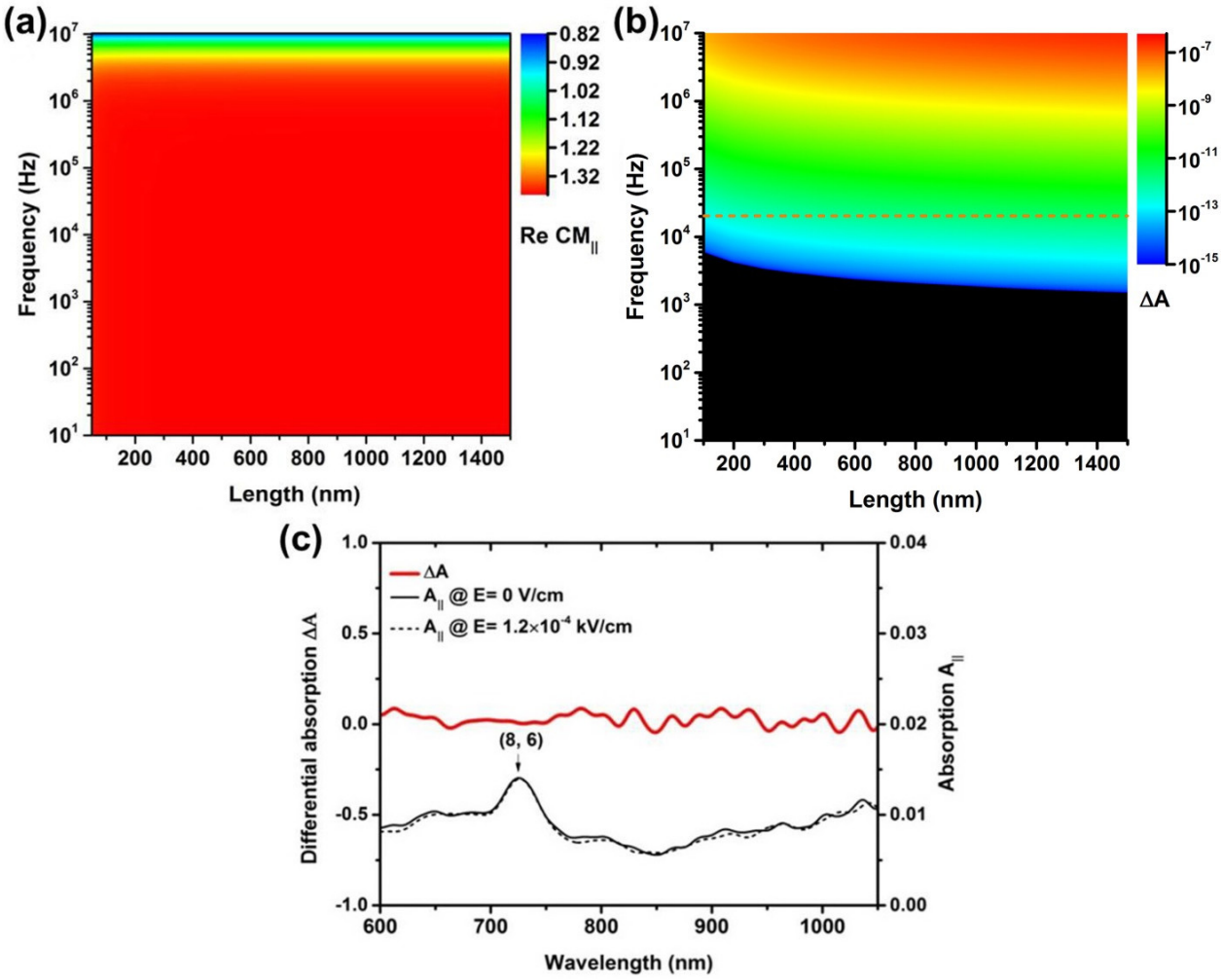

Figure 5.14: EFIDAS with semiconducting SWCNTs in aqueous surfactant solution. (a) Simulation of differential absorption ΔA as a function of field frequency ν and nanotube length l_{CNT}, for SWCNTs in 1-wt%-SDS in water. The horizontal dashed line indicates the field frequency used in the experiment. (b) Measurements of differential absorption spectra ΔA and absorption spectra $A_{||}$ at zero field and at $E_{rms} = 1.2 \cdot 10^{-4}$ kV/cm and $\nu = 20$ kHz. The electric field in water is reduced by 4 orders of magnitude and ΔA by at least 10 orders of magnitude as compared to toluene[79]. Calculation detials can be referred to the Matlab programs P5-2 and P5-3 in the attached CD.

A limitation of EFIDAS is that the method does not work for semiconducting SWCNTs in aqueous surfactant solution. This is because the conductivity of water with 1 wt-% SDS is $\sigma_{water} = 0.1$ S/m, and 10 orders of magnitude larger compared to toluene. This large

conductivity of the solution in combination with the dielectric constant of water ($\varepsilon_{water} = 81\,\varepsilon_0$) yields for the same applied voltage amplitude of V_{rms} = 2380 V an electric field of only E_{rms} = $1.2 \cdot 10^{-4}$ kV/cm at ν = 20 kHz, which is 4 orders of magnitude lower than in toluene. On the other hand, the $CM_{\parallel}$ of the SWCNTs dispersed in this aqueous surfactant solution, as shown in Figure 5.14(a), is in the order of 10^0, which is about 4 order magnitude smaller than that of toluene at ν = 20 kHz. This means that the polarizability of SWCNTs is much suppressed in the water case than toluene.

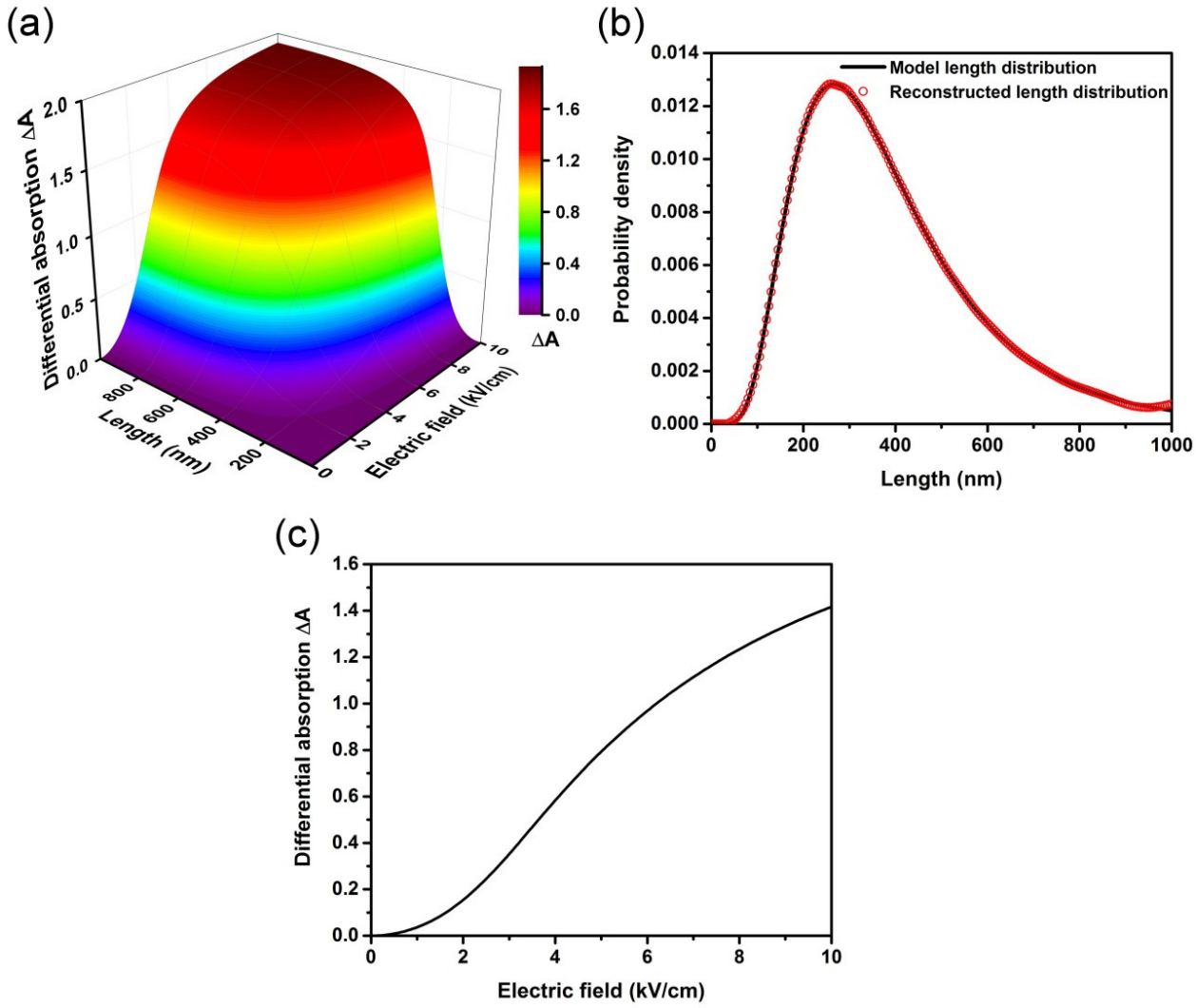

Figure 5.15: Strategy to determine (n,m)-specific length distribution of SWCNTs in dispersion with EFIDAS. (a) Simulation of the differential absorption ΔA as a function of SWCNT length l_{CNT} and electric field E_{rms}, for d_{CNT} = 1.30 nm and ν = 20 kHz. (b) Log-normal model length distribution (solid line) compared to the length distribution (open symbol) reconstructed from (c) as described in the text. (c) Differential absorption *versus* electric

field E_{rms} for the log-normal model length distribution shown in (b)[79]. Calculation detials can be referred to the Matlab program P5-4 in the attached CD.

As a consequence of the very low field amplitude and polarizability, ΔA is more than 10 orders of magnitude smaller compared to toluene, and hence not detectable as calculated in Figure 5.14(b) using $\sigma_{\parallel}^{CNT} = \sigma_{\perp}^{CNT} = 0.35 S/m$ [80,169]. The corresponding experimental data is shown in Figure 5.14(c) for (8, 6) SWCNTs in 1 wt-% SDS in water, from which no significant values for ΔA could be measured. Since E_{rms} in water increases with ν as shown in Figure 5.3, the dependence of ΔA on field frequency and SWCNT length for semiconducting SWCNTs in aqueous surfactant solution was simulated. The results are shown in Figure 5.14(b) and demonstrate that even at $\nu = 10^7$ Hz, where E_{rms} in water reaches $5.3 \cdot 10^{-2}$ kV/cm, ΔA is on the order of 10^{-6} and therefore still too small to measure.

Finally, the evaluation of the potential of EFIDAS not only determines the chiral-index resolved mean length of a dispersion but also the (n,m)-specific length distribution $g_{n,m}(l_{CNT})$. This requires measurement of $\Delta A_{n,m}$ as a function of the electric field E. $\Delta A_{n,m}$ is given by $\Delta A_{n,m}(E_{rms}) = \int g_{n,m}(l_{CNT}) \cdot f_{n,m}(l_{CNT}, E_{rms}) dl_{CNT}$, with $f_{n,m}(l_{CNT}, E_{rms}) = \Delta A_{n,m}(l_{CNT}, E_{rms})$ being the field E_{rms} and length l_{CNT} dependent (n,m)-specific differential absorption. The function $f_{n,m}$ is a result of the modelling as shown in Figure 5.15(a) and effectively maps the length distribution onto the field dependence.

For demonstration purposes, a log-normal model length distribution is used for $g_{n,m}(l_{CNT})$ as shown in Figure 5.15(b) and the calculated $\Delta A_{n,m}(E_{rms})$ is shown in Figure 5.15(c). The length distribution is encoded in $\Delta A_{n,m}(E_{rms})$ and can be extracted as follows. Firstly, the above integral in vector notation $\Delta \vec{A} = \bar{F} \cdot \vec{g}$ with the vectors $\Delta \vec{A} = \Delta A_{n,m}(E_{rms})$ and $\vec{g} = g_{n,m}(l_{CNT})$, and the matrix $\bar{F} = f(l_{CNT}, E_{rms})$ is rewritten. Then the inverse matrix $\bar{F}^{-1}$ can be numerically calculated, which finally allows to reconstruct the length distribution *via* $\vec{g} = \bar{F}^{-1} \cdot \Delta \vec{A}$. The result is shown in Figure 5.15(b) and demonstrates that the model length distribution has indeed been nicely reconstructed by the outlined procedure. Notably, the accuracy of the approach is only limited by the size of $\bar{F}$ and the computational power required for calculating $\bar{F}^{-1}$. However, $\bar{F}^{-1}$ itself is not a limiting factor. It has to be calculated only once for each (n,m)

SWCNT and can be further used as a look-up table. Hence it is convincing that EFIDAS can determine also the (n,m)-specific length distributions of SWCNTs in solution by measuring the electric-field dependent differential absorption spectrum.

5.4. Summary

The effects of solvents on the DEP of CNTs were studied using two types of media, toluene and water. Toluene demonstrated to be more efficient in enhancing the s-SWCNT polarizability compared to water. This was due to the former poor dielectric properties arising from its non-polar molecule and low ion-concentration. In order to achieve an experimental observation of this comparison, a CNT alignment experiment was conducted, known as the electric-field induced differential absorption spectroscopy (EFIDAS). It turned to be a fast, *in-situ*, simple and cost-effective method to measure the average length of SWCNTs as dispersed in low-conductance solvents, such as toluene. The EFIDAS results were consistent with ex-situ atomic force microscopy (AFM) data obtained for the same suspension fractions. This verified that the electric-field alignment of the nanotubes could be modeled on the basis of the dielectric properties of SWCNTs and toluene without free parameters. However, the method could not be applied to SWCNTs as dispersed in aqueous surfactant solution due to the high conductivity and permittivity of such solvent in which these properties screen and reduce the EFIDAS signal by orders of magnitude.

– This page intentionally left blank –

Chapter 6: Principles of SWCNT DEPs

6.1. Introduction

Reports of single-walled carbon nanotubes (SWCNTs) dielectrophoresis (DEP) so far mainly focuses on deposition of metallic (m-) SWCNTs rather than semiconducting (s-) ones, as the dielectric properties of m-SWCNTs are larger. Methods to improve DEP deposition of s-SWCNTs include enhancing the s-SWCNT polarizability using light-assisted dielectrophoresis (as discussed in Chapter 4)[78] and low-frequency dielectrophoresis based on low-k solvents (Chapter 5)[14,16]. However, even with these achievements, the packing density of SWCNTs by DEP is still below 50 tubes/μm[64,128], which is much lower than the commercial expectation of 125 tubes/μm to fulfill application requirements, as stated by IBM[243]. Understanding of the physics behind SWCNT-DEPs may be the key to realize the high packing-density and alignment deposition of s-SWCNTs by DEP.

In this Chapter, the physics of SWCNT-DEP is discussed systematically. Both surfactant-aqueous and polymer-toluene based SWCNT-DEPs are numerically analyzed to reveal the influence of medium on the depositions of s-SWCNTs with respect to different DEP biases. The toluene-based direct current DEPs (DC-DEPs) has been demonstrated as the most promising approach for high-quality s-SWCNT deposition. Furthermore, a possible method has been introduced to reverse the priority of depositing m-SWCNTs over s-SWCNTs by DEP.

6.2. DEP Circuit

1. Interface

Electric field distribution in a liquid can be calculated by Laplace equation as described in Chapter 2.4.4. However, it is only valid for regions remote from the interfaces. For liquids that contact with materials of different permittivity, the Laplace equation has to be modified by extending the simulation space beyond the liquid region using $\nabla(\varepsilon\nabla\varphi) = 0$.

In terms of CNT DEPs, highly conducting materials, such as metals, can be modeled as regions with infinitely high permittivity, or as surfaces with a fixed potential (Dirichlet boundary condition)[244]. Ionic conductors under external bias are more difficult to be modeled because of the charge accumulation at liquid-metal interface, which gives rise to the formation of an electrical double layer (EDL, as shown in Figure 2.15) as mentioned in Chapter 2.4.4. Generally,

the screening length in a liquid is given by $\lambda_{De} = \sqrt{\varepsilon D / \sigma} \approx \lambda_{DL}$ where λ_{De}, σ, ε, D and λ_{DL} are the Debye length, solvent conductivity, solvent permittivity, diffusion coefficient and thickness of EDL, respectivily. It is several orders of magnitude larger than that in a metal because of the low conductivity σ and low diffusivity D of ions. Obviously, the capacitance of the EDL C_{DL} is dominated by the properties of the liquid. The impedance of the EDL can also be modeled as an ideal capacitor using

$$Z_{DL} = \frac{1}{i\omega C_{DL}} \tag{6.1}$$

or as a constant phase element, which is more appropriate for imperfect dielectrics[157]

$$Z_{DL} = \frac{A}{C_{DL}(i\omega)^{\xi}} \tag{6.2}$$

Normally, the equivalent circuit for a liquid excluding double-layer would be a capacitance and a resistor in parallel

$$Z_L = \frac{R}{1 + i\omega RC}. \tag{6.3}$$

Firstly, when the screening length λ_{De} is much smaller than the gap scale L between DEP electrodes, the impedance of the system then adds up to $Z = Z_{DL} + Z_L$ as shown in the Figure 6.1(a).

The voltage φ that drops across the double layer is given by

$$\varphi(\omega, Z_{DL}, Z_L) = \frac{Z_{DL}}{Z_{DL} + Z_L}\varphi_0 \tag{6.4}$$

Since $\lambda_{De} \approx \lambda_{DL} << L$, one can model the field distribution in the liquid under external bias φ_0 by solving $\varepsilon \cdot \Delta\varphi = 0$, with the electrode potential set to $(\varphi_0 - \varphi)$: The double-layer is treated as a 2D layer which effectively weakens the internal electric field but does not change the field distribution.

Secondly, in the case where the screening length λ_{De} is much larger than the distance L between electrodes, the potential drop over the distance L within the double-layer is negligible and the total impedance of the system is $Z \approx Z_L$ as shown in the Figure 6.1(b). Consequently, the field distribution in the liquid under external bias φ_0 is described by $\varepsilon \cdot \Delta\varphi = 0$, with the electrode potential set to φ_0 : The double-layer has no influence on the internal electric field or on the field distribution.

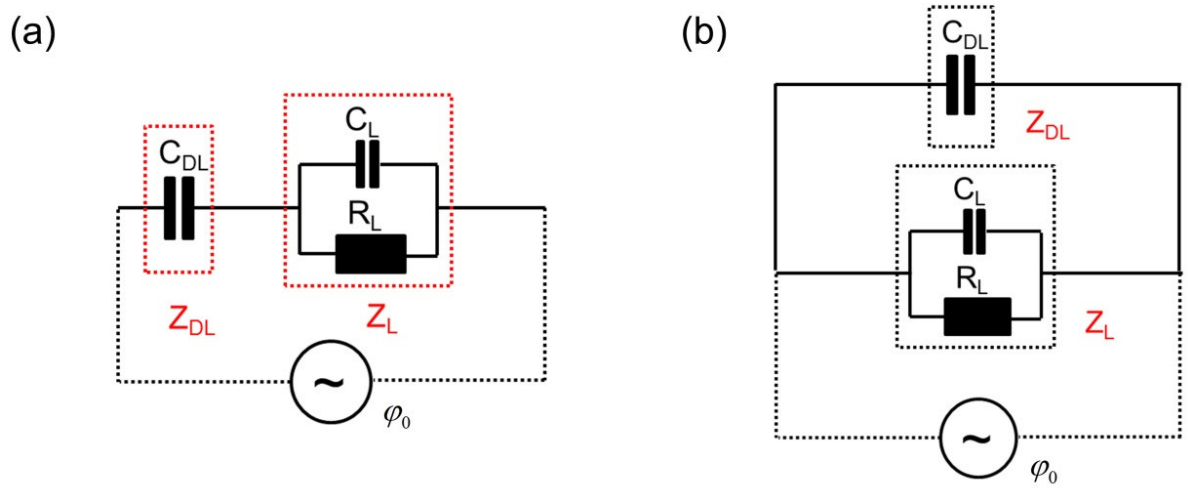

Figure 6.1: Schematics of equivalent impedance circuits of liquids with electrical double layer when (a) $\lambda_{DL} << L$ and (b) $\lambda_{DL} >> L$.

2. Frequency Dependence

When $\lambda_{DL} << L$, the impedance of the circuit $Z = Z_{DL} + Z_L$ is complex and therefore frequency dependent. For the generation of electric fields in liquids, typically low, medium and high field frequency ranges in the impedance have to be considered. Here two critical frequencies ω_{C1} and ω_{C2} (with $\omega_{C1} < \omega_{C2}$) are defined to account for two transitions in the impedance spectrum (introduced in the below) separating these ranges.

For $0 < \omega < \omega_{C1}$, the impedance of the system is dominated by the double layer $Z = Z_{DL}$. The external voltage drops predominantly across the double layer, leaving the liquid quasi field free. Thus in this low-frequency range, the double-layer capacitance dominates the total impedance resulting in $|Z| \propto \omega^{-1}$.

For $\omega_{C1} < \omega < \omega_{C2}$, the impedance is dominated by the resistive part of Z_L. Hence Z becomes independent from the frequency in this medium-frequency range, and the external voltage drops mainly across the liquid.

For $\omega > \omega_{C2}$, the impedance is dominated by the capacitive component of Z_L and again $|Z| \propto \omega^{-1}$. As in the high-frequency range, the external potential drops across the liquid.

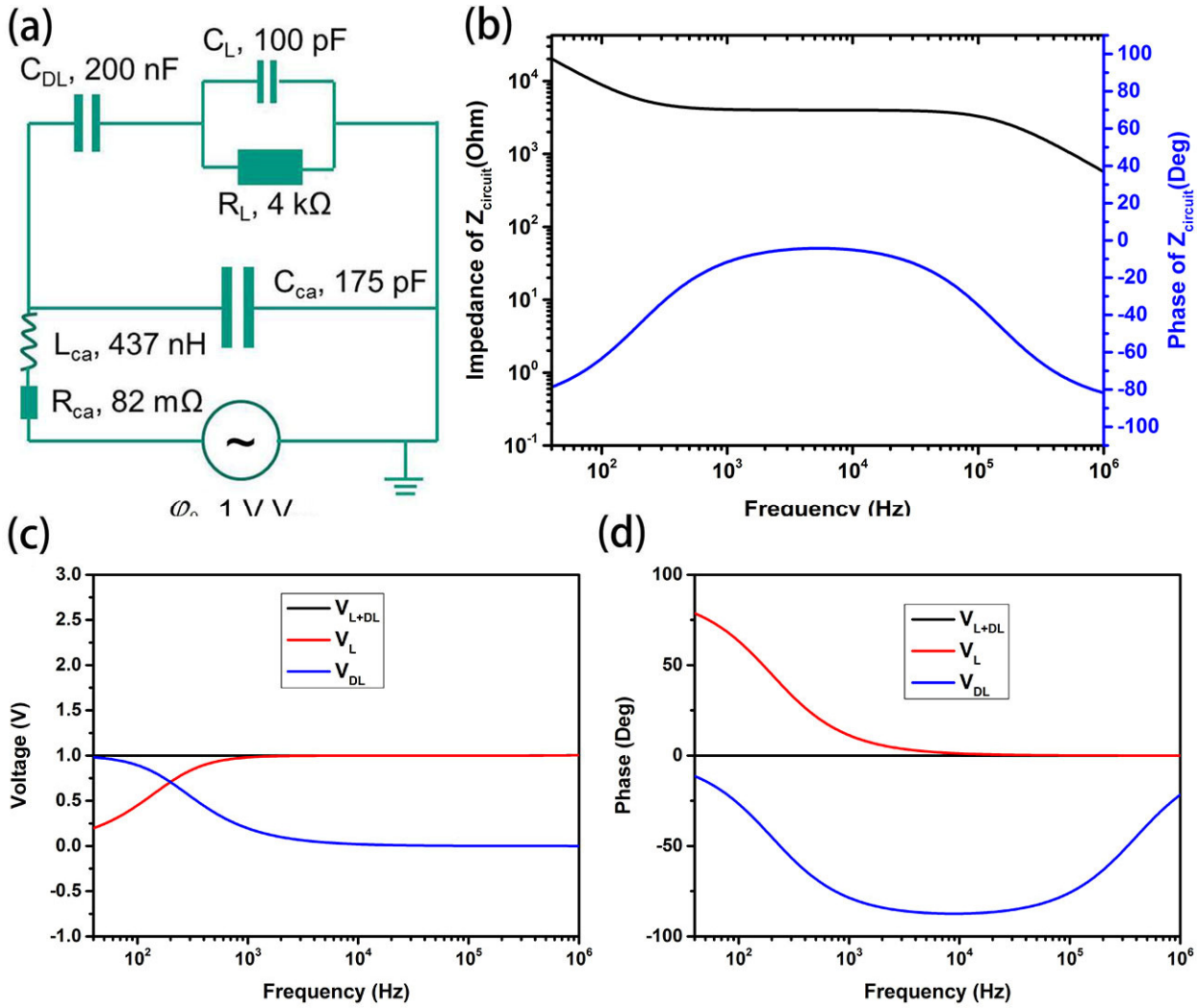

Figure 6.2: (a) Typical equivalent circuit diagram of liquids with the double-layer capacitance C_{DL} and the liquid layer capacitance C_L and resistance R_L when $\lambda_{DL} << L$. "ca" stands for the used cable of DEP circuits. (b) Impedance spectroscopy of the circuit. (c) The potential drop V_L across the liquid, V_{DL} across the double-layer, V_{L+DL} across the liquid and the double layer with their corresponding phase spectra (d). Parameters are taken from the analysis of corresponding impedance spectra described in Chapter 6.2.2. Simulation detials can be referred to the program MADE1 in the attached CD.

An equivalent circuit diagram of a typical water-based DEP performed in author's lab for the $\lambda_{DL} << L$ case is shown in Figure 6.2(a). The magnitude and phase of the corresponding impedance spectrum together with the potential difference across the liquid with and without the double-layer are simulated using the commercial Multisim Analog Devices Edition 10.0, and also shown in Figure 6.2.

Table 6-1: Comparisons of bias φ across liquid to the applied bias φ_0 with respect to different λ_{DL} and L.

λ_{DL} *vs* L	$\omega < \omega_{C1}$	$\omega_{C1} < \omega < \omega_{C2}$	$\omega > \omega_{C2}$
$\lambda_{DL} << L$	$\varphi < \varphi_0$	$\varphi \approx \varphi_0$	$\varphi \approx \varphi_0$
$\lambda_{DL} \approx L$	$\varphi \approx \varphi_0$	$\varphi \approx \varphi_0$	$\varphi \approx \varphi_0$
$\lambda_{DL} >> L$	$\varphi \approx \varphi_0$	$\varphi \approx \varphi_0$	$\varphi \approx \varphi_0$

Hence whether the applied potential φ_0 drops primarily across the liquid and/or across the double layer depends on the frequency ω and the screening length λ_{De} in relation to the system length L. This is schematically shown in table 6-1. For $\lambda_{De} \approx \lambda_{DL} >> L$, all frequency will be suitable for maximum internal field generation (equivalent circuit model of toluene-based DEPs shown in Figure 6.3), whereas for $\lambda_{DL} << L$, $\omega > \omega_{C1}$ is required.

6.2.1 Electrical Double Layer

The screening length $\lambda_{De} \approx \lambda_{DL}$ together with the electrode distance L determine the suitable frequency range for maximum internal field generations. Therefore, estimating the thickness of the double layer is crucial.

The formation of a Helmholtz electrical double layer stems from competition between electrostatic interactions and Brownian motion as described by Gouy and Chapman et.al.[157]. A common representation of the EDL goes back to Stern with an inner layer (called the compact layer), which is in contact with electrodes. And the ions are absorbed on to the electrode surfaces due to high electrostatic interactions. Outside the compact layer, there is a diffuse double layer in which the potential drops exponentially with distance. The potential at the interface, known as slip plane as shown in Figure 2.15, between the compact and the diffuse layer is called zeta potential ζ.

The potential distribution in the diffusive layer can be described with the non-linear Poisson-Boltzmann (PB) equation

$$\nabla(-\varepsilon\nabla\varphi) = \sum_i z_i e c_i^{\infty} \exp(-z_i e\varphi / k_B T) \tag{6.5}$$

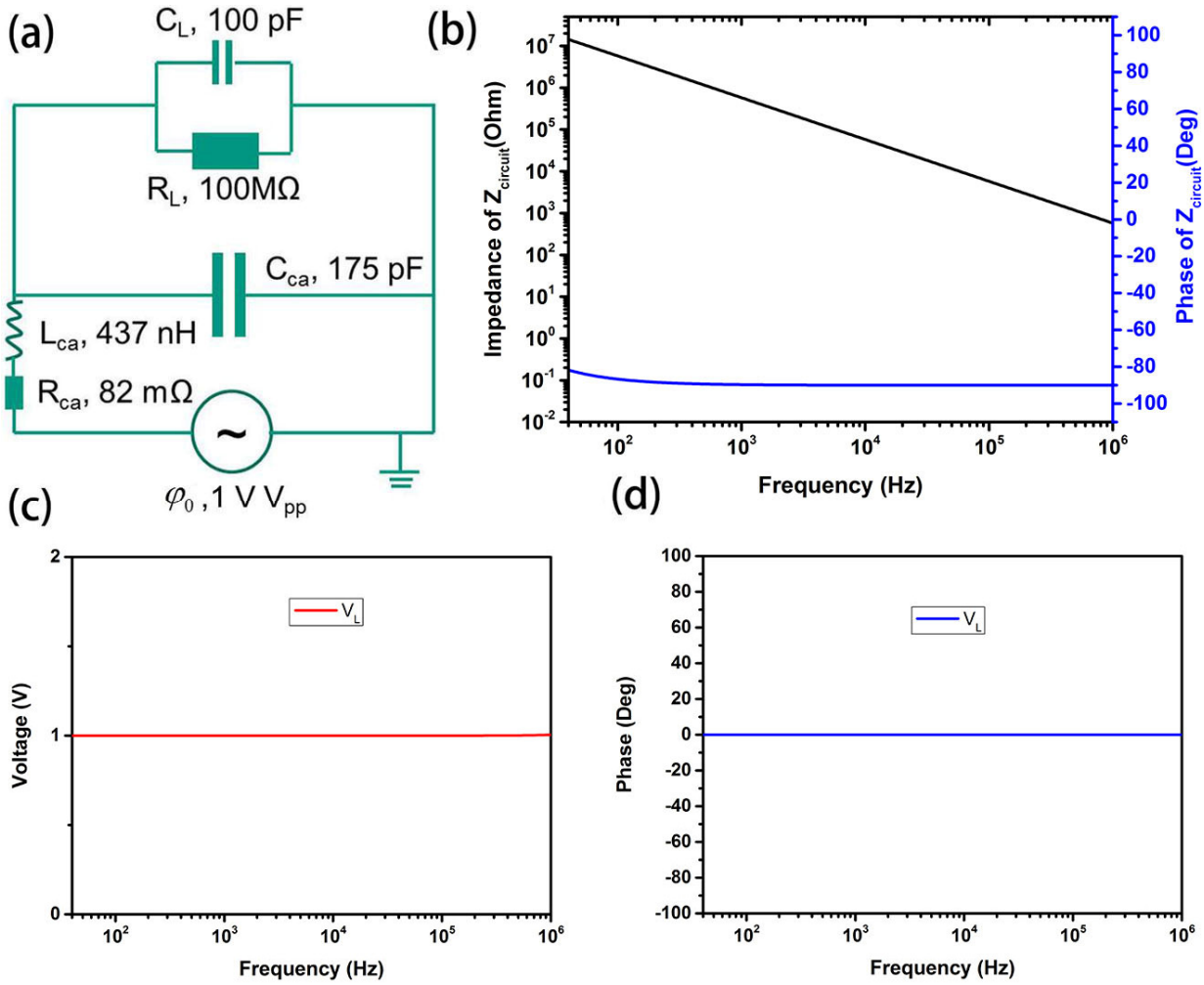

Figure 6.3: (a) Equivalent circuit diagram with the liquid layer capacitance C_L and resistance R_L when $\lambda_{DL} >> L$. "ca" stands for the used cable of DEP circuits. (b) Impedance spectroscopy of the circuit in liquid. (c) The potential drop V_L across the liquid and its corresponding phase spectra (d). Parameters are taken from the analysis of corresponding impedance spectra described in Chapter 6.2.2. Simulation detials can be referred to the program MADE2 in the attached CD.

with the bulk concentration c_i^{∞} and charge number z_i of all ions. For binary solutions the PB equation becomes the Gouy-Chapman (GC) equation. The Debye-Hückel (DH) theory is

obtained by linearization of the GC equation under the assumption that the electrostatic energy is smaller compared with the thermal energy $\varphi << k_B T / ze$. The solutions is then given by

$$\varphi(z) = \zeta \exp(-z / \kappa^{-1}). \tag{6.6}$$

Thus the potential decreases exponentially with distance from the polarized electrode. Here the characteristic length κ^{-1} is equivalent to the Debye length:

$$\kappa^{-1} = \lambda_{De} = \sqrt{\frac{\varepsilon k_B T}{2 z^2 e^2 c^{\infty}}} \tag{6.7}$$

However, the DH theory is not appropriate if the applied electrode potential is larger than the thermal energy where strong steric effect within EDLs should be taken into account. This is often observed during SWCNT-DEPs, thus the non-linear PB equation has then to be solved numerically. For binary symmetric semi-infinite electrolytes in contact with a flat polarized surface, an analytical solution of the non-linear PB equation exists, and can be expressed as

$$\varphi(x) = \frac{2k_B T}{ze} \ln \left[\frac{1 + \tanh\left(\frac{ze\varphi_0}{4k_B T} \right) \exp(-\kappa x)}{1 - \tanh\left(\frac{ze\varphi_0}{4k_B T} \right) \exp(-\kappa x)} \right] \tag{6.8}$$

Figure 6.4(a) demonstrates excellent agreement between the PB and the analytical solution for cases with $\varphi > k_B T / ze$. In contrast, the Debye length from Debye-Hückel theory slightly overestimates the double-layer thickness.

Still the PB and analytic equations have limited applicability at large surface potentials ($\varphi >> k_B T / ze$), because it is not considered that ions have a finite size. Therefore, the ion concentration at the electrodes can reach unrealistic values at large voltages.

To account for the steric effects of the ions, a modified Poisson-Boltzmann (MPB) equation which includes the finite ion sizes of the Stern layer in filed potential distribution has been proposed recently by Kilic *et al.*[245], and given by

$$\nabla(-\varepsilon\nabla\varphi) = \sum_i z_i e \frac{c_i^{\infty}\exp(-z_i e\varphi / k_B T)}{1+2\upsilon_{ion}\sinh^2(z_i e\varphi / 2k_B T)}\exp(z_i e\varphi / k_B T),$$
$$\varphi(x=0)=\zeta,\ \varphi(x\to\infty)=0,\ \frac{d\varphi}{dx}(x\to\infty)=0. \tag{6.9}$$

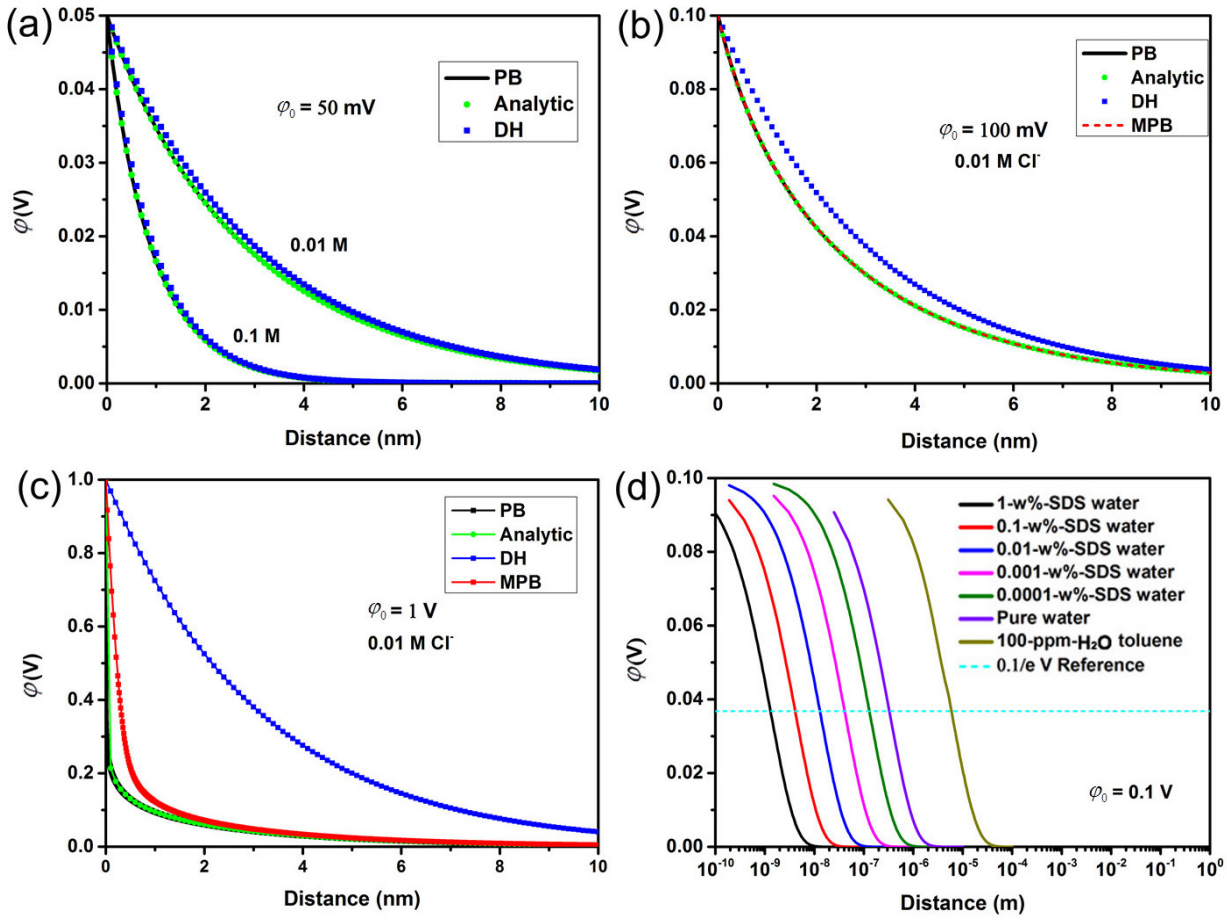

Figure 6.4: Comparisons of electric potential distributions calculated using PB, analytical, DH and MPB models under different (a) ion (Chlorine ion Cl^-, with "M" stands for mole) concentrations and different bias: (a) 50 mV, (b) 100 mV and (c) 1 V. (d) Electric potential distribution derived with MPB model for different ion-concentration media: 1-w%-SDS water, 0.1-w%-SDS water, 0.01-w%-SDS water, 0.001-w%-SDS water, 0.0001-w%-SDS water, pure water and 100-ppm-H_2O toluene. The light-blue dash line denotes the electric potential at λ_{De}. Simulation detials can be referred to the FlexPDE program FP1 in the attached CD.

here υ_{ion} denotes a packing parameter $\upsilon_{ion} = 2\chi^3 c^{\infty}$, and can be derived by taking the effective ions size $\chi = 6.6\,\text{Å}$ into account in this work. The way to characterize χ is to take it as a cutoff for the unphysical divergences of the PB theory. This parameter includes not only the solvation

shell ($\approx 6.6\,\mathring{A}$ for Cl^- and OH^- in aqueous[157,246]), but also the decrease of permittivity (by as much as a factor of 10 for water, as discussed below)[247], making χ larger than the measurable diameter of the ion.

For binary symmetric z:z electrolytes the MPB equation (6.9) can be simplified to

$$\nabla(-\varepsilon\nabla\varphi) = -zec^{\infty}\frac{2\sinh(z_i e\varphi / k_B T)}{1+2\upsilon_{ion}\sinh^2(z_i e\varphi / 2k_B T)} \tag{6.10}$$

Figures 6.4(b) and (c) demonstrate the limitation of the PB, analytic and DH in comparison to the MPB. It is obvious that the PB model can be used for voltages up to 0.1 V. Beyond that the MPB has to be solved.

Based on the above discussions, the double-layer thickness λ_{DL} at the water-electrode interface for different ion concentrations can be determined. Figure 6.4(d) shows the potential profile across the double layers formed in neutral water, aqueous solution with 1 wt-% SDS ($c^{\infty} = 0.034$ mol/L) and diluted solutions (dilution factors 10,10^2,10^3 and 10^4) as $\varphi_0 = 0.1V$. The simulation shows that the double-layer thickness is in the order of 10^0 nm for solutions of 1-w%-SDS water, and 1 µm for pure water. Practically, stable dispersions of individual CNTs require a surfactant concentration in the order of 1 w-% SDS. And for the dielectrophoretic deposition of CNTs, dispersions are often used either undiluted or diluted by factor up to 100. Hence the double-layer thickness in nanotube dispersions is never exceeding 100 nm. With an electrode distance of typically 1 µm, which means that the double layer thickness $\lambda_{DL} << L$. Hence φ_0 drops mainly across the double-layer but not across the liquid for $\omega < \omega_{C1}$.

ω_{C1} can be estimated using the expression for the cutoff frequency of an RC circuit

$$\omega_{C1} = (R_L C_{DL}/2)^{-1} = \left(\frac{\varepsilon}{\sigma}\frac{L}{2\lambda_{DL}}\right)^{-1} \tag{6.11}$$

with $C_{DL} = \varepsilon A / \lambda_{DL}$ and $R_L = L/(\sigma A)$, A are the effective cross-section area of parallel electrode pairs and σ the conductivity of the solution. $\varepsilon = 81\varepsilon_0$ for water with ε_0 the vacuum permittivity[79].

An overview of λ_{DL}, σ and ω_{C1} for pure water and water with various concentrated SDS is given in the table 6-2. The calculations show that for the dielectrophoretic deposition of CNTs in aqueous SDS dispersions onto micro-scale electrodes $L \approx 1$ µm, one should apply AC signals at $\omega > 0.1$ MHz instead of DC signals to ensure that the external voltage drops across the entire liquid. Moreover, since electrochemical reactions including the dissociation of water are suppressed at AC frequencies, higher peak-to-peak voltages can be considered.

Table 6-2: The experimentally derived λ_{DL}, σ, ω_{C1} with respect to different ion-concentration media.

Parameters	1-w-% SDS water	0.1-w-% SDS water	0.01-w-% SDS water	Water	Toluene
$\lambda_{DL}[m]$	3.2×10^{-9}	6.0×10^{-9}	19.8×10^{-9}	0.36×10^{-6}	13.5×10^{-6}
$\sigma[S/m]$	2.3×10^{-1}	2.9×10^{-2}	4.0×10^{-3}	5.5×10^{-6}	1×10^{-10}
$\omega_{C1}[Hz]/L[\mu m]$	2.1×10^{6}	5.0×10^{5}	2.3×10^{5}	5.5×10^{3}	0.038

Reported values for the conductivity of toluene range within $\sigma = 10^{-11} \sim 10^{-10}$ S/m[219]. The origin of the conductivity is not described in the literature, but most likely from the charged impurities such as dissociated water. The solubility limit of water in toluene is 330 ppm, and even anhydrous toluene is specified with a significant water content <100 ppm, corresponding to a water concentration of 10^{-3} mol/L. However, data on the ion concentration in Toluene has not been revealed in the literature. Therefore, the critical frequency has to be derived from impedance spectroscopy measurements (displayed in the following). Novikov *et al.*[219] measured a conductivity of $\sigma = 10^{-10}$ S/m and critical frequency $\omega_C \approx 1$ Hz for parallel electrodes at distance $L \approx 100$ µm. Therefore, the thickness of the double-layer can be estimated using the formula 6.11. With $\varepsilon = 2.38\varepsilon_0$ for Toluene, $\lambda_{DL} = 1.35 \cdot 10^{-5}$ m (as shown in the Table 6-2) was obtained. The calculations show that in Toluene $\lambda_{DL} >> L$ for electrodes with a gap size <10 µm. Therefore, φ_0 drops mainly across the liquid and is independent of the frequency.

However, when the thickness of the EDLs is too large compared to the gap distance L between electrodes, for instance the case of EDL overlapping, both the non-linear PB and MPB models are not valid for electrical potential analysis under such situation. This is because that the deformation of EDLs induced by the convection and polarization of electrolytes are absent in

the these models[248]. Additionally, in the vicinity of the electrode surface, normally within the range of few nanometers, the approximation of electro-neutral liquids based on equation (2.43) is not appropriate any longer due to charge separations induced by the local high electric field. In order to describe the behavior of such a thick diffuse double layer, the Nernst-Planck equations for all the ions, combined with Poisson's equation, known as the Poisson-Nernst-Planck (PNP) equations, should be applied[249].

$$\frac{\partial c_i}{\partial t} = \nabla(D_i \nabla c_i + \mu_i z_i e c_i \nabla \varphi) \tag{6.12}$$

$$\nabla(-\varepsilon \nabla \varphi) = \sum_i z_i e c_i \tag{6.13}$$

where μ_i is the mobility of the species i, and $D_i = \mu_i / kT$ stands for the Einstein's relation. Figure 6.5 demonstrates the corresponding electric potential distribution of EDLs using the PNP model under the concerning of an up-limitation of ion-concentration given by $\upsilon_{ion} = 2\chi^3 c^\infty$.

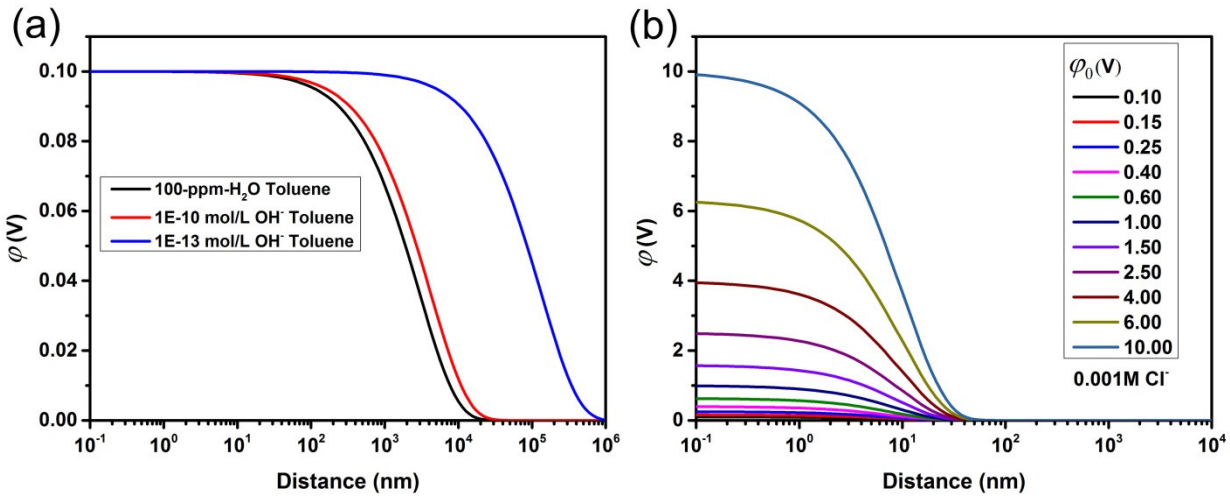

Figure 6.5: The PNP equations based EDL profiles with respect to different (a) ion-concentrations (100-ppm-H_2O toluene, 10^{-10} mol(M)/L OH^- toluene and 10^{-13} M/L OH^- toluene) and (b) surface potential (0.001 M/L Cl^-). Simulation detials can be referred to the COMSOL program CMSL1 in the attached CD.

For the stern layer, where immobile ions strongly adsorb to the electrode surface, implying no free charges exist, mathematically, the electric potential within this layer is also accessible and governed by

$$\nabla(-\varepsilon\nabla\varphi)=0 \tag{6.14}$$

However, in practice, the permittivity of polar electrolytes is not constant when the electric field becomes very large. This is because the orientation of electrolyte molecules becomes highly order due to the saturation of polarization under a very high electric field, resulting in the suppression of further orientation of these molecules even when the field intensity is further increased. This phenomenon leads to the decrease of the medium permittivity. As Booth stated[247], the divergence of the liquid permittivity can be divided into two region with respect to an artificial critical electric field intensity of 10^7 V/m. Above this intensity, the permittivity of the medium can be given by

$$\varepsilon_x(\left|\vec{E}\right|)=n^2+(\varepsilon_x(0)-n^2)\frac{3}{\beta\left|\vec{E}\right|}\left[\coth(\beta\left|\vec{E}\right|)-\frac{1}{\beta\left|\vec{E}\right|}\right] \tag{6.15}$$

with $\beta=5b/2kT\,(n^2+2)$, while for $\left|\vec{E}\right|<10^7$ V/m, $\varepsilon_x(\left|\vec{E}\right|)$ can be treated as the same as the permittivity at zero electric field $\varepsilon_x(0)$ which is equivalent to the bulk fluid permittivity ε_m. The parameter n denotes the refractive index of the liquid[250] and $b=1.85\times10^{-18}$ (CGSE units, for toluene $b\approx0.36\times10^{-18}$ [220]) presents the dipole moment of the water molecule.

Figure 6.6 shows the calculated electric-field dependent permittivity distributions (one can refer to the COMSOL program CMSL2 as included in the attached CD) of two kinds of electrolytes, 0.01-w-%-SDS water and 100-ppm-H_2O toluene (with water content of ≈100 ppm, $\lambda_{De}=9.519\cdot10^{-6}$ m, see Appendix A). When the applied potential is over 0.1 V, the permittivity of 0.01-w-%-SDS water decreases dramatically within the Stern layer (from $81\varepsilon_0$ to below $30\varepsilon_0$), while the permittivity for 100-ppm-H_2O toluene is almost unchanged (around $2.38\varepsilon_0$) before the potential rises up to 0.5 V. Therefore, in order to precisely derive the impedance of the EDLs, $Z_{DL}=1/i\omega C_{DL}$, the calibration of the permittivity change within the Stern layer should be taken into consideration.

Since the double layer capacitance C_{DL} can be treated as the series connection of the Stern capacitance C_S and the Diffuse capacitance C_D layers, given by

$$\frac{1}{C_{DL}} = \frac{1}{C_S} + \frac{1}{C_D},$$
$$C_S = \varepsilon_S \frac{A}{d_s},\ C_D = \varepsilon_D \frac{A}{d_D},\ d_S = \chi/2,\ d_D = \lambda_{De}. \tag{6.16}$$

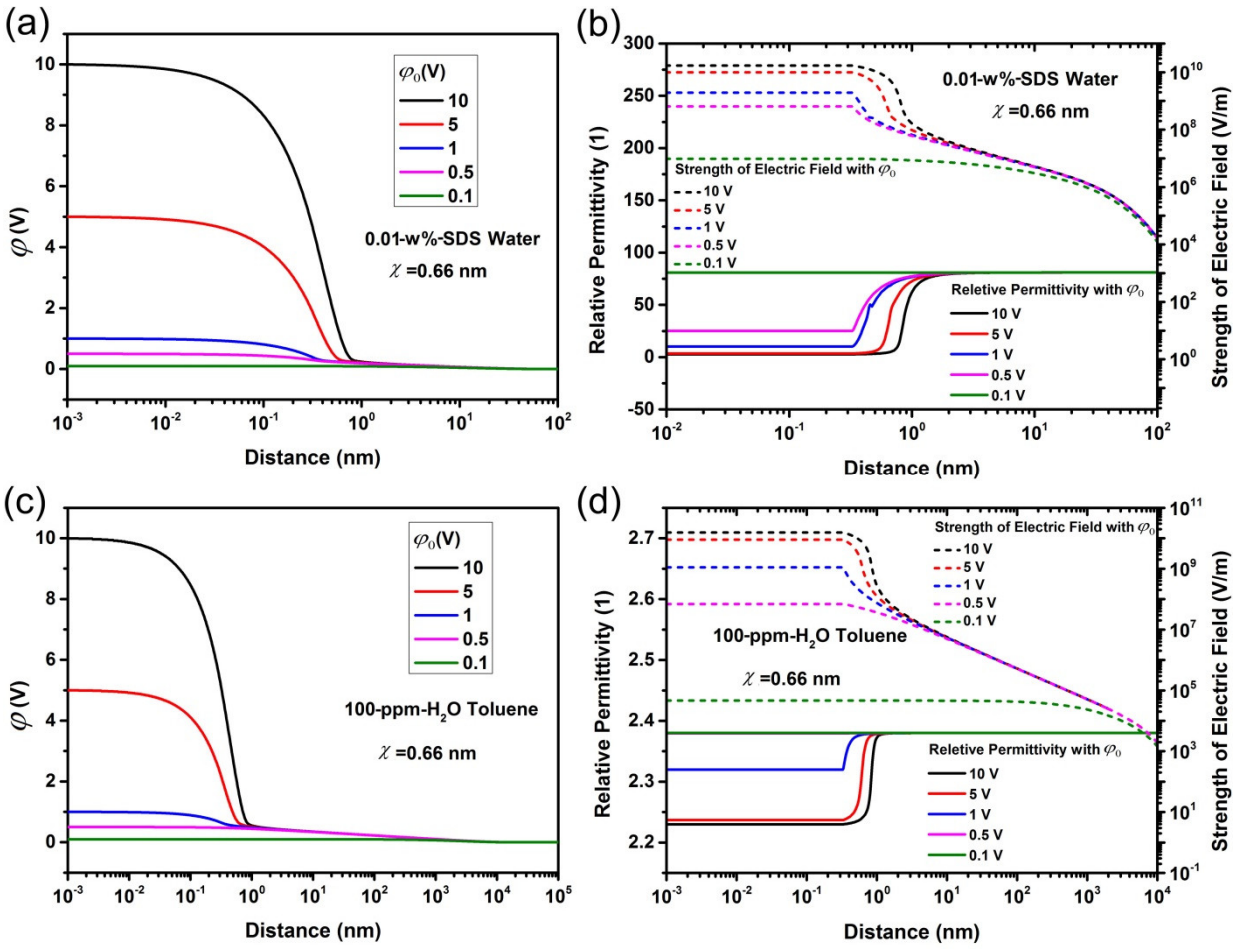

Figure 6.6: The calculated (a and c) electric potential, (b and d) permittivity and electric field strength distributions of 0.01-w%-SDS water and 100-ppm-H_2O toluene with taking stern layer into account. Simulation detials can be referred to the COMSOL program CMSL2 in the attached CD.

where the effective cross-section area of parallel electrode $A = 2.0\times10^{-5} m^2$ is derived based on the impedance spectroscopy discussed below. Considering the existence of two EDLs and the field-dependent ε, the weight ratio of the potential drop across the diffuse layer over the total potential applied on the EDLs can be derived using $\Lambda = C_S/(C_D + C_C)$, as described in Chapter 2.4.4. Furthermore, for Stern layers, the corresponding weight ratio is given by 1-Λ which possesses a value of ~0.07 for 0.01-w-%-SDS water and ~3.5×10^{-5} for 100-ppm-H_2O

toluene under an applied 0.5 V EDL potential. It increases up to 0.14 for the former solution, while almost keeping unchanged for the latter under 1.0 V bias due to the much smaller dipole moment of toluene molecular than that of water. Furthermore, under low frequencies, the impedance of the liquid bulk capacitance can be considered to be negligible compared to its ohmic resistance. Thus, the impedance within the bulk liquid is dominated by the conductivity σ_m . Under this situation, the potential drop across the EDLs can be formulated as $\Delta\varphi_{DL} = (\mathrm{V_{DEP}}/2)/(1+i\omega LC_{DL}/2\sigma_m)$ with L denoting the characteristic length of the DEP circuit.

Briefly, based on the concept of EDLs, one can address that the applied electrical bias cannot be completely used for the SDS-water or toluene based CNT-DEPs. The weight ratio of the lost potential over total bias is accessible with characterizations of EDL dielectrics and geometries using the MPB or PNP models. Now it comes with two questions, how much the applied bias can be used for DEPs while considering all the parasitic impedances of circuits practically, and what is the value of the EDL capacitance? In order to answer these questions, the impedance spectroscopy of typical DEP circuits should be investigated.

6.2.2 Impedance Spectroscopy

To investigate the impedance spectroscopy of capacitively coupled dielectrophoretic deposition-circuits, it is first important to understand the electrical contributions of all the system elements within the DEP circuits[251]. We have discussed above the way to characterize the double-layer thickness and critical frequencies for liquids relevant to nanotube dielectrophoresis, namely water with the ionic surfactant SDS and toluene with polymer. For micro-scale electrodes in toluene, the applied potential always drops across the liquid, whereas for water a critical frequency ω_{C1} exists. When a low frequency $\omega < \omega_{C1}$ field is applied, the potential mainly drops across the double layer, while at high frequencies it drops across the liquid. Experimentally, the critical frequency can be measured with impedance spectroscopy.

As shown in Figure 6.7, impedance spectra are distinctive with respect to different liquid media under similar measuring conditions. In terms of aqueous liquids, an obvious transition frequency exists in the impedance spectra. Moreover, it decreases with respect to the further dilution of SDS in water, verifying the discussions of the cutoff frequency ω_{C1} of the double layer as illustrated in the table 6-2.

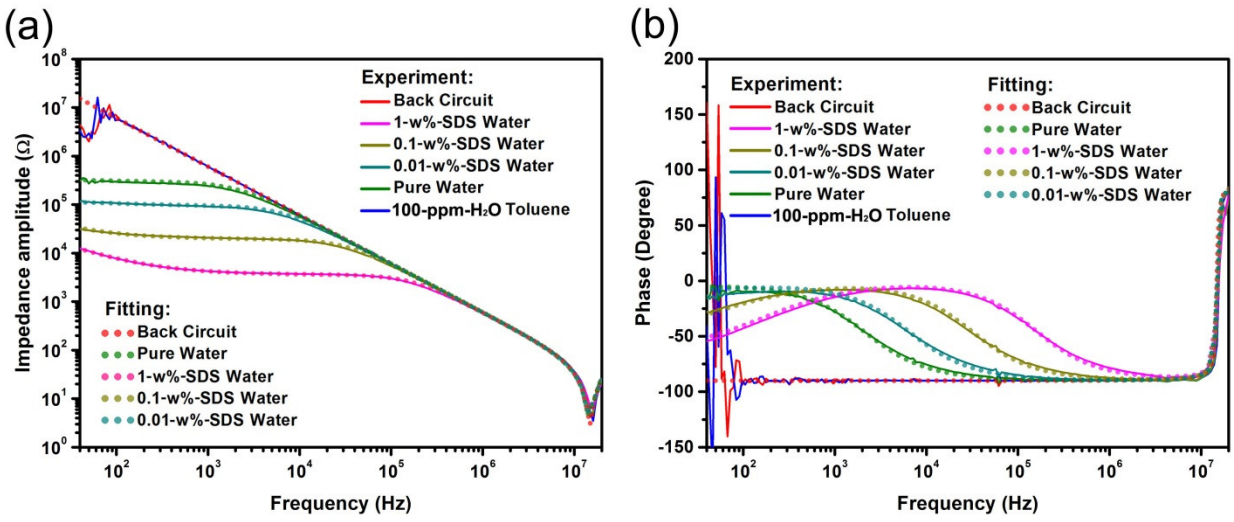

Figure 6.7: Experimental observations and calculated fittings of impedance (a) amplitudes and (b) phases for DEP circuits based on different media (1-w%-SDS water, 0.1-w%-SDS water, 0.01-w%-SDS water, pure water and 100-ppm-H_2O toluene) under a driving bias of 0.5 V. Back circuit stands for no liquid case.

By employing the circuit model as shown in Figure 6.2(a) and fitting the obtained EDL impedance with eq. 6.2, the corresponding EDL capacitance C_{DL} and exponent index ξ of the high ion-concentration media can be derived based on an assumption of pure water capacitance of 2.019 pF (as illustrated in the Table 6-3). Based on these variables, Figure 6.7 illustrates good agreements between the fitted data and the experimental observations. Three regimes are distinguishable in the impedance spectra for all electrolytes except toluene. For the latter, the impedance spectrum is indistinguishable from that arising from the back circuit where no liquid is placed between the electrode pairs. As a result, the corresponding fitting parameters cannot be derived properly. This indicates that the capacitance of the EDL for toluene is much smaller than the parasitic capacitance, verifying that the applied DEP bias mainly drops across the liquid because the $\lambda_{DL} >> L$ here. In order to quantitatively demonstrate this comparison, λ_{DL} for different SDS-concentration aqueous is also experimentally derived and given in Table 6-3. It is clear that the EDL thickness of SDS-water increases with respect to a decrease in the surfactant concentration, i.e. the ion concentration, which varies from 2.992 nm for 1-w%-SDS water to 17.921 nm for 0.01-w%-SDS water. Besides, considering relative permittivity changes induced by high local electric field within Stern layers, it is evident that the value of $\lambda_{De} + \lambda_S \varepsilon_m / \varepsilon_S$ gives out a better evaluation of the λ_{DL} than $\lambda_{De} + \lambda_S$ for these solutions. Furthermore, when taking a closer look at the derived exponent index ξ, this parameter arises

slightly from 0.6738 for 1-w%-SDS water up to 0.6851 for 0.01-w%-SDS water, indicating the dielectric EDLs becomes more lossless when the ion-concentration decreases. On the other hand, the EDL thickness reaches 0.036 μm for a double EDL circuit, which means that the capacitance of aqueous bulk cannot be treated to be constant any more when the electrolyte is heavily diluted. These lead to uncertainties in measuring the liquid capacitance, thereby the thickness of EDLs.

Table 6-3: The derived R_L, C_L, C_{DL} and ξ for different-media based DEP circuits with L_{ca}=437 nH, R_{ca}=3 Ω and C_{ca}=263 pF. ($\varphi_0 = 0.5V$)

Medium	R_L [Ω]	C_L [pF]	C_{DL} [μF]	ξ	λ_{DL} [(a)] [nm]	$\lambda_{De}+\lambda_S$ [nm]	$\lambda_{De}+\varepsilon_m\lambda_S/\varepsilon_S$ [nm]
1w-% SDS-Water	3556	2.019	2.396	0.6738	2.992	2.01	3.00
0.1w-% SDS-Water	19290	2.019	1.201	0.6845	5.968	5.63	6.62
0.01w-% SDS-Water	88580	2.019	0.400	0.6857	17.921	17.13	18.12

(a) λ_{DL} is half of the measured EDL thickness due to two symmetric EDLs formed on each interface of electrode pairs in experiments.

6.3. FEM Simulations and Experiments

6.3.1. CNT Suspensions

Using 0.01-w%-SDS water and 100-ppm-H_2O toluene as media, two kinds of CNT solutions, as shown in Figure 6.8, were prepared in this work through size-exclusion-chromatography (SEC) methods [79,128] and contents as introduced in Chapter 3.2. It is evident that both solutions contain multi-chiral s-SWCNTs, and possess a comparable concentration which can be verified with roughly the same optical absorption intensities. Although the s-SWCNT diameter varies with respect to the chirality, a proper conductivity and permittivity of the CNT bulk were used to qualitatively describe polarizabilities of nanotubes during DEPs[79], as displayed in Appendix A. It was observed that $\sigma = 4\times10^{-3} S/m$, $\varepsilon = 81\varepsilon_0$ for 0.01-w%-SDS water (diluted with distilled water (VWR CA1.16754.5000)), and $\sigma = 2\times10^{-10} S/m$, $\varepsilon = 2.38\varepsilon_0$ for 100-ppm-H_2O toluene (diluted with 100 ppm-water commercial toluene (Alfa Aesar, CAS-number 108-88-3)) are good enough to match with the experimental observations of DEPs using such CNT solutions with a dilution factor of 100. In terms of CNT length, a typical

characterized length of 1 μm was chosen for nanotube-DEP simulations, which is equal to the practical electrode gap applied in this chapter.

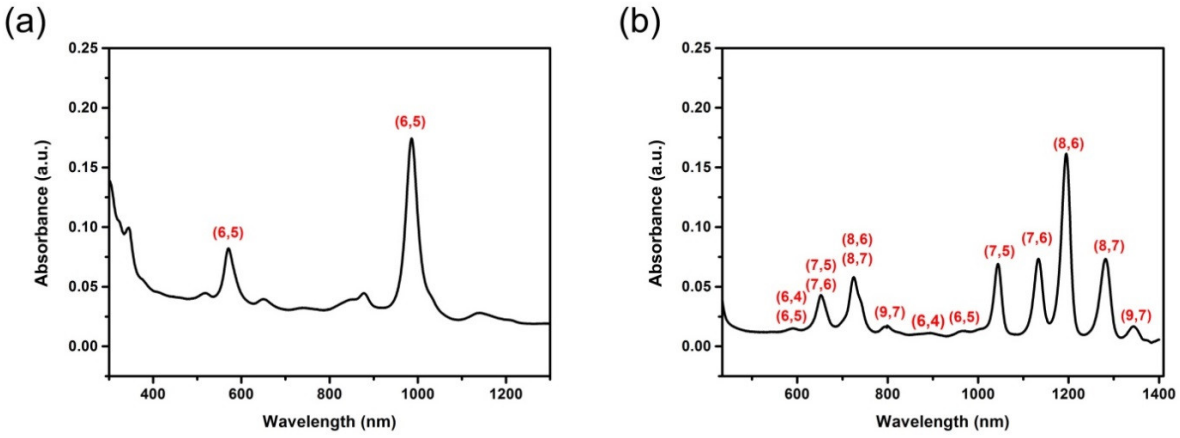

Figure 6.8: Typical optical absorption spectra of (a) 1-w%-SDS water and (b) 100-ppm-H_2O toluene dispersed CNTs used in this Chapter.

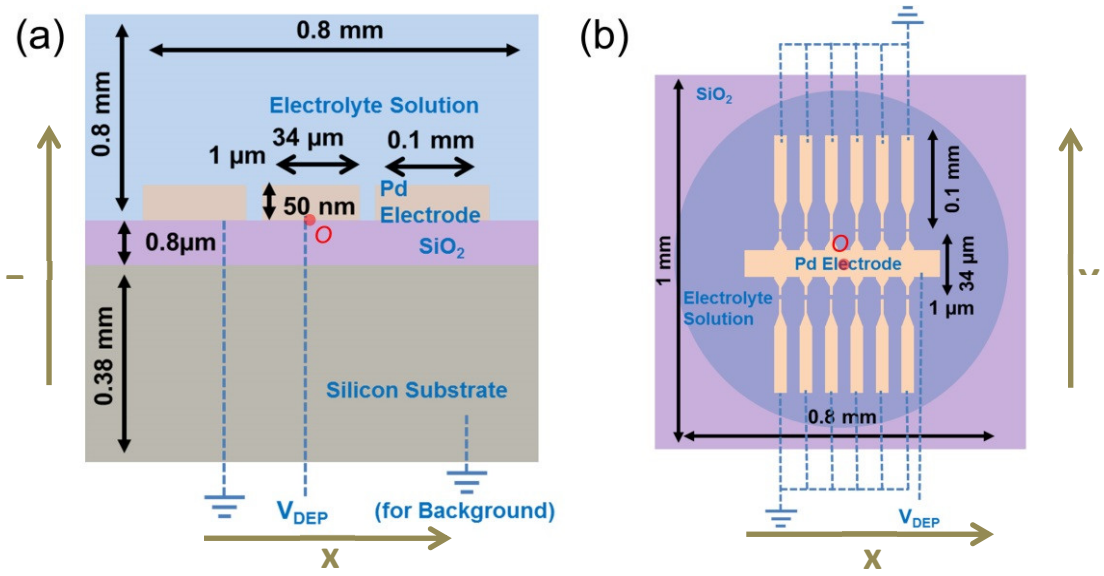

Figure 6.9: The (a) side and (b) top view of the DEP structure used in this work. Notably for the BG-DEPs, the silicon substrate is set to the ground ("O" stands for the original point).

6.3.2. DEP Geometry

The equations developed in Chapter 2.4.4 for solving electric field, temperature distribution, and fluid-velocity distribution of DEP systems are coupled with each other and can be solved sequentially under specific cases of DEPs. In order to numerically study geometry-based DEP,

we have employed an effective method, known as finite element method (FEM) simulations, which was performed with a commercial software package (COMSOL MULTIPHYSICS 5.0, as described in Chapter 3.5) in this chapter. A simplified schematic geometry without loss of generalities of CNT-DEPs in this study is given in Fig. 6.9 (a) (side view) and (b) (top view). With proper boundary conditions and structured meshes, all the electric potential, temperature and fluidic velocity distributions arising from applied dielectrophoretic bias V_{DEP} can be analyzed through FEMs. In the following discussion, both the field-frequency dependent translational and rotational motions of CNTs with length of 1 μm and diameter of 1.3 nm during DEPs were simulated. Furthermore, the efficiency and performance of practical CNT-DEPs were also discussed with respect to both different media and electric fields.

6.3.3. Potential Field

1. Boundary Condition

In order to simplify comparisons between the effects of different electric fields, such as AC and DC, on CNT-DEPs, the root-mean-square voltage V_{rms} of AC bias was picked for the following simulations.

Considering the existence of EDLs lying between metallic surfaces and bulk electrolytes, the proper boundary condition for electrodes is the charge conservation equation for the given double layers i.e. the current flowing into the element of the double layer is equal to the increase of the stored charges. For a high ion-concentration medium based CNT-DEP system, the electrode gaps are much larger than double layer thickness. For instance, the 0.01-w%-SDS water based DEP (with λ_{DL} around 17 nm, as shown in the Appendix A), the double-layer can be approximated theoretically as a distributed capacitor between electrodes and the bulk since the lateral currents along the double layer (either convection or conduction) are negligible in comparison with the normal current[67]. Thus the normal current flowing into the double layers is equal to the increase in the stored charges. Besides, the size of the double layer is so small that it does not enter into the problem space. Therefore, the conservation of charge condition can be given by

$$\sigma_m \frac{\partial \varphi}{\partial n_\perp} = \frac{\partial}{\partial t}(C_{DL}(\varphi - V_{Applied})) \tag{6.17}$$

where $n_{\perp}$ represents the outer normal, C_{DL} the EDL capacitance per unit area with a rather precise evaluation given by $C_{DL} = \varepsilon_m / (\lambda_D + \varepsilon_m \chi / 2\varepsilon_S)$. $V_{Applied}$ is the electrical potential applied for DEPs. φ denotes the electric potential just outside the double layer. Using complex amplitudes, the boundary condition for φ at the electrode surface can be converted to a mixed boundary condition:

$$\varphi - \frac{\sigma}{i\omega C_{DL}} \frac{\partial \varphi}{\partial n_{\perp}} = V_{Applied} \tag{6.18}$$

Under this situation, when a frequency $\omega > \sigma / \varepsilon$ is applied where the displacement current dominates, the potential φ just outside the double layer becomes equal to the applied potential $V_{Applied}$. This is crucial for successfully achieving the 0.01-w%-SDS water based CNT-DEPs.

However, for 100-ppm-H_2O toluene based DEPs, the above assumptions for boundary conditions of EDLs is invalid, since the thickness of EDLs is much larger than the characteristic length of their DEP systems ($L = 1\ um$ in this work). A reliable description of the electrical performance of EDLs under this case should enlarge the role of the Stern layers to replace that of the whole EDLs, thereby the electric fields can be electrostatically determined based on the equation (6.18) but with C_S instead of C_{DL}, which yields the electrode surface potential given by

$$\varphi - \frac{\sigma}{i\omega C_S} \frac{\partial \varphi}{\partial n_{\perp}} = V_{Applied} \tag{6.19}$$

For boundaries of gaps between the electrodes, i.e. the substrate/electrolyte interface, the boundary condition is given by the continuity of the total normal current density:

$$(\sigma_{SiO_2} + i\omega\varepsilon_{SiO_2}) \frac{\partial \varphi_{SiO_2}}{\partial n_{\perp}} = (\sigma_m + i\omega\varepsilon_m) \frac{\partial \varphi_m}{\partial n_{\perp}} \tag{6.20}$$

Notably, two grounded situations can be used for CNT-DEPs, which are known as back-grounded (BG) and top-grounded (TG) approaches. The former indicates that silicon wafers are set to the ground potential, and has been well developed for large scale CNT-DEP depositions[75]. Under that condition, all floating electrodes excluding the common one are modeled as floating potential and can be solved by applying an electric shielding boundary

condition. The TG connection means that all floating electrodes are set to the ground bias, and the common electrode is fixed with a potential derived from equations (6.18) or (6.19).

2. Simulations and Discussion

Figure 6.10 demonstrates the side view potential distributions of both 0.01-w%-SDS water and 100-ppm-H_2O toluene based DEP circuits with respect to different field frequencies. For the BG connection (Figures (a-h)), both DEPs lose their potential drop for CNT depositions due to the increased impedance of the 800-nm-thick SiO_2 layer of silicon wafer used in this thesis as the field frequency decreases (for water: 10 MHz ~1000 Hz; for toluene: 100 Hz~0.001 Hz as shown in Fig. 6.10(d) and (h)). Besides, it is apparent that the 100-ppm-H_2O toluene can preserve larger potential drop across the electrode gap for CNT depositions at rather low frequencies (>0.01 Hz) compared to the 0.01-w%-SDS water (>100000 Hz) DEPs, which is attributed to the low conductivity of the former, making the impedance of toluene comparable with the dielectric layer SiO_2 impedance even under low frequencies.

Figure 6.11 demonstrates the typical BG toluene-CNT-DEP deposition using a bias of 50 Hz and 3.5 V V_{rms} performed with an extended-width (90 μm) electrode structure. The SEM observation confirms the feasibility of low-frequency CNT-DEPs with BG connections based on toluene.

Based on eq. 2.27 and 2.28, it can be addressed that the lower frequency of electric field results in larger polarizability of the CNT. Thus how could one apply a magnitude-fixed electric field to preserve enough potential drop across liquids for CNT depositions while frequency further decreases? One approach is to change the ground connection from BG to TG (is used for all the following discussions) in avoid of potential loss within the dielectric layer of wafers. Figures 6.10(i-l) shows the potential characterizations of TG CNT-DEPs based on two kinds of media. It is noteworthy that although the operating frequency of 0.01-w%-SDS water based TG-DEPs (Fig. 6.10(i) and (j)) can be preserved to one order magnitude lower than the BG case, it still cannot drop down to 10 kHz since half the potential has already been wasted within the EDL. In addition, this frequency is detrimental for enhancing CNT polarizabilities. On the other hand, for 100-ppm-H_2O toluene based DEPs (Fig. 6.10(k) and (l)), the applied bias can be preserved well for DEP depositions with field frequency continuous decreasing, even down to DC. This is because the thickness of its EDLs is thicker than the electrode gap, making the impedance of

the whole circuit dominated by the capacitance of the diffuse layer rather than the Stern layer or the liquid. This phenomenon underlines the improvement of s-SWCNT DEP depositions as low frequency bias.

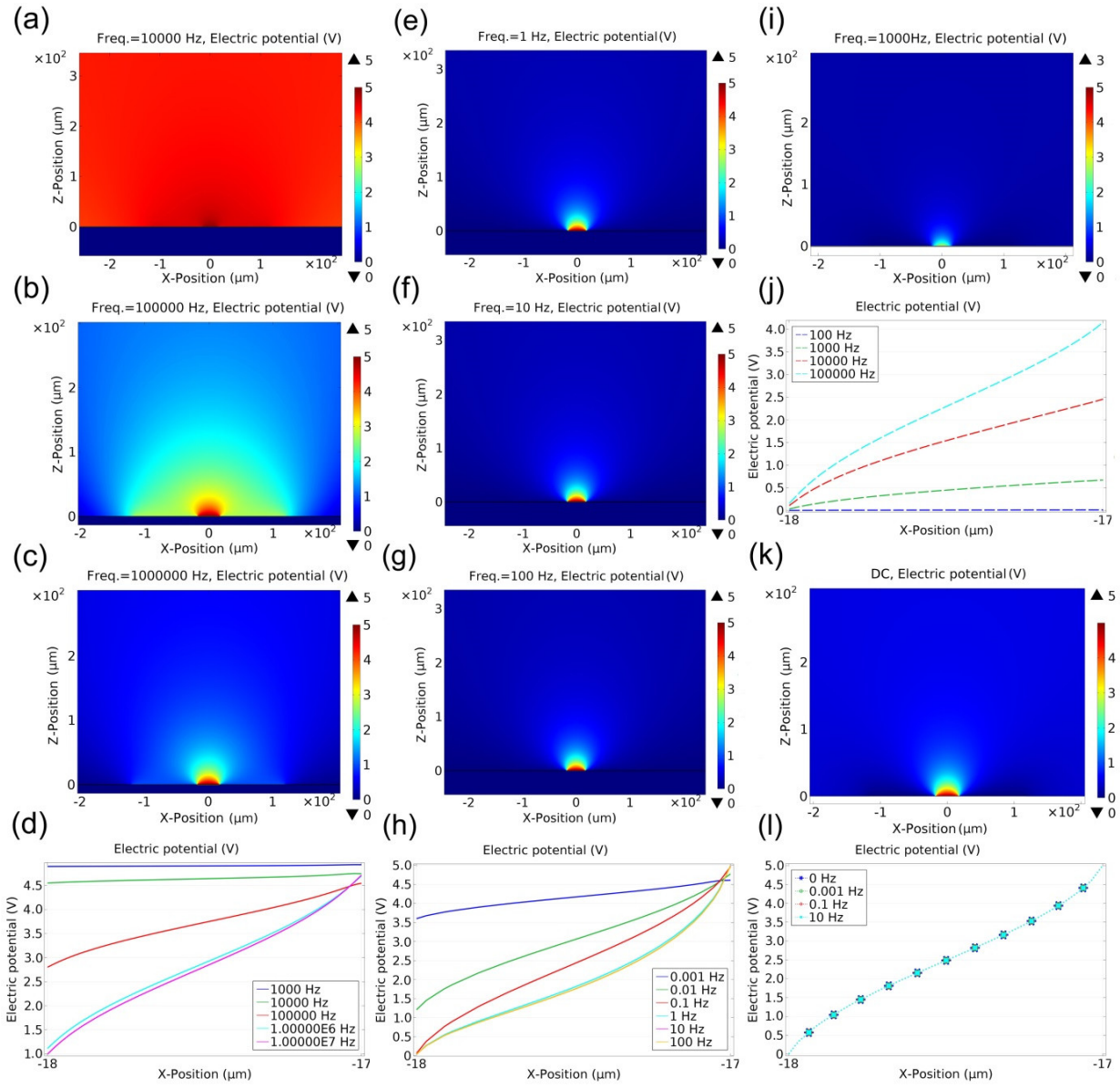

Figure 6.10: Characterizations of electric potential distribution for (BG: a-d, TG: i-j) 0.01-w%-SDS water and (BG: e-h, TG: k-l) 100-ppm-H_2O toluene based DEPs with respect to the field frequency. For the former, it shows the BG based potential-distribution surfaces with respect to frequencies of (a) 10 kHz, (b) 100 kHz and (c) 1 MHz, and (d) plots of potential drop across the electrode gap under different frequencies (1 kHz, 10 kHz, 100 kHz, 1 MHz and 10 MHz). The TG based (i) potential-distribution surface under frequency of 1 kHz and (g) plots of potential drop across electrode gaps with respect to frequencies of 100 Hz, 1 kHz, 10 kHz and 100 kHz are also displayed. For the latter, the

corresponding BG based potential-distribution surfaces with respect to frequencies of (e) 1 Hz, (f) 10 Hz and (g) 100 Hz, and (h) plots of potential drop across electrode gaps under different frequencies (0.001 Hz, 0.01 Hz, 1 Hz, 10 Hz and 100 Hz) are demonstrated. The TG based (k) potential-distribution surface under DC case and (l) plots of potential drop across electrode gaps with respect to DC and frequencies of 0.001 Hz, 0.01 Hz, 1 Hz and 10 Hz are also displayed. A bias of 5 V V_{rms} is applied for all cases. Simulation detials can be referred to the COMSOL programs CMSL3 and CMSL4 in the attached CD.

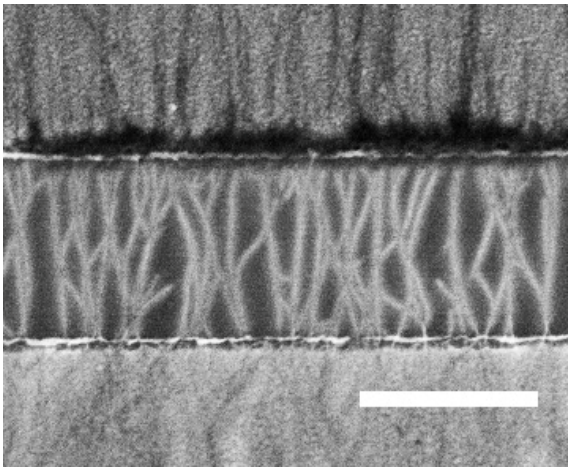

Figure 6.11: SEM image of typical BG toluene-CNT-DEP depositions using 50 Hz, 3.5 V V_{rms} bias based on 90-μm long, 1-μm wide electrode structures (scalar bar: 1 μm).

6.3.4. Thermal Field

1. Boundary Condition

Theoretically, boundary conditions for temperature fields are the continuity of temperature and normal heat fluxes at interfaces. The boundary conditions for the temperature field in micro-structures are significantly determined by the ambient environment, which can differ from one experiment to another. As shown in the Figure 6.9(b), the electrodes are large enough for efficiently heat dissipation, thus the corresponding temperature can be considered to be at room temperature (300 K in this work). In addition, the upper and lower boundaries are also considered to be at room temperature due to efficient heat exchange with ambient environment. On the lateral edges, a symmetry boundary condition is applied as $-n_{\perp} \cdot (-\mathrm{K}\nabla T) = 0$, because these edges are far away from the concentrated power generation near the electrode gap, and the resulting temperature gradients are almost negligible[251].

2. Simulations and Discussion

Figures 6.12 display the simulated results of the generated temperature fields of the mentioned solution based DEPs. It is evident that for a given electric field, the 0.01-w%-SDS water DEPs with TG connection yield more Joule heating, resulting in an increase in the local temperature as well as the gradient of temperature than the TG-connected 100-ppm-H_2O toluene based DEPs. The highest temperature of solution for the former case arose from 300 K up to 301.1 K, while it remains almost unchanged for the latter; the maximum gradient of temperature field of the SDS-water based DEPs is over 6 orders of magnitude larger than the toluene based ones. As mentioned above, the induced temperature gradient inevitably brings electrothermal effect on the fluid. Thus one can address that the ETF effect induced under the AC water-CNT DEPs is significant, while it is negligible for the DC toluene-CNT DEPs.

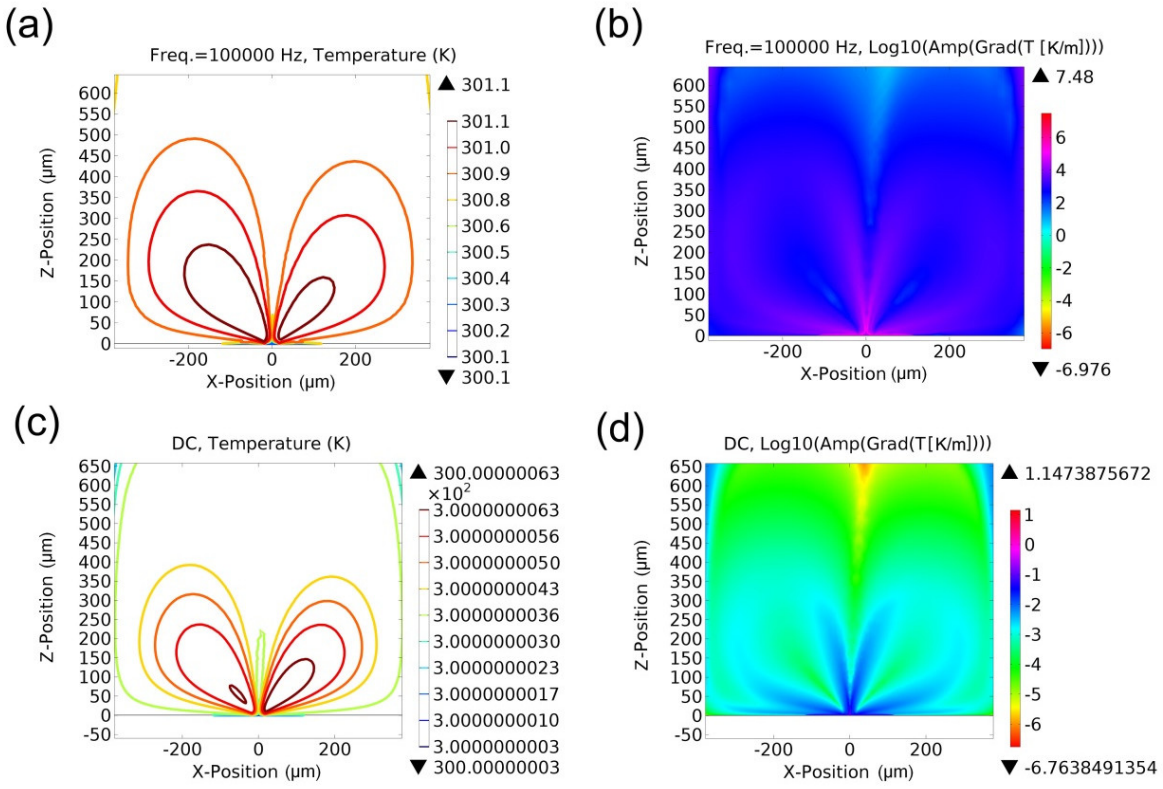

Figure 6.12: Temperature distribution characterizations of 0.01-w%-SDS water and 100-ppm-H_2O toluene based TG-DEPs. (a) Temperature contour and (b) surface graph of logarithmic temperature gradient of the former under a 5 V V_{rms}, 100 kHz bias compared to the (c) temperature contour and (d) surface graph of logarithmic temperature of the latter with a 5 V DC bias. Simulation detials can be referred to the COMSOL programs CMSL3 and CMSL4 in the attached CD.

6.3.5. Fluidic Field

1. Boundary Condition

No-slip conditions are imposed on all boundaries of the fluid domain: $v = 0$. In certain situations, however, it may be necessary to introduce a slip condition on the metallic electrodes in order to take the emergence of ACEO into account, especially in the frequency regime: $v_0 = v_{ACEO}$. Similar in the case when a DC offset is imposed between two electrodes, a slip condition on the dielectric silicon oxide substrate has to be introduced to account for DCEO: $v_0 = v_{DCEO}$. In this section, two situations are included: AC water-CNT DEPs and DC toluene-CNT DEPs. As discussed previously, the ACEO effect of the latter is very small compared to the former due to a much smaller EDL capacitance of toluene circuits. Therefore, here it is reasonable that the ACEO boundary condition is only defined for AC water-CNT DEPs, while DCEO only for DC toluene-CNT DEPs.

2. Simulations and Discussion

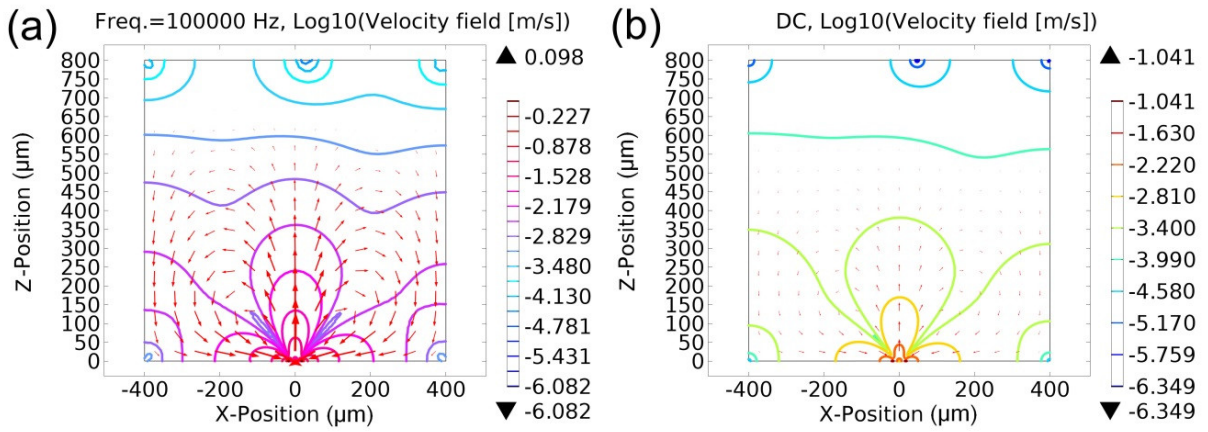

Figure 6.13: Fluidic velocity characterizations of 0.01-w %-SDS water and 100-ppm-H_2O toluene based TG-DEPs. (a) Logarithmic velocity contours and flow-direction-indication arrows of the former with a 5 V V_{rms}, 100 kHz bias compared to the corresponding (b) logarithmic velocity contours and direction-indication arrows of the latter using a 5V DC bias. Simulation detials can be referred to the COMSOL programs CMSL3 and CMSL4 in the attached CD.

Figure 6.13 demonstrates the fluidic velocity distribution of the 0.01-w%-SDS water and 100-ppm-H_2O toluene based TG-DEPs involving the proper ETF, ACEO and DCEO effects.

The steady-state fluid velocity of 0.01-w%-SDS water based DEPs is over 10 times larger than that of 100-ppm-H_2O toluene based DEPs, which can be attributed to its more pronounced ETF effects. Note that the motion of liquid above common electrode rises up from the top-surface of the electrode and symmetrically convection back to the electrode gaps from both left and right sides (Figure 6.13). This phenomenon is helpful for transporting CNTs into effective deposition regions. Additionally, the fluid convections in both cases are so large that CNT-DEP depositions should be dominated by convections instead of CNT-diffusions (around ~μm/s, caused by Brownian motion as introduced in Chapter 2.4.2) under high DEP bias (here 5 V for both cases).

6.3.6. DEP Efficiency

Figure 6.14 displays both side and top view characterizations of the velocity and alignment of CNT deposition using 0.01-w%-SDS water (Figures 6.14(a-d)) and 100-ppm-H_2O toluene (Figures 6.14(e-l)) based TG-DEPs.

For the case of side views, it is evident that the 100-ppm-H_2O toluene based DEPs yield a higher deposition efficiency and better CNT alignment than the 0.01-w%-SDS-water based ones even under the same bias conditions (5 V V_{rms}, 100 kHz as shown in Figures 6.14(a-b) and (i-j)). This is because the latter possesses a larger conductivity, thus screening the polarizability of CNTs during DEP depositions. Besides, the benefits of using low field-frequency DEPs for CNT depositions can be confirmed with observations as shown in Figures 6.14(e-f) and (i-j), where a maximum DEP velocity of about ~m/s and alignment angle (with respect to the x-axis) of 0.01° can be achieved with a 5 V DC DEP bias whereas they decrease to 0.27 m/s and 0.05° under a bias of 5 V V_{rms}, 100 kHz both based on toluene. This phenomenon can be attributed to the loss of CNT polarizabilities with respect to the increase of field frequency. Similar observations are also displayed in Figures 6.14(c-d), (g-h) and (k-l) for the top views of DEPs.

Additionally, in order to further evaluate the difference between DEP performance based on these two kinds of liquids, a simulation of 1 V DEP bias is performed and shown in Figures 6.14(g-h) and (k-l) for 100-ppm-H_2O toluene based DEPs with respect to field frequencies of DC and 100 kHz respecticely. It is clear that the performance of CNT deposition using toluene-based 1V-DC DEPs is even better than that using SDS-water based 5 V V_{rms}, 100 kHz DEPs as shown in Fig. 6.14(c-d), while the latter is already better than 1 V, 100 kHz DEPs based on toluene. Thus one can address that toluene based DC-DEPs with an applied bias below the

threshold voltage of electrode electrolysis is the most promising approach to perform CNT depositions under the scope of this thesis.

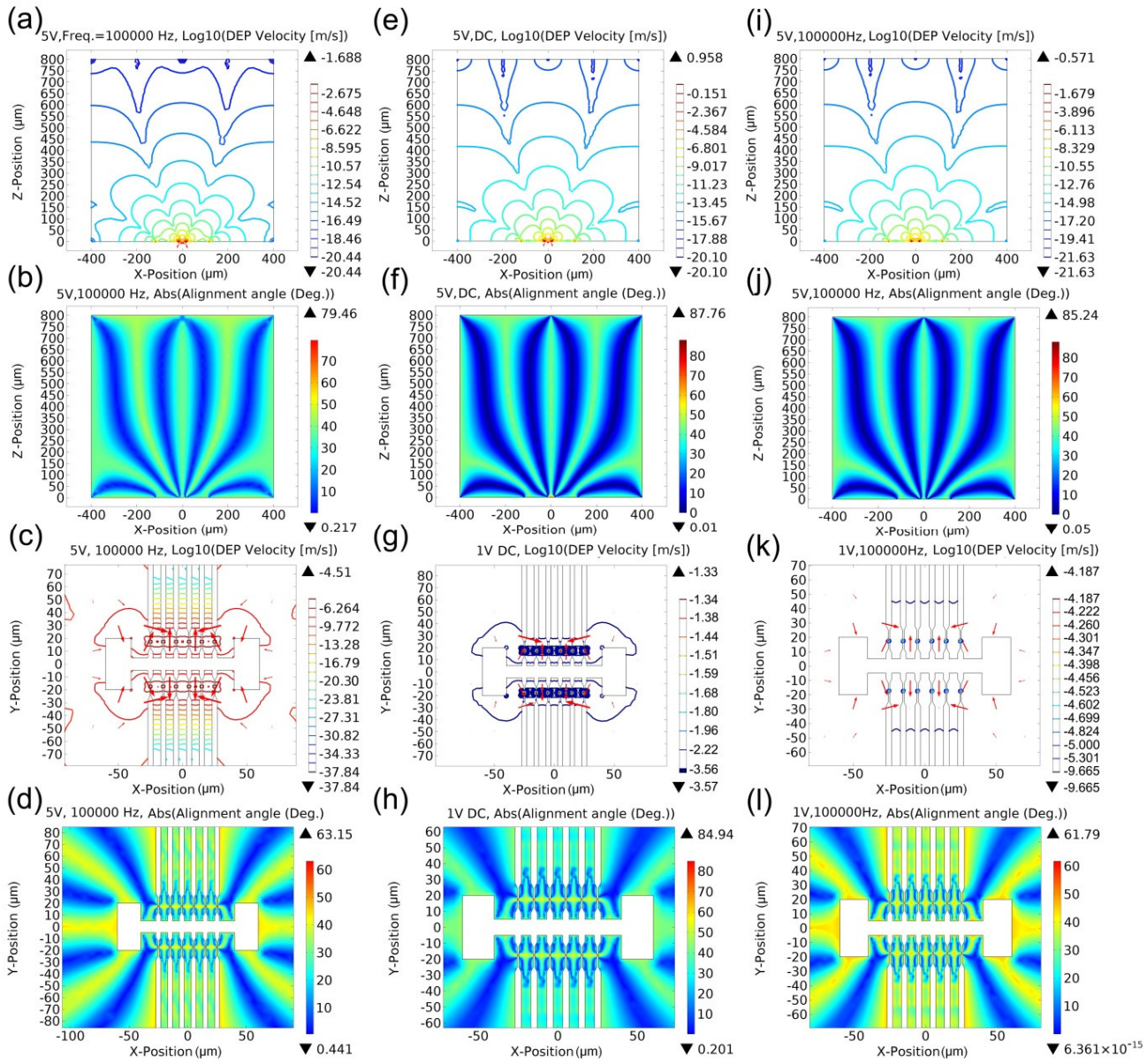

Figure 6.14: Side view and top view characterizations of velocity and alignment of depositing CNTs through 0.01-w%-SDS water and 100-ppm-H_2O toluene based TG-DEPs. Side view: (a), (b) show the logarithmic velocity contours and steady-state alignment surface (with respect to X-axis) of 0.01-w%-SDS water dispersed CNTs respectively during DEPs with a 5 V V_{rms}, 100 kHz bias. (e), (f) show the logarithmic velocity contours and steady-state alignment surface (with respect to X-axis) of 100-ppm-H_2O toluene dispersed CNTs respectively during DEPs with a 5 V DC bias, while the bias is changed to 5 V V_{rms}, 100 kHz and displayed in (i) and (j). Top view: (c), (d) show the logarithmic velocity contours and steady-state alignment surface (with respect to X-axis) of 0.01-w%-SDS

water dispersed CNTs respectively during DEPs with a 5 V V_{rms}, 100 kHz bias. (g), (h) show the logarithmic velocity contours and steady-state alignment surface (with respect to X-axis) of 100-ppm-H_2O toluene dispersed CNTs respectively during DEPs with a 1 V DC bias, while the bias is changed to 1 V V_{rms}, 100 kHz and demonstrated in (k) and (l). Simulation detials can be referred to the COMSOL programs CMSL3-6 in the attached CD.

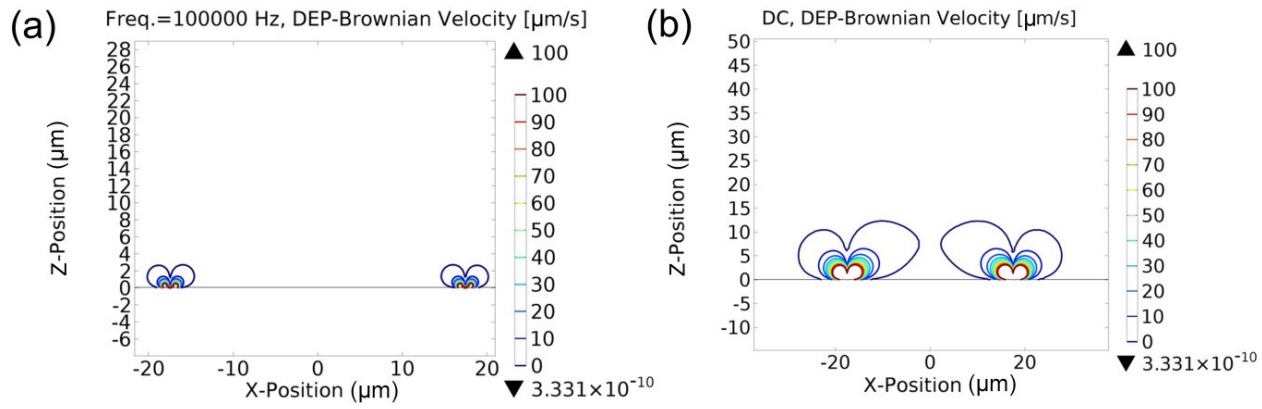

Figure 6.15: Side view contours of TG-DEP velocity overcoming the Brownian motion for (a) 0.01-w%-SDS-water and (b) 100-ppm-H_2O toluene dispersed CNT depositions using DEP bias of 5 V V_{rms}, 100 kHz and 5 V, DC respectively. Simulation detials can be referred to the COMSOL programs CMSL3 and CMSL4 in the attached CD.

In terms of quantitative comparison of the CNT deposition efficiency of SDS-water and toluene based DEPs, the corresponding velocity distributions where the DEP deposition overcoming the Brownian motion are simulated, as shown in Figure 6.15. The mean radius of effective regions, where CNTs can be deposited for the 0.01-w%-SDS water based 5 V, 100 kHz DEP is about 3 µm (Figure 6.15(a)). It is only one fourth of that based on 100-ppm-H_2O toluene based DEPs with a 5 V DC bias (Fig. 6.15(b)). Thereby, considering a 3D geometry of the DEP system, this observation reveals a difference with a factor of 64 between these two DEP situations, implying that the electric field generated during toluene based DEPs can influence SWCNTs further away from electrode gaps than SDS-water based ones. It is noteworthy that all the simulations above can only visualize the beginning situation of CNT depositions using DEPs. The parameters as well as variables used in these simulations will probably change after the nanotubes start to be deposited across the electrodes. Thus further analysis is required for specific cases.

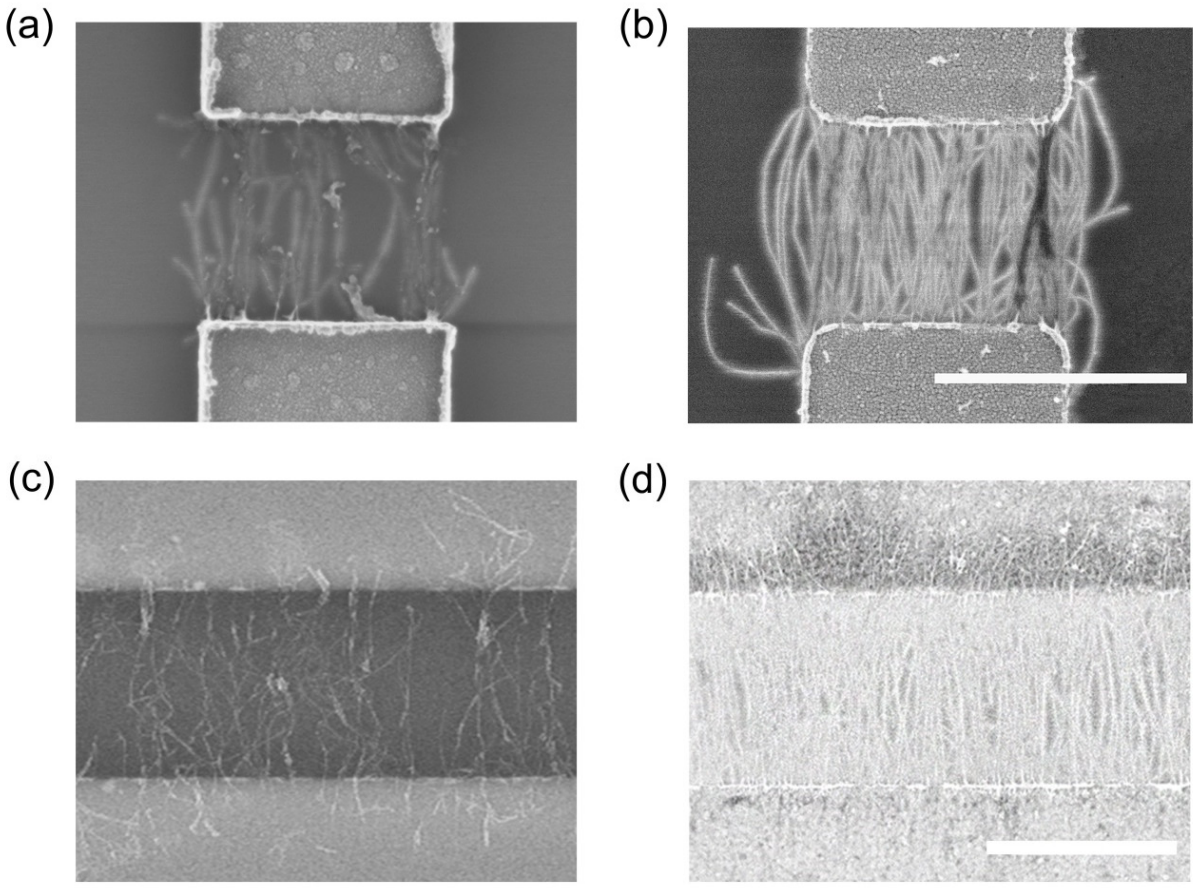

Figure 6.16: Typical SEM images of TG-DEP deposited CNTs based on media of 0.01-w%-SDS water using (a) 1×1 μm (5 V V_{rms}, 100 kHz), (c) 1×90 μm (15 V V_{rms}, 100 kHz) structures, and 100 ppm-H_2O toluene with (b) 1×1 (5 V, DC), (d) 1×90 μm (10 V, DC) structures (scalar bar: 1 μm).

Figure 6.16(a and b) shows the typical SEM images of CNT-DEP deposition based on 0.01-w%-SDS water (5 V V_{rms}, 100 kHz) and 100-ppm-H_2O toluene (5 V, DC) with standard electrode structures (with channel gap of 1×1 μm) respectively. As stated above, it is obvious that the alignment and density of CNT deposition based on 0.01-w%-SDS water DEPs is poorer and lower than the one based on 100-ppm-H_2O toluene DEPs under the same bias. In order to achieve large-scale or highly-dense CNT depositions for optoelectronics, an electrode structure with a 1×90 μm channel gap was also designed, as shown in Fig. 6.16(c and d). Again, toluene based DEPs (10 V, DC) achieved a higher-density and better-alignment CNT depositions than the SDS-water based ones (15 V V_{rms}, 100 kHz). This can be attributed to the more pronounced polarizabilities of CNTs from the former DEPs, making nanotubes more easily deposited within large scale electrode structures than the latter in which a much larger bias is required to compensate for its relatively smaller polarizabilities of nanotubes.

6.4. Summary

Physical principles of CNT-DEPs have been discussed theoretically with water and toluene as the medium. For the toluene case, the EDL thickness is much larger than the micron-scale electrode gap, thus DEPs can be performed at low frequency, even DC-DEP, which is much beneficial to enhance CNT polarizability through making use of its low-frequency extremum. SEM characterizations confirmed that the performance of toluene based DEPs for s-SWCNT deposition are much better than the water based DEPs. Besides, the toluene based DEPs with DC bias was verified to be the most promising approach for s-SWCNT depositions. Moreover, a quantitative efficiency-difference between the toluene based DC-DEP and water based AC-DEP was derived by considering the effective dielectrophoretic region for SWCNT deposition.

– This page intentionally left blank –

Chapter 7: Low-Frequency DEP for CNT-FETs

The work contained in this Chapter can be found in Ref.[128].

7.1. Introduction

s-SWCNTs have been recognized as a promising candidate for next-generation, high-performance field-effect transistors (FETs) because of their extraordinarily high carrier mobility or carrier saturation velocity[120,218]. However, many challenges need to be overcome before the commercialization of corresponding technology. One biggest of which is the implementation of SWCNTs-based high-performance logic. This requires s-SWCNTs to be integrated into individual devices at a device density comparable to existing or future MOSFET technologies. Significant progress in this direction has been made over the years, but precise control over the fabrication of individual devices at ultrahigh densities with reliable properties is still absent. On the other hand, it is significantly less challenging to build a short-channel FET from an aligned and tightly packed array of s-SWCNTs than individual ones[32,252–254]. These are of particular interest applications such as SWCNT-based high-frequency power amplification, where merely a high linear density of parallel aligned s-SWCNTs, all contacted to the same micron-scale source and drain electrodes for low-impedance matching is required[22,255].

So far, it has been difficult to fully exploit the exceptional properties of s-SWCNT arrays due to restrictions arising both from the material and fabrication techniques. These include alignment and placement of nanotubes, as well as the difficulty in fully removing residual metallic SWCNTs[256] and other impurities. For the alignment and placement of s-SWCNTs, low-frequency dielectrophoresis (DEP), which is based on low-conductive solvents (such as toluene), has been verified to be the most efficient way to integrate s-SWCNTs into devices, as discussed in Chapter 6. In terms of material quality, selective extraction of as-prepared SWCNT material by conjugated polymers has demonstrated to be an effective enrichment and isolation method to obtain high purity s-SWCNTs[150,257]. In particular, polyfluorene-based copolymers have shown to have one of the highest specific sorting abilities toward generating dispersed SWCNTs with purity of semiconducting content >99% in a single sonication/centrifugation step[57–59].

However, in order to realize applications, higher s-SWCNT purities are desirable. As reported[22], aiming at further improving SWCNT-based high-frequency power transistors, the

devices need to have significantly lower m-SWCNT content (less than 1%). The ultimate goal for digital logics is to reduce the m-SWCNT impurity level to less than parts-per-million or even parts-per-billion. Besides, an additional constraint toward these applications is that the impurity level needs to be realized for large diameter SWCNTs with d > 1.2 nm, so as to reduce current-limiting Schottky barriers and to dramatically improve the On/Off ratios relative to small-diameter SWCNTs[188,258]. Moreover, although absorption spectroscopy is typically used to characterize nanotube purity, it is found to be insufficient in quantifying s-SWCNT solutions of high purity (>98 to 99%) due to low signal-to-noise in the m-SWCNT absorption region. Therefore, a high throughput electrical testing method is required to quantify the ultrahigh purity of s-SWCNTs[51].

In this Chapter, s-SWCNT suspensions with purity of >99.7% based on toluene was achieved by using SEC to separate polymer wrapped s-SWCNTs with respect to nanotube length. This value was derived through statistically analyzing corresponding transistor performance involving their mobility, On/Off current ratio and current density. By using low frequency DEPs, the fabricated transistors of such s-SWCNTs possessed a hole mobility of up to 297 $cm^2V^{-1}s^{-1}$ and On/Off ratios as high as 2×10^8. Besides, by replacing SiO_2 based back-gate modulation with Al top-gate, a sub-threshold swing of 95 mV/decade for CNT transistors was achieved.

7.2. Experimental

PLV SWCNTs were synthesized for this study using methods introduced in Chapter 3.1[127]. The preparation of toluene-based suspensions was performed in the way introduced in Chapter 3.2.2[128].

In terms of the fabrication of CNT transistors, the site-selective integration of poly(9,9-di-n-dodecylfluorenyl-2,7-diyl) (PODOF)-wrapped SWCNTs from an dispersion fraction (fraction 2 as mentioned below) was achieved via low-frequency DEP with a DC, 5 V V_{rms} bias[259,260]. More details were as introduced in Chapter 3.6.

7.3. Results and Discussion

Figure 7.1 shows the chromatogram obtained by fractionating PODOF-wrapped starting suspensions. It is obvious that the chromatogram can roughly be divided in two regions: (i) elution time between ~20-35 min during which only the polymer-wrapped SWCNTs elute and (ii) elution time ~35-45 min during which both polymer-wrapped tubes and “free” polymer

elutes. Four fractions (Frac 1~4) of 5 to 10 ml were sequentially collected from the first broad band eluting from the column (see Figure 7.1).

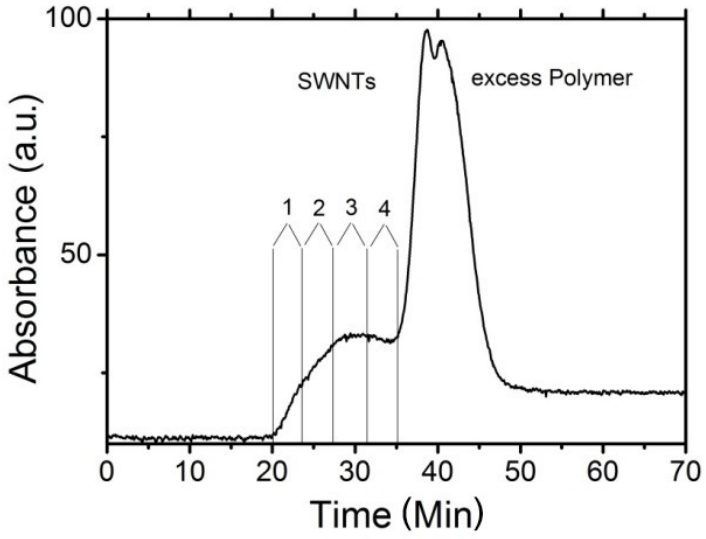

Figure 7.1: Chromatogram of PODOF wrapped PLV SWCNTs obtained at 430 nm. Gray lines indicate fractions collected for analysis[128].

Figure 7.2 demonstrates absorption spectra in the wavelength range of 300–2000 nm for these four fractions. These spectra show mainly the first (S_{11}), second (S_{22}) and third (S_{33}) interband transitions of s-SWCNTs. Compared to aqueous suspensions of the same SWCNT raw materials with surfactants as reported in Ref. [261] (see Appendix C), the spectra are more richly structured. This reflects primarily on (i) the pronounced S_{11} and S_{22} interband transitions arising from a strongly reduced (n, m)-distribution, and (ii) the essentially complete absence of the first metallic excitonic transitions, M_{11}, otherwise visible in the spectral region between ~500-700 nm. However, here quantitatively assessing the m-/s-purity of SWCNT suspensions by means of analyzing absorption spectra alone is difficult, because absorption features of side-products such as fullerenes, amorphous carbon and residual catalyst particles also normally appear in the M_{11} absorption region. Nevertheless, Fig. 7.2 clearly shows a reduction in background absorption versus S_{22}/S_{11} absorption when comparing the absorption spectrum of the starting suspension to that of chromatographically purified fractions. Therefore, it can be assumed that SEC removes metallic tubes as well as side-products.

In addition to the absorption feature of SWCNTs, there is also an absorption feature of the polymer at 384 nm. As shown, the intensity ratio of this peak to the SWCNT absorption is the

same for fractions 1-3. Since the molar mass (M_w ~20,000 amu as given by Sigma Aldrich) of polymer is much lower than that of SWCNTs (e.g. for ~500 nm long tubes, M_w ~600,000 amu), free polymers would be expected to move much more slowly through the SEC medium than nanotubes. Thus one can conclude that (i) the amount of polymer adsorbed on the tubes (which moves through the SEC gel together with the SWCNTs) and (ii) excess polymer can be removed from polymer-wrapped SWCNTs by SEC.

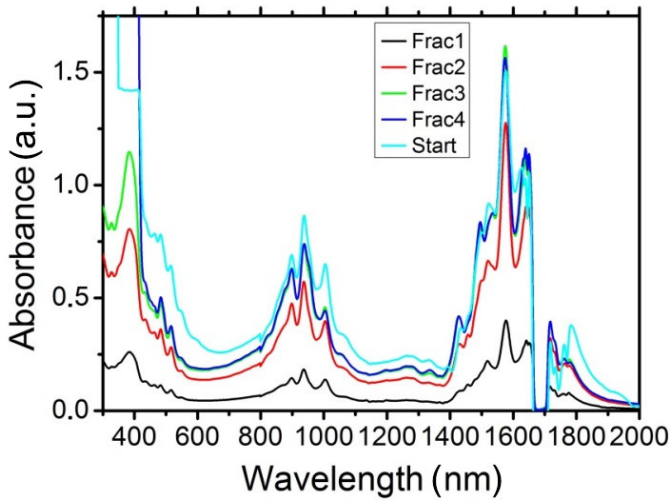

Figure 7.2: Absorption spectra of SEC fractions of PODOF-wrapped PLV SWCNTs in toluene (fractions refer to those indicated in Figure 7.1). "Start" indicates starting suspension (diluted by 5× for better comparison)[128].

Further removal of residual metallic tubes by SEC is supported by Raman measurements of SWCNTs sedimented out of suspensions by using ultracentrifugation (direct Raman analysis of suspensions is hindered by the strong interference of the organic solvent). Fig. 7.3 shows Raman spectra excited at 633 nm in the radial-breathing mode (RBM) and G mode regions of tubes in SEC fractions 1-4 in comparison to the starting suspension. The above excitation wavelength corresponds well to the region of M_{11} absorption of metallic tubes and weak (off-resonance) absorption window between S_{33} and S_{22} bands of semiconducting tubes (Fig. 7.2). As a result, the spectrum of SWCNTs in the starting suspension still clearly demonstrates features which can be attributed to residual metallic tubes – the characteristic broad shoulder (Breit-Wigner-Fano lineshape)[262][263] of the G^- band at ca. 1535 cm^{-1} and the RBM band at ca. 190 cm^{-1}. These features practically disappear in the spectrum of fractionated tubes, thus indicating a further substantial reduction of metallic tubes.

Notably, the RBM peaks observed at 253, 265 and 283 cm^{-1} may be attributed to (10,3), (7,6) and (7,5) semiconducting tubes, respectively[264], which are minor species in the PLV SWCNT material, but are resonantly excited at 633 nm. The major Raman signals detected from the fractionated tubes, *e.g.* RBM bands within ~140-200 cm^{-1}, are apparently contributed by the off-resonantly excited but abundant, larger diameter s-SWCNTs (see Fig. 7.2 and PLE maps in Fig. 7.4).

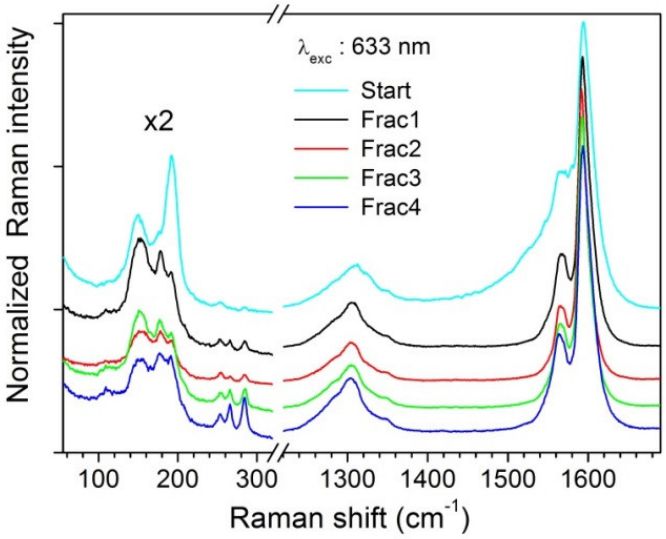

Figure 7.3: Raman spectra at 633 nm excitation of PODOF-wrapped PLV SWCNTs sedimented out of SEC fractions by ultracentrifugation. Different "Frac" refers to the corresponding fractions indicated in Figure 7.1, "Start" denotes the starting CNT suspension before SEC. The spectra are intensity-normalized at the G^+ band (at ca. 1594 cm^{-1}) and vertically shifted for clarity[128].

Fig. 7.4 shows PLE maps obtained for the four fractions. The chiral indices corresponding to local maxima in photoluminescence of CNTs were assigned on the basis of Ref. [233]. Besides the general observation that PODOF exclusively extracts close-to-armchair SWCNTs, there are also significant differences in the (n, m)-composition of eluting fractions as obtained from the PLE maps. It is evident that the early fractions are enriched in tubes with larger diameters, while later fractions have smaller average diameters.

AFM measurements on spin-coated samples, as described in Chapter 3.4.2, show that this diameter trend correlates with mean length. The images were acquired for 300-500 isolated tubes per fraction. Figure 7.5 shows a typical AFM image of PODOF-SWCNTs.

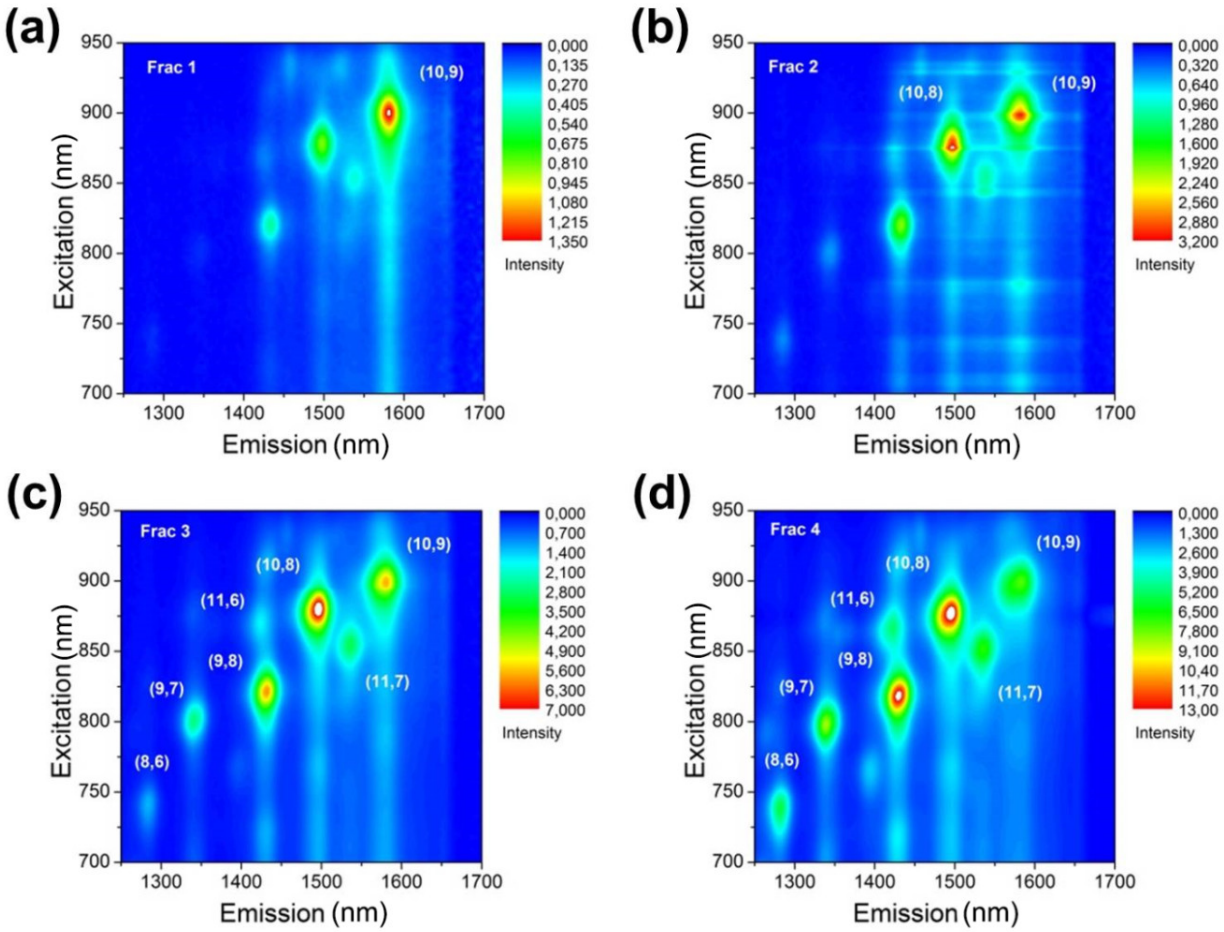

Figure 7.4: PLE maps of SEC fractions of PODOF wrapped PLV SWCNTs. Fractions refer to those indicated in Figure 7.1. Note that the chiral index distribution is somewhat dependent on fraction[128].

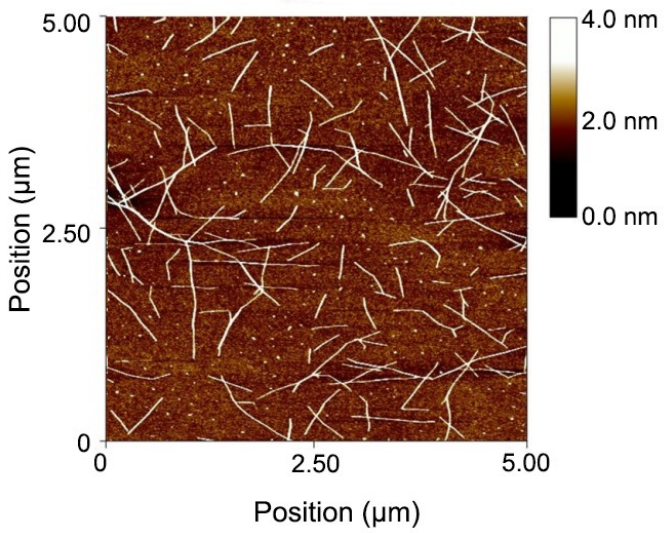

Figure 7.5: Representative AFM picture of PODOF wrapped PLV SWCNTs[128].

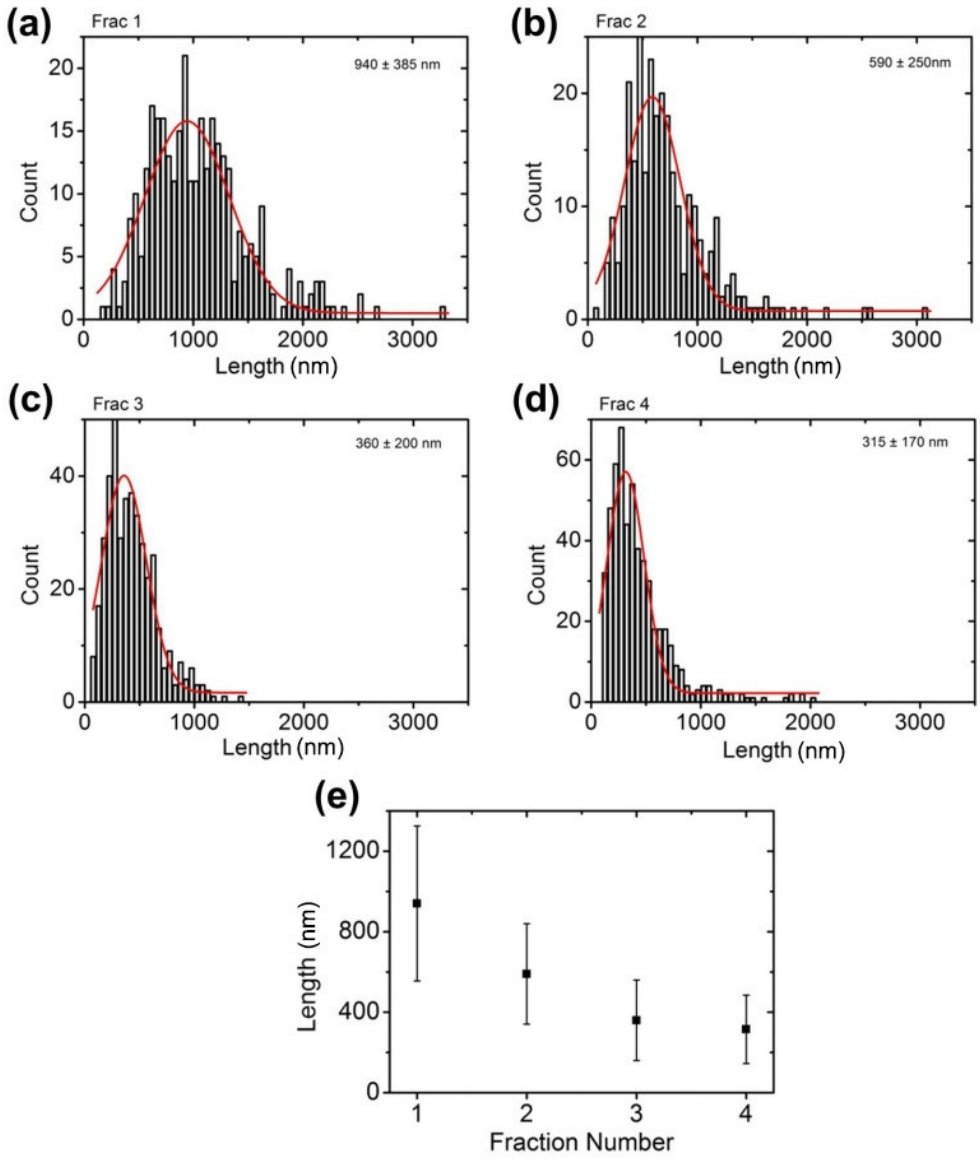

Figure 7.6: Length statistics extracted from AFM images obtained for spin-coated samples of SEC fractions of PODOF wrapped PLV SWCNTs. The red fitting curves are obtained based on the Gaussian function. Fractions correspond to those indicated in Figure 7.1. Note the systematic decrease in average length with increasing fraction number[128].

Through analyzing the obtained AFM images, the mean lengths of 940±385 nm for fraction 1, 590±250 nm for fraction 2, 360±200 nm for fraction 3 and 315±170 nm for fraction 4 (Fig. 7.6) were derived. In addition, from the AFM height analysis as shown in Figure 7.5, it is obvious that there is no indication of the presence of a significant amount of nanotube bundling. Consequently, it appears that larger diameter tubes are on average longer than the smaller diameter tubes. In earlier studies on length separation of surfactant suspended aqueous suspensions of SWCNTs, it was speculated that sonication induced scission is the possible

reason for analogous differences in (n, m)-distributions[200,261]. A correlation between the average diameter and the mean length is consistent with the current accepted conclusions regarding the mechanism by which SWCNTs are shortened during sonication[200,261].

Electrical characterizations of the high packing-density short-channel transistor devices were performed to assess the purity of the s-enriched large-diameter PODOF-wrapped SWCNTs. For this, nanotubes from fraction 2 were deposited to closely match the SWCNT length distribution to the transistor channel length, taking into account that DEP promotes the deposition of longer nanotubes in mixtures of different tube lengths, as described in Chapter 2.4.2. The SEM image of a characteristic transistor device, shown in the Figure 7.7(a), demonstrates that the s-SWCNTs are highly aligned along the channel length with a high density of ~30 SWCNTs per µm channel width. This deposition pattern is a result of the DEP conditions of the electrode design and allows to more effectively identify residual m-SWCNTs from high purity dispersions as compared to single-tube devices. Also, such devices are promising for SWCNT-based radio frequency power amplification electronics since they promote a higher on-state conductance. Figure 7.7(b) shows the electrical charge transfer performance of all the 12 devices prepared. As shown, all the transistors demonstrate a uniform p-type switching behavior with a typical On-state current density of ~10 µA/µm at 1V bias and an On/Off ratio of up to 2×10^8. The hole mobility is up to 297 $cm^2V^{-1}s^{-1}$ based on the standard model, described in the experimental section. In addition, the average and standard deviation is $272\pm30 cm^2/Vs$ for 6 out of 12 devices. The other half of the devices has an average mobility that is a factor of 2.5 less ($106\pm40 cm^2/Vs$) and seems to correlate with a higher nanotube density.

The outstanding performance of these transistors can be attributed to the high-density integration of nanotubes, the high degree of alignment using low-frequency DEP (as described in Chapter 6) and the high-purity enrichment of s-SWCNTs through PODOF wrapping in combination with SEC. Since longer s-SWCNTs are better aligned by DEP[169], one cannot distinguish the individual contributions of the length-sorting by SEC and the DEP to the enhanced degree of alignment. It is also not possible to clarify how important polymer removal by SEC is for the performance. This is because length sorting, polymer removal and DEP alignment are direct consequences of using SEC and cannot be studied separately. However, what can certainly be assumed is that PODOF-wrapped SWCNTs in toluene are better aligned by DEP than SWCNTs in aqueous surfactant solutions due to the low permittivity and conductance of toluene as well as low field frequency. Regarding the physics, one can find

detail descriptions in the literature of Ref. [169] and in Chapter 2.4.2. The purity of the dispersion can be estimated from the total number of contacted SWCNTs and the fact that none of the devices show the presence of metallic SWCNTs. Metallic SWCNTs would have caused an off-state current in the order of 1-10 µA and hence orders of magnitude higher than observed[265]. As counted by SEM, there are around 30 bridging SWCNTs per device in each of the 12 devices. Thus the estimated purity of s-SWCNTs should exceed $1-1/(12\cdot30) \approx 99.7\%$, taking into account that DEP preferentially deposits metallic SWCNTs[63] and no metallic tubes have been detected at all. Since there is no indication that the semiconducting and the residual metallic SWCNTs have a different length distribution, the observed results can be reasonably attributed to the purity of the dispersion.

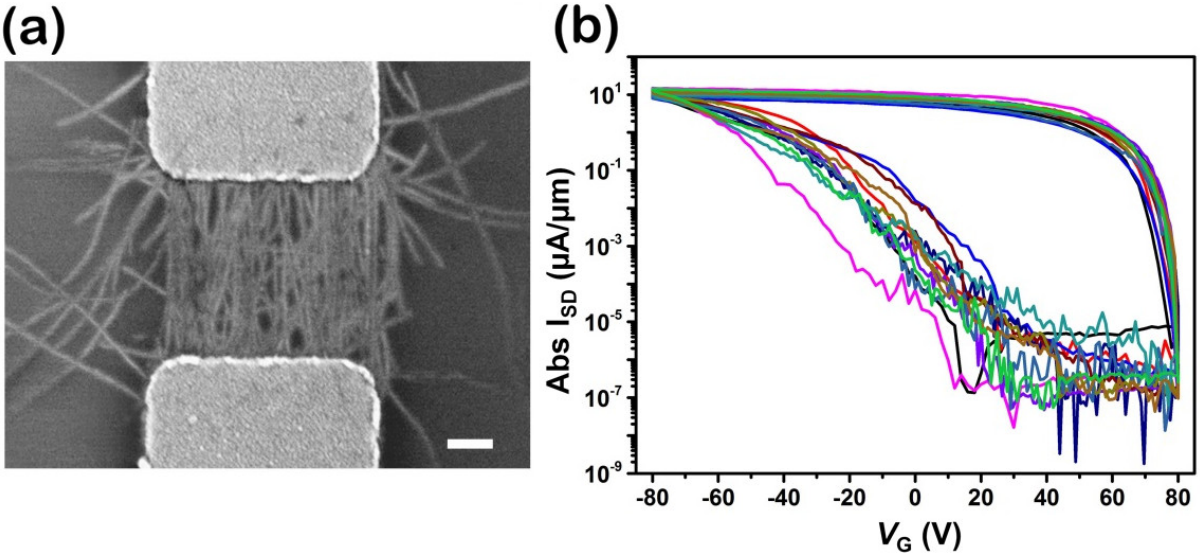

Figure 7.7: (a) SEM image of a typical high-density short-channel transistor made of s-enriched large-diameter PODOF-wrapped SWCNTs, deposited by DEP. The scale bar equals 200 nm. (b) Electrical transfer characteristics for all 12 devices tested. The source-drain current per µm channel width I_{SD} versus back-gate voltage V_G was recorded at source-drain voltage V_{SD} = 1V[128].

The use of high purity, length sorted material and low-frequency DEP significantly improve the reproducibility of devices. This becomes evident in Figure 7.8 when comparing the On-state conductance with the On/Off ratio: all 12 devices share a nearly identical On-state conductance of 10µS/µm and the On/Off-ratios cluster within one order of magnitude. Further improvements in the On-state conductance may be expected when using either longer SWCNTs or shorter channel lengths to ensure that the contact length exceeds the charge transfer length[266]. In comparison with recently reported transport data for devices prepared using s-SWNCTs

dispersed in water[64,78,267] and organic solvents[257,265,268–271], shown in Figure 7.8, it becomes evident that the enrichment of s-SWCNTs through PODOF wrapping in combination with SEC yields s-SWCNT material that allows the fabrication of high-density, short-channel transistors with high mobility, high On/Off ratio and a high On-state conductance with a reproducibility factor of 2. Overall, the improved device performance characteristics can be attributed not only to the high s-purity of SWCNTs in the ~0.95-1.5 nm diameter range (as estimated from absorption spectra[233]) but also to low-frequency DEP which allows for uniformly dense networks to form as the transistor channel.

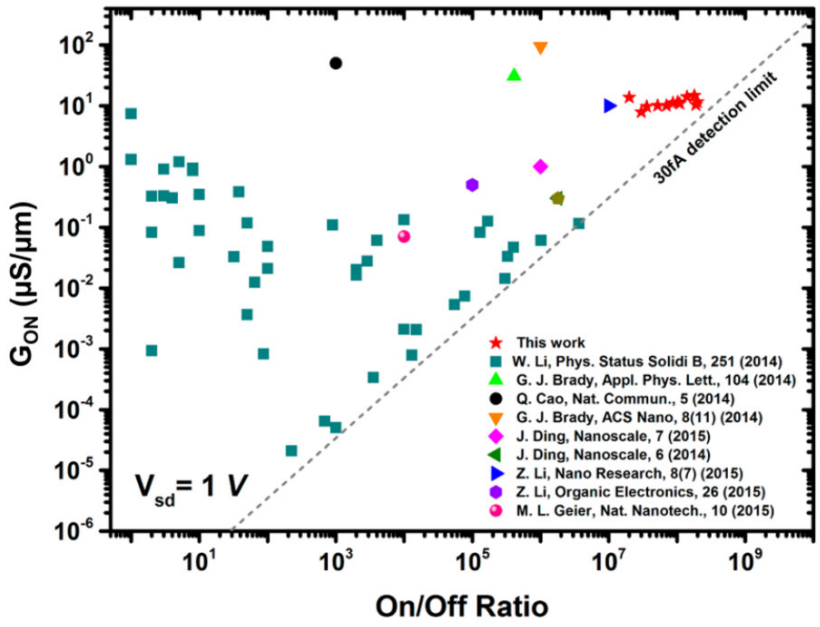

Figure 7.8: Red stars indicate on-state conductance per µm channel width (G_{ON}) versus On/Off ratio for all 12, short-channel, high-density s-SWCNT transistors studied here. (using SEC enriched PODOF-wrapped s-SWCNTs (d_{CNT} = 1.35-1.72nm) with V_{SD} = 1V). Also shown for comparison are recently reported data for devices prepared using aqueous s-SWCNT dispersions [Ref.[78], d_{CNT} = 0.76 nm; and Ref.[64], d_{CNT} = 0.6-2.0 nm; Ref. [267], d_{CNT} = 1.5 nm] and for polymer-wrapped s-SWCNTs dispersed in toluene [Ref.[265], d_{CNT} = 1.3-1.7 nm; and Ref.[257], d_{CNT} = 1.3-1.8 nm, Ref. [268], d_{CNT} = 1.3 nm; Ref. [269], d_{CNT} = 1.2-1.4 nm; Ref. [270], d_{CNT} = 1.3 nm, Ref. [271], d_{CNT} = 1.2-1.4 nm]. The region to the right of the dashed line is not accessible due to the low current detection limit of the setup[128].

Another important technical parameter of CNT transistors is hysteresis, which arises from charge-trap states of nanotube devices. Since these states can influence the gate modulation,

thereby changing the channel conductance in undesirable ways, the stability and reproducibility of SWCNT transistors would be reduced[272]. Furthermore, a pronounced hysteresis can also lead to dynamic changes in threshold voltage, which reduce the noise margin of digital systems, requiring a larger supply voltage[273]. Therefore, for most applications, hysteresis must be eliminated.

In terms of significant hysteresis observed in this work (as shown in Figure 7.7(b)), three causes can be attributed to: reversible charge doping into the SWCNTs by around atmospheric moieties[274,275], field-induced charges trapped and located at the gate insulator/air interface close to the nanotubes[276], and extra mobile charges associated with the insulating oxide layer[277,278]. Therefore, in order to reduce or remove the observed hysteresis, two attempts can be carried out: removing the SWCNT surrounding dopants by proper annealing treatment, and replacing the universal back gate of the used 800-nm-thick SiO_2 dielectric layer with a high-permittivity, small-scale and thin top gate.

Figure 7.9 shows the results of transfer performances of a typical PLV-SWCNT based transistor with different annealing treatments and gating geometries. Under back-gate measurements as shown in Figure 7.9(a), it is apparent that the hysteresis was slightly reduced after a 300 °C, 90 min air annealing compared to its previous performance before annealing, implying that the surrounding dopants of the SWCNT was slightly reduced due to the heating. Besides, an increased on-current was also observed after the annealing treatment, this can be attributed to the improved CNT-metal contact by removing the remaining solvent after deposition and an increased p-doping from oxygen lowering the Schottky barrier for conduction. Figures 7.9(a and b) demonstrate the measured transfer curves of the same transistor but operated with a weakly oxidized (annealing in air at 250 °C for 90 minutes) 30-nm-thick Al top gate (fabricated as described in Chapter 3.6.4). As one can see the hysteresis is significantly suppressed compared to the back-gate based measurements. This can be attributed to the much-enhanced dielectric capacitance C_{ox} as quite thin weakly oxidized Al top-gates employed in the test. On the one hand, the enlarged C_{ox} was helpful to enhance the gate modulation on the CNTs according to the electrostatics $\varphi_{CNT} \propto C_{ox}/C_{CNT}$, meaning small gate sweeping is accessible. On the other hand, the small contact cross-section between Al and CNTs can reduce the number of charge trap states surrounding the interface which need to be occupied when electric filed applied on.

Based on the above discussion, a sub-threshold swing (SS)[279] of 95 mV/decade was also derived using:

$$SS = \ln(10)\left[\mathrm{d}V_{GS} / \mathrm{d}(\ln I_{DS})\right] \tag{7.1}$$

which is quite close to the lowest theoretical limit of 60 mV /decade for SS at room temperature.

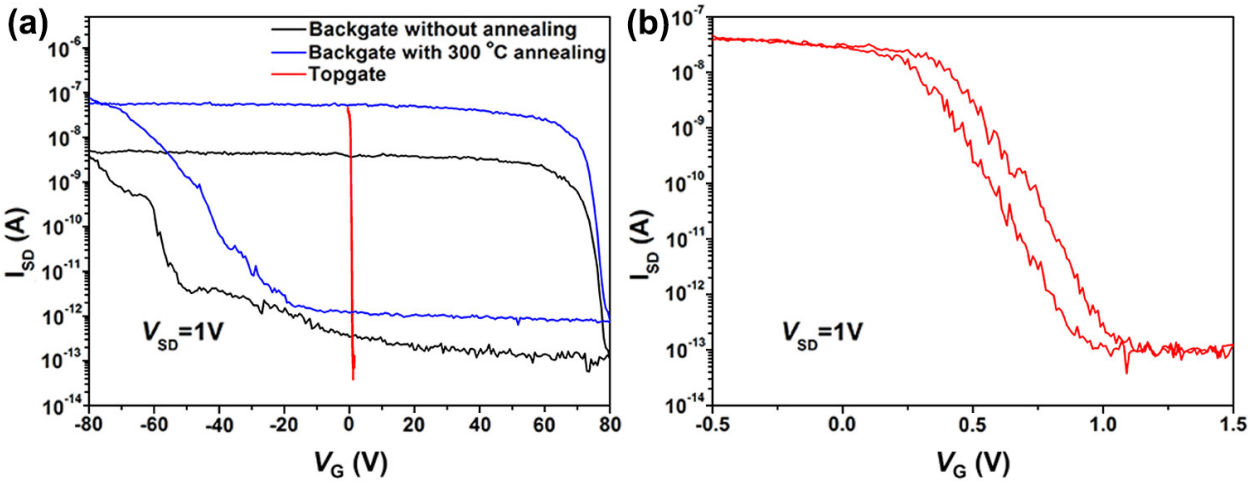

Figure 7.9: (a) Typical transfer performances of short-channel (1µm in length) PODOF wrapped PLV-single-SWCNT FETs with back gate before (black solid line) and after (blue solid line) 300 °C annealing, and top gate (red solid line). (b) The zoom-in transfer curve of the top-gate FET from (a).

7.4. Summary

Highly enriched semiconducting SWCNTs were prepared by combining PODOF-wrapping with size-exclusion chromatography. Length-sorted fractions with a high optical density were obtained which contained individually dispersed semiconducting nanotubes with purity of > 99.7%. The purity of the material was derived from the charge transfer characteristics of short-channel transistors, each of which comprised of ca. 30 densely aligned s-SWCNTs. The transistors with a hole mobility of up to 297 $cm^2V^{-1}s^{-1}$ and On/Off ratio as high as 2×10^8 were fabricated by low frequency dielectrophoresis. Furthermore, by replacing SiO_2 based back-gate modulation with Al top-gate, a sub-threshold swing of down to 95 mV/decade for nanotube based transistors was achieved. These performances are promising for commercial SWCNT-based electronic applications in near future.

Chapter 8: Conclusion and Outlook

This thesis focused on improvement of the dielectrophoretic deposition of semiconducting single-walled carbon nanotubes (s-SWCNTs), and thereby achieving high performance transistors. In particular, it aimed at a systematic comprehension of the dielectrophoresis (DEP) process and micro-fluidic electrohydrodynamics, and provided strategies to realize the high-quality dielectrophoretic deposition of s-SWCNTs.

8.1. Conclusion

The exploration of how to improve s-SWCNT DEP deposition was performed in three different ways by considering the effects of the optical resonant-excitation, dielectric solvent and electric field on polarizability of nanotube.

Firstly, enhancment of CNT polarizability was verified during the light-assisted dielectrophoresis (L-DEP), displaying the feasibility of using a strong optical resonant-excitation to improve the s-SWCNT deposition during high-field DEP. The mechanism behind this process was attributed to the combined effects of the strong excitation, pumping up the generation of excitons, and high dielectrophoretic field which induced the exciton-relaxation. Therefore more free charges were generated within nanotubes which gave rise to an oscillating current with respect to the DEP field, contributing to the polarizability of nanotubes.

Secondly, the influence of DEP based solvents on CNT polarizability was studied through the characterization of nanotube alignment using electric-field induced differential absorption spectroscopy (EFIDAS). Based on both theoretical calculations and experimental characterizations, this technique not only verified the pronounced polarizability of CNTs dispersed in toluene compared to water, but also offered an access to derive the chirality-resolved length distribution of nanotubes suspended in low-conductive solvents.

Thirdly, electric field effects on CNT polarizability was discussed via finite element simulations in which standard DEP chips were modelled and analyzed with respect to the obtained experimental observations. Combined with solvent effect, toluene based direct current (DC-) DEP was demonstrated to be the most efficient way to perform s-SWCNT depositions as compared to toluene based alternating current (AC-) DEP or water based AC-DEP.

Lastly, to achieve high performance CNT transistors, DC-DEPs were conducted on highly enriched s-SWCNTs (with purity of > 99.7%) which were prepared by combining PODOF-wrapping with size-exclusion chromatography based on toluene. A ~30 tubes/μm packing density of CNTs was achieved within the fabricated transistors, which resulted in an on-state conductance of ~10 μS/μm. Moreover, these transistors possessed a hole mobility up to 297 $cm^2V^{-1}s^{-1}$ and On/Off ratio as high as 2×10^8. Furthermore, by replacing SiO_2 based back-gate modulation with Al based top one, a sub-threshold swing of 95 mV/decade for CNT transistors was achieved.

8.2. Outlook

As stated in Chapter 4, by increasing charge flow thereby conductivity of s-SWCNTs, nanotube polarizability was enhanced within L-DEP experiments where the deposition of s-SWCNTs was improved in the presence of a laser compared to the normal DEPs. This achievement left an open-mind question: whether one can achieve the preferential deposition of s-SWCNTs over m-SWCNTs utilizing their permittivity-features. In terms of this purpose, strategy of using real-part nanotube permittivity for DEPs, as discussed in Chapter 4, is inaccessible because it is much smaller for s-SWCNTs. One possible approach is to make use of the imaginary part of nanotube permittivity. It has been reported that s-SWCNTs can be preferentially trapped and separated from a bulk solution in an infrared laser trapping system[210,212]. This phenomenon can be explained by the theory of near-resonance optical trapping as stated in Ref. [280]. In brief, on approaching optical resonance of CNTs using lasers with red-detuned wavelength, a trapping gradient force which is nanotube imaginary part of permittivity dependent and is induced by the intensity profile of the incident beam maximizes, while the scattering force arising from the Rayleigh scattering still has a small fraction of its value at the resonant absorption of CNTs. This provides an enhanced trapping stiffness compared to that at far-off-resonance frequencies of objects. Based on these discoveries, it is expectable that CNTs can be deposited by only applying light fields if these fields can be locally focused on the surface of the targeting substrates using techniques such as attenuated total reflection, etc[281]. Moreover, as an extra benefit of operating light field instead of electric field, large-scale deposition of s-SWCNT may be accessible under such condition.

The CNT geometry plays a crucial role in determining the polarizability of the nanotubes, thereby dominating the feasibility of DEP and performance of CNT-based electronics and optoelectronics. As commented in the thesis, the longer s-SWCNTs may be deposited in better

quality than the shorter m-SWCNTs as employed in toluene based DC-DEPs, which could pave the way to achieve nanotube-selective deposition for different demands concerning CNT-conductivity. Thus this topic is worthy for further studies in future.

The simulations of DEP systems in Chapter 6 were two-dimensional constructed, which decreased the precision of reflecting reality in experiments, especially for the top-view layout where the dielectric influence of solvents on DEPs occurring above metal electrodes is inaccessible. Therefore, a more practical simulation of CNT DEPs should be built using a three dimensional (3D) Comsol model, which will give researchers more information to analyze and design CNT-DEP circuits. Besides, using 3D simulations, one can further explore the whole process of nanotube DEPs, catching numerical details for building up automatic DEP systems in order to improve the reproducibility of CNT depositions in the future.

Notably, the currently achieved packing density of s-SWCNTs based on toluene and low frequency DEPs is about 30 tube/μm, which is still lower than the commercial expectation of 125 tube/μm as mentioned in Chapter 6. This poor achievement can be attributed to the fact that the DEP depositing rate will be slow down or even terminated due to the loss of V_{DEP} after numbers of nanotubes bridged over the electrodes. In order to solve this problem, increasing the applied electric field seems to be a good option to achieve a higher packing density. Furthermore, all the transistors involved in this thesis were tested under DC conditions, the AC performance of these devices are still unknown, which is expected to be attractive for novel radio frequency and microwave applications, and digital circuits because of the ultra-high charge transport mobility and velocity of CNTs. Thus based on the high-purity s-SWCNTs prepared using SEC with PODOF wrapping, the realization of high AC performance of corresponding transistors would be expected.

– This page intentionally left blank –

Appendix A

Table A-1: Parameters, variables and corresponding values used in the calculations and numerical simulations introduced in this thesis.

Variable	Definition	Value	References
l_{CNT}	SWCNT length	1 µm	
d_{CNT}	SWCNT diameter	1.3 nm	
T	Surrounding temperature	300 K	
$V_{DEP} = \varphi_0$	DEP voltage potential (V_{rms})	1~5 V	
ε_0	Vacuum permittivity	8.854×10^{-12} F/m	
ε_m	0.01-w%-SDS water permittivity	$81\times\varepsilon_0$	[79]
	100-ppm-H_2O toluene permittivity	$2.38\times\varepsilon_0$	[282]
	Silicon permittivity	$11.7\times\varepsilon_0$	[283]
	Silicon dioxide permittivity	$3.9\times\varepsilon_0$	[284]
ε_{CNT}	m-SWCNT permittivity	$10000\times\varepsilon_0$	[244]
	s-SWCNT permittivity	$35\times\varepsilon_0$	[79]
σ_m	0.01-w%-SDS water conductivity	0.004 S/m	Measured
	100-ppm-H_2O toluene conductivity	2×10^{-10} S/m	Measured
	Silicon conductivity	4.3×10^{-4} S/m	[285]
	Silicon dioxide conductivity	1×10^{-14} S/m	[286]
σ_{CNT}	m-SWCNT conductivity	1000 S/m	[287]
	s-SWCNT conductivity	0.35 S/m	[79]
ζ	Zeta potential	25 mV	[288]
λ_{De}	Debye length of 0.01-w%-SDS water	16.8 nm	Calculated
	Debye length of 100-ppm-H_2O toluene	9519 nm	Calculated
η	Dynamics viscosity of water	0.894×10^{-3} Pa s	[177]
	Dynamics viscosity of toluene	0.583×10^{-3} Pa s	[289]
K	Water thermal conductivity	0.60 W/(m K)	[177]
	Toluene thermal conductivity	0.14 W/(m K)	[290]
	Silicon thermal conductivity	163 W/(m K)	[177]
	Silicon dioxide thermal conductivity	1.4 W/(m K)	[177]

$\omega = 2\pi f$	Angular frequency	2π (DC, 0.001 Hz~10 MHz)	
ρ_m	Water density	1000 kg/m^3	[177]
	Toluene density	867 kg/m^3	[291]
	Silicon density	2329 kg/m^3	[177]
	Silicon dioxide density	2200 kg/m^3	[177]
ρ_{CNT}	(10, 9) SWCNT density	2363 kg/m^3	Calculated
c_p	Water specific heat capacity	4181 J/(kg K)	[292]
	Toluene specific heat capacity	1720 J/(kg K)	[292]
	Silicon specific heat capacity	706.75 J/(kg K)	[292]
	Silicon dioxide specific heat capacity	722 J/(kg K)	[292]
D	Water diffusion coefficient	2.2×10^{-5} cm^2/s	[293]
	Toluene diffusion coefficient	2.0×10^{-5} cm^2/s	[294]
k_B	Boltzmann constant	1.38×10^{-23} J/K	
L	Electrode gap length	1 µm	
χ	Effective ion size	0.66 nm	
$\vec{g}$	Gravitational acceleration	9.8 m/s^2	
μ_e	H^+ mobility	3.623×10^{-3} cm^2/(V s)	[295]
	OH^- mobility	2.064×10^{-3} cm^2/(V s)	[295]
e	Elementary charge	1.60×10^{-19} C	
c^∞	0.01-w%-SDS Water bulk ion concentration	3.4×10^{-4} mol/L	Measured
	100-ppm-H_2O toluene bulk ion concentration	5.0×10^{-11} mol/L	Measured
z	Valence of ions	+1,-1	

Appendix B

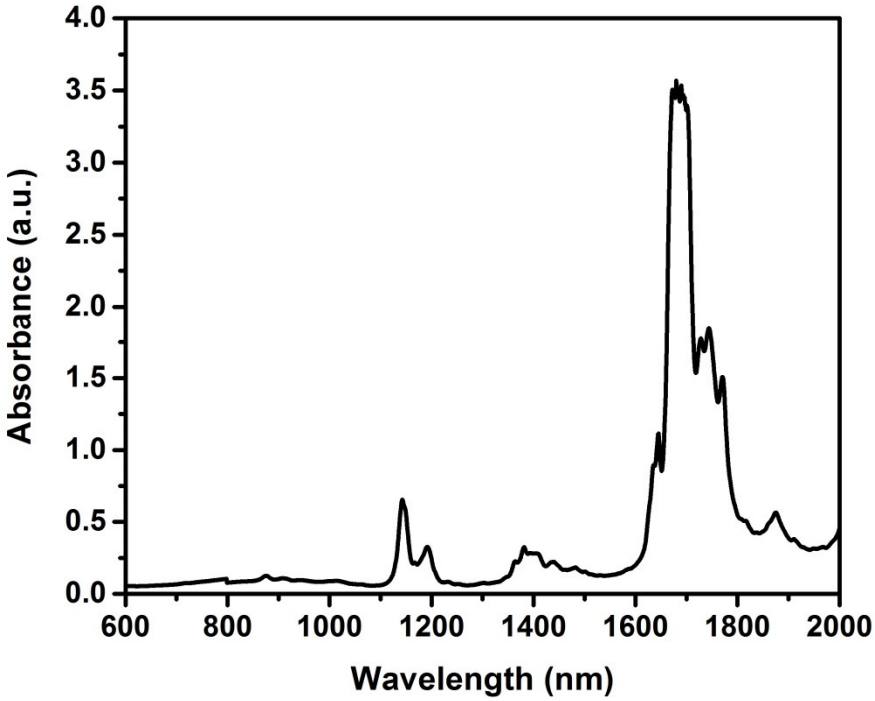

Figure B1: Optical absorption spectrum of toluene used in this thesis.

– This page intentionally left blank –

Appendix C

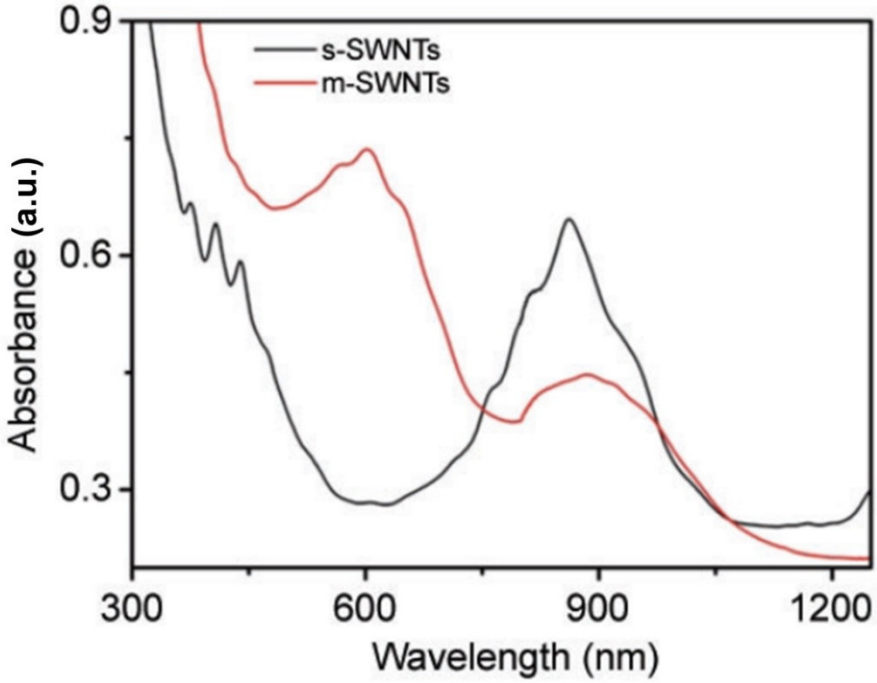

Figure C1: UV-vis-NIR spectra of the eluted SEC fractions of PLV nanotubes, as used in Chapter 7, dispersed in 1-wt%-SDS water (red) and 1-wt% sodium-cholate water (black), reproduced from Ref. [261].

– This page intentionally left blank –

List of Figures

List of Tables

– This page intentionally left blank –

List of Abbreviations

1D 1-Dimensional

AC Alternating Current

ACEO Altering Current Electro-Osmosis

AFM Atomic Force Microscopy

BG Back-Grounded

CCD Charge-Coupled Device

CMF Clausius-Mossotti Factor

CNT Carbon Nanotubes

CVD Chemical Vapor Deposition

DC Direct Current

DCEO Direct Current Electro-Osmosis

DEP Dielectrophoresis

DH Debye-Hückel

EBL Electron-Beam Lithography

EDL Electrical Double Layer

EFIDAS Electric-Field Induced Differential Absorption Spectroscopy

ETF Electrothermal Force

FEM Finite Element Method

FET Field-Effect Transistor

GC Gouy-Chapman

gcd Greatest Common Divisor

GPC Gel Permeation Chromatography

HiPco High Pressure Carbon Monoxide

IC Integrated Circuit

LAND Length Analysis By Nanotube Diffusion

L-DEP Light Assisted Dielectrophoresis

MIBK Methyl Isobutyl Ketone

MOSFET Metal–Oxide–Semiconductor Field-Effect Transistor

MPB Modified Poisson-Boltzmann

m-SWCNT Metallic Single-Walled Carbon Nanotube

MWCNT Multi-walled Carbon Nanotubes

PB Poisson-Boltzmann

PDE Partial Differential Equation

PFH-A Poly[9,9-dihexylfluorenyl-2,7-diyl)-co-(9,10-anthracene)]

PFO Poly(9,9-dioctylfluorene-2,7-diyl)

PFO-BT Poly[(9,9-dioctylfluorenyl-2,7-diyl)-co-1,4-benzo-[2,1'-3]-thiadiazole)]

PLE Photoluminescence

PLV Pulsed Laser Vaporization

PMMA Poly(methyl methacrylate)

PNP Poisson-Nernst-Planck

PODOF Poly(9,9-di-n-dodecylfluorenyl-2,7-diyl)

RBM Radial Breathing Mode

rms Root-Mean Square

SB Schottky Barrier

SC Sodium Cholate

SDS Sodium Dodecyl Sulphate

SEC Size Exclusion Chromatography

SEM Scanning Electron Microscopy

s-SWCNT Semiconducting Single-Walled Carbon Nanotube

SWCNT Single-Walled Carbon Nanotubes

TEM Transmission Electron Microscopy

TG Top-Grounded

vHs van Hove Singularities

Bibliography

[1] J. Svensson, E. E. B. Campbell, *J. Appl. Phys.* 2011, *110*, 111101.

[2] G. Moore, *Electronics* 1965, *38*, 113.

[3] S. Iijima, *Nature* 1991, *354*, 56.

[4] P. L. McEuen, *Phys. World* 2000, *13*, 31.

[5] W. A. de Heer, A. Chatelain, D. Ugarte, *Science* 1995, *270*, 1179.

[6] T. David, A. Jorio, G. Dresselhaus, M. S. Dresselhaus, *Carbon Nanotubes: Advanced Topics in the Synthesis, Structure, Properties and Applications*, Springer, New York, 2008.

[7] C. Thomsen, S. Reich, J. Maultzsch, *Carbon Nanotubes: Basic Concepts and Physical Properties*, Wiley-VCH Verlag GmbH, Weinheim, 2004.

[8] N. Sinha, J. T. W. Yeow, *IEEE Trans. Nanobioscience* 2005, *4*, 180.

[9] M. F. L. De Volder, S. H. Tawfick, R. H. Baughman, A. J. Hart, *Science* 2013, *339*, 535.

[10] R. Khare, S. Bose, *J. Miner. Mater. Charact. Eng.* 2005, *4*, 31.

[11] N. R. Wilson, J. V Macpherson, *Nat Nanotechnol* 2009, *4*, 483.

[12] N. M. Pugno, *J. Phys. Condens. Matter* 2006, *18*, S1971.

[13] S. Berber, Y.-K. Kwon, D. Tomanek, *Phys. Rev. Lett.* 2000, *84*, 4613.

[14] Joel Hruska, "This carbon nanotube heatsink is six times more thermally conductive, could trigger a revolution in CPU clock speeds," can be found under http://www.extremetech.com/extreme/175457-this-carbon-nanotube-heatsink-is-six-times-more-thermally-conductive-could-trigger-a-revolution-in-cpu-clock-speeds, 2014.

[15] Z. Han, A. Fina, *Prog. Polym. Sci.* 2011, *36*, 914.

[16] M. Pfohl, K. Glaser, J. Ludwig, D. D. Tune, S. Dehm, C. Kayser, A. Colsmann, R. Krupke, B. S. Flavel, *Adv. Energy Mater.* 2016, *6*, 1.

[17] S. Bahena-Garrido, N. Shimoi, D. Abe, T. Hojo, Y. Tanaka, K. Tohji, *Rev. Sci. Instrum.* 2014, *85*, 1.

[18] S. Khasminskaya, F. Pyatkov, B. S. Flavel, W. H. Pernice, R. Krupke, *Adv. Mater.* 2014,

26, 3465.

[19] Z. Shi, X. Hong, H. A. Bechtel, B. Zeng, M. C. Martin, K. Watanabe, T. Taniguchi, Y.-R. Shen, F. Wang, *Nat. Photonics* 2015, *9*, 515.

[20] F. Kreupl, *Nature* 2012, *484*, 321.

[21] M. M. Shulaker, G. Hills, N. Patil, H. Wei, H. Y. Chen, H. S. Wong, S. Mitra, *Nature* 2013, *501*, 526.

[22] M. Steiner, M. Engel, Y. M. Lin, Y. Wu, K. Jenkins, D. B. Farmer, J. J. Humes, N. L. Yoder, J. W. T. Seo, A. a. Green, M. C. Hersam, R. Krupke, P. Avouris, *Appl. Phys. Lett.* 2012, *101*, 053123.

[23] D. Sun, M. Y. Timmermans, Y. Tian, A. G. Nasibulin, E. I. Kauppinen, S. Kishimoto, T. Mizutani, Y. Ohno, *Nat. Nanotechnol.* 2011, *6*, 2.

[24] W.-S. Li, P.-X. Hou, C. Liu, D.-M. Sun, J. Yuan, S.-Y. Zhao, L.-C. Yin, H. Cong, H.-M. Cheng, *ACS Nano* 2013, *7*, 6831.

[25] R. Saito, M. Fujita, G. Dresselhaus, M. S. Dresselhaus, *Appl. Phys. Lett.* 1992, *60*, 2204.

[26] T. Ando, *J. Phys. Soc. Japan* 2004, *73*, 3351.

[27] M. S. Rao, A.M.; Richter, E.; Bandow, S.; Chase, B.; Eklund, P.C.; Williams, K.A.; Fang, S.; Subbaswamy, K.R.; Menon, M.; Thess, A.; Smalley, R.E.; Dresselhaus, G.; Dresselhaus, *Science* 1997, *275*, 187.

[28] P. Collins, P. Avouris, *Contemp. Concepts Condens. Matter Sci.* 2008, *3*, 49.

[29] H. Ünlü, N. J. M. Horing, J. Dabowski, *Low-Dimensional and Nanostructured Materials and Devices: Properties, Synthesis, Characterization, Modelling and Applications*, Springer, 2015.

[30] S. J. Tans, A. R. M. Verschueren, C. Dekker, *Nature* 1998, *672*, 669.

[31] D. N. Futaba, K. Hata, T. Yamada, T. Hiraoka, Y. Hayamizu, Y. Kakudate, O. Tanaike, H. Hatori, M. Yumura, S. Iijima, *Nat. Mater.* 2006, *5*, 987.

[32] Q. Cao, J. A. Rogers, *Adv. Mater.* 2009, *21*, 29.

[33] D. S. Bethune, C. H. Klang, M. S. De Vries, G. Gorman, R. Savoy, J. Vazquez, R. Beyers, *Nature* 1993, *363*, 605.

[34] C. Journet, W. K. Maser, P. Bernier, A. Loiseau, M. Lamy de la Chapelle, S. Lefrant, P.

Deniard, R. Lee, J. E. Fischer, *Nature* 1997, *388*, 20.

[35] A. Thess, R. Lee, P. Nikolaev, H. Dai, P. Petit, J. Robert, C. Xu, Y. H. Lee, S. G. Kim, A. G. Rinzler, D. T. Colbert, G. E. Scuseria, D. Tomanek, J. E. Fischer, R. E. Smalley, *Science* 1996, *273*, 483.

[36] A. M. Cassell, J. A. Raymakers, J. Kong, H. Dai, *J. Phys. Chem. B* 1999, *103*, 6484.

[37] P. X. Hou, W. S. Li, S. Y. Zhao, G. X. Li, C. Shi, C. Liu, H. M. Cheng, *ACS Nano* 2014, *8*, 7156.

[38] Y. Li, D. Mann, M. Rolandi, W. Kim, A. Ural, S. Hung, A. Javey, J. Cao, D. Wang, E. Yenilmez, Q. Wang, J. F. Gibbons, Y. Nishi, H. Dai, *Nano Lett.* 2004, *4*, 317.

[39] A. H. Chowdhury, N. Akhter, A. Al Faisal, in *Proc. Glob. Eng. Sci. Technol. Conf. 2012*, 2012, pp. 1–9.

[40] Intel, *Intel Discloses Newest Microarchitecture and 14 Nanometer Manufacturing Process Technical Details*, Intel, 2014.

[41] Z. Arefinia, A. A. Orouji, *Phys. E* 2008, *40*, 3068.

[42] H.-S. P. Wong, D. Akinwande, *Carbon Nanotube and Graphene Device Physics*, Cambridge University Press, 2011.

[43] J. Guo, S. Datta, M. Lundstrom, M. Brink, P. McEuen, A. Javey, H. Dai, H. Kim, P. McIntyre, in *Electron Devices Meet.*, 2002, pp. 711–714.

[44] R. Sahoo, R. Mishra, *Int. J. Electron. Eng. Res.* 2009, *1*, 117.

[45] Y. Ouyang, J. Guo, *Appl. Phys. Lett.* 2006, *89*, 183122.

[46] N. Komatsu, F. Wang, *Materials (Basel).* 2010, *3*, 3818.

[47] X. Xie, S. H. Jin, M. A. Wahab, A. E. Islam, C. Zhang, F. Du, E. Seabron, T. Lu, S. N. Dunham, H. I. Cheong, Y.-C. Tu, Z. Guo, H. U. Chung, Y. Li, Y. Liu, J.-H. Lee, J. Song, Y. Huang, M. A. Alam, W. L. Wilson, J. A. Rogers, *Nat. Commun.* 2014, *5*, 5332.

[48] J. Li, A. D. Franklin, J. Liu, *Nano Lett.* 2015, *15*, 6058.

[49] M. S. Arnold, A. A. Green, J. F. Hulvat, S. I. Stupp, M. C. Hersam, *Nat. Nanotechnol.* 2006, *1*, 60.

[50] A. Behnam, V. K. Sangwan, X. Zhong, F. Lian, D. Estrada, D. Jariwala, A. J. Hoag, L. J. Lauhon, T. J. Marks, M. C. Hersam, E. Pop, *ACS Nano* 2013, *7*, 482.

[51] G. S. Tulevski, A. D. Franklin, A. Afzali, *ACS Nano* 2013, *7*, 2971.

[52] T. Tanaka, H. Jin, Y. Miyata, S. Fujii, H. Suga, Y. Naitoh, T. Minari, T. Miyadera, K. Tsukagoshi, H. Kataura, *Nano Lett.* 2009, *9*, 1497.

[53] R. Voggu, K. V. Rao, S. J. George, C. N. R. Rao, *J. Am. Chem. Soc.* 2010, *132*, 5560.

[54] X. Li, L. Zhang, X. Wang, I. Shimoyama, X. Sun, W. K. Seo, H. Dai, *J. Am. Chem. Soc.* 2007, *129*, 4890.

[55] M. Zheng, A. Jagota, M. S. Strano, A. P. Santos, P. Barone, S. G. Chou, B. A. Diner, M. S. Dresselhaus, R. S. Mclean, G. B. Onoa, G. G. Samsonidze, E. D. Semke, M. Usrey, D. J. Walls, *Science* 2003, *302*, 1545.

[56] S.-N. Zhu, J. Zhang, Q.-W. Li, H.-B. Li, H.-H. Jin, Q.-J. Song, *Chinese J. Anal. Chem.* 2012, *40*, 1839.

[57] W. Gomulya, J. Gaoa, M. A. Loib, *Eur. Phys. J. B* 2013, *86*, 404.

[58] F. Lemasson, N. Berton, J. Tittmann, F. Hennrich, M. M. Kappes, M. Mayor, *Macromolecules* 2012, *45*, 713.

[59] K. S. Mistry, B. A. Larsen, J. L. Blackburn, *ACS Nano* 2013, *7*, 2231.

[60] M. C. LeMieux, M. Roberts, S. Barman, Y. W. Jin, J. M. Kim, Z. Bao, *Science* 2008, *321*, 101.

[61] Y. Wang, S. K. R. Pillai, M. B. Chan-Park, *Small* 2013, *9*, 2960.

[62] Q. Cao, S. Han, G. S. Tulevski, Y. Zhu, D. D. Lu, W. Haensch, *Nat. Nanotechnol.* 2013, *8*, 180.

[63] R. Krupke, F. Hennrich, H. V. Löhneysen, M. M. Kappes, *Science* 2003, *301*, 344.

[64] Q. Cao, S.-J. Han, G. S. Tulevski, *Nat. Commun.* 2014, *5*, 5071.

[65] H. A. Pohl, H. A. Pohl, *Dielectrophoresis: The Behavior of Neutral Matter in Nonuniform Electric Fields*, Cambridge University Press, Cambridge, 1978.

[66] R. Krupke, F. Hennrich, H. B. Weber, M. M. Kappes, H. v. Löhneysen, *Nano Lett.* 2003, *3(8)*, 1019.

[67] A. Castellanos, A. Ramos, A. González, N. G. Green, H. Morgan, *J. Phys. D. Appl. Phys.* 2003, *36*, 2584.

[68] R. Pethig, *Biomicrofluidics* 2010, *4*, 022811.

[69] S. Srivastava, *Biosens. Bioelectron.* 2015, *6*, 1000e136.

[70] R. Pethig, *Adv. Drug Deliv. Rev.* 2013, *65*, 1589.

[71] J. Vykoukal, D. M. Vykoukal, S. Freyberg, E. U. Alt, P. R. C. Gascoyne, *Lab Chip* 2008, *8*, 1386.

[72] H. Song, J. M. Rosano, Y. Wang, C. J. Garson, B. Prabhakarpandian, K. Pant, G. J. Klarmann, A. Perantoni, L. M. Alvarez, E. Lai, *Lab Chip* 2015, *15*, 1320.

[73] S. Yan, J. Zhang, M. Li, G. Alici, H. Du, R. Sluyter, W. Li, *Sci. Rep.* 2014, *4*, 5060.

[74] R. Krupke, F. Hennrich, H. 1 B. Weber, D. Beckmann, O. Hampe, S. Malik, M. M. Kappes, H. v Löhneysen, *Appl. Phys. A* 2003, *76*, 397.

[75] A. Vijayaraghavan, S. Blatt, D. Weissenberger, M. Oron-Carl, F. Hennrich, D. Gerthsen, H. Hahn, R. Krupke, *Nano Lett.* 2007, *7*, 1556.

[76] L. Jensen, O. H. Schmidt, K. V Mikkelsen, P.-O. Astrand, *J. Phys. Chem. B* 2000, *104*, 10462.

[77] V. Perebeinos, P. Avouris, *Nano Lett.* 2007, *7*, 609.

[78] W. Li, F. Pyatkov, S. Dehm, B. S. Flavel, R. Krupke, *Phys. Status Solidi B* 2014, *251*, 2475.

[79] W. Li, F. Hennrich, B. S. Flavel, M. M. Kappes, R. Krupke, *Nanotechnol.* 2016, *27*, 375706.

[80] R. Krupke, F. Hennrich, M. M. Kappes, H. V. Löhneysen, *Nano Lett.* 2004, *4*, 1395.

[81] S. Lijima, T. Ichihashi, *Nature* 1993, *364*, 737.

[82] P. R. Wallace, *Phys. Rev.* 1947, *71*, 622.

[83] J. C. Charlier, X. Blase, S. Roche, *Rev. Mod. Phys.* 2007, *79*, 677.

[84] C. L. Kane, E. J. Mele, *Phys. Rev. Lett.* 1997, *78*, 1932.

[85] M. J. O. Connell, S. M. Bachilo, C. B. Huffman, K. L. Rialon, P. J. Boul, W. H. Noon, C. Kittrell, J. Ma, R. H. Hauge, R. B. Weisman, R. E. Smalley, *Science* 2002, *297*, 593.

[86] J. W. G. Wilder, L. C. Venema, A. G. Rinzler, R. E. Smalley, C. Dekker, *Nature* 1998, *391*, 59.

[87] A. Jorio, A. Souza Filho, G. Dresselhaus, M. Dresselhaus, R. Saito, J. Hafner, C. Lieber,

F. Matinaga, M. Dantas, M. Pimenta, *Phys. Rev. B* 2001, *63*, 245416.

[88] A. Jorio, R. Saito, T. Hertel, R. B. Weisman, G. Dresselhaus, M. S. Dresselhaus, *MRS Bull.* 2004, *29*, 276.

[89] X. Benedict, S. G. Louie, M. L. Cohen, *Phys. Rev. B* 1995, *52*, 8541.

[90] H. Ajiki, T. Ando, *Phys. B* 1994, *201*, 349.

[91] Y. Miyauchi, M. Oba, S. Maruyama, *Phys. Rev. B* 2006, *74*, 205440.

[92] J. Lefebvre, J. Fraser, P. Finnie, Y. Homma, *Phys. Rev. B* 2004, *69*, 075403.

[93] S. Lebedkin, K. Arnold, F. Hennrich, R. Krupke, B. Renker, M. M. Kappes, *New J. Phys.* 2003, *5*, 140.1.

[94] J. M. Kinder, E. J. Mele, *Phys. Rev. B* 2008, *78*, 155429.

[95] H. Liu, D. Nishide, T. Tanaka, H. Kataura, *Nat. Commun.* 2011, *2*, 309.

[96] S. M. Bachilo, M. S. Strano, C. Kittrell, R. H. Hauge, R. E. Smalley, R. B. Weisman, *Science* 2002, *298*, 2361.

[97] P. Avouris, J. Chen, M. Freitag, V. Perebeinos, J. C. Tsang, *Phys. Status Solidi B* 2006, *243*, 3197.

[98] Z. M. Li, Z. K. Tang, H. J. Liu, N. Wang, C. T. Chan, R. Saito, S. Okada, G. D. Li, J. S. Chen, N. Nagasawa, S. Tsuda, *Phys. Rev. Lett.* 2001, *87*, 127401.

[99] S. M. Bachilo, M. S. Strano, C. Kittrell, R. H. Hauge, R. E. Smalley, R. B. Weisman, *Science* 2002, *298*, 2361.

[100] C. Spataru, S. Ismail-Beigi, L. Benedict, S. Louie, *Phys. Rev. Lett.* 2004, *92*, 077402.

[101] H. Haug, S. W. Koch, *Quantum Theory of the Optical and Electronic Properties of Semiconductors*, World Scientific, 1990.

[102] P. Avouris, M. Freitag, V. Perebeinos, *Nat. Photonics* 2008, *2*, 341.

[103] T. Ando, *J. Phys. Soc. Japan* 1997, *66*, 1066.

[104] J. Maultzsch, R. Pomraenke, S. Reich, E. Chang, D. Prezzi, a. Ruini, E. Molinari, M. Strano, C. Thomsen, C. Lienau, *Phys. Rev. B* 2005, *72*, 241402.

[105] F. Wang, D. J. Cho, B. Kessler, J. Deslippe, P. J. Schuck, S. G. Louie, A. Zettl, T. F. Heinz, Y. R. Shen, *Phys. Rev. Lett.* 2007, *99*, 227401.

[106] V. Perebeinos, J. Tersoff, P. Avouris, *Phys. Rev. Lett.* 2004, *92*, 257402.

[107] J. Shaver, J. Kono, O. Portugall, V. Krstic, G. L. J. A. Rikken, Y. Miyauchi, S. Maruyama, V. Perebeinos, *Nano Lett.* 2007, *7*, 1851.

[108] S. Berger, C. Voisin, G. Cassabois, C. Delalande, P. Roussignol, X. Marie, *Nano Lett.* 2007, *7*, 398.

[109] J. C. Meyer, M. Paillet, T. Michel, A. Moréac, A. Neumann, G. S. Duesberg, S. Roth, J.-L. Sauvajol, *Phys. Rev. Lett.* 2005, *95*, 217401.

[110] M. S. Dresselhaus, G. Dresselhaus, R. Saito, a. Jorio, *Phys. Rep.* 2005, *409*, 47.

[111] A. Jorio, R. Saito, J. H. Hafner, C. M. Lieber, M. Hunter, T. Mcclure, G. Dresselhaus, M. S. Dresselhaus, *Phys. Rev. Lett.* 2001, *86*, 1118.

[112] S. D. M. Brown, A. Jorio, P. Corio, M. S. Dresselhaus, G. Dresselhaus, R. Saito, K. Kneipp, *Phys. Rev. B* 2001, *63*, 155414.

[113] F. Hennrich, R. Krupke, S. Lebedkin, K. Arnold, R. Fischer, D. E. Resasco, M. M. Kappes, *J. Phys. Chem. B* 2005, *109*, 10567.

[114] S. Datta, *Electronic Transport in Mesoscopic Systems*, Cambridge University Press, 1997.

[115] P. McEuen, M. Bockrath, D. Cobden, Y.-G. Yoon, S. Louie, *Phys. Rev. Lett.* 1999, *83*, 5098.

[116] Z. Yao, C. Kane, C. Dekker, *Phys. Rev. Lett.* 2000, *84*, 2941.

[117] A. Javey, J. Guo, M. Paulsson, Q. Wang, D. Mann, M. Lundstrom, H. Dai, *Phys. Rev. Lett.* 2004, *92*, 106804.

[118] J. Y. Park, S. Rosenblatt, Y. Yaish, V. Sazonova, H. Üstunel, S. Braig, T. A. Arias, P. W. Brouwer, P. L. McEuen, *Nano Lett.* 2004, *4*, 517.

[119] S. Li, Z. Yu, C. Rutherglen, P. J. Burke, *Nano Lett.* 2004, *4*, 2003.

[120] T. Dürkop, S. A. Getty, E. Cobas, M. S. Fuhrer, *Nano Lett.* 2004, *4*, 35.

[121] S. Li, Z. Yu, S. F. Yen, W. C. Tang, P. J. Burke, *Nano Lett.* 2004, *4*, 753.

[122] A. Javey, J. Guo, Q. Wang, M. Lundstrom, H. Dai, *Nature* 2003, *424*, 654.

[123] A. Szabó, C. Perri, A. Csató, G. Giordano, D. Vuono, J. B. Nagy, *Materials (Basel).* 2010, *3*, 3092.

[124] P. Nikolaev, M. J. Bronikowski, R. K. Bradley, F. Rohmund, D. T. Colbert, K. a Smith, R. E. Smalley, *Chem. Phys. Lett.* 1999, *313*, 91.

[125] J. A. Isaacs, A. Tanwani, M. L. Healy, L. J. Dahlben, *J. Nanoparticle Res.* 2010, *12*, 551.

[126] P. C. Eklund, B. K. Pradhan, U. J. Kim, Q. Xiong, J. E. Fischer, a. D. Friedman, B. C. Holloway, K. Jordan, M. W. Smith, *Nano Lett.* 2002, *2*, 561.

[127] S. Lebedkin, P. Schweiss, B. Renker, S. Malik, F. Hennrich, M. Neumaier, C. Stoermer, M. M. Kappes, *Carbon* 2002, *40*, 417.

[128] F. Hennrich, W. Li, R. Fischer, S. Lebedkin, R. Krupke, M. M. Kappes, *ACS Nano* 2016, *10*, 1888.

[129] M. S. Arnold, S. I. Stupp, M. C. Hersam, *Nano Lett.* 2005, *5*, 713.

[130] K. Tvrdy, R. M. Jain, R. Han, A. J. Hilmer, T. P. McNicholas, M. S. Strano, *ACS Nano* 2013, 1779.

[131] M. Zheng, A. Jagota, E. D. Semke, B. A. Diner, R. S. McLean, S. R. Lustig, R. E. Richardson, N. G. Tassi, *Nat. Mater.* 2003, *2*, 338.

[132] A. Nish, J.-Y. Hwang, J. Doig, R. J. Nicholas, *Nat. Nanotechnol.* 2007, *2*, 640.

[133] J.-Y. Hwang, A. Nish, J. Doig, S. Douven, C.-W. Chen, L.-C. Chen, R. J. Nicholas, *J. Am. Chem. Soc.* 2008, *130*, 3543.

[134] A. H. Brozena, J. Moskowitz, B. Shao, S. Deng, H. Liao, K. J. Gaskell, Y. Wang, *J. Am. Chem. Soc.* 2010, *132*, 3932.

[135] S. Deng, A. H. Brozena, Y. Zhang, Y. Piao, Y. Wang, *Chem. Commun.* 2011, *47*, 758.

[136] R. Bandyopadhyaya, E. Nativ-Roth, O. Regev, R. Yerushalmi-Rozen, *Nano Lett.* 2002, *2*, 25.

[137] L. Cooper, H. Amano, M. Hiraide, S. Houkyou, I. Y. Jang, Y. J. Kim, H. Muramatsu, J. H. Kim, T. Hayashi, Y. A. Kim, M. Endo, M. S. Dresselhaus, *Appl. Phys. Lett.* 2009, *95*, 233104.

[138] J. L. Hudson, M. J. Casavant, J. M. Tour, *J. Am. Chem. Soc.* 2004, *126*, 11158.

[139] S. Banerjee, S. S. Wong, *Nano Lett.* 2004, *4*, 1445.

[140] K. H. An, J. S. Park, C. M. Yang, S. Y. Jeong, S. C. Lim, C. Kang, J. H. Son, M. S. Jeong, Y. H. Lee, *J. Am. Chem. Soc.* 2005, *127*, 5196.

[141] E. T. Mickelson, C. B. Huffman, A. G. Rinzler, R. E. Smalley, R. H. Hauge, J. L. Margrave, *Chem. Phys. Lett.* 1998, *296*, 188.

[142] A. J. Blanch, C. E. Lenehan, J. S. Quinton, *J. Phys. Chem. B* 2010, *114*, 9805.

[143] B. S. Flavel, K. E. Moore, M. Pfohl, M. M. Kappes, F. Hennrich, *ACS Nano* 2014, *8*, 1817.

[144] N. R. Tummala, A. Striolo, *ACS Nano* 2009, *3*, 595.

[145] Z. Xu, X. Yang, Z. Yang, *Nano Lett.* 2010, *10*, 985.

[146] J. Han, Q. Ji, S. Qiu, H. Li, S. Zhang, H. Jin, Q. Li, *Chem. Commun.* 2015, *51*, 4712.

[147] K. E. Moore, D. D. Tune, B. S. Flavel, *Adv. Mater.* 2015, *27*, 3105.

[148] F. M. Chen, B. Wang, Y. Chen, L. J. Li, *Nano Lett.* 2007, *7*, 3013.

[149] W. Gomulya, G. D. Costanzo, E. J. F. De Carvalho, S. Z. Bisri, V. Derenskyi, M. Fritsch, N. Fröhlich, S. Allard, P. Gordiichuk, A. Herrmann, S. J. Marrink, M. C. Dos Santos, U. Scherf, M. A. Loi, *Adv. Mater.* 2013, *25*, 2948.

[150] S. K. Samanta, M. Fritsch, U. Scherf, W. Gomulya, S. Z. Bisri, M. A. Loi, *Acc. Chem. Res.* 2014, *47*, 2446.

[151] F. Lemasson, J. Tittmann, F. Hennrich, N. Stürzl, S. Malik, M. M. Kappes, M. Mayor, *Chem. Commun.* 2011, *47*, 7428.

[152] M. J. Shea, R. D. Mehlenbacher, M. T. Zanni, M. S. Arnold, *J. Phys. Chem. Lett.* 2014, *5*, 3742.

[153] H. Wang, B. Hsieh, G. Jiménez-Osés, P. Liu, C. J. Tassone, Y. Diao, T. Lei, K. N. Houk, Z. Bao, *Small* 2015, *11*, 126.

[154] L. Jensen, P.-O. Astrand, K. V Mikkelsen, *J. Phys. Chem. A* 2004, *108*, 8795.

[155] B. Kozinsky, N. Marzari, *Phys. Rev. Lett.* 2006, *96*, 166801.

[156] G. Falkovich, *Fluid Mechanics: A Short Course for Physicists*, Cambridge University Press, 2011.

[157] H. Morgan, N. G. Green, *AC Electrokinetics: Colloids and Nanoparticles*, Research Studies Press, 2003.

[158] R. Saito, G. Dresselhaus, M. S. Dresselhaus, others, *Physical Properties of Carbon Nanotubes*, World Scientific, 1998.

[159] R. Rao, D. Liptak, T. Cherukuri, B. I. Yakobson, B. Maruyama, *Nat. Mater.* 2012, *11*, 213.

[160] T. Hida, in *Brownian Motion*, Springer, 1980, pp. 44–113.

[161] D. A. Tsyboulski, S. M. Bachilo, A. B. Kolomeisky, R. B. Weisman, *ACS Nano* 2008, *2*, 1770.

[162] S. Broersma, *J. Chem. Phys.* 1981, *74*, 6989.

[163] Y. Han, A. M. Alsayed, M. Nobili, J. Zhang, T. C. Lubensky, A. G. Yodh, *Science* 2006, *314*, 626.

[164] F. Perrin, *J. phys. radium* 1934, *5*, 497.

[165] F. Perrin, *J. phys. radium* 1936, *7*, 1.

[166] H. A. Pohl, *Dielectrophoresis: The Behavior of Neutral Matter in Nonuniform Electric Fields*, Cambridge University Press, Cambridge, 1978.

[167] Y. Kim, S. Hong, S. Jung, M. S. Strano, J. Choi, S. Baik, *J. Phys. Chem. B* 2006, *110*, 1541.

[168] T. B. Jones, *Electromechanics of Particles*, Cambridge University Press, Cambridge, 1995.

[169] S. Blatt, F. Hennrich, H. V. Löhneysen, M. M. Kappes, A. Vijayaraghavan, R. Krupke, *Nano Lett.* 2007, *7*, 1960.

[170] A. Ramos, H. Morgan, N. G. Green, A. Castellanos, *J. Phys. D. Appl. Phys.* 1998, *31*, 2338.

[171] A. Castellanos, *Electrohydrodynamics*, Springer, New York, 1998.

[172] D. A. Saville, *Annu. Rev. Fluid Mech.* 1997, *29*, 27.

[173] E. Hückel, P. Debye, *Phys. Zeitschrift* 1923, *24*, 185.

[174] J. R. Melcher, G. I. Taylor, *Annu. Rev. Fluid Mech.* 1969, *1*, 111.

[175] C. W. Fetter, *Contaminant Hydrogeology*, Prentice Hall, New Jersey, 1999.

[176] N. G. Green, A. Ramos, A. González, A. Castellanos, H. Morgan, *J. Electrostat.* 2001, *53*, 71.

[177] D. R. Lide, W. M. Haynes, *CRC Handbook of Chemistry and Physics*, CRC, London,

2009.

[178] R. F. Probstein, *Physicochemical Hydrodynamics: An Introduction*, John Wiley & Sons, 2005.

[179] B. J. Kirby, *Micro-and Nanoscale Fluid Mechanics: Transport in Microfluidic Devices*, Cambridge University Press, 2010.

[180] J. N. Reddy, *An Introduction to the Finite Element Method*, McGraw-Hill New York, 1993.

[181] R. T. Tung, *Appl. Phys. Rev.* 2014, *1*, 11304.

[182] S. Tans, A. Verschueren, C. Dekker, *Nature* 1998, *672*, 669.

[183] R. Martel, T. Schmidt, H. R. Shea, T. Hertel, P. Avouris, *Appl. Phys. Lett.* 1998, *73*, 2447.

[184] C. W. Zhou, J. Kong, H. J. Dai, *Appl. Phys. Lett.* 2000, *76*, 1597.

[185] F. Leonard, J. Tersoff, *Phys. Rev. Lett.* 2000, *84*, 4693.

[186] S. Heinze, J. Tersoff, R. Martel, V. Derycke, J. Appenzeller, P. Avouris, *Phys. Rev. Lett.* 2002, *89*, 106801.

[187] X. Cui, M. Freitag, R. Martel, L. Brus, P. Avouris, *Nano Lett.* 2003, *3*, 783.

[188] Z. Chen, J. Appenzeller, J. Knoch, Y. Lin, P. Avouris, *Nano Lett.* 2005, *5*, 1497.

[189] M. J. Biercuk, S. Ilani, C. M. Marcus, P. L. Mceuen, *Top. Appl. Phys.* 2008, *111*, 455.

[190] A. Javey, J. Guo, D. B. Farmer, Q. Wang, E. Yenilmez, R. G. Gordon, M. Lundstrom, H. Dai, *Nano Lett.* 2004, *4*, 1319.

[191] A. Javey, R. Tu, D. B. Farmer, J. Guo, R. G. Gordon, H. Dai, *Nano Lett.* 2005, *5*, 345.

[192] J. Chen, C. Klinke, A. Afzali, P. Avouris, *arXiv Prepr. cond-mat/0511039* 2005.

[193] A. Javey, J. Guo, D. B. Farmer, Q. Wang, D. Wang, R. G. Gordon, M. Lundstrom, H. Dai, *Nano Lett.* 2004, *4*, 447.

[194] L. D. Circuits, A. Raychowdhury, K. Roy, *Ieee Trans. Circuits Syst. Regul. Pap.* 2007, *54*, 2391.

[195] A. Raychowdhury, S. Mukhopadhyay, K. Roy, *IEEE Trans. Comput. Des. Integr. Circuits Syst.* 2004, *23*, 1411.

[196] J. Vavro, M. C. Llaguno, J. E. Fischer, S. Ramesh, R. K. Saini, L. M. Ericson, V. A. Davis, R. H. Hauge, M. Pasquali, R. E. Smalley, *Phys. Rev. Lett.* 2003, *90*, 065503.

[197] Y. Nonoguchi, K. Ohashi, R. Kanazawa, K. Ashiba, K. Hata, T. Nakagawa, C. Adachi, T. Tanase, T. Kawai, *Sci Rep* 2013, *3*, 3344.

[198] J. Chen, C. Klinke, A. Afzali, P. Avouris, *Appl. Phys. Lett.* 2005, *86*, 1.

[199] J. Park, P. Deria, J.-H. Olivier, M. J. Therien, *Nano Lett.* 2014, *14*, 504.

[200] D. A. Heller, R. M. Mayrhofer, S. Baik, Y. V. Grinkova, M. L. Usrey, M. S. Strano, *J. Am. Chem. Soc.* 2004, *126*, 14567.

[201] B. J. Bauer, M. L. Becker, V. Bajpai, J. A. Fagan, E. K. Hobbie, K. Migler, C. M. Guttman, W. R. Blair, *J. Phys. Chem. C* 2007, *111*, 17914.

[202] S. Lebedkin, F. Hennrich, O. Kiowski, M. M. Kappes, *Phys. Rev. B* 2008, *77*, 165429.

[203] J. K. Streit, S. M. Bachilo, S. Ghosh, C.-W. Lin, R. B. Weisman, *Nano Lett.* 2014, *14*, 1530.

[204] N. Nair, M. L. Usrey, W.-J. Kim, R. D. Braatz, M. S. Strano, *Anal. Chem.* 2006, *78*, 7689.

[205] R. B. Pipes, S. J. V Frankland, P. Hubert, E. Saether, *Compos. Sci. Technol.* 2003, *63*, 1349.

[206] J. R. Moffitt, Y. R. Chemla, S. B. Smith, C. Bustamante, *Biochemistry* 2008, *77*, 205.

[207] A. Ashkin, *Proc. Natl. Acad. Sci.* 1997, *94*, 4853.

[208] D. G. Grier, *Nature* 2003, *424*, 810.

[209] J. Plewa, E. Tanner, D. Mueth, D. Grier, *Opt. Express* 2004, *12*, 1978.

[210] S. Tan, H. A. Lopez, C. W. Cai, Y. Zhang, *Nano Lett.* 2004, *4*, 1415.

[211] J. Fagan, J. Simpson, B. Landi, L. Richter, I. Mandelbaum, V. Bajpai, D. Ho, R. Raffaelle, a. Walker, B. Bauer, E. Hobbie, *Phys. Rev. Lett.* 2007, *98*, 147402.

[212] J. C. McDonald, G. M. Whitesides, *Acc. Chem. Res.* 2002, *35*, 491.

[213] R. B. Capaz, C. D. Spataru, S. Ismail-Beigi, S. G. Louie, *Phys. Rev. B* 2006, *74*, 121401.

[214] Y. Kumamoto, M. Yoshida, a. Ishii, a. Yokoyama, T. Shimada, Y. K. Kato, *Phys. Rev. Lett.* 2014, *112*, 117401.

[215] D. J. Bindl, A. J. Ferguson, M.-Y. Wu, N. Kopidakis, J. L. Blackburn, M. S. Arnold, *J. Phys. Chem. Lett.* 2013, *4*, 3550.

[216] A. D. Mohite, P. Gopinath, H. M. Shah, B. W. Alphenaar, *Nano Lett.* 2008, *8*, 142.

[217] A. Mohite, J.-T. Lin, G. Sumanasekera, B. W. Alphenaar, *Nano Lett.* 2006, *6*, 1369.

[218] Y. F. Chen, M. S. Fuhrer, *Phys. Rev. Lett.* 2005, *95*, 236803.

[219] G. F. Novikov, M. V. Gapanovich, E. V. Rabenok, L. M. Bogdanova, L. I. Kuzub, *Russ. Chem. Bull.* 2011, *60*, 419.

[220] A. L. McClellan, *Tables of Experimental Dipole Moments*, Rahara Enterprises, EI Cerrito, CA, 1974.

[221] Z. Gao, L. Oudjedi, R. Faes, F. Moroté, C. Jaillet, P. Poulin, B. Lounis, L. Cognet, *Sci. Rep.* 2015, *5*, 17093.

[222] D. Simien, J. A. Fagan, W. Luo, J. F. Douglas, K. Migler, J. Obrzut, *ACS Nano* 2008, *2*, 1879.

[223] S. Wang, Z. Liang, B. Wang, C. Zhang, *Nanotechnology* 2006, *17*, 634.

[224] R. Piner, R. S. Ruoff, *arXiv Prepr. cond-mat/0206117* 2002.

[225] S. Badaire, P. Poulin, M. Maugey, C. Zakri, *Langmuir* 2004, *20*, 10367.

[226] J. Y. Lee, J. S. Kim, K. H. An, K. Lee, D. Y. Kim, D. J. Bae, Y. H. Lee, *J. Nanosci. Nanotechnol.* 2005, *5*, 1045.

[227] B. J. Bauer, J. a. Fagan, E. K. Hobbie, J. Chun, V. Bajpai, *J. Phys. Chem. C* 2008, *112*, 1842.

[228] A. M. Shetty, G. M. H. Wilkins, J. Nanda, M. J. Solomon, *J. Phys. Chem. C* 2009, *113*, 7129.

[229] L. F. Pease, D.-H. Tsai, J. A. Fagan, B. J. Bauer, R. A. Zangmeister, M. J. Tarlov, M. R. Zachariah, *Small* 2009, *5*, 2894.

[230] J. K. Streit, S. M. Bachilo, A. V. Naumov, C. Khripin, M. Zheng, R. B. Weisman, *ACS Nano* 2012, *6*, 8424.

[231] J. P. Casey, S. M. Bachilo, C. H. Moran, R. B. Weisman, *ACS Nano* 2008, *2*, 1738.

[232] C. a Silvera Batista, M. Zheng, C. Y. Khripin, X. Tu, J. a Fagan, *Langmuir* 2014, *30*, 4895.

[233] R. B. Weisman, S. M. Bachilo, *Nano Lett.* 2003, *3*, 1235.

[234] A. I. Oliva-Avilés, F. Avilés, V. Sosa, A. I. Oliva, F. Gamboa, *Nanotechnology* 2012, *23*, 465710.

[235] M. Monti, M. Natali, L. Torre, J. M. Kenny, *Carbon* 2012, *50*, 2453.

[236] S. Kaida, J. Matsui, T. Sagae, Y. Hoshikawa, T. Kyotani, T. Miyashita, *Carbon* 2013, *59*, 503.

[237] Y. Fujimura, T. Kamijo, H. Yoshimi, *Int. Soc. Opt. Photonics* 2003, 96.

[238] M. J. Stephen, J. P. Straley, *Rev. Mod. Phys.* 1974, *46*, 617.

[239] N. Izard, E. Gaufrès, S. Kazaoui, Y. Murakami, D. Marris-Morini, E. Cassan, S. Maruyama, L. Vivien, *Phys. E* 2012, *44*, 932.

[240] N. Izard, E. Gaufrès, X. Le Roux, S. Kazaoui, Y. Murakami, D. Marris-Morini, E. Cassan, S. Maruyama, L. Vivien, *Eur. Phys. J. Appl. Phys.* 2011, *55*, 20401.

[241] G. S. Duesberg, M. Burghard, J. Muster, G. Philipp, *Chem. Commun.* 1998, *3*, 435.

[242] H. Lin, J. Lagoute, V. Repain, C. Chacon, Y. Girard, J.-S. Lauret, F. Ducastelle, A. Loiseau, S. Rousset, *Nat. Mater.* 2010, *9*, 235.

[243] A. D. Franklin, *Nature* 2013, *498*, 443.

[244] S. Blatt, *Dielectrophoresis of Single-Walled Carbon*, Forschungszentrum Karlsruhe GmbH, Karlsruhe, 2008.

[245] M. S. Kilic, M. Z. Bazant, A. Ajdari, *Phys. Rev. E* 2007, *75*, 1.

[246] J. N. Israelachvili, *Intermolecular and Surface Forces: Revised Third Edition*, Academic Press, 2011.

[247] F. Booth, *J. Chem. Phys.* 1955, *23*, 453.

[248] H. Liu, S. Qian, H. H. Bau, *Biophys. J.* 2007, *92*, 1164.

[249] M. S. Kilic, M. Z. Bazant, A. Ajdari, *Phys. Rev. E* 2007, *75*, 021503.

[250] V. N. Paunov, R. I. Dimova, P. A. Kralchevsky, G. Broze, A. Mehreteab, *J. Colloid Interface Sci.* 1996, *182*, 239.

[251] B. R. Burg, V. Bianco, J. Schneider, D. Poulikakos, *J. Appl. Phys.* 2010, *107*, 124308.

[252] Y. Che, H. Chen, H. Gui, J. Liu, B. Liu, C. Zhou, *Semicond. Sci. Technol.* 2014, *29*,

073001.

[253] C. Wang, K. Takei, T. Takahashi, A. Javey, *Chem. Soc. Rev.* 2013, *42*, 2592.

[254] S. Park, M. Vosguerichian, Z. Bao, *Nanoscale* 2013, *5*, 1727.

[255] L. Nougaret, G. Dambrine, S. Lepilliet, H. Happy, N. Chimot, V. Derycke, J. P. Bourgoin, *Appl. Phys. Lett.* 2010, *96*, 042109.

[256] D. Jariwala, V. K. Sangwan, L. J. Lauhon, T. J. Marks, M. C. Hersam, *Chem. Soc. Rev.* 2013, *42*, 2824.

[257] G. J. Brady, Y. Joo, M.-Y. Wu, M. J. Shea, P. Gopalan, M. S. Arnold, *ACS Nano* 2014, *8*, 11614.

[258] W. Kim, A. Javey, R. Tu, J. Cao, Q. Wang, H. Dai, *Appl. Phys. Lett.* 2005, *87*, 1.

[259] A. Vijayaraghavan, F. Hennrich, N. Stürzl, M. Engel, M. Ganzhorn, M. Oron-Carl, C. W. Marquardt, S. Dehm, S. Lebedkin, M. M. Kappes, R. Krupke, *ACS Nano* 2010, *4*, 2748.

[260] M. H. P. Pfeiffer, N. Stürzl, C. W. Marquardt, M. Engel, S. Dehm, F. Hennrich, M. M. Kappes, U. Lemmer, R. Krupke, *Opt. Express* 2011, *19*, A1184.

[261] K. Moshammer, F. Hennrich, M. M. Kappes, *Nano Res.* 2009, *2*, 599.

[262] R. Saito, M. Hofmann, G. Dresselhaus, A. Jorio, M. S. Dresselhaus, *Adv. Phys.* 2011, *60*, 413.

[263] P. Finnie, J. Ding, Z. Li, C. T. Kingston, *J. Phys. Chem. C* 2014, *118*, 30127.

[264] J. Maultzsch, H. Telg, S. Reich, C. Thomsen, *Phys. Rev. B* 2005, *72*, 205438.

[265] G. J. Brady, Y. Joo, S. S. Roy, P. Gopalan, M. S. Arnold, *Appl. Phys. Lett.* 2014, *104*, 083107.

[266] M. Engel, M. Steiner, R. S. Sundaram, R. Krupke, A. a Green, M. C. Hersam, P. Avouris, *ACS Nano* 2012, *6*, 7303.

[267] M. L. Geier, J. J. McMorrow, W. Xu, J. Zhu, C. H. Kim, T. J. Marks, M. C. Hersam, *Nat. Nanotechnol.* 2015, *10*, 944.

[268] J. Ding, Z. Li, J. Lefebvre, F. Cheng, J. L. Dunford, P. R. L. Malenfant, J. Humes, J. Kroeger, *Nanoscale* 2015, *7*, 15741.

[269] J. Ding, Z. Li, J. Lefebvre, F. Cheng, G. Dubey, S. Zou, P. Finnie, A. Hrdina, L. Scoles,

G. P. Lopinski, C. T. Kingston, B. Simard, P. R. L. Malenfant, *Nanoscale* 2014, *6*, 2328.

[270] Z. Li, J. Ding, P. Finnie, J. Lefebvre, F. Cheng, C. T. Kingston, R. L. Malenfant, 2015, *8*, 2179.

[271] Z. Li, J. Ding, J. Lefebvre, P. R. L. Malenfant, *Org. Electron.* 2015, *26*, 15.

[272] M. S. Fuhrer, B. M. Kim, T. Dürkop, T. Brintlinger, *Nano Lett.* 2002, *2*, 755.

[273] R. Park, M. M. Shulaker, G. Hills, L. S. Liyanage, S. Mitra, H. S. P. Wong, *ACS Nano* 2016, *10*, 4599.

[274] P. G. Collins, K. Bradley, M. Ishigami, A. Zettl, *Science* 2000, *287*, 1801.

[275] W. Kim, a Javey, O. Vermesh, O. Wang, Y. M. Li, H. J. Dai, *Nano Lett.* 2003, *3*, 193.

[276] J. S. Lee, S. Ryu, K. Yoo, I. S. Choi, W. S. Yun, J. Kim, *J. Phys. Chem. C* 2007, *111*, 12504.

[277] K. Bradley, J. Cumings, A. Star, J. C. P. Gabriel, G. Grüner, *Nano Lett.* 2003, *3*, 639.

[278] M. Radosavljevic, M. Freitag, K. V. Thadani, A. T. Johnson, *Nano Lett.* 2002, *2*, 761.

[279] Q. Qian, G. Li, Y. Jin, J. Liu, Y. Zou, K. Jiang, S. Fan, Q. Li, *ACS Nano* 2014, *8*, 9597.

[280] R. R. Agayan, F. Gittes, R. Kopelman, C. F. Schmidt, *Appl. Opt.* 2002, *41*, 2318.

[281] N. J. Harrick, *Internal Reflection Spectroscopy*, Harrick Scientific Corp., 1967.

[282] G. Ritzoulis, N. Papadopoulos, D. Jannakoudakis, *J. Chem. Eng. Data* 1986, *31*, 146.

[283] W. C. Dunlap, Jr., R. L. Watters, *Phys. Rev.* 1953, *92*, 1396.

[284] P. R. Gray, P. Hurst, R. G. Meyer, S. Lewis, *Analysis and Design of Analog Integrated Circuits*, Wiley, New York, 2001.

[285] G. Eranna, *Crystal Growth and Evaluation of Silicon for VLSI and ULSI*, CRC Press, 2014.

[286] J. K. Srivastava, M. Prasad, J. B. Wagner, *J. Electrochem. Soc.* 1985, *132*, 955.

[287] B. R. Burg, J. Schneider, V. Bianco, N. C. Schirmer, D. Poulikakos, *Langmuir* 2010, *26*, 10419.

[288] P. Somasundaran, T. W. Healy, D. W. Fuerstenau, *J. Phys. Chem.* 1964, *68*, 3562.

[289] F. J. V Santos, C. A. Nieto De Castro, J. H. Dymond, N. K. Dalaouti, M. J. Assael, A. Nagashima, *J. Phys. Chem. Ref. Data* 2006, *35*, 1.

[290] C. A. N. de Castro, S. F. Y. Li, A. Nagashima, R. D. Trengove, W. A. Wakeham, *J. Phys. Chem. Ref. data* 1986, *15*, 1073.

[291] N. F. Glen, A. I. Johns, *J. Chem. Eng. Data* 2009, *54*, 2538.

[292] D. R. Lide, *CRC Handbook of Chemistry and Physics*, CRC Press, 2004.

[293] D. E. O'Reilly, E. M. Peterson, *J. Chem. Phys.* 1971, *55*, 2155.

[294] D. E. O'Reilly, E. M. Peterson, *J. Chem. Phys.* 1972, *56*, 2262.

[295] P. W. Atkins, J. De Paula, *Atkins' Physical Chemistry*, Oxford University Press, London, 2010.

– This page intentionally left blank –

Attached CD

– This page intentionally left blank –